3-2022

# Capability Development for Advanced (n,x) Nuclear Data Measurements

Brian G. Frandsen


# Capability Development for Advanced (n,x) Nuclear Data Measurements

DISSERTATION

Brian G. Frandsen, Major, USAF

AFIT-ENP-DS-22-M-091

**DEPARTMENT OF THE AIR FORCE**
**AIR UNIVERSITY**

***AIR FORCE INSTITUTE OF TECHNOLOGY***

**Wright-Patterson Air Force Base, Ohio**

AFIT-ENP-DS-22-M-091

# CAPABILITY DEVELOPMENT FOR ADVANCED (N,X) NUCLEAR DATA MEASUREMENTS

DISSERTATION

Presented to the Faculty

Graduate School of Engineering and Management

Air Force Institute of Technology

Air University

Air Education and Training Command

in Partial Fulfillment of the Requirements for the

Degree of Doctor of Philosophy in Nuclear Engineering

Brian G. Frandsen, M.S.

Major, USAF

March 2022

AFIT-ENP-DS-22-M-091

# CAPABILITY DEVELOPMENT FOR ADVANCED (N,X) NUCLEAR DATA MEASUREMENTS

DISSERTATION

Brian G. Frandsen, M.S.
Major, USAF

Committee Membership:

Maj James E. Bevins (Chairman)

Dr. John W. McClory (Member)

Dr. Darren L. Bleuel (Member)

Dr. Juan J. Manfredi (Member)

Dr. Mark E. Oxley (Member)

AFIT-ENP-DS-22-M-091

# Abstract

Nuclear reaction data are at the heart of radiation transport calculations, models, and simulations. In the Department of Defense, these data are critical for nonproliferation, nuclear forensics, and nuclear weapon applications. Unique approaches are required to improve the measurement capability for many reactions where data are inaccurate or do not exist. First, the newly developed Gamma Energy Neutron Energy Spectrometer for Inelastic Scattering (GENESIS) provides the ability to measure neutron inelastic scattering cross sections on different targets. GENESIS was demonstrated to have a uniform neutron beam, average incident neutron timing resolution of 9.0 ns, and total gamma (1.408 MeV) and total neutron detection efficiencies of $\geq$0.13% and 0.183%, respectively. An initial experiment measuring the $^{16}$O(n,n'$\gamma$) reaction calculated the count rate from the second excited state using the full energy and escape peaks. Second, a set of photocurable scintillator resin formulations capable of neutron-gamma discrimination were developed to support light-based 3D printing applications for advanced nuclear physics measurements. The formulations resulted in hard, clear, PSD-capable plastic scintillators that cured within 10 seconds using 405 nm light, produced a light yield up to 83% of EJ-276, and a pulse shape discrimination figure of merit of 1.28 at 450-550 keVee. Lastly, a fast neutron beam facility was established to improve thermal-neutron sensitive experiments by designing and installing a tungsten collimator that reduced the thermal neutron background by $\sim$778x. Overall, this research contributed to the establishment of two new experimental facilities, a 3D-printable plastic scintillator formulation, and proof-of-principle methods to conduct novel measurements to address nuclear data needs.

# Acknowledgements

I would like to thank my research advisor and dissertation committee chair, Maj James Bevins, whose relentless support and guidance made this research achievable. I would like to thank my dissertation research committee members, Dr. John McClory, Dr. Darren Bleuel, Dr. Juan Manfredi and Dr. Mark Oxley for their valuable contributions and support. I would like to thank the amazing scientists, engineers and researchers that I have been able to work with and learn from at Lawrence Berkeley National Laboratory, University of California-Berkeley, and Oak Ridge National Laboratory, namely Dr. Lee Bernstein, Dr. Josh Brown, Joey Gordon, Dr. Bethany Goldblum, Dr. Thibault Laplace, Dr. Jon Batchelder, Chris Brand, Dr. Mike Febbraro, and Thomas Ruland. Lastly and most importantly, I want to thank the person who has given me the most love and support, my wife. Thank you!

Brian G. Frandsen

*This dissertation is dedicated to my family, for their constant love and support.*

# Table of Contents

Page

Page

Page

# List of Figures

# List of Tables

# CAPABILITY DEVELOPMENT FOR ADVANCED (N,X) NUCLEAR DATA MEASUREMENTS

# I. Introduction

## 1.1 Motivation

Nuclear reaction data are at the heart of radiation transport calculations, models, and simulations. In the Department of Defense, these data are critical for radiation detection [1, 2], nuclear weapon detonation detection [3], nuclear forensics [4–6], and nuclear weapon effects studies [7], including analysis supporting certification of the survivability of systems in nuclear environments. Unfortunately, there are large discrepancies in the data and gaps where data do not exist at all. Therefore, it is critical to conduct experiments that measure nuclear data to improve the accuracy and fill in known gaps [8–11].

## 1.2 Background

There are several organizations across the world that have identified nuclear data needs for different applications. The Organisation for Economic Co-operation and Development (OECD) Nuclear Energy Agency (NEA) maintains the Nuclear Data High Priority Request List (HPRL), which contains 111 requests for nuclear reaction data [8]. Of those 111 requests, four are inelastic scattering cross section requests for $^{56}$Fe, $^{206}$Pb, $^{207}$Pb, and $^{238}$U and 25 are for $^{252}$Cf spontaneous fission neutron spectrum-averaged cross sections.

Recently, there have been multiple efforts to bring the community together to address nuclear data shortcomings. In 2013, the Nuclear Energy Agency (NEA) created the Collaborative International Evaluated Library Organization (CIELO) Pilot Project, which was an international collaboration to improve the evaluated nuclear data for $^{1}$H, $^{16}$O, $^{56}$Fe, $^{235}$U, $^{238}$U, and $^{239}$Pu [10]. In 2015, the Workshop on Nuclear Data Needs and Capabilities for Applications (NDNCA) compiled the nuclear data needs for a wide spectrum of nuclear applications, such as nuclear energy, national security, isotope production, and other industrial applications [9]. Included in the multitude of data needs was the need for more accurate inelastic scattering cross section data for H, Li, Be, B, N, O, Mg, Al, Si, Ti, V, Cr, Fe, Ni, Cu, Ga, Zr, Nb, Mo, Eu, Gd, Ta, W, Ir, Pt, Au, Pb, Po, Ra, Th, U, Np, Pu, and Am.

Since the NDNCA in 2015, there have been several meetings and workshops to identify and discuss the nuclear data needs from the community and to prioritize and address discrepancies and gaps including:

- 2015 - Nuclear Data Working Group [12]
- 2016 - Nuclear Data Exchange Meeting [12]
- 2016 - Nuclear Data Interagency Working Group [12]
- 2018 - Nuclear Data Roadmapping Workshop (NDREW) [13]
- 2019 - Workshop for Applied Nuclear Data Activities (WANDA) [14]
- 2020 - Workshop for Applied Nuclear Data Activities (WANDA) [15]
- 2021 - Workshop for Applied Nuclear Data Activities (WANDA)

These organizations and meetings have shown the immediate and continuing need of nuclear data over the entire spectrum of nuclear applications. This research aimed

to enable the complex and challenging experiments that are required to properly and accurately measure these identified nuclear data needs.

## 1.3 Problem

The current nuclear data needs require novel approaches to measure specific reactions where data is inaccurate or does not exist in the areas of neutron inelastic scattering cross sections, high spatial resolution for neutron measurements and fast neutron imaging, and thermal neutron sensitive measurements.

### 1.3.1 Inelastic Scattering Measurements

Neutron inelastic scattering cross sections are not fully characterized, and there is a significant need for better data [8–10]. For $^{16}$O, there is a need for more accurate inelastic cross section measurements across a broad range of neutron energies up to 20 MeV for national security, counter-proliferation, and nuclear energy applications [9, 10]. Currently, the experimental data available for $^{16}$O do not cover a wide range of neutron energies, some of the partial levels are combined into one cross section, and the discrepancies between the experimental data are high [16–29]. Additionally, experimental data measurements are missing, to include the partial differential cross sections. The existing data is described further in Section 4.1.2.

### 1.3.2 Light-based, 3D-Printable Plastic Scintillators

Plastic scintillators are among the most commonly used radiation detection materials due to their low costs, ease of fabrication, fast response time, and ability to distinguish between neutron and gamma-ray interactions [30–38]. Application of additive manufacturing (AM) 3D printing techniques, such as light-based stereolithography (SLA) and digital light processing (DLP), allows for the

fabrication of complex geometries and multi-material composites that are either impossible or cost prohibitive to produce using conventional methods.

Successful 3D printing of plastic scintillators requires development of a suitable feedstock material that is similar in cost to conventional scintillator and has mechanical, chemical, and optical properties suitable for the 3D printing process. A few researchers have developed formulations of scintillating resins that either have or can be used in light-based 3D printers, but the light yield of these scintillators is low (∼35% of commercially available plastic scintillators) [39–41] and pulse-shape discrimination (PSD) is not reported. Other recent research reports a DLP 3D printed scintillator with light yield up to 67% of BC-408 plastic scintillator [42, 43]. However, like the other light-based, 3D-printable formulations, PSD performance is not reported.

### 1.3.3 Thermal Neutron Sensitive Measurements

The HPRL currently contains 25 requests for the $^{252}$Cf spectrum-averaged cross section (SACS) measurement for different reactions to improve the International Reactor Dosimetry and Fusion File (IRDFF) [44, 45]. Additionally, there are several reactions, such as $^{10}$B(n,$\alpha$)$^{7}$Li and $^{6}$Li(n,t)$^{4}$He, that do not have a $^{252}$Cf SACS measurement. These reactions are endothermic and have high thermal neutron cross sections, which significantly complicate the measurement of the $^{252}$Cf SACS due to thermalized neutrons in the experimental environment.

Neutrons from $^{252}$Cf that do not interact directly with the target can interact with the walls, ceiling, floor, and other materials within the room, and these interactions reduce the neutron energy. This creates thermal and lower energy neutrons that are uniformly distributed throughout the room [46, 47]. For reactions with high thermal neutron cross sections, the thermalized room-return neutrons will

dominate the reaction detection and prevent a correct measurement of the $^{252}$Cf SACS from neutrons directly from $^{252}$Cf.

## 1.4 Research Objectives and Accomplishments

The purpose of this research was to advance the development of unique capabilities to improve neutron nuclear data measurement in the areas of neutron inelastic scattering cross section measurements, including $^{16}$O(n,n'$\gamma$), plastic scintillator formulations that can be used in light-based 3D printing for fast neutron imagery and high spatial resolution neutron detection, and thermal neutron sensitive measurements. This research contributed to the establishment of two new experimental facilities at Lawrence Berkeley National Laboratory and AFIT, a new, 3D printable scintillator formulations, and proof of principle for methods to conduct novel measurements to address long-standing nuclear data gaps.

The newly developed Gamma Energy Neutron Energy Spectrometer for Inelastic Scattering (GENESIS) at Lawrence Berkeley National Laboratory provides the ability to measure the neutron inelastic scattering cross section on different targets, to include $^{16}$O. This research to advance neutron inelastic scattering cross section measurements accomplished the following objectives:

- Develop and characterize GENESIS capabilities,
- Develop code and algorithms to process the data, and
- Calculate the $^{16}$O(n,n') detection spectrum of the 2$^{nd}$ excited state.

Light-based 3D printing of organic scintillators allows the production of complex shapes and sizes and can significantly reduce the manufacturing cost and time. This research to advance neutron and gamma radiation detection and measurements by taking advantage of light-based 3D printing accomplished the following objectives:

- Develop a formulation that can be rapidly photo-cured,
- Analyze the constituents in the formulation to provide the best radiation detection performance, and
- Analyze the long-term stability and approaches to improve stability and performance.

Thermal neutrons caused by room return need to be significantly reduced to provide the needed environment for thermal neutron sensitive experiments, such as $^{10}$B(n,$\alpha$) and $^{6}$Li(n,t) $^{252}$Cf SACS measurement, and neutron detection characterization. This research to advance thermal neutron sensitive experiments accomplished the following objectives:

- Design and model a unique collimator that significantly reduced the thermal neutron environment,
- Build and install the designed collimator, and
- Characterize the collimator performance.

## 1.5 Dissertation Layout

This document covers the breadth of the research and development of unique capabilities to improve neutron nuclear data measurements. Chapter 2 discusses the fundamental theory supporting the research. Chapter 3 discusses the development and capabilities of GENESIS to measure inelastic scattering cross sections and Chapter 4 discusses the results and analysis on the first measurement of $^{16}$O(n,n'$\gamma$) using GENESIS. Chapter 5 discusses the development of a fast-, light-cured plastic scintillator formulation with the observations and radiation performance of the formulations that can be used in 3D printing. Chapter 6 discusses the need and

capability of newly installed neutron collimator to reduce room return and thermal neutrons. Chapter 7 discusses the conclusions of this research.

# II. Theory

## 2.1 Nuclear Structure

Nuclear structure is the arrangement of the protons and neutrons in the nucleus, each with values of angular momentum, spin, and parity that contribute to the total angular momentum and parity of the nucleus. A nucleus can be moved to an excited state (i.e. a different arrangement of protons and neutrons) by neutron inelastic scattering, and the gammas and transitions from the nucleus's excited states are dependent on the nuclear structure.

### 2.1.1 Binding Energy

The nucleus of the atom is comprised of protons and neutrons that are bound together by the nuclear force, which is required to overcome the Coulombic repulsion of the protons. The binding energy of the nucleus is computed as the masses of individual protons and neutrons minus the mass of the nucleus given as

$$B = (Zm_p + Nm_n - [m({}^{A}_{Z}X_N) - Zm_e])c^2, \tag{2.1}$$

where $m_p$, $m_n$, and $m_e$ are the masses of a proton, neutron, and electron, respectively, $m({}^{A}_{Z}X_N)$ is the mass of the atom, and $c$ is the speed of light. The shorthand used here for nuclear isotopes is the form ${}^{A}_{Z}X_N$, where $X$ is the elemental symbol, $Z$ is the number of protons, $N$ is the number of neutrons, and $A$ is the combined number of protons and neutrons. However, for brevity, an isotope can be specified in the form ${}^{A}X$, since elemental symbol indicates the number of protons in the nucleus and the number of neutrons can be determined from $A$ and $Z$.

For $^{9}$Be, which contains 4 protons and 5 neutrons, the combined mass of the individual nucleons is $4(1.00728 \text{ amu}) \times 5(1.00866 \text{ amu}) = 9.0724$ amu. The mass of

$^{9}$Be is 9.0121 amu. Therefore, the binding energy is 58.154 MeV or 6.462 MeV/nucleon.

The separation energy of the neutron, $S_n$, is the energy needed for a neutron to exceed the binding energy and be removed from the nucleus and can be calculated as,

$$S_n = B({}^{A}_{Z}X_N) - B({}^{A-1}_{Z}X_{N-1}) = [m({}^{A-1}_{Z}X_{N-1}) - m({}^{A}_{Z}X_N) - m_n]c^2, \tag{2.2}$$

where $B({}^{A}_{Z}X_N)$ and $B({}^{A-1}_{Z}X_{N-1})$ are the binding energies of the nucleus with and without the neutron, respectively. The neutron separation energies for $^{9}$Be and $^{16}$O are 1.665 MeV and 15.664 MeV, respectively. For this reason, $^{9}$Be makes a good target for neutron production while $^{16}$O would require a much higher incident energy particle and result in less neutron production as a function of particle energy.

### 2.1.2 Nuclear Angular Momentum and Parity

Each nucleon (proton and neutron) in the nucleus has an angular momentum, $\ell$, spin, $s$, and total angular momentum, $j = \ell + s$. The angular momentum of a nucleus, $I$, is the summation of the nucleons' total angular momentum. Since a single nucleon has an integer value of angular momentum and 1/2 value of spin, a single nucleon has a total angular momentum of half integer. The angular momentum of an odd-A nucleus is a half-integer value and the angular momentum of a even-A nucleus is a whole integer value. Additionally, the parity of the nucleus is the product of the nucleons' parity, which is either even (+) or odd (-). The angular momentum and parity of a nucleus are often written together as $I^{\pi}$, such as $2^{+}$.

### 2.1.3 Shell Model

The shell model depicts nuclear structure and its associated excited states, similar to the model of electron excited states of an atom. One version of the shell model uses the potential, $V(r) = -V_0/(1 + e^{(r-R)/a})$, to model the mean field potential resulting from all nucleon interactions, where $V_0$ is the depth of the well, $R$ is the mean radius, $a$ is the skin thickness, and $r$ is the radius. A spin-orbit interaction is included in the shell model in order to produce the correct ordering of the individual orbitals in the nucleus. Figure 2.1 depicts an example shell model potential and the discrete energy states using spin-orbit coupling [48].

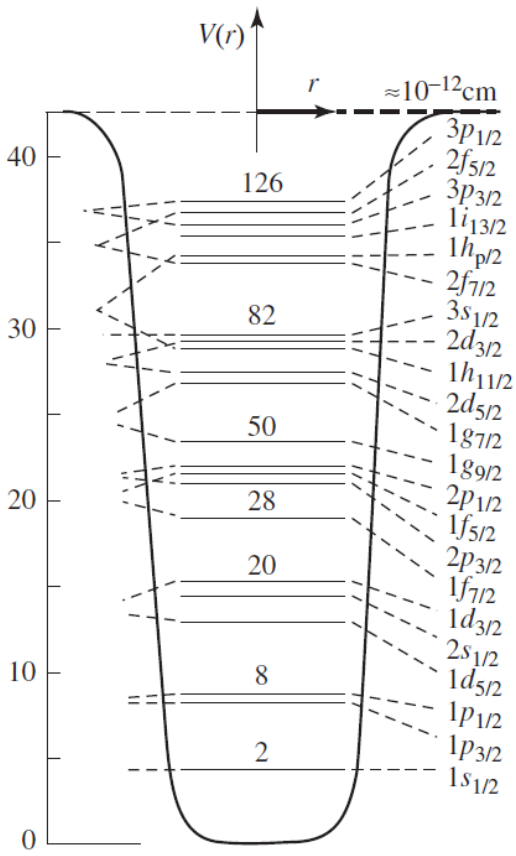


**Figure 2.1. The shell model of the nucleus using spin-orbit coupling to model the nuclear structure [48].**

For an odd-A isotope, the angular momentum and parity are determined by the

unpaired nucleon. Using $^{9}$Be as an example, there are 4 protons and 5 neutrons. The unpaired neutron will determine the angular momentum and parity of the nucleus. From Figure 2.1, the unpaired neutron will be in the $1p_{3/2}$ state, which means the angular momentum of $^{9}$Be in the ground state is $I = 3/2$. The parity is determined by angular momentum of the unpaired neutron, $\ell = p = 1$, which is equivalent to a odd parity. Thus, the angular momentum and parity of $^{9}$Be in the ground state is $3/2^{-}$.

For an odd-odd isotope that contains an odd numbers of protons and neutrons, such as $^{10}$B (5 protons and 5 neutrons), the angular momentum and parity are determined from both the unpaired nucleons. Both the unpaired proton and neutron are in the $1p_{3/2}$ state, which means the angular momentum of $^{10}$B in the ground state is $I = 3/2 + 3/2 = 3$. The parity is determined by angular momentum of the unpaired neutron and proton, $\ell = p = 1$, which are equivalent to a odd parity. The parity of the nucleus is even, since $\pi = (-)(-) = (+)$. Thus, the angular momentum and parity of $^{10}$B in the ground state is $3^{+}$.

For an even-even isotope that contain an even numbers of protons and neutrons, such as $^{16}$O, the angular momentum and parity of the ground state is $0^{+}$, since there is not an unpaired nucleon.

As the nucleus gains energy and moves to excited states, individual nucleons move up to new levels, which may change the nucleon pairing and, therefore, the angular momentum and parity of the nucleus. For example, the second excited state of $^{16}$O has an angular momentum and parity of $3^{-}$, which occurs when one of the paired nucleons from the $1p_{1/2}$ state moves to the $1d_{5/2}$ state. This leaves unpaired nucleons in both the $1p_{1/2}$ and $1d_{5/2}$ states. Therefore, the angular momentum is $I = 1/2 + 5/2 = 3$ and the parity is odd, $\pi = (-)(+) = (-)$.

A nucleus in an excited state will release energy as it returns to the ground state

by emitting gamma rays, particles, such as protons or neutrons, or ejecting inner shell electrons in the process of internal conversion. As the nucleus returns to the ground state, it may occupy other lower intermediate excited states, which then creates a cascade of gammas from the higher energy states. Figure 2.2 shows the first 18 excited states of $^{16}$O and the possible paths for each excited state as the nucleus de-excites to the ground state [49]. The values on the left side are the angular momentum and parity of each state. The values on the right (above the lines) are the excitation energies and the values on the far right are the half-life of the transition in units of time (i.e. fs, ps) or energy equivalence (i.e. keV) using the Heisenberg uncertainty. However, not all the excited states predominantly decay by gamma-ray emission. Another process that competes with gamma decay is internal conversion, which occurs when the energy of the excited nucleus is transferred to an atomic electron. Additionally, most of the excited states of $^{16}$O decay predominantly by alpha, proton, or neutron emission [49], which prevents observing gamma rays from those excited states.

### 2.1.4 Gamma Radiation

Gamma radiation is produced when an excited nucleus relaxes to a lower energy state. The nucleus is usually placed in an excited state due to a radioactive decay process or a nuclear reaction, such as neutron inelastic scattering. Since the excited states of the nucleus are discrete, the gamma rays from those states are also discrete. Depending on the excited state of the nucleus, a cascade of gamma rays can be emitted as the nucleus descends to lower energy states, as shown in Figure 2.2.

The gamma ray emitted from the nucleus contains most of the energy difference between the excited states, but some of the energy is taken by the recoiling nucleus.

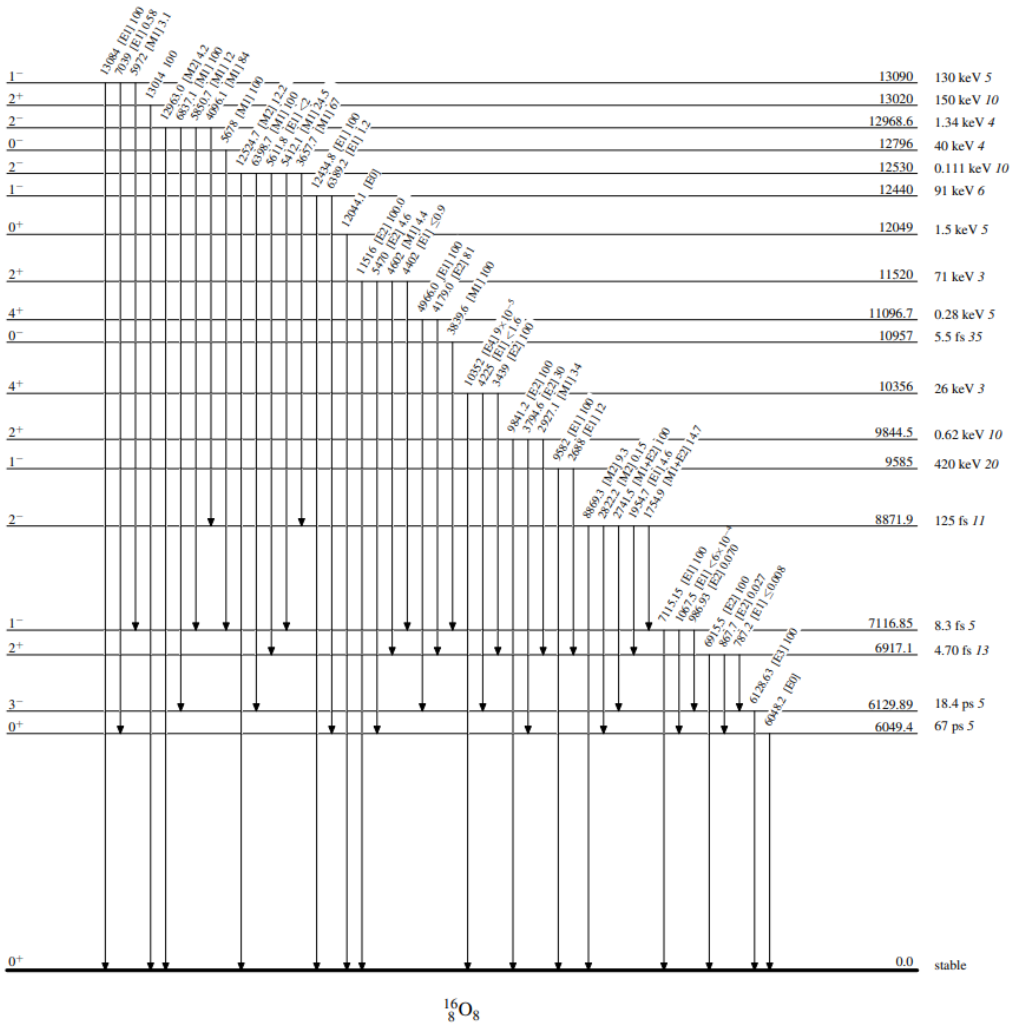


**Figure 2.2. First 18 excited states of $^{16}$O and the possible gamma decays from each state [49].**

The energy of the gamma, $E_\gamma$, is

$$E_\gamma = mc^2\sqrt{1 + \frac{2(E_i^* - E_f^*)}{mc^2}} - mc^2, \tag{2.3}$$

where $m$ is the mass of the nucleus, $c$ is the speed of light, $E_i^*$ is the initial state, and $E_f^*$ is the final state. From the 6129.89 keV excited state of $^{16}$O to the ground state, the gamma ray emitted is 6128.63 keV, 99.98% of the energy, and the recoil nucleus takes 0.02% of the energy.

#### 2.1.4.1 Gamma-ray Selection Rules

Gamma rays emitted from the nucleus take angular momentum along with energy [50]. The angular momentum of the gamma ray, $L$, can be determined by

$$|I_i - I_f| \leq L \leq I_i + I_f \quad I_\gamma \neq 0, \tag{2.4}$$

where $I_i$ and $I_f$ are the angular momentum of the initial and final state of the nucleus, respectively. However, $L$ cannot equal 0, because the gamma ray has to have angular momentum. The multipoles are $L = 1$ (dipole), $L = 2$ (quadrupole), $L = 3$ (octupole), $L = 4$ (hexadecapole), and so forth.

The change in parity between the initial and final states indicates if the radiation field is even or odd. A change in parity ($\Delta\pi$=yes) indicates the radiation field is even with either an even magnetic multipole or an odd electric multipole. Inversely, an equal parity ($\Delta\pi$=no) indicates the radiation field is odd with either an odd magnetic multipole or an even electric multipole.

$$\Delta\pi\text{=yes} \rightarrow \text{Even magnetic or odd electric}$$
$$\Delta\pi\text{=no} \rightarrow \text{Odd magnetic or even electric}$$

For $^{16}$O, the first excited state at 6.049 MeV has an angular momentum and parity of $0^+$, which is the same as the ground state. Since there is no change in angular momentum, the nucleus is unable to relax to the ground state by gamma-ray emission. Therefore, the first excited state relaxes to the ground state by internal conversion, which occurs when the energy is released by an ejected orbital electron [50].

The second excited at 6.129 MeV has an angular momentum and parity of $3^-$. With the ground state at $0^+$, the angular momentum of the gamma ray is 3 and there is a change in parity ($\Delta\pi$=yes). Therefore, the transition is an electric octupole (E3).

Table 2.1 lists the excited states of $^{16}$O that predominantly relax to the ground state by gamma-ray emission; not all excited states of a nucleus primarily emit a gamma ray as it drops to the ground state. The left three columns list the excited state with its corresponding energy, angular momentum and parity, and half-life. The middle three columns list the possible gamma ray(s) from the excited state with the corresponding energy, intensity and multipolarity. The right columns list the final state of the transition with its corresponding energy and angular momentum and parity.

**Table 2.1. Excited states of $^{16}$O that transition from the excited state to the ground state by gamma-ray emission [49].**

| **Initial State** | | | **Gamma** | | | **Final State** | |
|---|---|---|---|---|---|---|---|
| **Energy [keV]** | $\mathbf{I^{\Pi}}$ | $\mathbf{T_{1/2}}$ | $\mathbf{E_\gamma}$ **[KeV]** | $\mathbf{I_\gamma}$ **[%]** | $\mathbf{M_\gamma}$ | **Energy [keV]** | $\mathbf{I^{\Pi}}$ |
| 0.0 | $0^+$ | Stable | | | | | |
| 6049.4 | $0^+$ | 67 ps | | | | | $0^+$ |
| 6129.9 | $3^-$ | 18.4 ps | 6128.6 | 100 | E3 | 0.0 | $0^+$ |
| 6917.1 | $2^+$ | 4.7 fs | 787.2 | $\leq$ 0.008 | E1 | 6129.9 | $3^-$ |
| | | | 867.7 | 0.027 | E2 | 6049.4 | $0^+$ |
| | | | 6915.5 | 100 | E2 | 0.0 | $0^+$ |
| 7116.9 | $1^-$ | 8.3 fs | 986.9 | 0.07 | E2 | 6129.9 | $3^-$ |
| | | | 1067.5 | $\leq$ 6e-4 | E1 | 6049.4 | $0^+$ |
| | | | 7115.2 | 100 | E1 | 0.0 | $0^+$ |
| 8871.9 | $2^-$ | 125 fs | 1754.9 | 14.7 | M1+E2 | 7116.9 | $1^-$ |
| | | | 1954.7 | 4.6 | E1 | 6917.1 | $2^+$ |
| | | | 2741.5 | 100 | M1+E2 | 6129.9 | $3^-$ |
| | | | 2822.2 | 0.15 | M2 | 6049.4 | $0^+$ |
| | | | 8869.3 | 9.3 | M2 | 0.0 | $0^+$ |
| 10957 | $0^-$ | 5.5 ps | 3839.6 | 100 | M1 | 7116.9 | $1^-$ |

The gamma-ray intensity, $I_\gamma$, is based on the percentage of the most intense gamma from that state. For example, from the 6917.1 keV excited state, there are three transitions to the ground state and emission of a 6915.5 keV gamma ray is the most intense, which is indicated by the gamma-ray intensity of 100%. The other transitions to the 6129.9 MeV and 6049.4 MeV excited states occur $\leq$ 0.008% and 0.027% of the time relative to the 6915.5 keV gamma ray.

## 2.2 Nuclear Interactions

A nuclear interaction can be visualized as depicted in Figure 2.3, where a particle (1), such as a neutron, is incident on a nucleus (2). After the reaction, one reaction product (3) leaves at an angle of $\theta$ and another reaction product (4) leaves at an angle of $\phi$.

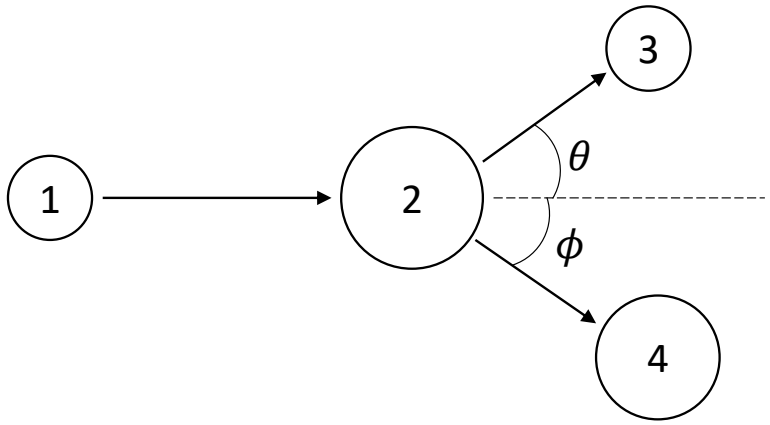


**Figure 2.3. Illustration of a nuclear reaction resulting in two reaction products.**

These reactions are written to describe the reactants and products as

$$R_1 + R_2 \rightarrow P_3 + P_4, \tag{2.5}$$

where $R_1$ is the incident particle on the nucleus $R_2$, $P_3$ is the outgoing particle, and $P_4$ is the outgoing nucleus. Often nuclear reactions are written in short hand as

$$R_2(R_1, P_3)P_4. \tag{2.6}$$

For example, $^{9}$Be(d,n)$^{10}$B represents the reaction of a deuteron particle incident on $^{9}$Be, which produces an outgoing neutron and a $^{10}$B nucleus. Furthermore, this reaction can also be written as $^{9}$Be(d,n), where the product nucleus is not included, but can be determined using the other information.

The amount of energy absorbed or released during the nuclear reaction, the Q value, can be calculated using the mass or kinetic energy of the particles in the reaction as [48]

$$Q = (m_1 + m_2 - m_3 - m_4)c^2 = E_3 + E_4 - E_1, \tag{2.7}$$

where $m_1$ is the mass of the incident particle, $m_2$ is the mass of the nucleus, $m_3$ and $m_4$ are the masses of the products, $c$ is the speed of light, $E_3$ and $E_4$ are the kinetic energies of the products, and $E_1$ is the kinetic energy of the incident particle. Using conservation of momentum and energy, the relationship of the Q value and the energy of the particles is [48]

$$Q = E_3(1 + m_3/m_4) - E_1(1 - m_1/m_4) - 2/m_4\sqrt{m_1 m_3 E_1 E_3}\cos\theta, \tag{2.8}$$

where $\theta$ is the angle of the outgoing particle 3. From Equation 2.8, the kinetic energy of particle 3 can be calculated as

$$\sqrt{E_3} = \frac{(m_1 m_3 E_1)^{1/2}\cos\theta \pm \{m_1 m_3 E_1 \cos^2\theta + (m_3 + m_4)[m_4 Q + (m_4 - m_1)E_1]\}^{1/2}}{m_3 + m_4}, \tag{2.9}$$

and of particle 4 as

$$E_4 = Q + E_1 - E_3. \tag{2.10}$$

### 2.2.1 Compound Reactions

A compound reaction occurs when the incident particle interacts with the nucleus and creates an intermediate compound nucleus, $C^*$, as

$$R_1 + R_2 \rightarrow C^* \rightarrow P_3 + P_4. \tag{2.11}$$

The energy of the incident nucleus is transferred to the nucleons throughout the nucleus due to multiple intranuclear collisions [51]. After the formation, the compound nucleus decay and creation of secondary products is independent of the particle that created the compound nucleus and is dependent on the energy and angular momentum of the compound nucleus. The products are emitted isotropically from the compound nucleus and the the time scale of compound reactions are on the order of $10^{-16}$ to $10^{-18}$ seconds [50].

### 2.2.2 Direct Reactions

In a direct reaction, the incident particle interacts with individual nucleons, typically at the surface of the nucleus. These reactions occur when the incident particles have high energies and their wavelengths are small enough to interact with individual nucleons. Since there is no creation and energy transfer as within a compound nucleus, the time scale for direct reactions is much faster, on the order of $10^{-22}$ seconds [50]. The angular emission of the products in a direct reaction is not isotropic and rather is forward focused.

Two specific varieties of direct reactions are stripping and pickup reactions. In a stripping reaction, part of the incident particle is absorbed by the nucleus and the other part is emitted. In a pickup reaction, the incident particle is emitted from the reaction with other nucleons from the nucleus [52].

### 2.2.3 Pre-Equilibrium Reactions

Pre-equilibrium reactions are reactions that occur between direct and compound reactions, where the incident particle creates multiple intranuclear collisions but the reaction concludes before complete equilibrium within the nucleus forms a compound nucleus. Figure 2.4 illustrates the different characteristics between compound, pre-

equilibrium, and direct reactions, which include the reaction time, the energy of the outgoing particle, $E_{out}$, and the excited state of the nucleus, $E_x$ [51].

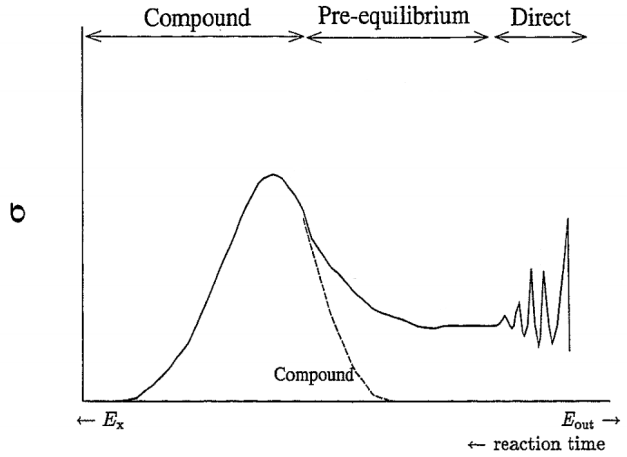


**Figure 2.4. Illustration of the different characteristics between compound, pre-equilibrium and direct reactions, which include the reaction time, the energy of the outgoing particle, $E_{out}$, and the excited state of the nucleus, $E_x$ [51].**

## 2.3 Reaction Cross Sections

In simple terms, the cross section is the probability that a particle will interact with a material. The probability of the interaction depends on the "area" seen by the incoming particle compared to the empty space. Classically thinking, the particle will only interact with a nucleus if the particle hits any portion of the nucleus' areal cross section, which has an area of $\sigma$ typically given in units of barns ($10^{-24}$ cm$^2$). One could image a baseball thrown at a car. It will "interact" with the car as long as it hits any place on the car. To the baseball, the area of the car is only the areal cross section of the car.

For a particle, such as a neutron, traveling through a material, there are several nuclei with which the particle can interact. Figure 2.5 illustrates a beam of particles that are incident on the nuclei in a material. The number of nuclei in a material is $NA\Delta x$, where $N$ is the nuclear density (nuclei/cm$^3$), $A$ is the area of the material

($cm^2$) and $\Delta x$ is the thickness of the material (cm). Thus, classically, the probability of reaction, $P_R$, is the total area of the nuclei divided by the total area, as

$$P_R = \frac{\sigma N A \Delta x}{A} = \sigma N \Delta x. \tag{2.12}$$

However, the cross section is not constrained to the physical size of the nucleus but is dependent on the wave functions of the particles [48].

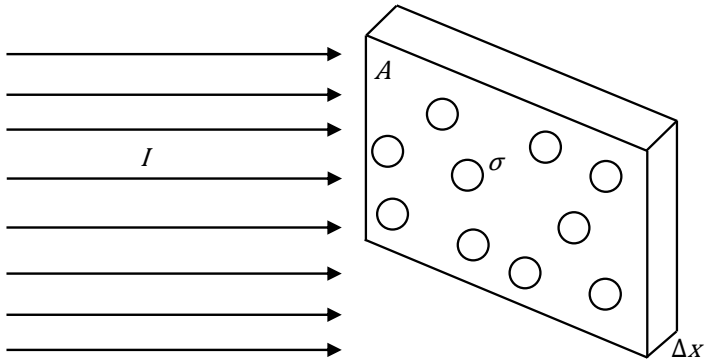


**Figure 2.5. Nuclear cross section illustration.**

The cross section can be experimentally measured by measuring the particles before and after the reaction. The probability of reaction, $P_R$, can be calculated by dividing the rate of the incident particles, $I$, to the rate of particles that have reacted with the material, $I_R$, as

$$P_R = \frac{I_R}{I}. \tag{2.13}$$

For example, the probability of scattering can be calculated by measuring the incident beam of particles on a material and the number of particles that have scattered due to the material. Therefore, the cross section can be calculated as

$$\sigma = \frac{I_R}{IN\Delta x}. \tag{2.14}$$

The reaction cross section is dependent on the incident particle energy. Therefore, Equation 2.14 can be properly written as

$$\sigma(E) = \frac{I_R}{I(E)N\Delta x}, \tag{2.15}$$

to include the incident energy dependence, $E$. Another term for $\sigma$ is the microscopic cross section, because of its dependence of the reaction on a single nucleus.

### 2.3.1 Macroscopic Cross Section

The macroscopic cross section, $\Sigma$, is the probability the particle will interact within bulk material and can be calculated as

$$\Sigma = N\sigma, \tag{2.16}$$

where $N$ is the nuclei density of the material (nuclei/cm$^3$) and can be calculated using

$$N = \frac{\rho N_A}{MW}, \tag{2.17}$$

where $\rho$ is the density of the material, $N_A$ is the Avogadro's number, and $MW$ is the molecular weight of the material. The mean free path of a particle, $\lambda$, the average distance a particle will travel in a material without a reaction, can be calculated by the inverse of the macroscopic cross section as

$$\lambda = \frac{1}{\Sigma}. \tag{2.18}$$

### 2.3.2 Differential Cross Section

An incident particle on a nucleus creates products that are emitted at different angles and energies, which are interdependent, as shown in Figure 2.3 and discussed in Section 2.2. The angular differential cross section is the probability that the reaction will result in the emitted particle at a certain angle and can be calculated by measuring the reaction rate, $I_R$, at a specific angle, $\Omega$, after the reaction as

$$\frac{d\sigma}{d\Omega} = \frac{I_R(\Omega)}{I(E)N\Delta x}. \tag{2.19}$$

Similarly, the energy differential cross sections is the probability that the reaction will result in the emitted particle with a certain energy and can be calculated by measuring the reaction rate, $I_R$, at a specific energy, $E'$, after the reaction as

$$\frac{d\sigma}{dE'} = \frac{I_R(E')}{I(E)N\Delta x}. \tag{2.20}$$

The double differential cross section can be calculated by measuring the reaction rate, $I_R$, of the reactants at a specific angle, $\Omega$, and energy, $E'$, after the reaction, as

$$\frac{d^2\sigma}{dE'\,d\Omega} = \frac{I_R(E', \Omega)}{I(E)N\Delta x}. \tag{2.21}$$

### 2.3.3 Partial Cross Section

Nuclear reactions can leave the product nucleus in an excited state, as long as the incident particle energy and Q value of the reaction exceeds the excited state energy of the nucleus. Since the nucleus has several excited states, the partial cross section is the probability the reaction will leave the nucleus in a specific excited state. Therefore, the partial double differential cross section is the probability that an incident particle of a specific energy, $E$, will leave the nucleus in an excited state,

$E^*$, and result in an outgoing particle at a specific angle, $\Omega$, and energy, $E'$, as

$$\frac{d^3\sigma(E_n)}{dE'\,d\Omega\,dE^*} = \frac{I_R(E', \Omega, E^*)}{I(E)N\Delta x}. \tag{2.22}$$

The partial cross section provides information on the nuclear structure of the isotope along with the excited states and transitions.

## 2.4 Neutron-Induced Reactions

For neutrons incident on $^{16}$O, there are several reactions that can occur; the cross sections for each are plotted in Figure 2.6. The most dominant reaction to occur, regardless of the neutron energy, is elastic scattering, $^{16}$O(n,n)$^{16}$O, which is discussed in Section 2.4.1. Neutron radiative capture, $^{16}$O(n,$\gamma$)$^{17}$O, also can occur at any neutron energy and is discussed in Section 2.4.3. All other reactions can only occur if the incident neutron has enough energy to surpass the threshold energy of the reaction as shown in Figure 2.6. These reaction types are discussed in Sections 2.4.2 and 2.4.4.

### 2.4.1 Elastic Scattering

For most isotopes at most energies, the most dominant neutron reaction is elastic scattering (n,n), which occurs when the neutron scatters off of a nucleus. The scattering event changes direction of the neutron and reduces its energy by the amount of energy it imparts to the nucleus. The kinetic energy of the scattered neutron can be calculated using Equation 2.9. However, we can simplify the equation where $m_n = m_1 = m_3$ and $m_A = m_4$. Also, in an elastic scattering event, there is no change in the mass of the reactants and products ($m_1 = m_3$ and $m_2 = m_4$), therefore $Q = 0$. Thus, the simplified equation to calculate the kinetic

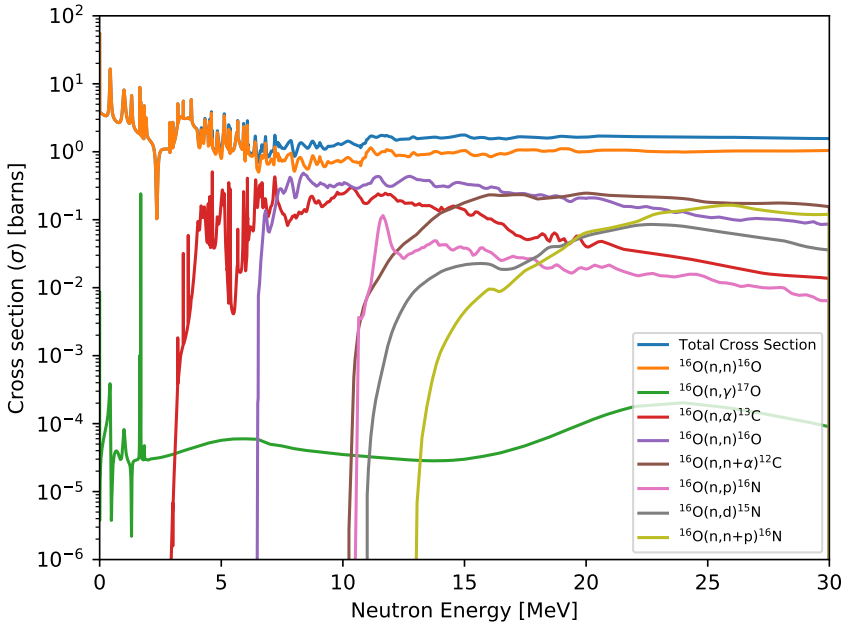


**Figure 2.6. Neutron cross section for the most common reactions on $^{16}$O.**

energy of the scattered neutron is

$$\sqrt{E_n'} = \frac{\sqrt{E_n}}{m_A + m_n}\left(m_n \cos\theta + \sqrt{m_n^2\cos^2\theta + m_A^2 - m_n^2}\right), \tag{2.23}$$

where $E_n = E_1$ is the initial neutron energy, $E_n' = E_3$ is the kinetic energy of the scattered neutron, $\theta$ is the scattering angle of the neutron, $m_n$ is the mass of the neutron, and $m_A$ is the mass of the nucleus.

As shown in Equation 2.23, the scattered neutron energy is dependent on the nucleus and the scattering angle. Figure 2.7 shows the scattered neutron energy relative to the incident neutron energy ($E_n'/E_n$) as a function of scattering angle for a few different nuclei.

The maximum energy that can be imparted from a neutron to a nucleus is when $\theta = \pi$. The kinetic energy of the scattered neutron at $\theta = \pi$ is given as

$$E_n' = E_n\left(\frac{m_A - m_n}{m_A + m_n}\right)^2. \tag{2.24}$$

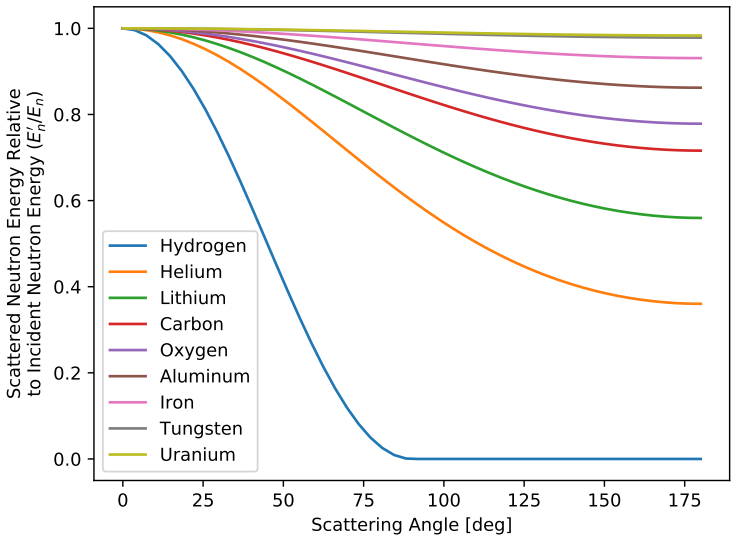


**Figure 2.7. Elastically scattered neutron energy as a function of scattering angle for different nuclei.**

For a hydrogen nucleus (proton), where the neutron and proton mass are the almost the same, the neutron can impart all its energy to the proton and leave the outgoing neutron with zero kinetic energy, as shown in Figure 2.7. The maximum energy that a neutron can lose with oxygen, aluminum, and uranium is 22.32%, 13.90% and 1.68%, respectively.

### 2.4.2 Inelastic Scattering

In inelastic scattering, the incident neutron leaves the nucleus in a higher energy state. The nucleus then emits a gamma ray as it relaxes back down to the ground state. The Q value of the inelastic reaction is $Q = m_1c^2 + m_2c^2 - m_3c^2 - m_4c^2 - E^* = -E^*$, where $E^*$ is the excited state of the nucleus and masses of the equation are reduced because $m_1 = m_3$ and $m_2 = m_4$. Therefore, Equation 2.8 can be reduced to

$$E_{th} = \frac{E^*}{1 - \frac{m_n}{m_A}} \tag{2.25}$$

to calculate the threshold energy, $E_{th}$, of the incident neutron to excite the nucleus in an inelastic scattering event, where the scattered neutron energy is practically zero ($E_3 \approx 0$). The first excited state of $^{16}$O is 6.049 MeV; therefore, the minimum neutron energy needed to excite the $^{16}$O nucleus into the first excited state is $E_{th} = 6.456$ MeV. The additional energy, beyond the energy of the excited state, goes into the required mass increase [48].

Depending on the energy of the incident neutron, inelastic scattering can be a direct or compound reaction [50], which effects the angular distribution of the scattered neutron. Figure 2.8 plots the angular distribution of inelastically scattered neutrons on $^{16}$O that left the nucleus in the different excited states from an incident neutron energy of 21.6 MeV [18]. The angular distribution from the $E^* = 6.130$ MeV state, indicates that the reaction mechanism for that state is mostly direct reactions. Whereas, the isotropic distribution from the $E^* = 8.872$ MeV state, indicates that the reaction mechanism for that state is mostly compound reactions. As the excitation energy of the nucleus increases, the reaction moves from a direct reaction to a compound reaction, which agrees with Figure 2.4.

### 2.4.3 Radiative Capture

Radiative capture occurs when an incident neutron is absorbed by a nucleus, which then causes it to transmute into an new isotope in an excited state. The excited nucleus then releases a gamma ray as it relaxes to the ground state. An example of radiative capture is a thermal neutron (0.025 eV) on $^{16}$O, which causes it to change to $^{17}$O. The Q value for this reaction is 4.143 MeV, which is exothermic and places the $^{17}$O nucleus in a excited state of 4.413 MeV above its ground state. The excited $^{17}$O nucleus will then emit a cascade of gamma rays as it relaxes down to the ground state, as shown in Figure 2.9. One cascade would create three gammas

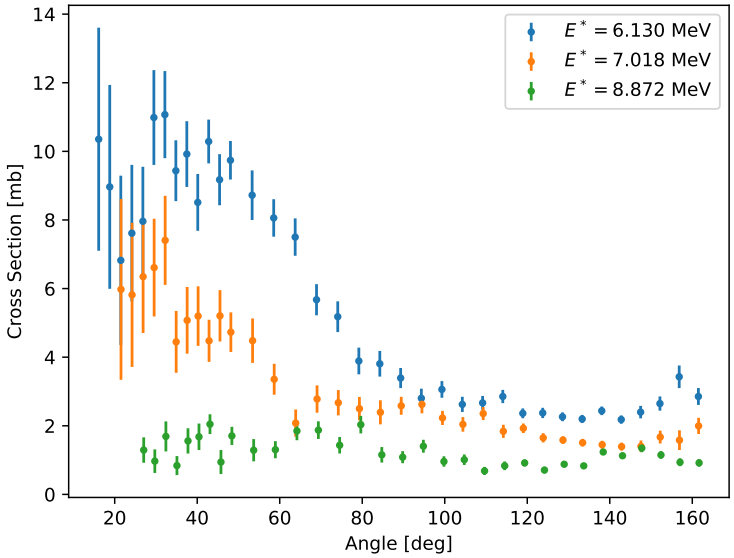


**Figure 2.8. The angular distribution of inelastically scattered neutrons on $^{16}$O that left the nucleus in the different excited states (6.13, 7.018, and 8.872 MeV). The 7.108 MeV state is the combination of the 6.917 and 7.117 MeV states in $^{16}$O that could not be resolved in the experiment. The incident neutron energy was 21.6 MeV [18].**

(1.088, 2.184, and 0.87 MeV), occurring 82% of the time. The other cascade would create two gamma rays (3.272 and 0.87 MeV), occurring 18% of the time [53, 54]. Radiative capture is a compound reaction and the angular distribution of the gamma rays from the transmuted nucleus is isotropic.

### 2.4.4 Particle Production Reactions

Incident neutrons on a nucleus can react and cause the emission of other particles, such as protons, deuterons, and alpha particles. Similar to inelastic scattering, all these reactions on $^{16}$O are endothermic, meaning that the neutron must have enough energy for the reaction to occur, known as the threshold energy. Table 2.2 lists the threshold energies for the six lowest threshold reactions on $^{16}$O. The angular distribution of the particles is isotropic at the energies considered (<20 MeV), since the energy of the incident neutron is dispersed in the newly created compound nucleus.

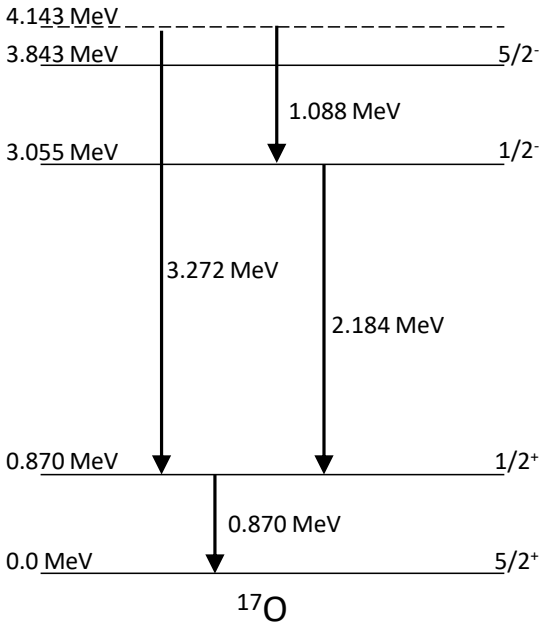


**Figure 2.9. Gamma production from thermal neutron capture on $^{16}$O [53, 54].**

**Table 2.2. Threshold energy for the specific reactions on $^{16}$O.**

| Reaction | Threshold Energy [MeV] |
|---|---|
| $^{16}$O(n,$\alpha$)$^{13}$C | 2.355 |
| $^{16}$O(n,n')$^{16}$O | 6.427 |
| $^{16}$O(n,n+$\alpha$)$^{12}$C | 7.614 |
| $^{16}$O(n,p)$^{16}$N | 10.247 |
| $^{16}$O(n,d)$^{15}$N | 10.528 |
| $^{16}$O(n,n+p)$^{15}$N | 12.892 |

## 2.5 Nuclear Data Pipeline

The cross-section data for nuclear reactions mentioned above are compiled from experiments, evaluated, and stored in nuclear data libraries. These libraries provide users with precise, accurate, and standardized data that can be utilized for modeling, simulations, and calculations. The "Nuclear Data Pipeline" helps visualize the process from experiments to using the data in applications [55, 56], as shown in Figure 2.10.

The first part in the pipeline is for the nuclear data from experiments to be

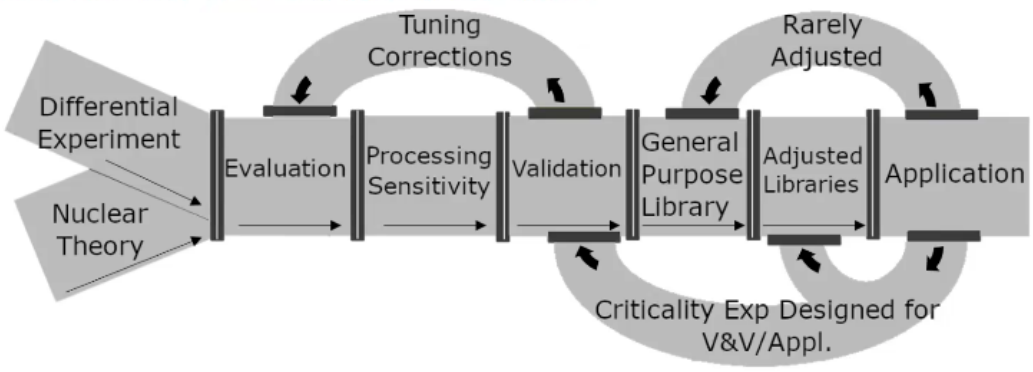


**Figure 2.10. Nuclear data pipeline [55, 56].**

published, which can be done in many journals, such as the Nuclear Data Sheets. The second part is a compilation of the experimental data, such as the EXFOR database, which contains nuclear reaction data from 22,888 experiments from all over the world and continues to grow as new experimental data are available. The database allows retrieval of data based on reactions, targets, measurements, products, etc. [57, 58].

The third part is evaluation, which incorporates the experimental data and models to produce standard nuclear data values. There are several different databases that contain evaluated nuclear data. The most common databases that contain evaluated neutron cross sections are

- ENDF-Evaluated Nuclear Data File (USA) [59],
- JEFF-Joint Evaluated Fission and Fusion Nuclear Data Library (Europe) [60],
- JENDL-Japanese Evaluated Nuclear Data Library (Japan) [61],
- CENDL-Chinese Evaluated Nuclear Data Library (China) [62], and
- BROND-Russian Recommended Evaluated Neutron Data Library (Russia) [63].

The fourth part of the pipeline is processing, which packages the data into formats to be used for specific applications. The fifth part is validation, where the nuclear data is tested and validated by well-characterized experiments, models, and benchmarks.

The final part of the pipeline is use, where the nuclear data can be utilized for calculations, models, and simulations.

As described, there are many steps and processes to provide precise and accurate nuclear data to the end user community. This work will measure the neutron inelastic cross section on $^{16}$O, which provides additional input to the beginning of the pipeline to complement and weight other experimental inelastic cross-section data.

## 2.6 Gamma-ray Interactions

Gamma-rays interact with matter by three primary mechanisms: the photoelectric effect, Compton scattering, and pair production. The gamma-ray interactions within a material are dependent on the material composition and photon energy, as shown Figure 2.11, which depicts the dominant interactions as a function of energy [64]. The photoelectric effect is predominant at lower photon energies, Compton scattering occurs at moderate photon energies, and pair production can only occur at energies above 1.022 MeV.

The primary gamma rays produced from $^{16}$O(n,n') are from 2.742 to 7.117 MeV, which will primarily interact by Compton scattering for low Z materials and by pair production on all other materials. After a gamma ray interacts by Compton scattering, the energy of the gamma ray may be low enough to interact by the photoelectric effect.

### 2.6.1 Photoelectric Effect

The photoelectric effect occurs when a gamma ray is absorbed by an atom and the energy is sufficient to overcome the binding energy of an atomic electron, thereby ejecting the electron from the atom. The energy of the photoelectron, $E_e$ is the energy

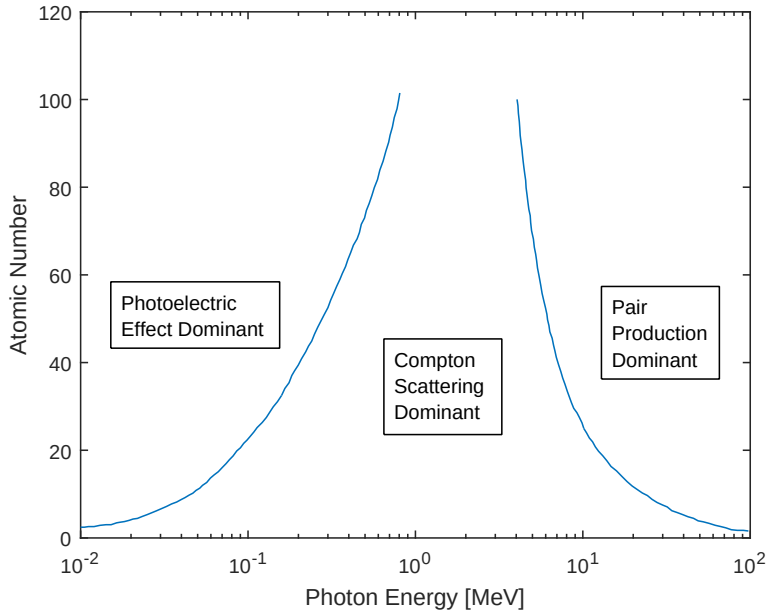


**Figure 2.11. Dominate photon interactions as a function of atomic number and photon energy [64].**

of the gamma ray, $E_\gamma$, minus the binding energy of the electron, $E_B$, as

$$E_e = E_\gamma - E_B. \tag{2.26}$$

### 2.6.2 Compton Scattering

Compton scattering occurs when a photon interacts with and scatters off an electron, transferring a portion of its energy to the electron in the process. The transferred energy from the gamma ray to the electron is sufficient to overcome the binding energy of the electron and release it from the atom. The energy of the scattered gamma ray, $E'_\gamma$, is

$$E'_\gamma = \frac{E_\gamma}{1 + \left(\frac{E_\gamma}{m_e c^2}\right)(1 - \cos\theta)}, \tag{2.27}$$

where $E_\gamma$ is the energy of the incident gamma ray, $m_e c^2$ is the rest mass of the electron

(0.511 MeV), and $\theta$ is the scattering angle [48]. The energy of the electron is

$$E_e = E_\gamma \left( \frac{\left(\frac{E_\gamma}{m_e c^2}\right)(1-\cos\theta)}{1+\left(\frac{E_\gamma}{m_e c^2}\right)(1-\cos\theta)} \right). \tag{2.28}$$

The maximum energy transferred from the gamma to the electron occurs when $\theta = \pi$. Therefore, the minimum energy of the scattered gamma ray is

$$E'_{\gamma,min} = \frac{E_\gamma}{1+\left(\frac{2E_\gamma}{m_e c^2}\right)}, \tag{2.29}$$

and the maximum energy of the electron is

$$E_{e,max} = \frac{E_\gamma}{1+\left(\frac{m_e c^2}{2E_\gamma}\right)}. \tag{2.30}$$

The Klein-Nishina formula, which calculates the probability that an incident gamma ray will be scattered at an angle $\theta$ about $d\Omega$ [50], is given as

$$\frac{d\sigma_c}{d\Omega} = \frac{r_e^2}{2}(1-\cos^2\theta)\left[\frac{1}{1+\alpha(1-\cos\theta)}\right]^2\left[1+\frac{\alpha^2(1-\cos\theta)^2}{(1+\cos^2\theta)[1+\alpha(1-\cos\theta)]}\right], \tag{2.31}$$

where $r_e$ is the classic electron radius ($r_e = e^2/(4\pi\epsilon_0 mc^2) = 2.818$ fm) and $\alpha = E_\gamma/m_e c^2$. Figure 2.12 plots the normalized angular distribution of Compton scattered gammas for five different incident gamma-ray energies.

### 2.6.3 Pair Production

Pair production occurs when a photon creates a positron and electron pair due to the electromagnetic coupling with another particle, such as the nucleus of the atom. The energy of the gamma goes into the creation of the electron and positron, $m_e c^2$

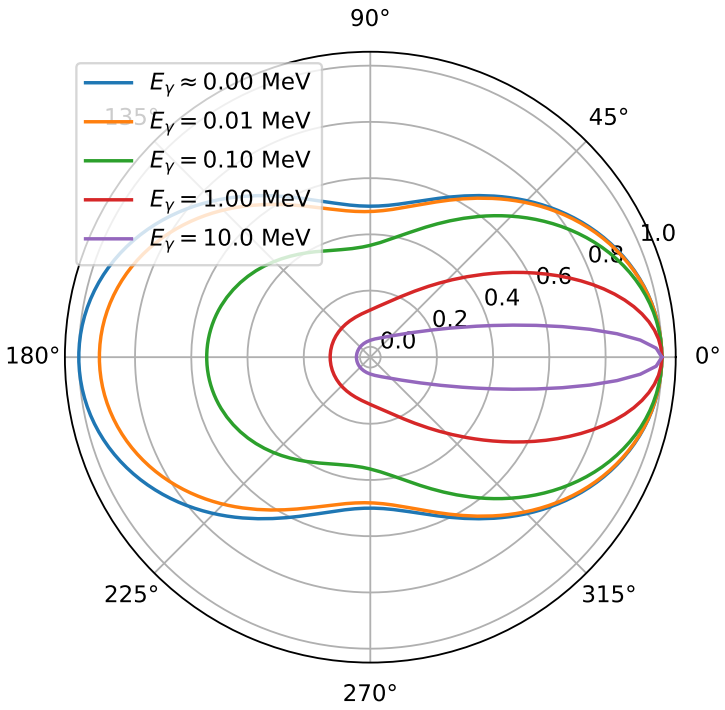


**Figure 2.12. The normalized angular distribution of Compton scattered gamma rays for five different incident gamma-ray energies. Low energy gamma rays (near zero energy) have the same probability to scatter backwards as they do forward. As the energy of the gamma ray increases, it will more likely scatter in the forward direction.**

and $m_p c^2$, and their kinetic energy, $E_e$ and $E_p$, respectively, as

$$E_\gamma = m_e c^2 + E_e + m_p c^2 + E_p. \tag{2.32}$$

The positron soon annihilates with an electron and creates two 0.511 MeV photons in coincidence.

## 2.7 Scintillator Radiation Detectors

Scintillation detectors create light from gamma-ray and neutron interactions in the detector from the primary interaction mechanisms described in Sections 2.6 and 2.4, respectively. The amount of light that is created is a function of the energy deposition from the radiation. There are two categories of scintillator detectors: inorganic and

organic.

### 2.7.1 Inorganic Scintillators

For inorganic scintillators, such as NaI and $LaBr_3$ detectors, the crystalline molecular arrangement creates a valence and conduction band structure. Normally, the electrons are bound in lattice sites, the valence band, and are not able to move freely throughout the crystal. However, if enough energy is provided to overcome the band gap, the electrons can move into the conduction band and move freely throughout the crystal.

Gamma rays interact with the detector material by the photoelectric effect, Compton scattering, or pair production, in each case creating secondary electrons in the material. These secondary electrons excite other electrons in the material promoting them from the valence band to the conduction band, allowing the electrons to move freely throughout the crystal and leaving behind empty "holes" (vacant lattice sites) in the valence band.

In radiation detectors, the crystals are doped with other elements to create activator sites, which are positioned in the band gap of the pure crystal. NaI detectors are usually doped with thallium, and $LaBr_3$ detectors are doped with cesium. These activator sites allow the electrons to drop from the conduction band to the excited activator site and then to the ground activator site. The de-excitation between the activator sites produces visible light, shown in Figure 2.13. The amount of visible light created in the detector is a function of the amount of radiation deposited in the detector. The photons are then collected in a photomultiplier tube (PMT), where the light is converted into an electric pulse. The timing of the scintillation for inorganic detectors depends on the decay time of the scintillation mechanisms. For NaI and $LaBr_3$, the decay time is 230 and 26 ns, respectively [65].

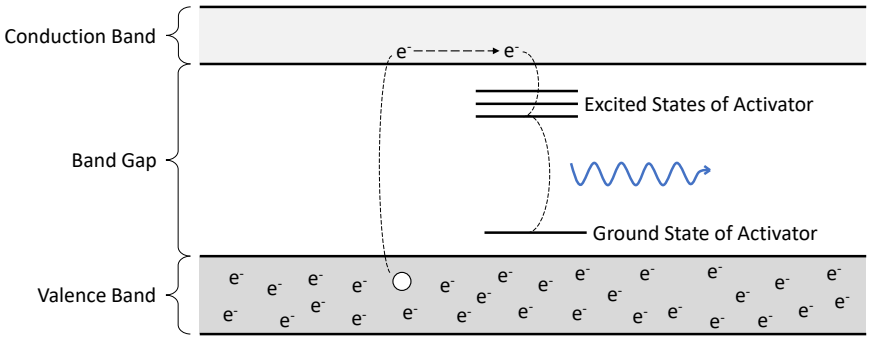


**Figure 2.13. Illustration of the inorganic scintillation mechanism of a crystal due to the movement of electrons from the activation sites.**

The intrinsic efficiency of a detector is

$$\varepsilon_{int} = \frac{\text{number of particles detected}}{\text{number of particles incident on the detector}} \tag{2.33}$$

and is dependent on the material (density and elemental composition) and volume of the detector. Figure 2.14 plots the efficiencies of a 2"×2" NaI detector and a 1.5"×1.5" $LaBr_3$ detector [66].

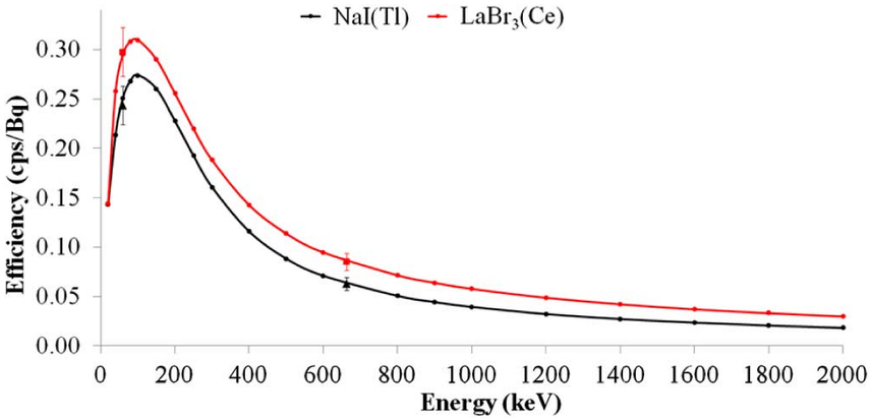


**Figure 2.14. The efficiencies of a 2"×2" NaI detector and a 1.5"×1.5" $LaBr_3$ detector [66].**

### 2.7.2 Organic Scintillators

Organic scintillators, such as EJ-309, are aromatic hydrocarbons that are able to detect and distinguish between gamma rays and fast neutrons. Gamma rays primarily interact with the hydrogen and carbon electrons by Compton scattering, which only produces a Compton continuum spectrum. Fast neutrons are more easily detected in organic scintillators than inorganic scintillators because the neutron can deposit more energy to low-A materials via elastic scattering. For the hydrogen nucleus (proton) in organic scintillators, the neutron can transfer up to all its energy to the proton. The neutron efficiency of an 2"×2" EJ-309 is shown in Figure 2.15 with four different light thresholds [67].

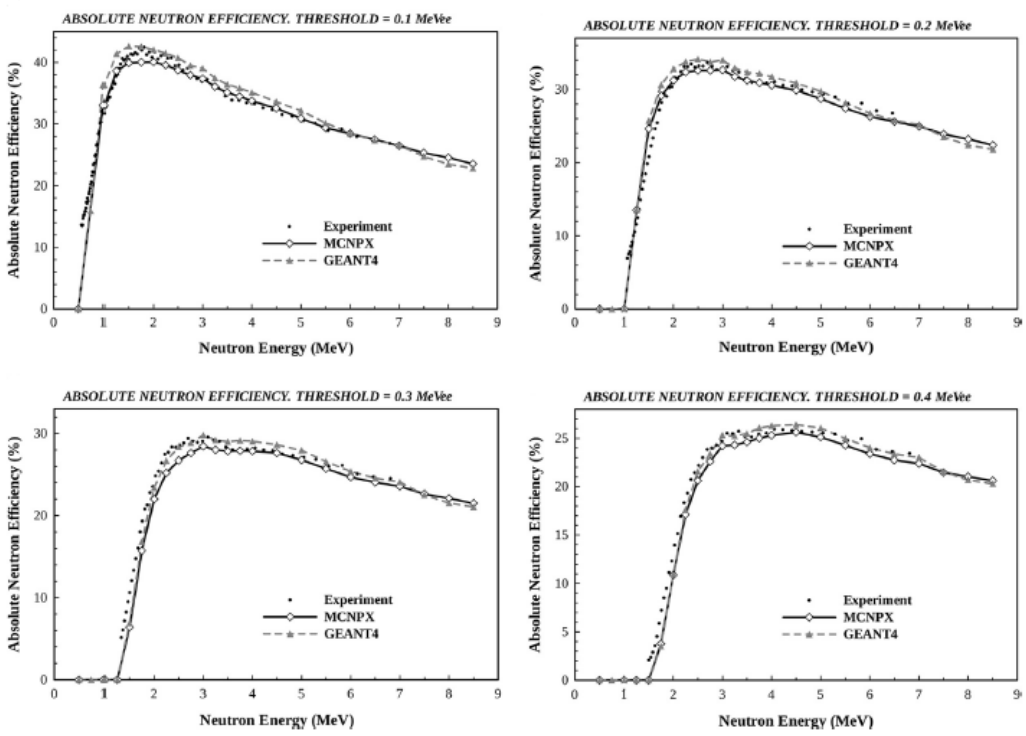


**Figure 2.15. Neutron efficiency of an 2"×2" EJ-309 organic scintillator at four different light thresholds [67].**

The secondary electrons created from the Compton scattering of the gamma ray in the material and the recoil protons created from the neutron elastic scattering

interactions excite the molecules in the detector by Coulombic interactions. The excited molecules then emit visible photons as they de-excite [65]. Figure 2.16 depicts the molecular excitation due to the absorption of energy followed by the emission of photons due to fluorescence and phosphorescence from the singlet and triplet states, respectively. The absorption of energy changes the configuration of the electrons, which places the molecule in a higher excited state, such as the singlet state, S13. The molecule loses energy through non-radiative processes as it drops to the $S_{10}$ state. For organic scintillators, the spacing between the singlet states is about 3 to 4 eV, and the spacing between the vibration states is on the order of 0.15 eV [65]. As the molecule transitions from the $S_{10}$ state to one of the vibrational states in the ground state, $S_0$, it emits a photon, which is known as fluorescence.

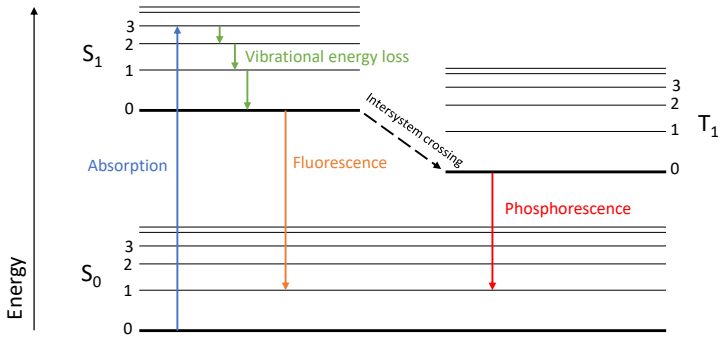


**Figure 2.16. Jablonski diagram of the absorption of energy and the emission of photons due to fluorescence and phosphorescence from the singlet and triplet states, respectively.**

The excited singlet state may also transition to a triplet state, known as intersystem crossing. As the molecule transitions from the triplet state to the ground state, it emits a photon, known as phosphorescence. This process is incredibly slow compared to fluorescence.

The photons are then collected in a PMT, where the light is converted into an electric pulse. The timing of the scintillation of organic detectors depends on the decay time of the scintillation mechanisms. The absorption and fluorescence for

organic scintillators is very quick. For EJ-309, the decay constant is 3.5 ns [65]. The transition from the triplet state to the ground state takes a longer time than the fast fluorescence process, which may can be up to milliseconds [65]. The creation of singlet and triplet states, with their corresponding prompt and delayed fluorescence, from gamma-ray and neutron radiation effects the decay time of the electronic pulse from the detector, enabling discrimination of the particle type through analysis of the pulse shape.

#### 2.7.2.1 Wavelength Shifters

Energy deposited in the scintillator will non-radiatively transfer from the solvent to the fluor or primary dye, which emits light. Wavelength shifters, or secondary dyes, are sometimes added to organic scintillators to shift the spectrum of the light output from lower to higher wavelengths to more closely match the wavelengths with high quantum efficiency in the PMT. These wavelength shifters absorb the lower wavelength emitted light from the organic scintillator and emit at a higher wavelength, such as shown in Figure 2.17 of POPOP [68–70], a common wavelength shifter, in cyclohexane.

## 2.8 Plastic Scintillators

A plastic scintillator is a polymer matrix containing an organic scintillator. Dissolving the organic scintillator into a monomer solvent enables polymerization of the monomer to create a scintillating plastic. The most common monomer solvents used in plastic scintillators are styrene, vinyltoluene, and methylmethacrylate [65].

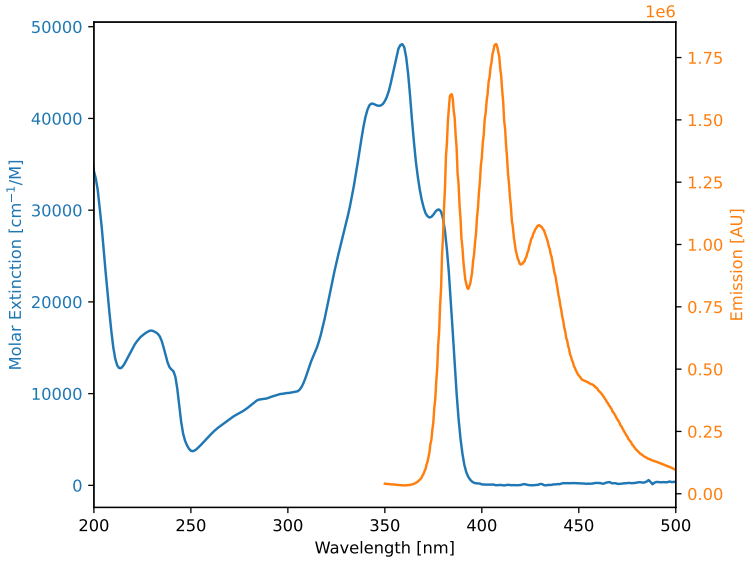


**Figure 2.17. Absorption (blue) and emission (orange) spectra of POPOP in cyclohexane [68–70].**

### 2.8.1 Free Radical Polymerization

In the formation of the plastic, a monomer is polymerized to from long polymer chains. One of the most common polymerization methods is free radical polymerization, which uses an initiator. Using heat or light, the initiator breaks into two radicals, which react with the monomer to begin the polymerization. As the bonds of the monomer change due to the interaction with the radical, it binds with other monomers to created a polymer chain [71].

## 2.9 Semiconductor Radiation Detectors

High purity germanium detectors (HPGe) are semiconductor detectors [72, 73]. Placing a reverse voltage bias on the HPGe crystal increases the depletion region of the semiconductor and the electric field across that region. The thickness of the depletion region, $d$, is

$$d = \left(\frac{2\epsilon V}{eN}\right)^{1/2}, \tag{2.34}$$

where $\epsilon$ is the dielectric constant, $V$ is the applied voltage, $e$ is the electron charge and $N$ is the net impurity concentration of the bulk in the detector material [65].

The secondary electrons created from the photoelectric effect, Compton scattering, and pair production in the material excite other electrons in the detector by Coulombic interactions creating electron-hole pairs. The average energy needed to create an electron-hole pair in Ge is 2.96 eV at 77K [74]. In the electric field, these electrons and holes are pulled in opposite directions. When they reach the surface contacts, they generate an electron pulse that is proportional to the amount of energy deposited in the detector. Figure 2.18 illustrates the incident gamma ray creating electron-hole pairs in the depletion region, which are then attracted to the surface contacts due to the electric field.

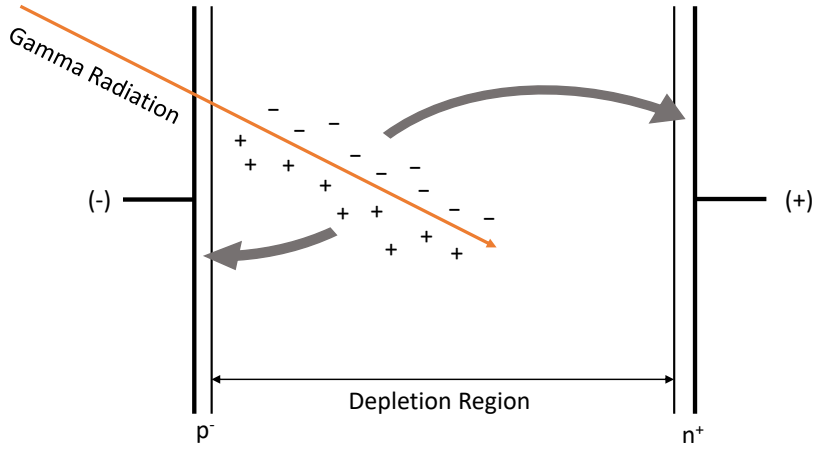


**Figure 2.18. Illustration of gamma ray creating electron-hole pairs in the depletion region of a HPGe detector. The electrons and holes are then attracted to the surface contacts due to the electric field.**

The electron and hole movement to the surface can be calculated using, respectively,

$$\nu_e = \mu_e \mathcal{E} \tag{2.35}$$

and

$$\nu_h = \mu_h \mathcal{E}, \tag{2.36}$$

where $\nu_e$ and $\nu_h$ are the drift velocities for electrons and holes, respectively, $\mu_e$ and $\mu_h$ are the mobility for electrons and holes, respectively, and $\mathcal{E}$ is the electric field. The electron and hole mobilities are intrinsic properties of the detector material. Even with a high electric field, the electrons and holes reach a terminal drift velocity in the crystal, which is the maximum velocity of the electrons and holes due to Coulombic forces and collisions that inhibit higher velocities.

The electric charge pulse, especially the rise time, is dependent on the drift velocity and the location of the electron-hole creation in the detector volume. Large HPGe detectors have pulse rise times on the order of 100 ns and as the detector volume increases, the variation in the rise time of the pulses also increases. This can contribute to a large uncertainty in timing measurements.

The full-peak intrinsic efficiency of a HPGe detector is primarily dependent on the volume of the detector. However, as the volume increases, the increase in detector efficiency is offset but the increase in the timing variation. Figure 2.19 plots the absolute full-peak efficiency of a 8.81 cm $\times$ 9.97 cm coaxial p-type HPGe detector at 25 cm from the source [65].

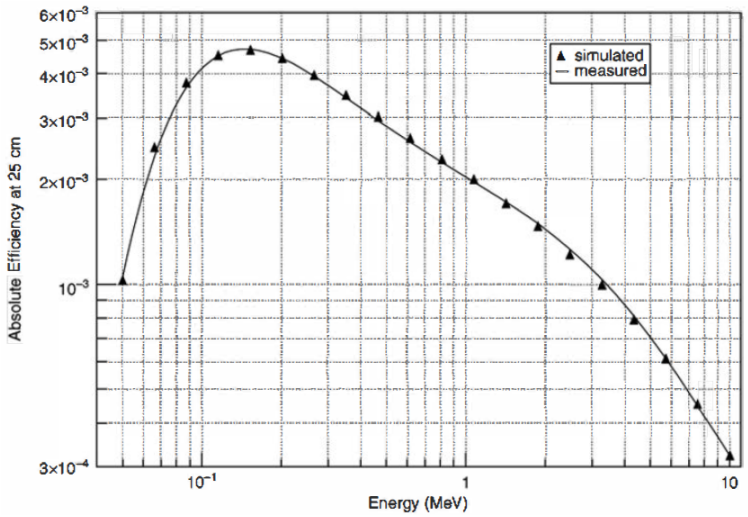


**Figure 2.19. The absolute full-peak efficiency of a 8.81 cm $\times$ 9.97 cm coaxial p-type HPGe detector at 25 cm from the source [65].**

## 2.10 Gamma-ray Spectroscopy

The ideal spectrum obtained from a detector, as depicted in Figure 2.20 (a), is obtained when all the energy from the gamma ray is collected in the detector and produces a full energy peak on the spectrum. However, gamma rays may escape the detector volume after interacting with the material by Compton scattering, leaving only a portion of the energy in the detector. The deposited energy produces a Compton continuum, and the full energy peak is reduced, as illustrated in Figure 2.20 (b).

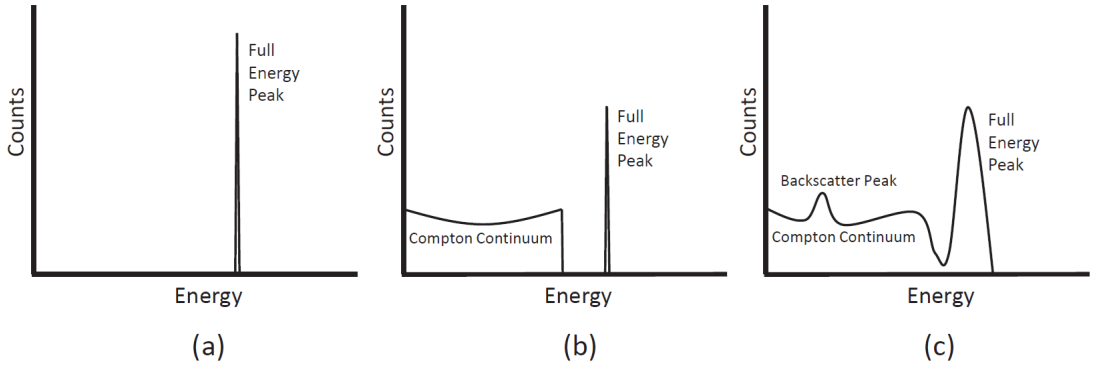


**Figure 2.20. Representation of a typical energy spectrum from mono-energetic gammas. (a) illustrates all the energy is collected in the detector, (b) illustrates that some of the gammas leave the detector after depositing some energy due to Compton scattering and (c) illustrates a realistic spectrum with a Compton continuum, backscatter peak, and broadening.**

The Compton continuum is a continuous energy spectrum due to the portion of gamma energy imparted to the electron which can be calculated using Equation 2.28. The electron then deposits its energy into the detector, and the scattered photon leaves the detector volume. The Compton edge, which appears as the cutoff in the spectrum just prior to the full energy peak, occurs when the photon is back-scattered at 180 degrees and transfers the maximum energy to the ionized electron, as shown

in Equation 2.30. The distance between the full energy peak and Compton edge is

$$E_\gamma - E_{CE} = \frac{E_\gamma}{1 + \left(\frac{2E_\gamma}{m_e c^2}\right)}. \tag{2.37}$$

For high energy gamma rays, the distance between the full energy peak and Compton edge becomes constant and $E_\gamma - E_{CE} \approx m_e c^2/2 = 0.256$ MeV.

In addition to the smaller full energy peak and the Compton continuum, there is usually a backscatter peak, shown in Figure 2.20 (c). The backscatter peak, appearing around 0.25 MeV, is from the gamma ray interacting with the surrounding environment by Compton scattering and then being collected in the detector.

### 2.10.1 Energy Resolution

The broadening of the spectrum seen in Figure 2.20 (c) is due to the variations in the generation and collection of the information carriers in the detectors, and the variance in the electronic equipment. In an ideal detector, the broadening of the full energy peak is a Gaussian distribution given as

$$f(E) = \frac{A}{\sigma\sqrt{2\pi}} e^{-\frac{1}{2}\left(\frac{E-\mu}{\sigma}\right)^2}, \tag{2.38}$$

where $E$ is the energy, $A$ is the area of the peak, $\mu$ is the mean, and $\sigma$ is the standard deviation.

The resolution of a detector is

$$\text{Resolution} = \frac{FWHM}{\mu}, \tag{2.39}$$

where $FWHM$ is the full-width, half-max and $\mu$ is the mean of the full energy peak,

which is depicted in Figure 2.21. For a Gaussian distribution, $FWHM \approx 2.35\sigma$. The resolution for NaI, LaBr, and HPGe at 662 keV ($^{137}$C) is 7%, 2.8-4%, and 0.2%, respectively [75]. In organic scintillators, such as EJ-309, the gamma rays interact by Compton scattering and are unable to deposit all their energy and produce a full energy peak.

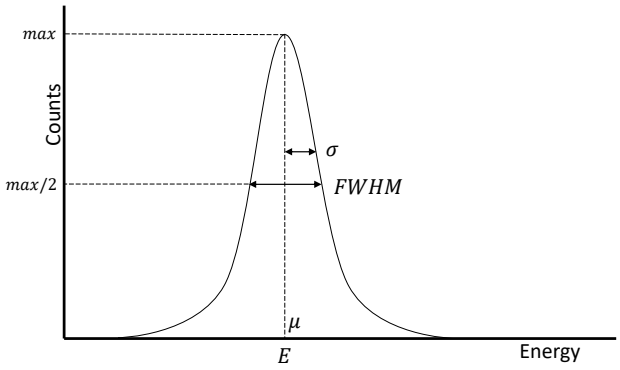


**Figure 2.21. Gaussian distribution of the full deposition of a gamma ray in a detector.**

### 2.10.2 Escape Peaks

Two other distinct characteristics in a gamma-ray spectrum from high energy gamma-ray interactions are the single and double escape peaks, which appear when either one or both of the two photons from positron/electron annihilation escape the detector volume. A single escape peak will show on a spectrum at 0.511 MeV to the left of the full energy peak and a double escape peak will show on a spectrum at 1.022 MeV to the left of the full energy peak. For inelastic scattering on $^{16}$O, the first three gamma rays are 6.129, 6.916 and 7.115 MeV, which are well above 1.022 MeV and will produce single and double escape peaks in the detector, as listed in Table 2.3.

**Table 2.3. The first three gamma rays from $^{16}$O and their associated single and double escape peaks.**

| Eγ [MeV] | Single Escape Peak [MeV] | Double Escape Peak [MeV] |
|---|---|---|
| 6.129 | 5.618 | 5.107 |
| 6.916 | 6.407 | 5.896 |
| 7.115 | 6.604 | 6.093 |

## 2.11 Detection Event Classification and Processing

The electric pulse from a detector can be digitally processed to extract the information from the pulse. The pulse from the scintillators is processed by a digitizer, which samples the pulse at a specific frequency and characterizes the height of the pulse using an analog-to-digital converter (ADC). Figure 2.22 illustrates an analog pulse from a PMT being digitized.

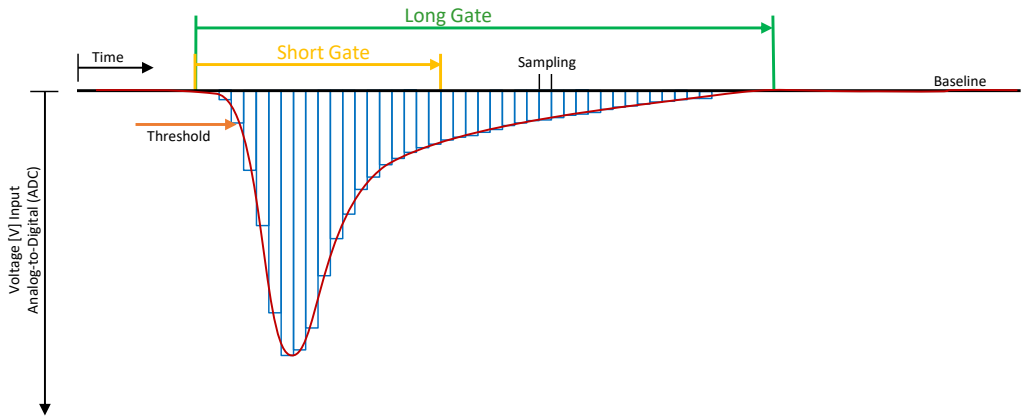


**Figure 2.22. A pulse from a detector is digitized by sampling the pulse using an ADC.**

The energy in the pulse is measured using pulse integration, which integrates the pulse over a specified length of time, which is known as the long gate. Additionally, for PSD, a short gate can also be set to integrate the energy in the peak of the pulse.

For pulses from a pre-amplifier, such as pulses from a HPGe detector, the pulses are analyzed using triangle shaping. Triangle shaping consists of a differentiator (high pass filter) followed by a integrator (low pass filter), which converts the long-tail pre-

amplifier signal into a triangular waveform. The height or amplitude of the triangle is relative to the height of the pre-amplifier pulse and the energy deposited in the detector.

### 2.11.1 Pulse Shape Discrimination

As mentioned in Section 2.7.2, organic scintillators can distinguish between gamma rays and neutrons due to the increased delayed fluorescence emission from neutron interactions that creates a pulse with a longer tail than gamma rays, as shown in Figure 2.23.

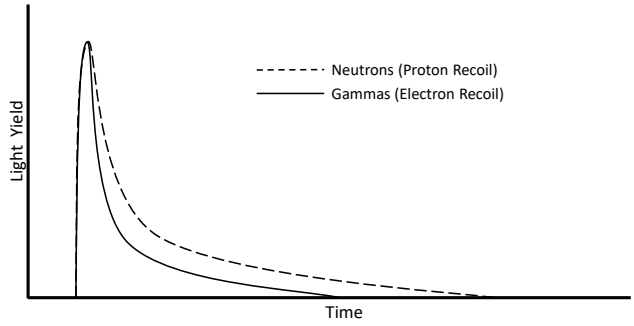


**Figure 2.23. The pulses created in an organic scintillation detector from fast neutrons (proton recoil) and gammas rays (electron recoil).**

Therefore, gamma rays and fast neutrons can be distinguished using pulse shape discrimination (PSD). One of the most common methods of calculating the PSD value of a pulse, the tail-to-total method, is calculated as

$$PSD = \frac{E_{long} - E_{short}}{E_{long}}, \tag{2.40}$$

where $E_{long}$ is the integrated energy of the entire pulse and $E_{short}$ is the integrated energy in the peak of the pulse.

The quality of the pulse shape discrimination is dependent on several factors, which include the detector material, high voltage bias of the photodetector, and the

length of the short and long integration gates. The figure of merit (FoM) can be used to quantify how well neutrons and gamma rays are distinguished and is calculated as

$$FoM = \frac{\mu_n - \mu_\gamma}{FWHM_n - FWHM_\gamma}, \tag{2.41}$$

where $\mu_\gamma$ and $FWHM_\gamma$ are the mean and full-width, half-max (FWHM) of the peak generated by the gamma rays, respectively, and $\mu_n$ and $FWHM_n$ are the mean and FWHM of the Gaussian peak generated by the neutron events, respectively. Figure 2.24a depicts the two Gaussian peaks that represent neutrons and gamma rays in a PSD histogram, and Figure 2.24b is an example of a PSD vs total energy histogram using an organic scintillation detector (EJ-309). As shown in the figures, the fast neutrons and gamma rays can be distinguished with the neutrons having higher PSD values than the gamma rays.

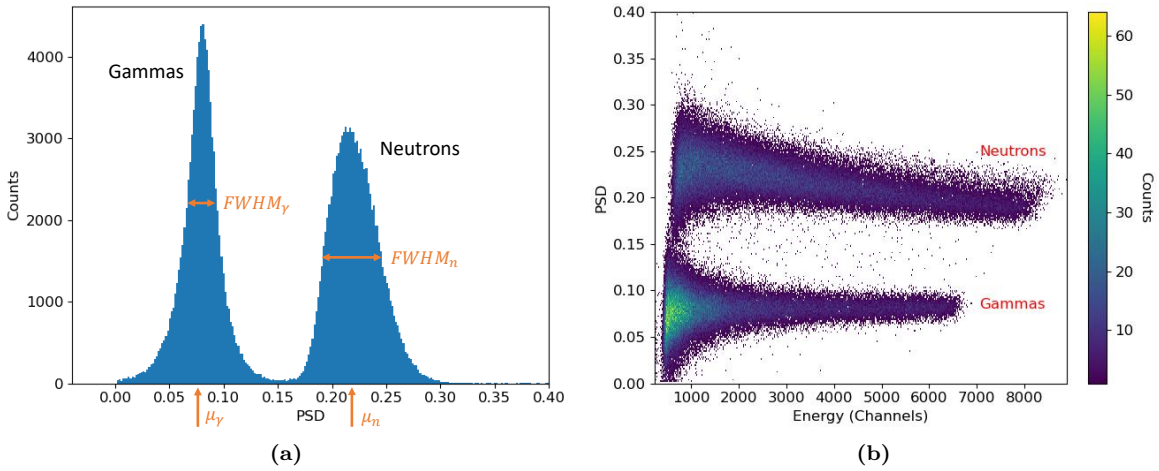


**Figure 2.24. (a) Pulse shape discrimination (PSD) histogram and (b) PSD vs energy plot from AmBe source using an EJ-309 detector.**

### 2.11.2 Pulse Timing

The two most common techniques of pulse timing are leading edge and constant fraction discriminator (CFD). The timing of the pulse using the leading edge

technique is determined when the pulse exceeds a set threshold. However, this method is vulnerable to amplitude walk, which occurs when pulses of different amplitudes offset the correct timing of the pulse. As shown in Figure 2.25, the pulses occur at the same time; however, the timing of the larger pulse is measured sooner than the smaller pulse.

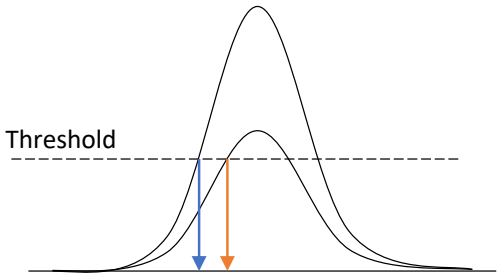


**Figure 2.25. The leading edge pulse timing technique can lead to amplitude walk where the timing of a pulse is dependent on the amplitude of the pulse.**

The other common pulse timing method, which eliminates the problem of amplitude walk, is using a constant fraction discriminator. Using the CFD method, the pulse from the detector is split into two identical pulses. One of the pulses is delayed by a specified amount, and the second pulse is inverted and attenuated by a set percentage. Finally, the two pulses are added together, which creates a crossover point. The timing of the pulse using the CFD method is determined at the crossover point. Figure 2.26 depicts the CFD pulse timing method.

### 2.11.3 Detector Dead Time

For all radiation equipment, there is a given time needed to process a radiation detection event in which other events in a given time will not be detected or will contribute to pile-up events that complicate reconstruction of the energy of the interacting particle. The time to properly detect and process each event is known as the dead time, $\tau$. Systems are generally modeled as paralyzing or non-paralyzing. In a non-paralyzing system, if an event occurs within the system's dead time, the

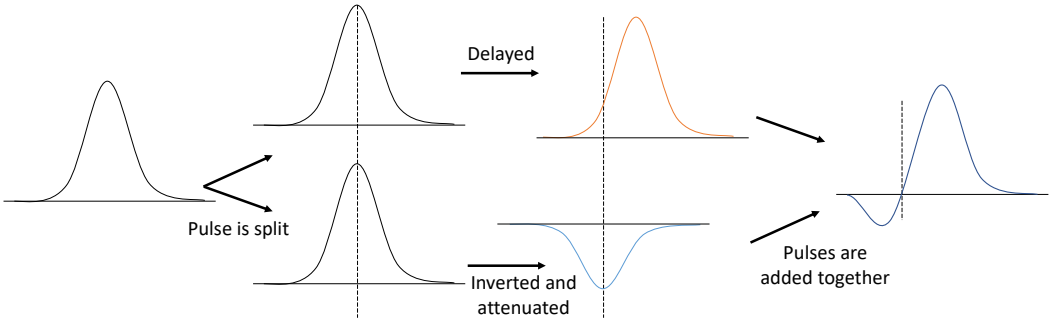


**Figure 2.26. Illustration of the CFD method. The pulse from the detector is split into two identical pulses. One of the pulses is delayed by a specified amount, and the second pulse is inverted and attenuated by a set percentage. The summation of the two pulses creates a crossover point, which determines the pulse timing.**

event is simply discarded. The true event rate, $R_t$, to the detected event rate, $R_d$, in a non-paralyzing system is

$$R_t = \frac{R_d}{1 - R_t\tau}. \tag{2.42}$$

In paralyzing systems, if an event occurs within the system's dead time, it compounds the system's dead time by adding to it. The true event rate, $R_t$, is related to the detected event rate, $R_d$, in a paralyzing system as

$$R_d = R_t e^{-R_t\tau}. \tag{2.43}$$

For both non-paralyzing and paralyzing systems, at low event rates ($R_t << 1/\tau$), the detected event rate, $R_d$ is

$$R_d = R_t(1 - R_t\tau). \tag{2.44}$$

### 2.11.4 Neutron Time-of-Flight

There are several methods used to determine the kinetic energy of a neutron. One of the most common methods calculates the kinetic energy by measuring the neutron

time of flight over a known distance as

$$E_n = \frac{1}{2} m_n v_n^2 = \frac{1}{2} m_n \left( \frac{d}{t} \right)^2, \tag{2.45}$$

where $E_n$ is the kinetic energy of the neutron, $m_n$ is the mass of the neutron, $v_n$ is the velocity of the neutron, $d$ is the known distance, and $t$ is the elapsed time for the neutron to travel.

Generally, if the neutron's velocity is more than 10% of the speed of light, which is equivalent to a 4.7 MeV neutron, relativistic effects need to be considered. The neutron kinetic energy, considering relativistic effects, is

$$E_n = m_n c^2 \left( \frac{1}{\sqrt{1 - \frac{(d/t)^2}{c^2}}} - 1 \right). \tag{2.46}$$

From Equations 2.45 and 2.46, the time-of-flight of a neutron over a known distance using classic kinematics is

$$t = \frac{d}{\sqrt{\frac{2E_n}{m_n}}} \tag{2.47}$$

and incorporating relativistic effects the time-of-flight is

$$t = \frac{d}{\sqrt{c^2 \left( 1 - \left( \frac{1}{\frac{E_n}{m_n c^2} + 1} \right)^2 \right)}}. \tag{2.48}$$

## 2.12 88-Inch Cyclotron

A cyclotron is a particle accelerator that accelerates ions using an oscillating electric field between a pair of hemisphere magnets. Figure 2.27 (a) illustrates the

magnetic field created by the magnets (blue arrows) between the electric field (orange arrows). The electric field changes direction, as shown in Figure 2.27 (b), each time the particles pass through, which allows them to continuously accelerate. The particles follow a circular path in the magnetic field, due to the Lorentz force, and accelerate each time they cross through the electric field, as shown in Figure 2.27 (c). The particles are then extracted from the cyclotron at a desired energy.

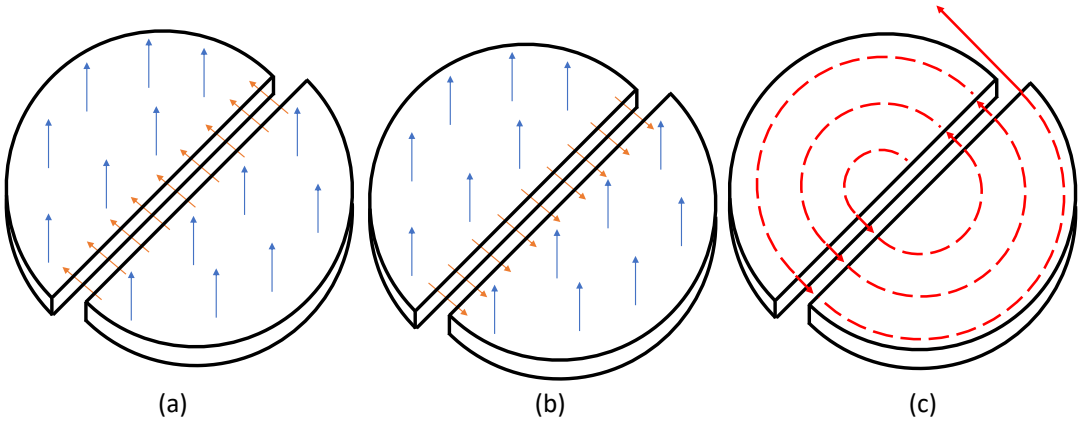


**Figure 2.27. (a) A cyclotron contains two hemispheric magnets, which create a strong magnetic field (blue arrows) between an electric field (orange arrows). (b) The electric field flips each each time the particles cross the field to accelerate the particles. (c) The particles follow a circular path between the magnets and accelerate each time they cross the electric field.**

The cyclotron frequency of the oscillating electric field is [50]

$$f = \frac{qB}{2\pi m}, \tag{2.49}$$

where $q$ is the charge of the particle, $B$ is the magnetic field, and $m$ is the mass of the particle. The maximum kinetic energy of a particle from a cyclotron is

$$T = \frac{1}{2}mv^2 = \frac{q^2b^2R^2}{2m}, \tag{2.50}$$

where $R$ is the radius of the cyclotron. The 88-Inch Cyclotron at Lawrence Berkeley National Laboratory, used in this research, can accelerate deuterons up to 65 MeV.

### 2.12.1 Deuteron Breakup

The weakly bound deuteron, with a binding energy of 2.22 MeV, enables the neutron to be easily stripped from the proton in a nuclear reaction. These reactions serve as the basis for creating intense neutron beams at the 88-Inch Cyclotron [76]. Since first discussed by Oppenheimer in 1935 [77], several theories have been postulated on the reaction mechanisms for deuteron breakup.

In Coulombic deuteron breakup, the deuteron incident on a nucleus "feels" the Coulombic repulsion between the protons in the nucleus to the proton in the deuteron. As the deuteron gets closer to the nucleus, the Coulombic force is enough to breakup the proton from the neutron [78].

The energy of the neutron, $E_n$, is

$$E_n = \frac{1}{2}\left(E_d - \frac{Ze^2}{R_B} - 2.22\right), \tag{2.51}$$

where $E_d$ is the energy of the incident deuteron, $Z$ is the number of protons in the nucleus, $e$ is the elementary charge, and $R_B$ is the distance between the nucleus and deuteron at breakup [79–81]. Deuteron breakup due to Coulombic forces (outside of the nuclear field) dominates at lower energies for higher atomic number, $Z$, targets and the resulting neutron is focused at forward angles. However, for lower Z targets, like Be and C, nuclear breakup plays a role [80, 81].

Deuteron breakup occuring in the nuclear field of the target nucleus is more probable via the inelastic interaction, where either the proton or neutron is absorbed by the nucleus to form a compound nucleus, than the elastic interaction, where both the proton and neutron are emitted [79, 82]. In a direct inelastic

reaction, also known as stripping, the deuteron interacts with the edge of the target nucleus, stripping the proton from the deuteron and resulting in a neutron with an energy of about half of the incident deuteron energy [83, 84]. This reaction produces forward-focused neutrons which broaden in angular distribution as the atomic number of the target nucleus increases due to the additional Coulombic forces of higher Z targets [83].

The deuteron can also interact with the target nucleus and form a compound nucleus which distributes the energy amongst the nucleons. Neutrons emitted from the compound nucleus are emitted isotropically with a maximum energy of the kinetic energy plus the binding energy of the deuteron.

Deuteron breakup on $^{9}$Be was the primary high-energy neutron source used at the 88-Inch Cyclotron. The $^{9}$Be(d,n)$^{10}$B reaction has a Q value of 4.362 MeV, which means the emitted neutron can have a maximum energy of 4.362 MeV above the incident deuteron energy. Figure 2.28a shows the neutron spectrum from 16 and 33 MeV deuterons on $^{9}$Be [85]. At energies of 16 and 33 MeV, the $^{9}$Be(d,n) reaction is predominately a direct and Coulombic breakup reaction and the outgoing neutrons are primarily directed in the forward direction as shown in Figure 2.28b.

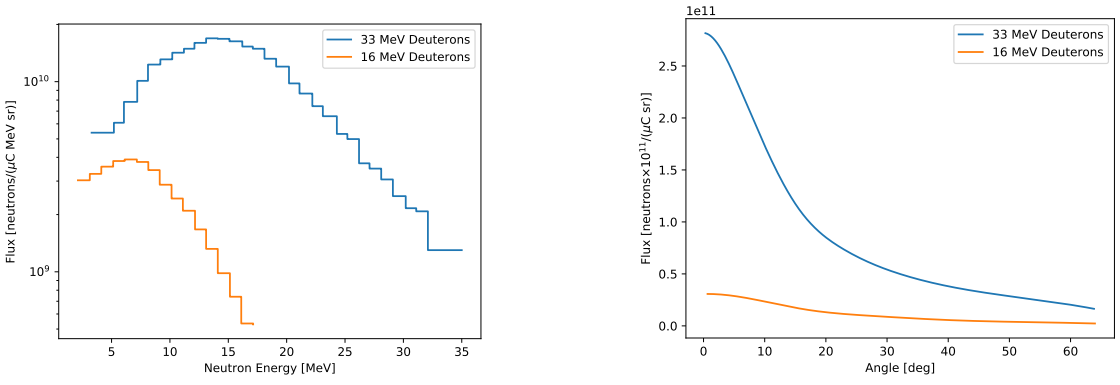


**(a)** **(b)**

**Figure 2.28. Neutron (a) spectrum and (b) angular distribution from $^{9}$Be(d,n) with 16 and 33 MeV deuterons [85].**

# III. GENESIS: Gamma-Energy Neutron-Energy Spectrometer for Inelastic Scattering

This chapter was derived from a manuscript to be submitted to *Nuclear Instruments and Methods in Physics Research Section A: Accelerators, Spectrometers, Detectors and Associated Equipment* titled "GENESIS: Gamma Energy Neutron Energy Spectrometer for Inelastic Scattering." The author list included Joseph M. Gordon, Josh A. Brown, Lee A. Bernstein, Bethany L. Goldblum, Darren L . Bleuel, Chris A. Brand, Jon Charles Batchelder, Thibault A. Laplace, Brian G. Frandsen, and James E. Bevins. The article has been modified to fit this dissertation format; however, the content was unchanged. The author contributed to the characterization of the collimated neutron beam, high energy efficiency calibration of the HPGe detectors, and timing between the HPGe detectors, EJ-309 scintillators, and cyclotron RF signal.

## 3.1 Abstract

Improved neutron inelastic scattering cross sections and neutron-induced gamma-ray production data are needed to inform integral benchmark studies and advance nuclear applications in a wide range of areas including detection, forensics, and non-destructive assay. To meet these needs, the Gamma Energy Neutron Energy Spectrometer for Inelastic Scattering (GENESIS) was constructed, an array that couples high-resolution $\gamma$-ray detectors and neutron detectors at a high-flux tunable neutron source at the 88-Inch Cyclotron at Lawrence Berkeley National Laboratory to achieve coincident n/$\gamma$ detection over a wide energy range. The current configuration of the array includes 26 organic liquid scintillators, two 2-fold segmented and two single-crystal high-purity germanium detectors, and a single inorganic scintillator. The array was constructed with minimal supporting material

and designed to cover a wide range of secondary particle angles and energies with limited inter-element scattering. Data acquisition is accomplished using Mesytec MDPP-16 multi-channel, fast, high-resolution, digital pulse processing modules. The array characteristics were measured, including gamma-ray and neutron energy resolution, timing resolution, and detection efficiency. The major sources of neutron background and uncertainty in the determination of incident and secondary neutron energy were determined. GENESIS provides a new resource to address nuclear data needs and advance capabilities in the use of secondary gamma emissions for neutron interrogation applications.

## 3.2 Motivation

Nuclear data are the foundation of the design, development, and operation of any nuclear technology, from nuclear energy and security applications to isotope production, outer space and terrestrial radiation shielding, and other industrial applications. Nuclear data deficiencies, including inaccuracies in neutron inelastic scattering cross sections, can have a significant adverse impact on calculations, models, and simulations important for curiosity-driven science and applications [86]. For example, poor neutron inelastic cross section data will impact neutron transport calculations, as neutrons can lose a significant fraction of their kinetic energy in a single inelastic scattering event. Secondary $\gamma$-ray production from active neutron interrogation also requires robust nuclear data to facilitate signature discovery for material assay [87]. Unfortunately, there are large discrepancies in the data and gaps where data do not exist at all; it is critical to conduct experiments to resolve discrepancies and fill in these gaps.

There are several organizations across the world that have identified nuclear data needs for different applications. The Nuclear Energy Agency, an intergovernmental

organization dedicated to multinational cooperation on nuclear technology, maintains the "Nuclear Data High Priority Request List," which currently features more than 100 requests for improved nuclear reaction data [88]. In 2015, the Workshop on Nuclear Data Needs and Capabilities for Applications (NDNCA) compiled nuclear data deficiencies for a wide array of nuclear applications [89]. Included in the record was the need for more accurate inelastic scattering cross section data for a large section of the periodic table, from light and medium nuclei like $^{23}$Na and $^{56}$Fe to heavier isotopes such as $^{206}$Pb, $^{207}$Pb, and $^{238}$U. Following the NDNCA meeting, there has been a series of workshops coordinated in conjunction with the U.S. Nuclear Data Program to identify and prioritize nuclear data needs along with an interagency effort to resolve these gaps [90–93].

To address highlighted nuclear data needs related to neutron inelastic scattering and fast neutron-induced $\gamma$-ray production, the Gamma Energy Neutron Energy Spectrometer for Inelastic Scattering (GENESIS) was established at the 88-Inch Cyclotron at Lawrence Berkeley National Laboratory (LBNL). By combining high resolution $\gamma$-ray spectroscopy using a collection of high-purity germanium (HPGe) detectors with an array of organic liquid scintillators for neutron detection, GENESIS provides the capability for a more accurate determination of neutron inelastic scattering cross sections and neutron yields by observing events in coincidence with characteristic $\gamma$ rays. Table 3.1 provides a comparison of the capabilities of various current and historical facilities where similar experimental campaigns were conducted.

Section 3.3 provides an overview of the GENESIS facility, including the neutron source, beam collimation, detector array instrumentation, and data acquisition. In Section 3.4, the characteristics of GENESIS that enable more accurate $(n, n'\gamma)$ cross section measurements are discussed, including the temporal resolution, energy

**Table 3.1. Comparison of GENESIS to other $(n, n'\gamma)$ facilities.**

| | Neutron beam | | | | | Spectroscopy | |
|---|---|---|---|---|---|---|---|
| Facility | Energy Range [MeV] | Spectral Source | Flux Monitoring | FWHM [ns] | Rate [MHz] | $\gamma$ Ray | Neutron |
| GENESIS | $\leq 50$ | $d$ breakup | sTOF[a] | $\leq$10 | 5.92 | HPGe | EJ-309 |
| Chi-Nu | $\leq 800$ | spallation | F.C.[b] | 0.3 | 0.55 | none | Li-glass, liquid scint. |
| GAINS | $\leq 20$ | photoneutron | F.C. | 1.0 | 0.0008 | HPGe | none |
| GEANIE | $\leq 800$ | spallation | F.C. | 0.3 | 0.55 | HPGe | none |

[a]scatter Time-of-Flight, [b]Fission Chamber

resolution, and efficiency of both the neutron and $\gamma$-ray detectors. Details on the development of a simulation of the GENESIS array are also provided. Section 3.5 addresses sources of background and uncertainty quantification. Concluding remarks are given in Section 3.6.

## 3.3 Experimental Design

The ability to perform high quality measurements of relevant nuclear data, from neutron inelastic scattering to fast neutron-induced $\gamma$-ray production, introduced several constraints on the design and operational characteristics of GENESIS. The first requirement is a pulsed, bright, well-characterized, and unobstructed neutron beam that overfills the area of scattering targets at the center of the GENESIS array. The repetition rate of the neutron beam and the distance from the neutron production source to the center of the array must be large enough to allow the determination of the energy of reacting neutrons via the time-of-flight (TOF) technique. Second, the detectors in the array must be located in positions that span a large range of outgoing particle angles. To determine the energy of outgoing neutrons through TOF, with a $\gamma$-ray interaction in one of the HPGe detectors acting as a start time, the neutron detectors must be separated from one another to minimize the amount of inter-element scattering, and at a far enough distance from the scattering target to provide adequate resolution on the TOF. Finally, the data acquisition system must have a high throughput to allow for the recording of single

or coincident events from any of the over thirty detectors in GENESIS and the ability to reconstruct coincident events in post-processing.

### 3.3.1 Beam Characteristics at the 88-Inch Cyclotron

The 88-Inch Cyclotron at LBNL, home to the GENESIS array, is a $K = 140$, sector-focused cyclotron that delivers pulsed beams of charged particles. Neutrons are created at the facility using thick-target deuteron break-up (TTDB) on low-Z (e.g., Be, C [94]) or higher-Z targets (e.g., Ti, Ta [95, 96]). Neutron production targets are mounted in a Faraday cup to monitor charged-particle flux and equipped with water cooling loops to ensure thermal integrity. Due to the high deuteron beam repetition rate at the 88-Inch Cyclotron, fast neutrons created from the most recent beam pulse can arrive at experimental stations at the same time as slower neutrons from previous pulses, a phenomenon known as frame overlap [94].

The neutron spectrum from TTDB was previously measured at the 88-Inch Cyclotron for 16 MeV deuterons on a Be target using a double time-of-flight (dTOF) technique [94] and activation foil unfolding [96]. Neutron production using TTDB has also been theoretically studied [97] and extensively experimentally measured [98–100], but the discrepancies in measured TTDB spectra, the angular dependence of the TTDB spectrum, and the possibility of other neutron production methods necessitates the use of active neutron beam monitoring in GENESIS experiments, both for shape and fluence. This neutron beam monitoring is accomplished via activation foils and a scatter time-of-flight (sTOF) spectrometer adapted from the dTOF technique [94].

A schematic of the 88-Inch Cyclotron and select experimental endstations is shown in Figure 3.1. GENESIS is currently housed in the Cave 5 experimental area, which is separated from the cyclotron and neutron production target by a 2.44 m wall, with

1.52 m of concrete on the experimental area side and 0.91 m of steel on the source side. A 10-cm-diameter iron beam pipe penetrates the shielding wall to allow an open-air neutron beam to enter the experimental area. Current configurations admit neutron flight paths ranging from 6.856 m to 7.856 m.

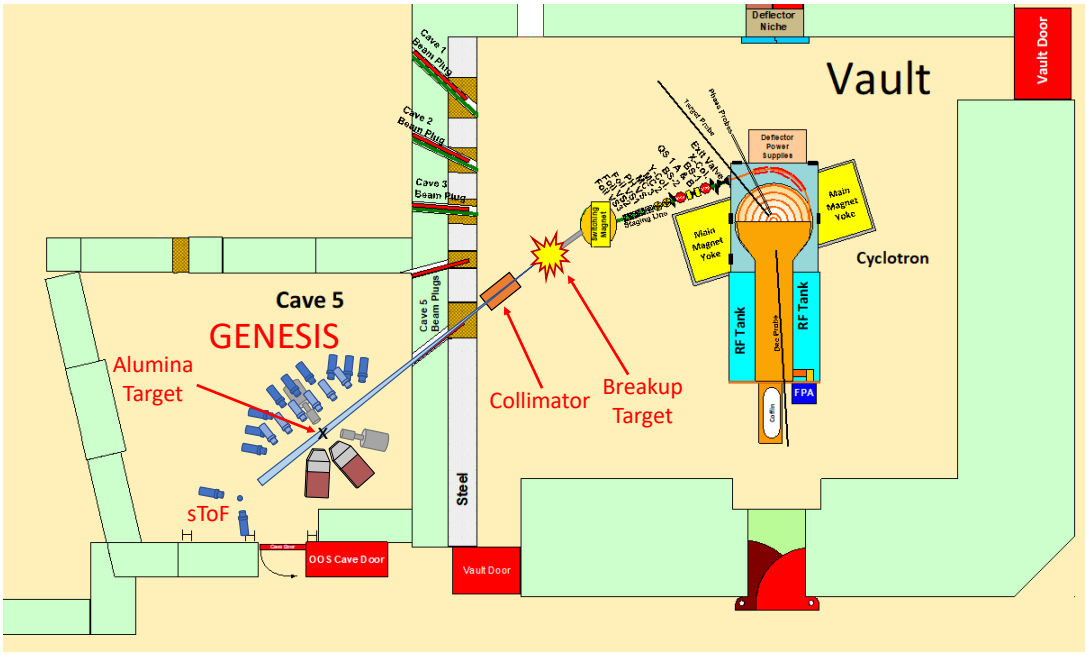


**Figure 3.1. Overhead view of the 88-Inch Cyclotron, deuteron breakup target, and copper collimator in the vault and GENESIS in Cave 5. Downstream of the GENESIS array is the sTOF neutron beam monitor.**

### 3.3.2 Neutron Beam Collimation

A collimator was designed and installed between the neutron source and the shielding wall in the vault (see Fig. 3.1) to constrain the beam spot size to target dimensions and reduce background rates. The copper collimator is a cylinder, 7.62 cm in radius and 60 cm in length, divided in six 10-cm-segments with borehole radii ranging from 0.33 cm to 0.6 cm, in 0.05 or 0.06 cm increments, with the smallest opening nearest to the neutron source. Copper was selected as the collimation medium based on simulation studies conducted using Geant4 [101] with

the Shielding physics list, the G4NDL4.6 library [102], and a uniform neutron beam from $0 - 40$ MeV. A factor of eight lower activation per $\mu$Amp·hr was observed in simulation space for copper relative to brass seven days following irradiation. The collimator was tested experimentally using a 16 MeV TTDB on Be beam in two positions, roughly 12 and 20 cm downstream of the neutron source. The positioning of the collimation system relative to the neutron source allows for smaller or larger neutron beam sizes at the GENESIS target location, and the collimator was aligned transversely to maximize direct transmission and beam uniformity. The neutron beam spot size was imaged using a ∅1.27 x 1.27 cm right circular cylinder of pulse-shape discriminating (PSD) EJ-309 scintillator [103], coupled to a Hamamatsu H6533 photomultiplier tube (PMT) [104] and mounted on a motorized, remotely-operated, two-dimensional translation stage.

To measure the efficacy of the collimator in reducing fast neutron backgrounds, two ORTEC PopTop 90% HPGe detectors were deployed, positioned at the height of the beam approximately 20 cm from beamline center and approximately 7.5 m from the breakup target. One HPGe detector was placed perpendicular to the neutron beam direction, and one was positioned at approximately 70°. The collimation system resulted in a significant reduction in background noise, as shown in Fig. 3.2. Data taken with the neutron imaging system placed downstream of the HPGe detectors showed a factor of approximately 6.75 reduction in the 847 keV $2_0^+ \rightarrow 0_0^+$ $^{56}$Fe transition, a factor of $\sim 3.5$ reduction in the 844 keV $\gamma$ ray from the decay of $^{27}$Mg produced via $(n, p)$ on aluminum in the GENESIS frame, and a factor of $\sim 1.7$ reduction in the 596 keV $2_0^+ \rightarrow 0_0^+$ $^{74}$Ge transition.

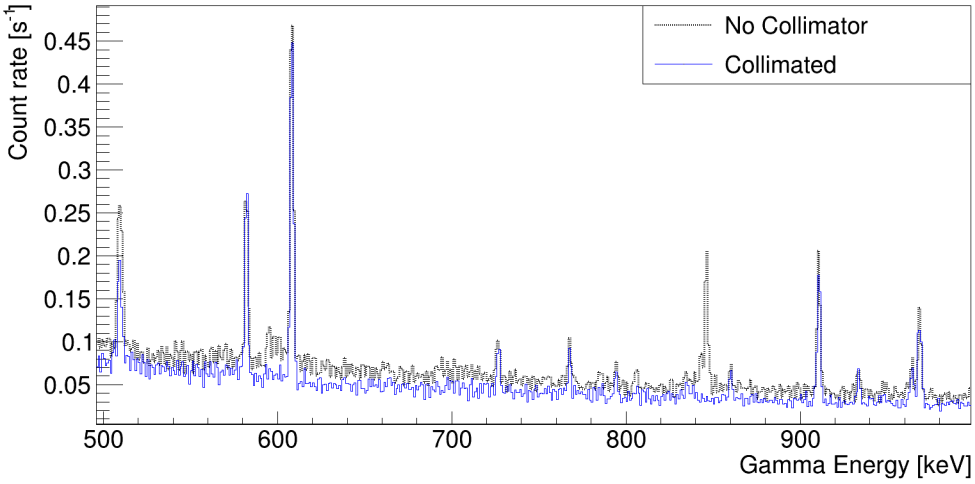


**Figure 3.2.** $\gamma$-ray spectra obtained with the perpendicular HPGe detector for an uncollimated neutron beam and a neutron beam with the collimator positioned such that the beam spot size was 8 cm in diameter at 7.5 m downstream of the production target. Prominent are the disappearance of the triangular features, indicative of fast-neutron scattering on the HPGe active volume, and the disappearance of the wide peak at approximately 478 keV, arising from fast-neutron induced breakup of boron in the beam dump.

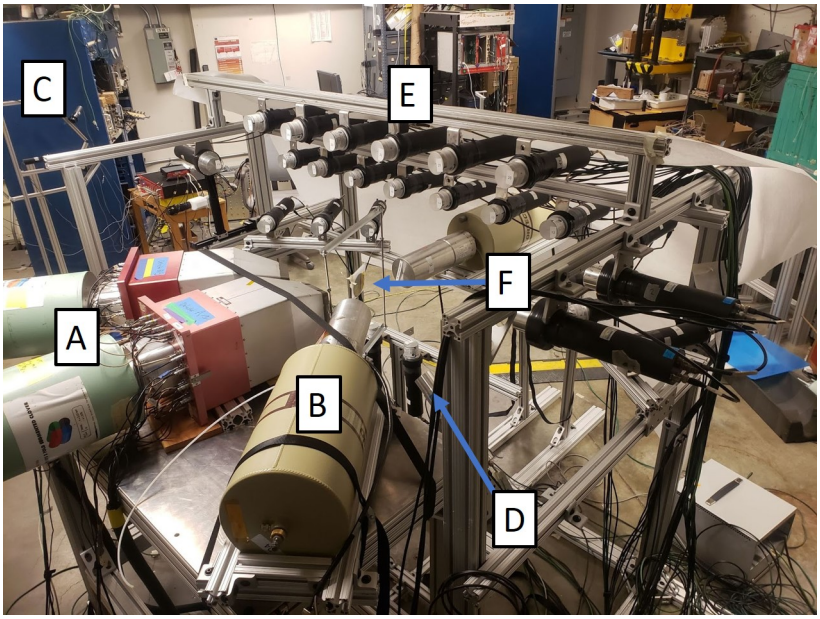


**Figure 3.3.** A view looking downstream, lower right to upper left, at GENESIS. A) Eurisys HPGe Clover detectors with BGO anti-Compton shields, B) Ortec PopTop HPGe detector, C) sTOF Neutron Beam Monitor, D) Saint-Gobain $LaBr_3$(Ce), E) EJ-309 organic liquid scintillators, and F) inelastic scattering foil.

### 3.3.3 The GENESIS Array

GENESIS is located in Cave 5 at the 88-Inch Cyclotron at Lawrence Berkeley National Laboratory, depicted in Fig. 3.1. For neutron detection, GENESIS currently features twenty-six 5.08 cm x 5.08 cm right-circular cylindrical, PSD-capable EJ-309 organic liquid scintillators [103] coupled to Hamamatsu H1949-51 or H2431-50 PMTs [105, 106]. For $\gamma$-ray detection, GENESIS also includes two EURISYS 2-fold segmented HPGe N-type clover detectors with Scionix V-0210 bismuth germanate oxide (BGO) anti-Compton shields, two Ortec PopTop HPGe detectors, and a single Saint-Gobain type B380, 5.08 cm x 5.08 cm right-circular cylindrical $LaBr_3(Ce)$ crystal mounted to a Hamamatsu R2083 PMT. Activation foils and the sTOF spectrometer (see Sec. 3.3.1) are fielded in conjunction with the GENESIS array for neutron beam flux monitoring. Figure 3.3 shows the elements of the GENESIS array staged in typical runtime configuration. The array is positioned approximately 1.2 m above the floor of Cave 5, a room 2.44 m in height.

The EJ-309 cells are arranged in a quarter-shell centered on the GENESIS target location, spanning roughly $11 - 165^\circ$ with respect to the neutron beam direction, and at radial distances of $35 - 85$ cm, with an average standoff of 60 cm. The locations of all 26 scintillators are given in A.1. To reduce inter-element neutron scattering, the scintillators are placed at least 20 cm from their nearest neighbor, which was determined via a simulation study to yield an inter-element scattering rate of $< 0.1\%$ across the neutron energy range of $0 - 20$ MeV. Each EJ-309 scintillating volume is contained within a 1-mm-thick aluminum cylinder and capped with a 3-cm-radius, 1-mm-thick quartz window. The quartz window is coupled to a PMT via a thin layer of EJ-550 silicone optical grease [107]. The PMTs are housed in a 1-mm-thick aluminum magnetic shield, 23.5 cm long and 3.0 cm in radius. The EJ-309 detector is

mounted on the GENESIS frame with an L-bracket attached just behind scintillator-PMT interface, providing an unobstructed line-of-sight from the target to the active detector volume. For simplicity in construction and modeling of the GENESIS array, the scintillator detectors are mounted perpendicular to the 80/20 aluminum bars. Bias voltages are supplied through a single 16-channel CAEN R8033DN [108] and two 8-channel CAEN R1470ETD [109] power supplies, which are controlled and monitored remotely.

The two HPGe clover detectors are placed in the hemisphere opposite the EJ-309 array on a table made of 3030-type 80/20 aluminum bars. The center of the clovers are positioned at beam height center. One clover (Clover 0) is placed perpendicular to the neutron beam, at a radial distance of approximately 20 cm, measured to the front face of the HPGe crystals. The second clover (Clover 1) is place at a forward angle, roughly 54° and at a radial distance of approximately 26 cm. Each HPGe clover is a two-fold segmented crystal spanning a roughly square cross section, 80 mm across and 90 mm deep. Signals from each of the four crystals are read out individually and signals from edge-contact anodes, which can provide coarse interaction tracking, are not currently used. Surrounding each clover is approximately 25 kg of BGO in 16-fold segmentation, with four segments on each side of the clover, housed in a trapezoidal aluminum casing with a removable, 2.54-cm-thick Hevimet cap to prevent direct illumination of the BGOs. The signals from the 16 Hamamatsu R3998-2 PMTs [110] mounted to the BGOs are "daisy-chained" together and read out as one signal, a choice motivated by studies of the Compton-rejection efficiency. The Ortec PopTops are also located at beam height center, one on the table with the clover HPGe detectors, at approximately 130°, and one in the opposite hemisphere at 90°. Several PopTops are available for use in GENESIS, with efficiencies ranging from 18% to 90%. Bias voltages for the clovers are supplied via an 8-channel CAEN R1470ETD power supply [109], and the BGO

and PopTops are supplied through an iseg NHR-42-60r high voltage module [111].

### 3.3.4 Data Acquisition

Three Mesytec MDPP-16 boards are used to acquire list-mode data [112, 113]. Scintillator signals, with the exception of the BGO, are processed through two boards, configured with the Mesytec QDC firmware to handle pulse integration and timing. For each collected event, a short integral, long integral, and timestamp are read out [114]. The HPGe signals, from the Clover and PopTop detectors, are processed on the third board with the firmware set to the SCP configuration, which manages adjustable trapezoidal filtering and timing filtering. For each collected event, the pulse amplitude and timestamp are read out [115]. The best timing resolution for the HPGe detectors, as determined through experimental studies with $^{22}$Na and $^{133}$Ba sources, was achieved by setting the shaping constant for the timing branch of the on-board signal processing to the lowest allowable value. This choice introduced a charge-dependent event loss that has been characterized, as described in Sec. 3.4.3.1. A constant-fraction discriminated timing signal from the cyclotron RF is fed into a secondary trigger channel on each board, to provide a nominal start time for incoming neutron time-of-flight determination. Each channel on all three boards is allowed to generate a trigger signal, which is passed to a Lecroy 429A logic fan-in/fan-out module [116] and propagated back to all three boards to ensure the inter-board synchonicity.

## 3.4 Array Characteristics

This section covers characteristics of the GENESIS array important for performing high-resolution $\gamma$-ray and neutron spectroscopy using the tunable neutron source at the 88-Inch Cyclotron. Section 3.4.1 describes the means by which coincident events are timed within the GENESIS array, including details on

timing resolution. Section 3.4.2 details the measured energy resolution of the HPGe detectors. In Sec. 3.4.3, the efficiency of the detector array is covered. Section 3.4.4 describes efforts in detector array modeling, which was performed using the Geant4 software package.

### 3.4.1 Coincident Timing with GENESIS

To reconstruct coincident events from the list mode data and determine the neutron time-of-flight (either incoming or outgoing), calibration is required to correct for temporal delays in the signal chain. Figure 3.4 provides a timing diagram for a representative neutron-gamma coincident event, showcasing the principles of the GENESIS TOF technique. The TOF of the incoming neutron can be determined using the detection time $T_{\gamma'}$ of $\gamma$ rays produced via inelastic scattering in the target that traveled a distance $D_\gamma$ from the center of the GENESIS array to the $j^{th}$ HPGe detector:

$$TOF_n^j = T_\gamma^j - \frac{D_\gamma^j}{c} - n \times T_{RF} + (\Delta_n^i - \Delta_\gamma^j) - (\Delta_n^i - \Delta_{RF}), \tag{3.1}$$

where $c$ is the speed of light, $T_{RF}$ is the measured time of the RF signal, and $\Delta_n^i$, $\Delta_\gamma^j$, and $\Delta_{RF}$ are the time delays of the $i$th neutron detector, $j$th $\gamma$-ray detector, and RF signal, respectively. Due to the frame overlap of beam pulses at the 88-Inch Cyclotron, the reacting neutrons could have come from the $n$th previous charged-particle bunch [94].

Similarly, the TOF of an outgoing neutron detected in the $i$th neutron detector and in coincidence with a gamma-ray in the $j$th gamma-ray detector is

$$TOF_{n'}^{ij} = T_n^i - T_\gamma^j + \frac{D_\gamma^j}{c} - (\Delta_n^i - \Delta_\gamma^j), \tag{3.2}$$

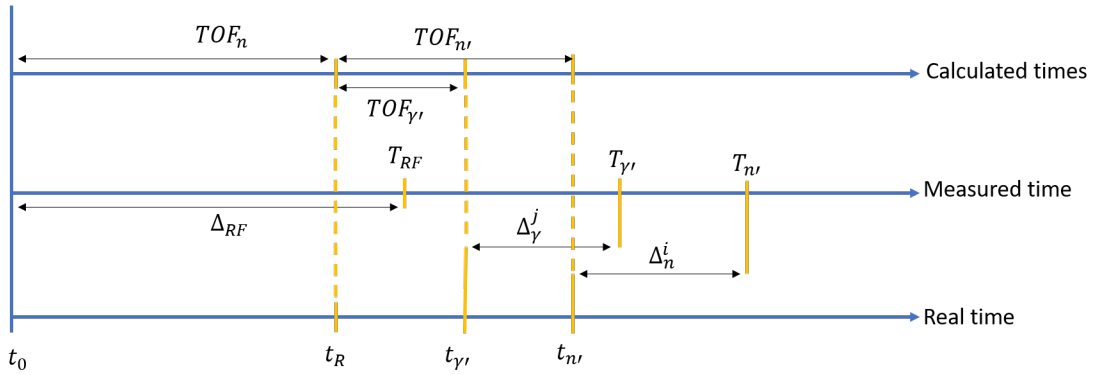


**Figure 3.4. A timing diagram for the GENESIS TOF technique. The real times, $t_0$, $t_R$, $t_{\gamma'}$, and $t_{n'}$ represent the arrival of the charged particle beam bunch on the neutron production target, the arrival of neutrons at the target in the GENESIS array, the arrival of an inelastic gamma ray at an HPGe detector, and the arrival of an outgoing neutron on a scintillator, respectively. The signal processing delays, $\Delta_{RF}$, $\Delta_\gamma^j$, and $\Delta_n^i$, indexed by detector, give rise to measured times $T_{RF}$, $T_{\gamma'}$, and $T_{n'}$, respectively.**

where $T_n^i$ is the measured time of the neutron detected in the $i$th neutron detector. The detection times $T_\gamma$ and $T_n$ are uncertain by the intrinsic timing resolution of the detectors.

The time resolution and signal processing offsets were determined through a coincidence measurement. A 0.96 $\mu$g $^{252}$Cf spontaneous fission source was placed in the center of the GENESIS frame. The time differences between prompt fission $\gamma$-ray events in one EJ-309 neutron detector and all other detectors were determined. Figure 3.5 shows an example of such a histogram for time differences between an EJ-309 detector and Clover 0, Leaf 0. The width of the peak represents the quadrature-sum of the resolution of the individual detectors, here $\sim$ 350 ps for the EJ309 and $\sim$ 3.3 ns for the leaf. The mean of the peak gives an inter-board timing offset constant, $(\Delta_n^i - \Delta_\gamma^j)$, that can be used to correct for signal processing delays when constructing coincidences using signals from two different MDPP16 boards, here $\sim$ 14.6 ns.

Intra-board timing constants, $(\Delta_n^i - \Delta_{RF})$, can be determined using the flash of gamma rays created when the charge particle beam interacts in the neutron

production target Compton-scatter off the target in the center of the GENESIS frame. The timing resolution of the HPGe detectors is such that the gamma flash, whose time spread is proportional to that of the charged particle beam, is not clearly identifiable. The incoming neutron TOF is therefore calculated using the inter-board timing constant to an EJ-309 and that scintillators intra-board constant.

### 3.4.2 Energy Resolution

The energy resolution of the HPGe detectors is measured using a Eu-152 calibration source placed in the center of GENESIS. The FWHM of a photopeak can be written as a quadrature sum of a constant noise term and a term proportional to the energy [117],

$$\text{FWHM} = \sqrt{\alpha E_\gamma + N^2}. \tag{3.3}$$

The parameters $\alpha$ and $N$ are reported in Table 3.2 for each leaf. Prior to every

**Table 3.2. HPGe energy resolution**

| **HPGe Detector** | $\boldsymbol{\alpha(\times 10^{-3})}$ **[keV]** | $\boldsymbol{N}$ **[keV]** |
|---|---|---|
| Clover 0, Leaf 1 | $1.65 \pm .07$ | $2.58 \pm .02$ |
| Clover 0, Leaf 2 | $2.18 \pm .04$ | $2.26 \pm .02$ |
| Clover 0, Leaf 3 | $2.24 \pm .04$ | $2.27 \pm .02$ |
| Clover 0, Leaf 4 | $2.00 \pm .04$ | $2.87 \pm .02$ |
| Clover 1, Leaf 1 | $2.22 \pm .05$ | $2.06 \pm .02$ |
| Clover 1, Leaf 2 | $2.44 \pm .05$ | $2.34 \pm .02$ |
| Clover 1, Leaf 3 | $2.21 \pm .07$ | $2.22 \pm .03$ |
| Clover 1, Leaf 4 | $2.92 \pm .06$ | $2.25 \pm .03$ |

experiment, the 16 BGO PMTs in both shields are individually gain aligned using a single $^{137}$Cs source and then daisy chained, by connecting the output each PMT to the input of its neighbor, without any termination. The calibration of the light-yield in the EJ-309 scintillators was accomplished by minimizing a simulated

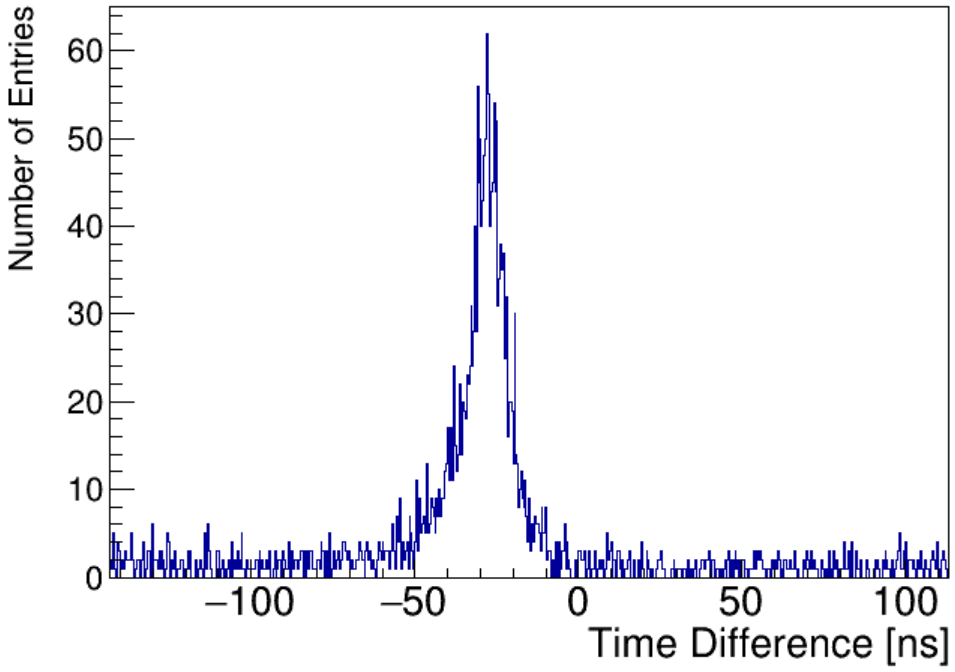


**Figure 3.5.** $^{252}$**Cf prompt gamma ray time differences between all gamma-ray events in EJ-309 detector 0 and gamma rays between 710 and 1910 keV in Clover 0, Leaf 0, in ns. A Gaussian distribution of true coincidences, with mean** $-24.3 \pm .2$ **ns, standard deviation** $4.07 \pm .43$ **ns.**

pulse-integral spectrum broadened by a simultaneously-fit Dietze and Klein resolution function [118], against an experimental spectrum collected from a $^{137}$Cs point source located at the center of the GENESIS frame. The simulated spectrum is generated from a GEANT4 [101] model of the EJ-309+PMT detector, which includes the container of the liquid scintillator, the magnetic shield surrounding the PMT, and the quartz window between the PMT and the scintillating volume.

### 3.4.3 Array Efficiency

#### 3.4.3.1 Gamma-Ray Efficiency

The experimental gamma ray detection efficiency, $\epsilon_\gamma$, of the HPGe detectors in GENESIS has been measured through the use of a .916 $\mu$Ci $^{152}$Eu calibrated point source. Data was gathered at the center of the GENESIS frame, and at roughly

an inch off-center in the direction of the clovers and in the direction of the EJ-309 detectors. To characterize the event loss from the choice of the timing parameter (Sec. 3.3.4), data was gathered with a $^{152}$Eu source at the center of the frame at multiple values of the timing parameter, ranging from the lowest allowable value (where the most event loss was observed) to the highest (where no event loss was observed). A logistic function for the event-loss probability

$$P(E_\gamma) = 1 - \frac{1}{1 + e^{-k(E_\gamma - E_0)}} \tag{3.4}$$

was fitted for each leaf in the clover and each Pop-Top and used to correct the simulated gamma-ray efficiency. Values for k range from 0.12 to .019 keV$^{-1}$ and values of $E_0$ range from 97.0 to 234.0 keV.

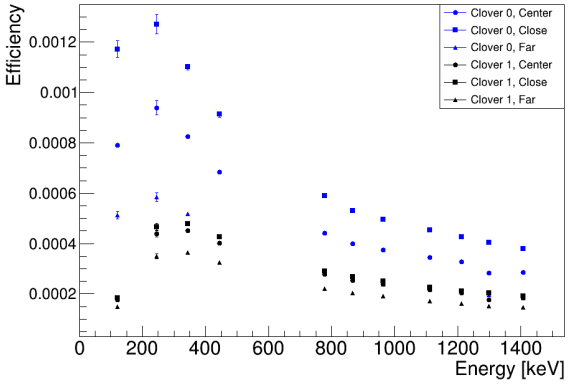


**(a) Gamma efficiency for Clover 0 (at 90°) and Clover 1 (at 54°) measured with a 0.916 µCi $^{152}$Eu at the target location and 1" closer and away from Clover 0. The results are the total of each leaf in the clover, but does not include add-back.**

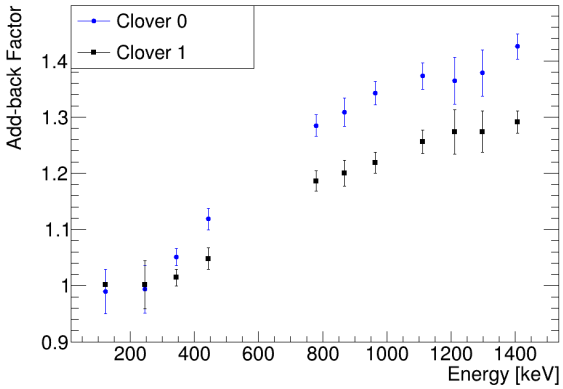


**(b) Add-back factor for Clover 0 and Clover 1 measured using a $^{152}$Eu source. There is no loss in efficiency at low energy, and a gain of up to 45% at 1408 keV.**

**Figure 3.6. Gamma efficiency and add-back factor measured using a $^{152}$Eu calibrated point source.**

Figure 3.6a shows the non-added back full clover efficiency for the three $^{152}$Eu source measurements. The effect of the event-loss probability can be seen in the decrease in efficiency at low gamma energy. The add-back factor is a measure of the increase in photo-peak efficiency from a clover operating in full add-back mode over a

clover operating in full singles mode [117]. Figure 3.6a also shows the add-back factor for 2-, 3-, and 4-fold summing measured with $^{152}$Eu. As anticipated, there is no loss in efficiency at low energy, and a gain of up to 45% at 1408 keV.

#### 3.4.3.2 Neutron Efficiency

The neutron detection efficiency, $\epsilon_n$, has been determined through a measurement with a .96 $\mu$g $^{252}$Cf neutron source. The $^{252}$Cf was enclosed in a closed cylinder of 304L stainless steel, 0.254 cm thick on the sides, 0.775 cm thick on top, and 0.851 cm thick on the bottom. Data was taken with the source at the center of the GENESIS frame without the clovers, BGOs, and Pop-tops present. Neutron energy was determined via TOF with gamma-ray interactions in the LaBr(Ce) acting as the start time. The relative efficiency as a function of neutron energy can be calculated using the LaBr(Ce) and TOF and the known $^{252}$Cf neutron spectrum [119]. The efficiency is relative because a full accounting of the neutron/gamma multiplicity, angular, and energetic correlations would be needed to properly calculate the efficiency. Work is underway to evaluate these correlations. Figure 3.7b shows the relative neutron efficiency as a function of neutron energy for a single EJ-309 detector. The relative efficiency is strongly dependent on the threshold of the detector, which was .2 MeVee.

For neutron detection in non-coincidence mode, the only information is the pulse integral spectrum. Unfolding techniques exist to derive a neutron energy spectrum from the pulse integral, but equally valuable is an integrated efficiency, which can be used to develop an numerical understanding of the bulk array performance. Figure 3.7b shows the non-coincidence neutron efficiency, integrated from .2 to 3 MeVee. As stated earlier, the array has an angular coverage of 11° to 165°, with the most efficiency near the center of the array (90°). Given the sizes and distances of the EJ-309 detectors, the amount of $4\pi$ solid-angle coverage is low, and the total integrated

efficiency of the array is $1.83 \times 10^{-3}$.

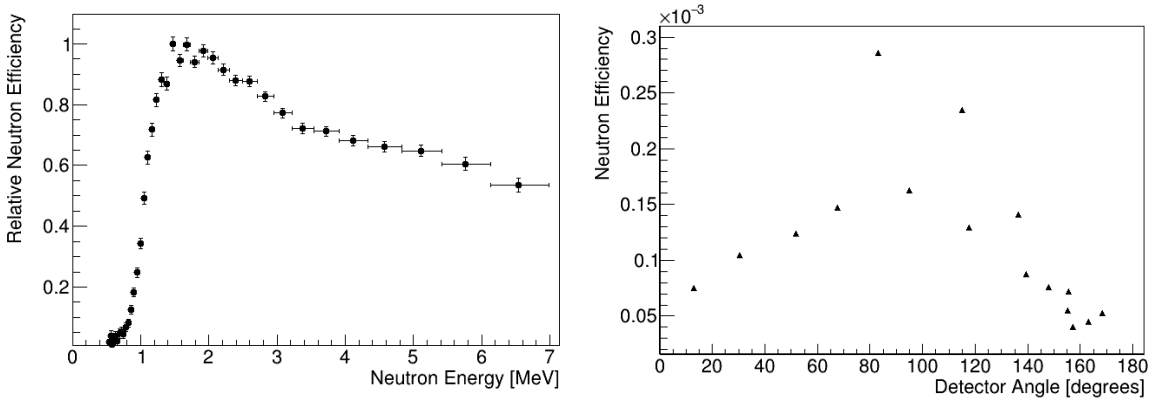


**(a) Relative neutron efficiency as a function of neutron energy as determined by the TOF method with the LaBr(Ce) acting as the start signal, for a single EJ-309 scintillator.**

**(b) Non-coincident neutron efficiency from a $^{252}$Cf source, integrated over a light yield range of 0.2 to 3 MeVee, as a function of polar angle (with respect to the direction of a neutron beam).**

**Figure 3.7. Neutron efficiency determined using a**

### 3.4.4 Array Modeling

A model of the GENESIS array is a useful tool for a variety of reasons, most critical however is the ability to calculate the neutron and gamma-ray detection efficiency for a non-point source radiator. A detailed GEANT4 model has been developed that includes the GENESIS 80/20 frame, a $2.44 \times 2.44$ m section of the concrete floor and ceiling of the room, the scintillator+PMT detector (including the 3% air bubble []), the Pop-Tops, the Clover+BGO detectors, and the LaBr(Ce). The simulation outputted step information for all particles within the detector volume, which included kinetic energy, global time, location, energy deposited in the detector volume, and the energy of the source particle.

A uniform, point, gamma ray source from 0 to 4 MeV was used to study the response of the primary gamma-ray detectors (Clover, Pop-top, and LaBr(Ce)). The *Shielding* Physics List with the *G4EmStandardPhyics option4* was used to most accurately model the performance of the detector at lower gamma ray energies. The

three-location $^{152}$Eu data [Sec. 3.4.3.1] was used to validate this aspect of the GEANT4 model, mainly through a calculation and comparison of the gamma-ray detection efficiency. As with previous attempts to develop Monte Carlo models of HPGe detectors [], a thin dead layer at the front of each individual crystal, of thickness $t_{dl}$, and a larger dead region surrounding the inner contact, of radius $r_{dl}$ and length $h_{dl}$, was required to achieve agreement between the simulated and experimental efficiency. The dead layer was implemented in post-processing of the raw simulation output by excluding steps within the dead regions. The parameters of these dead regions was varied to minimize, across the three $^{152}$Eu measurements, the standard deviation of the percent difference between the simulated and experimental efficiency. Figure 3.8 shows the current state of the validation effort in a comparison of simulated to experimental gamma-ray efficiency for a single clover leaf. The simulated efficiency was multiplied by the trigger probability [Sec. 3.4.3.1]. Across the energy range available, the simulation matches the experimental data within 10%. Further efforts, both experimental and in development of the model, are underway to achieve 5% agreement.

The neutron response of the GEANT4 model is being validated against the $^{252}$Cf data used in the experimental determination of neutron efficiency. The *Shielding* physics list with the ENDF/B-VIII.0 G4NDL [102] cross section library was used in a all simulations. Proton energy depositions are converted into light using Birk's relation and [Hong 309 data] and broadened using the measured scintillator resolutions [Sec. 3.4.2].

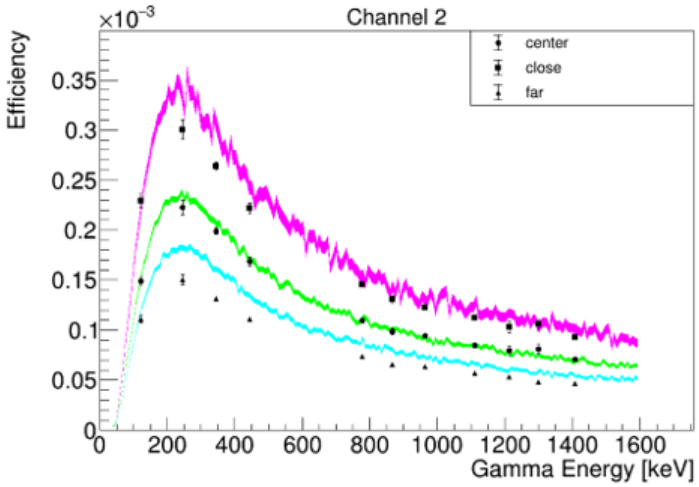


**Figure 3.8. A comparison of simulated and experimental gamma-ray efficiency for a single Clover-leaf, for experimental data collected at 3 locations: the center of the GENESIS array, 1" closer to the Clover, and 1" farther from the Clover. The colored bands are the simulated efficiencies, and the width of the bands are the uncertainties. The event-loss probability [Sec. 3.4.3.1] has been applied to the simulated efficiency.**

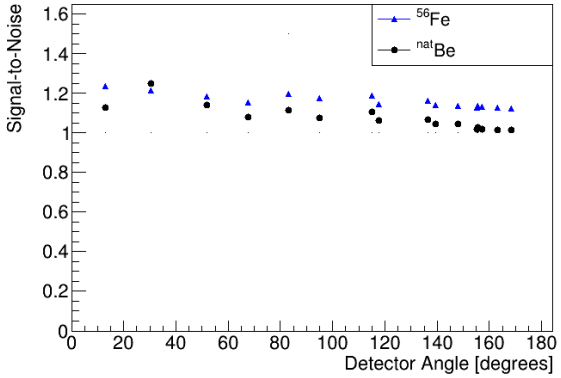


**(a) The signal-to-noise ratio for neutrons without requiring a coincident $\gamma$-ray event in a HPGe clover detector.**

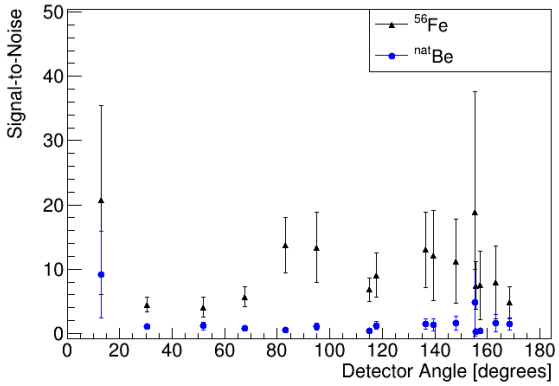


**(b) The signal-to-noise ratio for neutrons in coincidence with a 847 keV $\gamma$ ray from $^{56}$Fe$(n, n')$.**

**Figure 3.9. The signal-to-noise ratio for neutrons without and with a coincident $\gamma$-ray detection in a HPGe clover detector.**

## 3.5 Backgrounds and uncertainties

### 3.5.1 Neutron Background

The primary source of background in GENESIS experiments is the scattering of fast neutrons by air. Three data sets were taken using a 14 MeV TTDB beam with different targets hanging in the GENESIS frame: a thin $^{56}$Fe sample, a thin $^{nat}$Be

sample, and no target ("Blank"). The primary method to reduce background in the neutron data is by utilizing the HPGe detectors to tag on characteristic gamma rays given off as the nuclei in the target sample de-excite following a reaction. Figure 3.9 shows the signal-to-noise ratio (SNR), taken as the ratio of count rates when either the $^{56}$Fe or $^{nat}$Be target was in the GENESIS frame to the count rate when no target was present. When no gamma-ray coincidence is required, the rate of neutrons scattered into the detectors by the targets is roughly $10 - 20\%$ above the rate of neutrons scattered into the detectors by the air. When a coincidence with a gamma-ray in the region of the first $2 \rightarrow 0$ transition in $^{56}$Fe around 847 keV is required, the SNR improves by as much as a factor of 10.

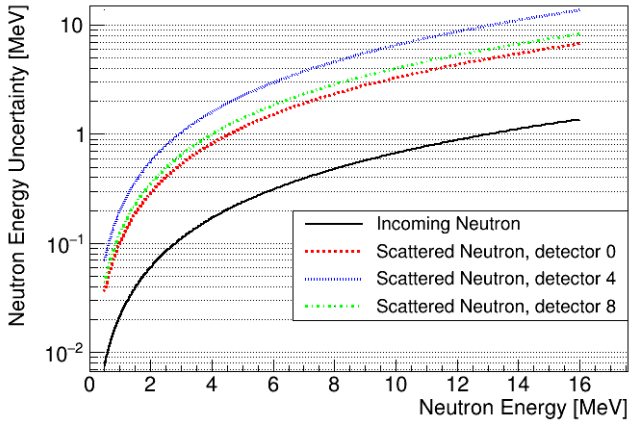


**Figure 3.10. The uncertainty in neutron energy for incoming neutrons, over a 7.29 m flight path, is primarily determined by the deuteron beam pulse width, in this case 11 ns FWHM, and the time resolution of the clover-leafs, in this case 7.1 ns FWHM. The uncertainty in the scattered neutron energy, over the short flight paths of 0.6766 m, 0.4278 m, and 0.8205 m for detectors 0, 4, and 8 respectively is primarily determined by the clover-leaf time resolution of 7.1 ns FWHM.**

### 3.5.2 Neutron Energy Uncertainty

The analysis of uncertainties is specific to each GENESIS experiment and the types of quantities derived from the data. In experiments that yield data as a function of incoming neutron energy, the width of the deuteron beam pulses from

the cyclotron will contribute an uncertainty to the calculation of neutron energy from TOF. The deuteron beam pulse width varies between experiments, but typical values are between 8 and 14 ns FWHM. Figure 3.10 shows the expected incoming neutron energy resolution for a beam pulse width of 11 ns FWHM combined with the measured time resolution of the Clover leafs [Sec 3.4.1], over a flight of 7.29 m, which is standard for GENESIS experiments. An additional source of uncertainty in the determination of neutron energy is due to the time resolution of the clover-leafs. This contribution is significant in the case of scattered neutrons, where the flight path ranges from 0.3848 m to 0.9422 m.

## 3.6 Summary and Outlook

A new spectrometer, GENESIS, was constructed at the 88-Inch Cyclotron at Lawrence Berkeley National Lab. The array was designed to conduct coincidence experiments, simultaneously observing both neutrons and $\gamma$ rays resulting from neutron-induced nuclear reactions. Several development and benchmarking experiments were conducted to establish the operating characteristics and capabilities of the array. A data post-processing and analysis framework is under construction with specific interest in using the differential data products in a forward model approach. This necessitates a well-established model of the array response which is currently being developed and benchmarked. A variety of scattering targets have been mounted in the GENESIS frame, including natural uranium, $^{56}$Fe, sapphire, and NaCl. Analysis of the data is currently underway.

## Acknowledgments

This material is based upon work supported by the Department of Energy National Nuclear Security Administration through the Nuclear Science and Security

Consortium Award No. DE-NA0003180 and performed under the auspices of the U.S. Department of Energy by Lawrence Livermore National Laboratory Contract DE-AC52-07NA27344 and by Lawrence Berkeley National Laboratory Contract No. DE-AC02-05CH11231 and by the Defense Threat Reduction Agency Grant HDTRA1033292.

# IV. Measurement of $^{16}$O(n,n'$\gamma$) Cross Section

## 4.1 Introduction

While there are a plethora of nuclear data needs, inelastic scattering cross section and gamma-ray production measurements are needed for national security, counter-proliferation, active interrogation, and nuclear energy applications for fuel, structural, and common environmental isotopes [9, 56]. Specifically for $^{16}$O, it is important to improve the inelastic cross section data because oxygen is ubiquitous in nuclear applications and can be especially important for high atmosphere nuclear weapons simulations where the $^{16}$O(n,n'$\gamma$) threshold energy is exceeded. For example, transport in the atmosphere affects the neutron and gamma-ray source terms arriving at a sensor used to detect and characterize a nuclear weapon detonation or a weapon system that must survive the nuclear detonation [120]. Since the gamma rays generated from inelastic scattering on oxygen are high energy, they carry an increasing relative importance compared to the original fission gamma rays as the transport distance increases for total fluence calculations. Additionally, due to the distances involved in atmospheric transport and the relative speed of neutrons and gamma rays, atmospheric scattering of neutrons leads to secondary gamma rays with a different timing profile than prompt fission gamma rays [7]. Correspondingly, secondary gamma-ray dose rate effects (due to different pulse length than prompt fission gamma rays) have been identified as an important environment to consider for microelectronic upset.

Unsurprisingly, the need for more accurate $^{16}$O inelastic cross section measurements across a broad range of neutron energies up to 20 MeV has been documented for national security, counter-proliferation, and nuclear energy applications [9, 10]. Currently, the experimental data available for $^{16}$O(n,n'$\gamma$) do not

cover a wide range of neutron energies, some of the partial levels are combined into one cross section, and the discrepancies between the experimental data are high [16–29]. Additionally, certain experimental data measurements, such as partial double differential cross sections, are missing. Measurements of neutron inelastic scattering on $^{16}$O have only measured the outgoing gamma ray [121–123] or scattered neutron [17–19] but have not measured both in coincidence and correlated the outgoing gamma rays and neutrons. The GENESIS array described in Chapter 3 allows for the detection of the outgoing gamma rays and neutrons to calculate all the partial and differential cross sections for (n,n'$\gamma$) measurements.

This chapter discusses the current experimental data in EXFOR, the characterization of GENESIS, and the current state of the $^{16}$O(n,n'$\gamma$) measurement using GENESIS.

### 4.1.1 $^{16}$O Structure

Discovered in 1919, $^{16}$O has an atomic mass of 15.9949 amu and is the most common oxygen isotope (99.757% natural abundance) [124–126]. As a magic number, even-even isotope, the angular momentum and parity of the ground state is $0^+$ and the neutron and proton separation energies are extremely high: 15.664 and 12.127 MeV, respectively [49].

Table 4.1 lists the first several excited states of $^{16}$O. The left three columns list the excited state with its corresponding energy, angular momentum and parity, and half-life. The middle two columns list the possible gamma ray(s) from the excited state with the corresponding energy and intensity. The right columns list the final state of the transition with its corresponding energy and angular momentum and parity.

Not all excited states of the $^{16}$O nucleus primarily emit a gamma ray, such as the

**Table 4.1. First excited states of $^{16}$O [49].**

| Initial State | | | Gamma Ray | | Final State | |
|---|---|---|---|---|---|---|
| **E [keV]** | **$I^{\Pi}$** | **$T_{1/2}$** | **$E_\gamma$ [KeV]** | **$I_\gamma$ [%]** | **E [keV]** | **$I^{\Pi}$** |
| 0.0 | $0^+$ | Stable | | | | |
| 6049.4 | $0^+$ | 67 ps | | | | $0^+$ |
| 6129.9 | $3^-$ | 18.4 ps | 6128.6 | 100 | 0.0 | $0^+$ |
| 6917.1 | $2^+$ | 4.7 fs | 787.2 | $\leq$0.008 | 6129.9 | $3^-$ |
| | | | 867.7 | 0.027 | 6049.4 | $0^+$ |
| | | | 6915.5 | 100 | 0.0 | $0^+$ |
| 7116.9 | $1^-$ | 8.3 fs | 986.9 | 0.07 | 6129.9 | $3^-$ |
| | | | 1067.5 | $\leq$6e-4 | 6049.4 | $0^+$ |
| | | | 7115.2 | 100 | 0.0 | $0^+$ |
| 8871.9 | $2^-$ | 125 fs | 1754.9 | 14.7 | 7116.9 | $1^-$ |
| | | | 1954.7 | 4.6 | 6917.1 | $2^+$ |
| | | | 2741.5 | 100 | 6129.9 | $3^-$ |
| | | | 2822.2 | 0.15 | 6049.4 | $0^+$ |
| | | | 8869.3 | 9.3 | 0.0 | $0^+$ |
| 9585 | $1^-$ | 420 keV | 2688 | 12 | 6917.1 | $2^+$ |
| | | $\alpha$=100% | 9582 | 100 | 0.0 | $0^+$ |
| | | IT=6.7e-6% | | | | |
| 9844.5 | $2^+$ | 0.62 keV | 2927.1 | 34 | 6917.1 | $2^+$ |
| | | $\alpha$=100% | 3794.6 | 30 | 6049.4 | $0^+$ |
| | | IT=0.0016% | 9841.2 | 100 | 0.0 | $0^+$ |
| 10356 | $4^+$ | 26 keV | 3439 | 100 | 6917.1 | $2^+$ |
| | | $\alpha$=100% | 4225 | <1.6 | 6129.9 | $3^-$ |
| | | IT=2.4e-4% | 10352 | 9E-5 | 0.0 | $0^+$ |
| 10957 | $0^-$ | 5.5 ps | 3839.6 | 100 | 7116.9 | $1^-$ |

9.585, 9.845, and 10.356 MeV states which primarily decay by alpha emission. All the excited states above 10.957 MeV decay primarily by alpha and proton emission. Additionally, the first excited state at 6.049 MeV has an angular momentum and parity of $0^+$, which is the same as the ground state. Since there is no change in angular momentum ($0^+ \rightarrow 0^+$), the nucleus is unable to relax to the ground state by gamma-ray emission. Therefore, the first excited state relaxes to the ground state by internal conversion, which occurs when the energy is released by an ejected orbital electron [50].

In a neutron inelastic scattering event, the $^{16}$O nucleus could be placed in any

of its excited states as long as the neutron energy equals or exceeds the threshold energy ($\sim 1.0625E^*$) for that excited state energy ($E^*$) [48]. However, only 5 excited states are easily measured with gamma-ray detection: 6.129, 6.917, 7.117, 8.872, and 10.356 MeV.

### 4.1.2 $^{16}$O(n,n') Existing Experimental Cross Section Data

The EXFOR database is the largest repository of experimental nuclear reaction data [57]. The available EXFOR data for the $^{16}$O(n,n') reaction are:

- Partial cross section calculated from outgoing neutrons [17–19, 23, 25, 26, 29],
- Partial angular differential cross section of outgoing neutrons [16–28],
- Cross section calculated from outgoing gamma rays [127–130],
- Partial cross section of outgoing gamma rays [121–123, 130–137], and
- Partial angular differential cross section of outgoing gamma rays [29, 122, 123, 127, 128, 138–146].

The EXFOR data for the $^{16}$O(n,n') reaction that do not exist include:

- Total cross section calculated from outgoing neutrons,
- Partial energy differential cross section of outgoing neutrons, and
- Partial double differential cross section of outgoing neutrons.

#### 4.1.2.1 $^{16}$O(n,n') Partial Cross Section Data using Neutrons

The EXFOR database contains data from thirteen experiments that measured the $^{16}$O(n,n') partial angular differential cross section [16–28] of the outgoing scattered neutrons and seven experiments that calculated the $^{16}$O(n,n') partial cross section [17–

19, 23, 25, 26, 29] using the outgoing scattered neutron. Figure 4.1 plots the available $^{16}$O(n,n') partial cross-section (CS) and partial angular differential (AD) cross-section data using the outgoing neutron in EXFOR for the excited states of $^{16}$O. The primary name of the author, the year the data were published, and the neutron energy(ies) are indicated by each shaded portion. For experiments with more than one incident energy, the number of neutron energies in the data is represented by the number in the parentheses.

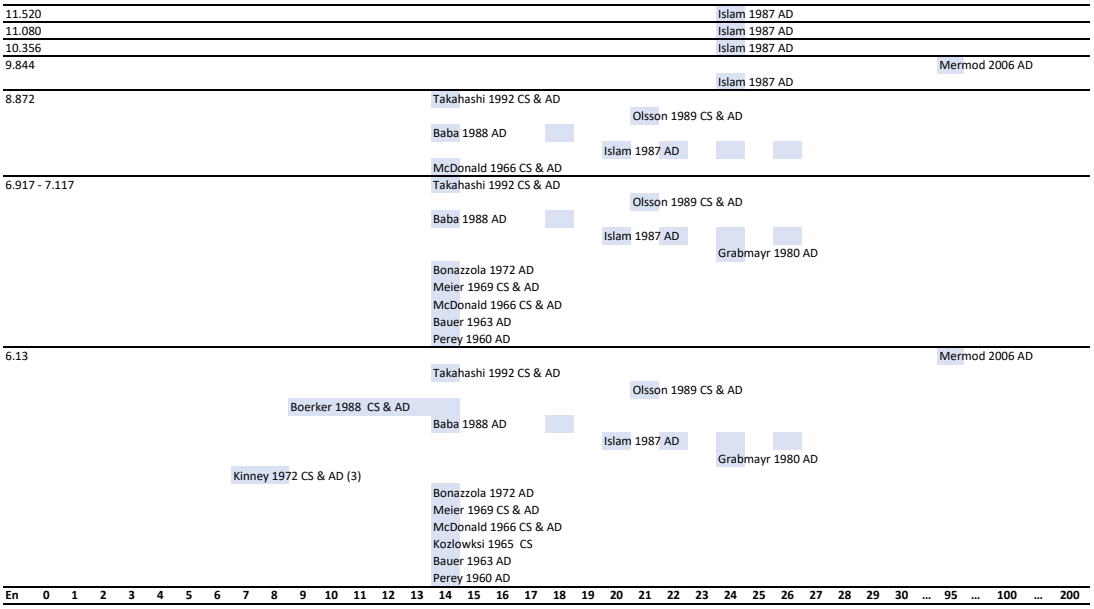


**Figure 4.1. Available $^{16}$O(n,n') partial cross-section (CS) and partial angular differential (AD) cross-section data using the outgoing neutron in EXFOR for the excited states of $^{16}$O. The primary name of the author, the year the data were published, and the neutron energy(ies) are indicated by each shaded portion. For experiments with more than one incident energy, the number of neutron energies in the data is represented by the number in the parentheses [16–29].**

Most of these experiments used the same method to calculate the $^{16}$O(n,n') partial cross section and partial angular differential cross section. These experiments consisted of an $^{16}$O target placed near a monoenergetic neutron source and a neutron detector placed at a distance away. The scattered neutrons, elastic and inelastic, would be detected in the neutron detector, and their energies would be calculated using the time-of-flight method. The elastic neutrons would arrive

first, followed by the inelastically scattered neutrons, which would come in "waves" corresponding to the excited states of the target.

Figure 4.2 shows an example of the neutron time-of-fight with the elastically and inelastically scattered neutrons that correspond the the excited states of $^{16}$O. This experiment was conducted using 5 MeV deuterons on tritium, which produced 21.6 MeV neutrons. The target was a hollow cylinder of $SiO_2$, which was placed 14.5 cm from the source. The neutron detector was a NE-213 liquid scintillator placed 5 m from the target. The 6.1 MeV peak includes the 6.049 and 6.130 MeV excited states, and the 7.0 MeV peak includes the 6.917 and 7.117 MeV excited states that could not be resolved in the experiment [18].

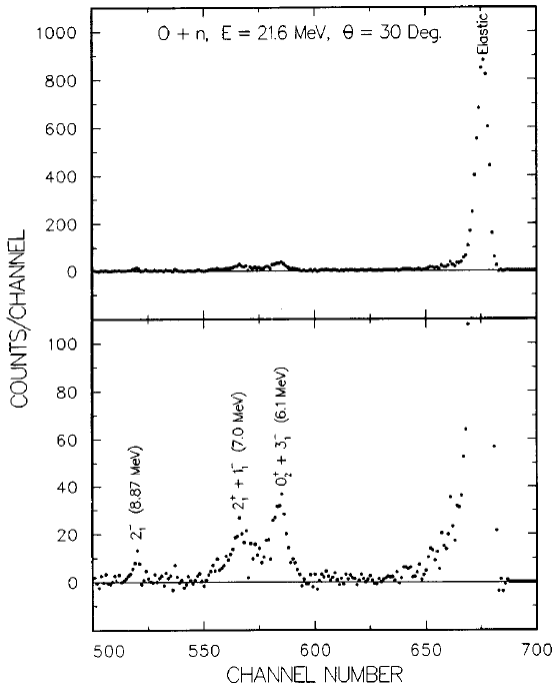


**Figure 4.2. Time-of-flight spectrum of scattered (elastic and inelastic) neutrons from $^{16}$O [18]. The 6.1 MeV peak includes the 6.049 and 6.130 MeV excited states, and the 7.0 MeV peak includes the 6.917 and 7.117 MeV excited states that could not be resolved in the experiment.**

#### 4.1.2.2 $^{16}$O(n,n') Partial Cross Section Data using Gamma Rays

The EXFOR database contains data from eleven experiments that measured the $^{16}$O(n,n') partial cross section [121–123, 130–137] and four experiments that measured the $^{16}$O(n,n') total cross section using the outgoing gamma rays [127–130]. Figure 4.3 plots the available $^{16}$O(n,n') partial cross-section and total cross-section data using the outgoing gamma rays in EXFOR. The primary name of the author, the year the data were published, and the neutron energy(ies) are indicated by each shaded portion. For experiments with more than one incident energy, the number of neutron energies in the data is represented by the number in the parentheses.

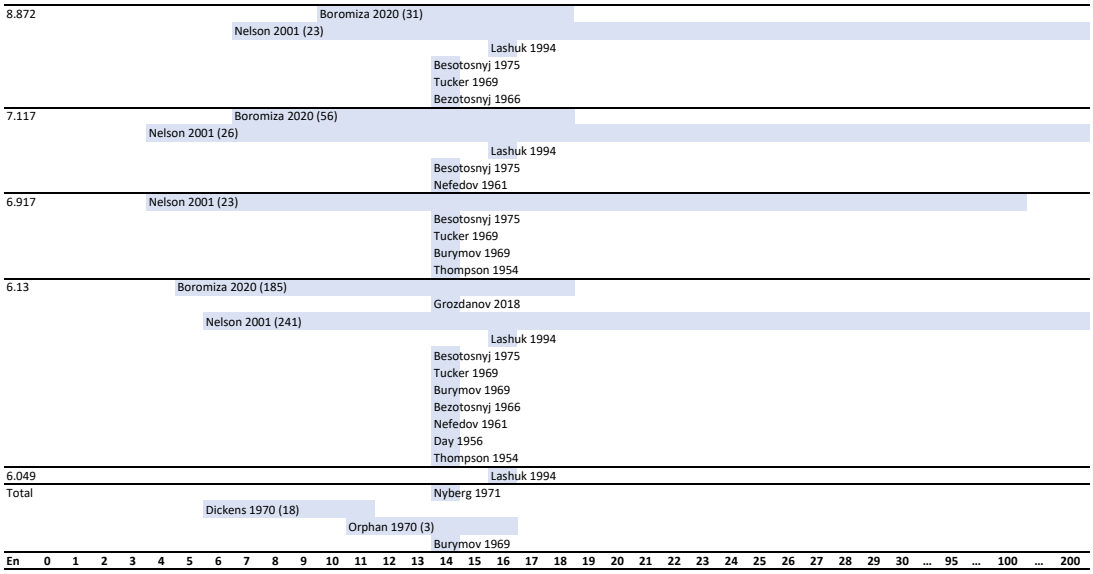


**Figure 4.3. Available $^{16}$O(n,n') partial cross-section and total cross-section data using the outgoing gamma rays in EXFOR. The primary name of the author, the year the data were published and the neutron energy(ies) are indicated by each shaded portion. For experiments with more than one incident energy, the number of neutron energies in the data is represented by the number in the parentheses [121–123, 127–137].**

All these experiments, besides two, used monoenergetic neutrons on a target and measured the gamma rays at different angles from the target. The experiment performed by Nelson *et al.* in 2001 used a pulsed, white source of neutrons with the target 41 m from the source. Gamma-ray detectors near the target measured the

outgoing gamma rays at different angles. Figure 4.4a plots the gamma-ray spectrum from the BeO target at 125° using 4-200 MeV neutrons. The incident neutron energy was measured using the time-of-flight technique between the pulse and detected gamma ray. Figure 4.4b plots the production cross section of the 6.129 MeV gamma ray from $^{16}$O, which is also the partial inelastic scattering cross section [123].

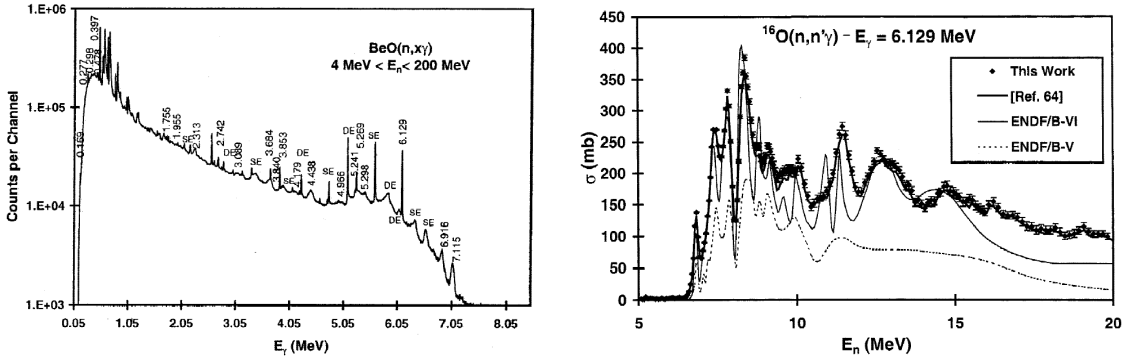


**Figure 4.4. (a) The gamma-ray spectrum from the BeO target at 125° using 4-200 MeV neutrons, and (b) the production cross section of the 6.129 MeV gamma ray from $^{16}$O, which is also the partial inelastic scattering cross section [123].**

### 4.1.3 $^{16}$O(n,n') Evaluated Cross Section Data

For neutron inelastic scattering on $^{16}$O, the evaluated cross sections for the different evaluated nuclear data files do not agree, as shown in Figure 4.5a. ENDF [59], JEFF [60], and BROND [63] contain the same evaluation, but the independent JENDL [61] and CENDL [62] do not agree. The maximum difference in the evaluated cross-section data is between JENDL and CENDL at 19 MeV, where the JENDL cross section value is almost 10 times higher than CENDL value.

In addition to the large disagreements in the $^{16}$O(n,n') total cross section evaluated data, the ENDF library does not contain complete data for the $^{16}$O(n,n') reaction. The current ENDF library for the $^{16}$O(n,n') reaction includes:

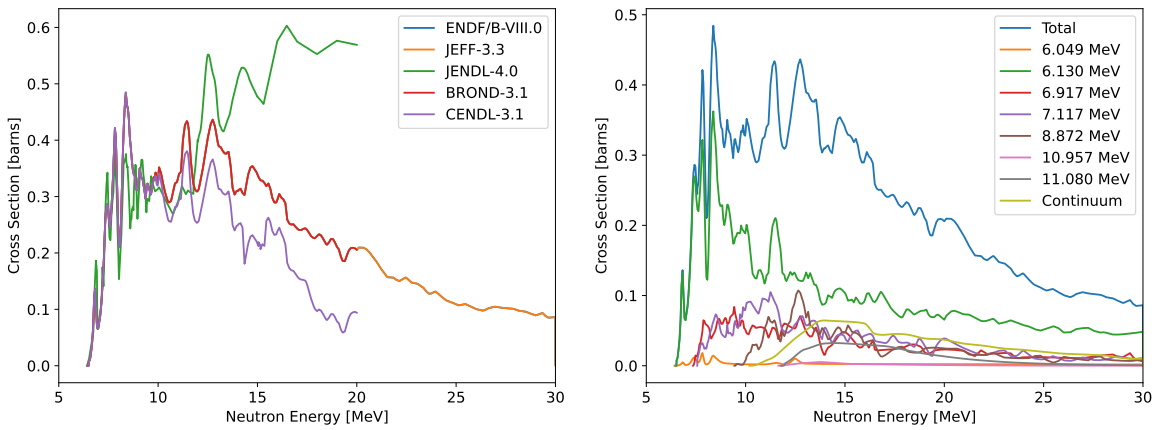


**(a) Total from different libraries.** **(b) Total and partial from ENDF/B-VIII.0.**

**Figure 4.5. Evaluated $^{16}$O(n,n') total cross section data (a) from different libraries [59–63] and (b) total and partial cross section data from ENDF/B-VIII.0 [59].**

- Total cross section,
- Partial cross section for 7 excited states (plotted in Figure 4.5b),
- Angular distribution of secondary particles for 2 excited states (7.117 and 8.872 MeV),
- Photon production cross sections, and
- Photon angular distributions.

### 4.1.4 Other Reactions of Interest

In addition to the $^{16}$O(n,n') reaction, other inelastic scattering reactions of possible interest, assuming a $Al_2O_3$ (alumina) target, include $^{17}$O(n,n'), $^{18}$O(n,n'), and $^{27}$Al(n,n'). However, the natural abundance of $^{17}$O and $^{18}$O is 0.038% and 0.205%, respectively, which will make the reaction less likely to occur and be measured. The natural abundance of $^{27}$Al is 100% and the first excited state of $^{27}$Al is 0.844 MeV [126, 147], which has a threshold energy of ~0.875 MeV. However, while low threshold energy reactions, such as $^{27}$Al(n,n'), are easily detected, these

are difficult to properly measure at GENESIS due to neutron wrap around, which occurs when the fast neutrons from the current beam pulse overtake the slower neutrons from a previous pulse (see Section 4.2.5.3). This issue is being investigated independent of this work.

In addition to the inelastic scattering reactions, neutrons on $^{16}$O and $^{27}$Al can cause other reactions, which are listed in Table 4.2 [49, 147]. All these reactions are endothermic and Table 4.2 lists the threshold energy for the lowest threshold reactions on $^{16}$O and $^{27}$Al except for neutron inelastic scattering.

**Table 4.2. Threshold energy for the specific reactions on $^{16}$O and $^{27}$Al [49, 147].**

| **Reaction** | $E_{th}$ **[MeV]** |
|---|---|
| $^{27}$Al(n,p)$^{27}$Mg | 1.896 |
| $^{16}$O(n,$\alpha$)$^{13}$C | 2.355 |
| $^{27}$Al(n,$\alpha$)$^{24}$Na | 3.250 |
| $^{27}$Al(n,d)$^{26}$Mg | 6.273 |
| $^{16}$O(n,n+$\alpha$)$^{12}$C | 7.614 |
| $^{27}$Al(n,n+p)$^{26}$Mg | 8.581 |
| $^{16}$O(n,p)$^{16}$N | 10.247 |
| $^{16}$O(n,d)$^{15}$N | 10.528 |
| $^{27}$Al(n,n+p)$^{25}$Mg | 11.290 |
| $^{16}$O(n,t)$^{15}$N | 12.892 |

GENESIS is only able to measure the gamma rays from the the excited daughter nuclei from these reactions. The incident neutron would require enough energy to place the daughter nuclei in an excited state in addition to the needed threshold energy. For $^{13}$C and $^{12}$C, the first excited states are 3.089 and 4.440 MeV, respectively, which would require a neutron energy of at least $\sim$5.444 and $\sim$13.058 MeV to measure the partial cross sections of $^{16}$O(n,$\alpha$)$^{13}$C and $^{16}$O(n,n+$\alpha$)$^{12}$C, respectively, using GENESIS. These higher threshold reactions are more difficult or impossible to measure if the neutron beam energy is not high enough and the run time is too short.

### 4.1.5 Research Objectives

The primary objective of this research was to measure the outgoing gamma rays and neutrons from the $^{16}$O(n,n') reaction using GENESIS to calculate the

- Partial cross section,
- Partial angular differential cross section of outgoing neutrons,
- Partial energy differential cross section of outgoing neutrons, and
- Partial double (angular and energy) differential cross section of outgoing neutrons.

The desire was to calculate the partial cross sections for each of the five excited states of $^{16}$O that decay completely by gamma-ray emission (6.130, 6.917, 7.117, 8.872, and 10.957 MeV. Additional reactions from Section 4.1.4 were secondary objectives.

Unfortunately, several factors limited the scope of work presented here. The two most limiting factors were the low energy neutron beam and limited beam time, which decreased the probability and detection of higher excited states of $^{16}$O above 6.130 MeV, other higher threshold reactions, and correlated outgoing neutrons. Additionally, without a complete HPGe efficiency calibration at higher gamma-ray energies and a characterized neutron beam, a complete cross-section calculation is not possible. Finally, analyses of the beam wrap-around and beam intensity, which are being investigated independent of this work, are incomplete at this time limiting the ability to measure low-lying excited states and normalize the measured cross sections, respectively.

The research presented in this Chapter accomplished the following objectives:

- Develop and characterize GENESIS capabilities,
- Develop code and algorithms to process the data, and

- Calculate the $^{16}$O(n,n') detection spectrum of the 2$^{nd}$ excited state.

## 4.2 Experimental Methodology

The 88-Inch Cyclotron accelerated deuterons at 14 MeV into a thick carbon target, which created neutrons with a wide range on energies up to about 16.225 MeV (the deuteron kinetic energy plus the Q-value of the deuteron breakup). Figure 4.6 plots the neutron spectrum from 14 MeV deuterons on thick carbon target [148].

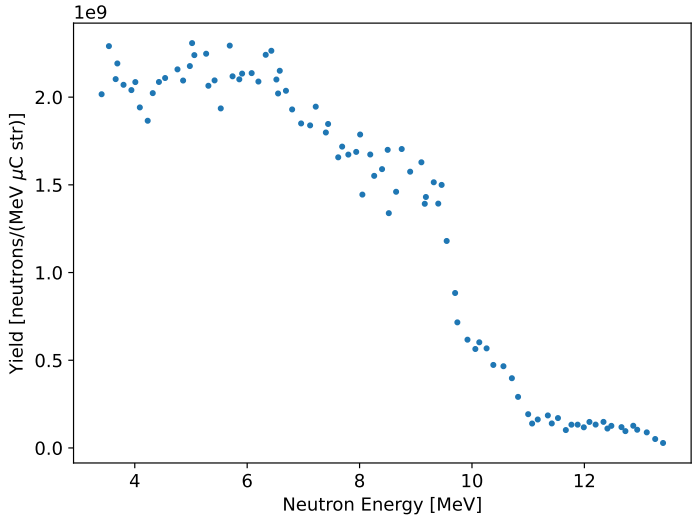


**Figure 4.6. Neutron spectrum from 14.05 MeV deuterons on a thick carbon target at $\theta = 0.35°$ [148].**

The neutron beam was collimated using a copper collimator located near the deuteron breakup target in the 88-Inch Cyclotron vault, as pictured in Figure 4.8, before traveling 7.3 m to the $^{16}$O target located at the center of the GENESIS array, shown in Figure 4.7.

The target was a 60×60×0.5 mm piece of alumina ($Al_2O_3$) with a purity of 99.6% from Goodfellow Corporation. The density and molecular weight of alumina are 3.9 g/cm$^3$ [149] and 101.961 g/mol [150], respectively.

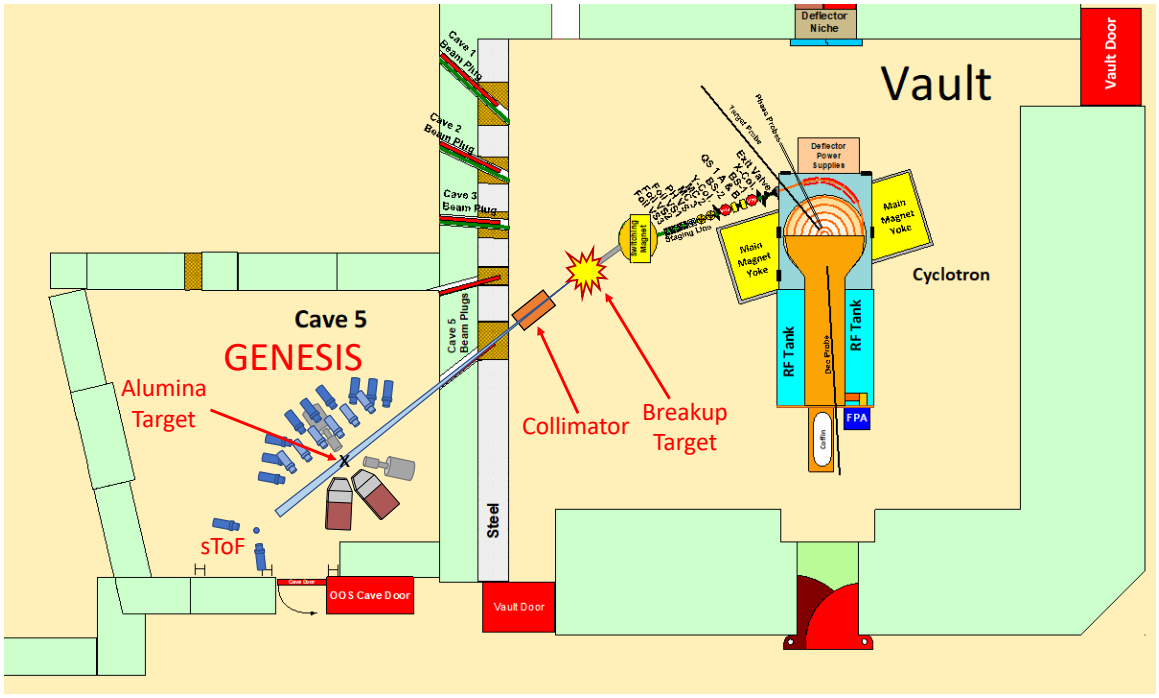


**Figure 4.7. Top view of the 88-Inch Cyclotron, deuteron breakup target, and copper collimator in the vault and the GENESIS array, sToF, and alumina target in Cave 5.**

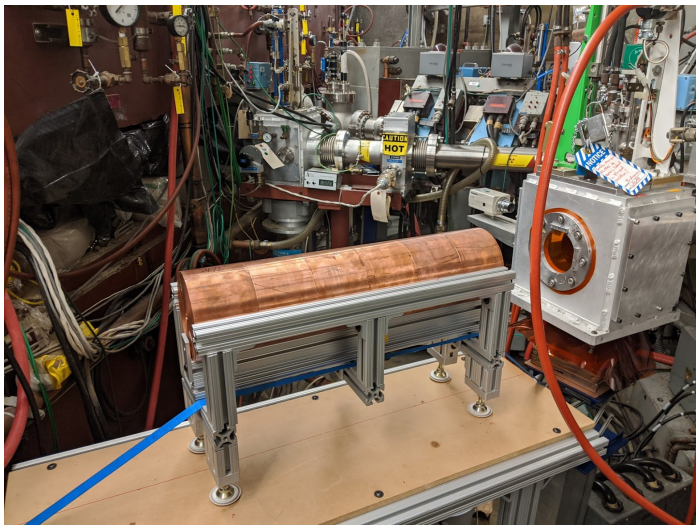

**Figure 4.8. Copper collimator next to the aluminum beam box, which houses the carbon target.**

### 4.2.1 Inelastic Scattering Measurements using GENESIS

GENESIS is capable of measuring the inelastic scattering cross section by using the detectors and equipment to correlate the gamma rays and scattered neutrons

from the inelastic scattering event. Figure 4.9 illustrates the GENESIS concept of operation (some detectors have been removed for clarity).

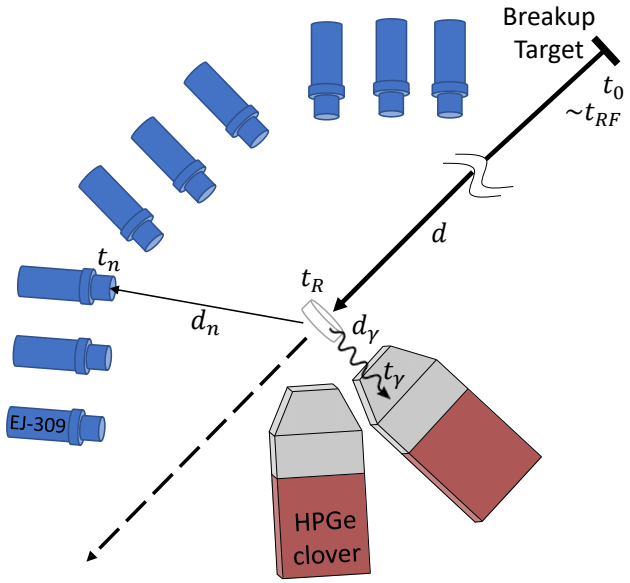


**Figure 4.9. GENESIS concept of operation. A neutron born from the deuteron break up at $t_0$ travels a distance of $d$ to the target, which reacts with the target nucleus at time, $t_R$. In an inelastic scattering event, the gamma ray travels a distance of $d_\gamma$ to the detector and is detected at time $t_\gamma$ and the scattered neutron travels a distance of $d_n$ to an EJ-309 detector, where it is detected at time $t_n$.**

A neutron from the deuteron break up at time $t_0$, which is approximated by cyclotron radio-frequency (RF) signal ($t_{RF}$), travels a distance of $d$ to the target. For an inelastic scattering event, the neutron reacts with the target nucleus at time, $t_R$, exciting the nucleus. As the nucleus relaxes to the ground state and emits a gamma ray, the gamma ray travels a distance of $d_\gamma$ to the detector and is detected at time $t_\gamma$. The scattered neutron travels a distance of $d_n$ to an EJ-309 detector where it is detected at time $t_n$. The incident and inelastically scattered neutron energy can be computed using the time-of-flight technique.

### 4.2.2 Detector Positions and Settings

For the experiment, there were 26 EJ-309 organic liquid scintillators, two Eurosys HPGe clover detectors with BGO shields, and one 3"x3" LaBr detector. Due to the inadequate energy resolution of the LaBr detector, it was not used in the analysis. There were two Ortec Pop-Tops in the GENESIS array; however, they were not performing correctly at the time of the experiment and were not used in the analysis. The positions of the HPGe clover detectors and EJ-309 scintillators were measured using a Leica DISTO S910 [151]. Table 4.3 lists the positions of the HPGe clover detectors and EJ-309 scintillator that were used in the results and analysis. Only one EJ-309 scintillator was used in the analysis, which was for the timing characterization (Section 4.3.3). The positions of all the EJ-309 scintillators are listed in Table A.1 of Appendix A. Figure 4.10 is a picture of the detectors in the GENESIS array which is similar to the arrangement of the detectors used in this experiment.

**Figure 4.10. Picture of GENESIS array with HPGe clovers, HPGe Pop-Tops, and EJ-309 scintillators. The detectors where located in similar positions for this experiment.**

The signals from the HPGe detectors and the BGO shields were processed on a Mesytec MDPP-16 board using the SCP firmware (SCP) and the signals from the

EJ-309 scintillators were processed on two Mesytec MDPP-16 boards using the QDC firmware (QDC1 and QDC2) [113, 152, 153]. The board identification numbers for the SCP, QDC1, and QDC2 boards were 17, 18, and 19, respectively. Additionally, the trigger input and RF signal were inserted into trigger input 1 (ch 32) and trigger input 2 (ch 33), respectively, for each of the MDPP-16 boards. Table 4.3 lists the MDPP-16 board and channel configuration for the HPGe clover detectors and EJ-309 scintillator that were used in the results and analysis. All the inputs for the three MDPP-16 boards are listed in Table B.1 of Appendix B. The settings used in the Mesytec mvme software for the MDPP-16 boards are listed in Appendix C.

**Table 4.3. Position of the center, front face of the HPGe clover detectors and EJ-309 scintillator relative to the target location.**

| | Position | | | | MDPP-16 | |
|---|---|---|---|---|---|---|
| **Detector** | **x [m]** | **y [m]** | **z [m]** | **d [m]** | **Board** | **Channel** |
| Clover 3-1 | -0.1919 | -0.2263 | 0.0315 | 0.2984 | SCP | 0 |
| Clover 3-2 | -0.2258 | -0.2034 | 0.0315 | 0.3055 | SCP | 1 |
| Clover 3-3 | -0.2252 | -0.2036 | -0.0115 | 0.3038 | SCP | 11 |
| Clover 3-4 | -0.1920 | -0.2260 | -0.0101 | 0.2967 | SCP | 3 |
| Clover 4-1 | 0.0075 | -0.2446 | 0.0305 | 0.2466 | SCP | 4 |
| Clover 4-2 | -0.0394 | -0.2417 | 0.0303 | 0.2468 | SCP | 5 |
| Clover 4-3 | -0.0391 | -0.2420 | -0.0113 | 0.2454 | SCP | 6 |
| Clover 4-4 | 0.0079 | -0.2442 | -0.0105 | 0.2445 | SCP | 7 |
| EJ-309 8 | -0.7526 | 0.1503 | -0.0219 | 0.7678 | QDC1 | 8 |

### 4.2.3 Neutron Flux Monitoring

The neutron flux from the beam was continuously monitored using the scatter time of flight (sToF) method [76]. The system is located at the end of the beam line behind the GENESIS array as show in Figure 3.1. A scintillator detector is located in the center of the beam with other scintillator detectors around the center detector at a given distance away and out of the beam. A neutron in the beam may elastically scatter in the center detector and then into one of the scattering detectors, depicted

in Figure 4.11.

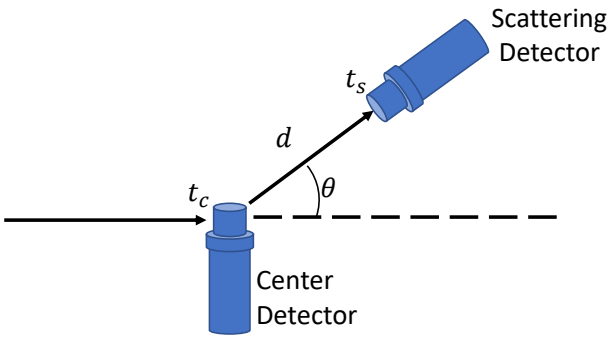


**Figure 4.11. Illustration of the compact, scattering time-of-flight set up at the end of the beam line to measure the total flux.**

The scattered neutron energy is calculated using the time of flight method and the time difference between the detection in the center and scattered scintillators. The incident neutron energy can be calculated by rearranging Equation 2.23. The neutron beam flux from 14 MeV deuteron breakup on the carbon target used in the $^{16}$O experiment (and others) is currently in the process of being fully characterized by another researcher.

### 4.2.4 Experimental Runs

The preliminary and scoping experiment for the $^{16}$O(n,n') cross-section measurement was conducted in conjunction with other GENESIS experiments on 4-5 Apr 2021. With the neutron beam on the alumina target, data were collected for 5 hours and 50 minutes, segmented into 7 runs. Table 4.4 lists the run ID with its start and stop times.

Figure 4.12 plots the count rate of the HPGe clover detectors for events between 1-8 MeV, along with the deuteron beam current, for each run. Due to the short length of experimental time, there was not enough data to correlate gamma rays from the HPGe detectors and neutrons from the EJ-309 scintillators. This limitation only allowed partial cross section measurements to be calculated from the gamma-ray

**Table 4.4. Experimental runs on alumina target (HH:MM:SS).**

| Experimental Run ID | Start Time | Stop Time | Run Time |
|---|---|---|---|
| GENESIS_Al2O3_039_210404_204110 | 20:41:09 | 21:37:45 | 0:56:36 |
| GENESIS_Al2O3_040_210404_224817 | 22:48:16 | 23:14:42 | 0:26:26 |
| GENESIS_Al2O3_041_210404_232640 | 23:26:38 | 00:23:16 | 0:56:38 |
| GENESIS_Al2O3_042_210405_002411 | 00:24:10 | 01:35:02 | 1:10:52 |
| GENESIS_Al2O3_043_210405_013604 | 01:36:02 | 02:40:04 | 1:04:02 |
| GENESIS_Al2O3_044_210405_024128 | 02:41:27 | 03:34:50 | 0:53:23 |
| GENESIS_Al2O3_045_210405_033550 | 03:35:49 | 03:57:49 | 0:22:00 |

data collected by the HPGe detectors.

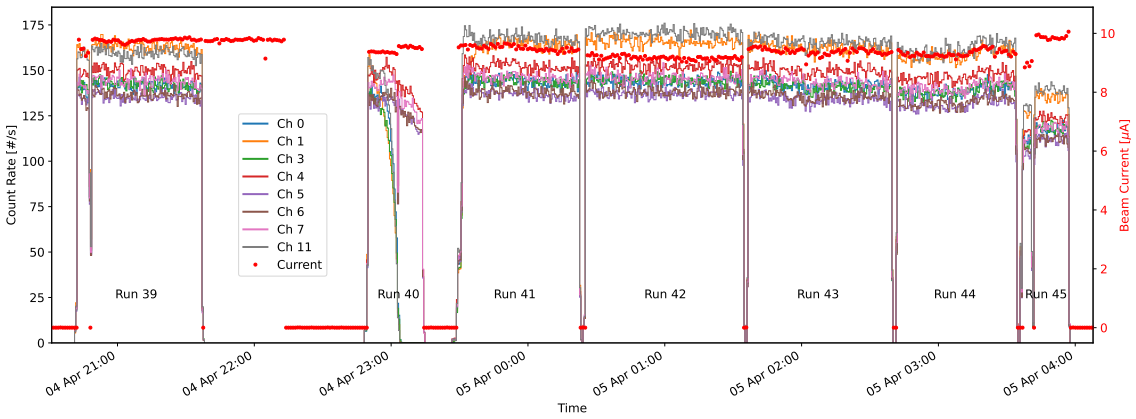


**Figure 4.12. Count rate in the HPGe clover detectors for events between 1-8 MeV over the entire experiment along with the deuteron beam current.**

### 4.2.5 Timing Characterization

Each of the MDPP-16 boards was set to have the timing window start at -1,500 ns from the trigger input (ch 32) with a window width of 4,500 ns, as shown in Figure 4.13. While the window is open, all events within the window are recorded and stamped with a TDC time, which starts from the beginning of the window. The timing resolution for each board was set to 0.098 ns per TDC channel.

The incident neutron energy is determined by the neutron time of flight, $nToF$, calculated as

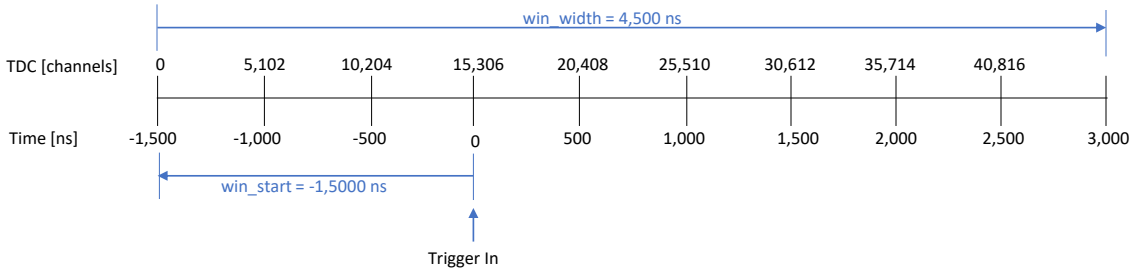


**Figure 4.13. Timing of the MDPP-16 boards. For each board, the window would start -1,500 ns from the trigger input and was open for ~4,500 ns. The timing resolution was 0.098 ns per TDC channel.**

$$nToF = t_\gamma - t_{RF} - \frac{d_\gamma}{c} - \Delta t, \tag{4.1}$$

where $t_\gamma$ and $t_{RF}$ were the measured time of the gamma-ray detection in the HPGe and RF signal, respectively, $d_\gamma$ was the distance of the HPGe detector from the target, $c$ was the speed of light, and $\Delta t$ is the timing delay between the HPGe detector and RF signal. Figure 4.9 illustrates the positions of the targets and detectors and the parameters used to calculate the incident neutron time of flight.

#### 4.2.5.1 Delay and Uncertainty

Two methods were examined to calculate the timing delay and uncertainty between the HPGe detectors and RF signal, which was needed to properly calculate the incident neutron time of flight in Equation 4.1. The first method calculated the timing delay and uncertainty using the gamma-ray flash from the deuteron break-up target that Compton scattered into the HPGe detectors, calculated as

$$\Delta t = t_\gamma - t_{RF} - \frac{d + d_\gamma}{c}, \tag{4.2}$$

where $d$ is the distance between the deuteron break up target and alumina target, which was 7.3 m.

The second method calculated the timing delay and uncertainty by combining the timing delay and uncertainty of Compton-scattered gamma-ray flash in one of the EJ-309 scintillators and the delay and uncertainty between the HPGe detectors and the EJ-309 scintillator determined from prompt fission gamma rays of a $^{252}$Cf source located at the target location. The delay between the EJ-309 scintillator and RF signal, using the Compton-scattered gamma-ray flash, was calculated as

$$\Delta t_{EJ-RF} = t_n - t_{RF} - \frac{d + d_n}{c}, \tag{4.3}$$

where $d_{EJ}$ is the distance between the target and the EJ-309 scintillator. The delay between the EJ-309 scintillator and HPGe detectors was calculated as

$$\Delta t_{EJ-HPGe} = t_n - t_\gamma - \frac{d_n - d_\gamma}{c}, \tag{4.4}$$

and combining the two delays provides the delay between the HPGe detectors and RF signal as

$$\Delta t = \Delta t_{EJ-RF} - \Delta t_{EJ-HPGe}. \tag{4.5}$$

#### 4.2.5.2 RF Signal Timing

The RF signal from the cyclotron was inserted into trigger input 1 (ch 33) for each board. Figure 4.14 plots the TDC time difference between the RF signals in the QDC1 board of run 42. An average time difference of 169.93 ns (5.885 MHz) was obtained.

Figure 4.15 plots the number of RF signals within each ∼4,500 ns timing window for each of the boards of run 42. Since the RF signal input is constant, the number of RF signals processed by the board for each timing window should be the same,

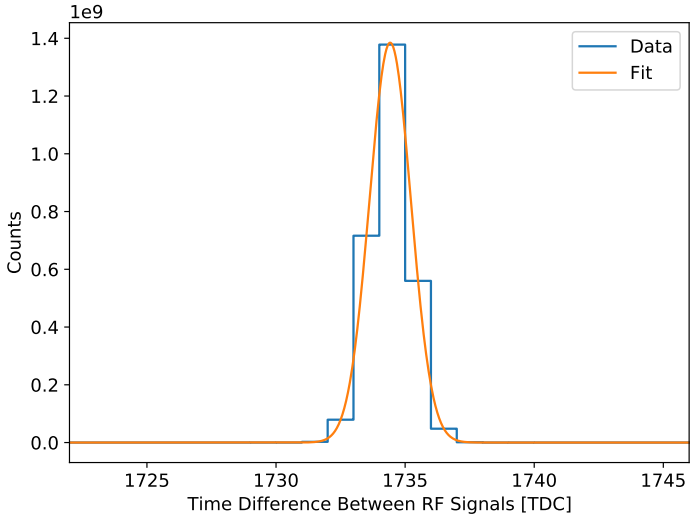


**Figure 4.14. Timing difference between the RF signals in the QDC1 board from run 42. The average time difference between RF signals was 169.93 ns, which equates to a cyclotron pulse frequency of 5.885 MHz.**

which is 26-27 RF signals within each timing window. This was the case for the QDC boards, but not the SCP board. Therefore, the RF signal from the QDC1 board was used for the all the timing analyses.

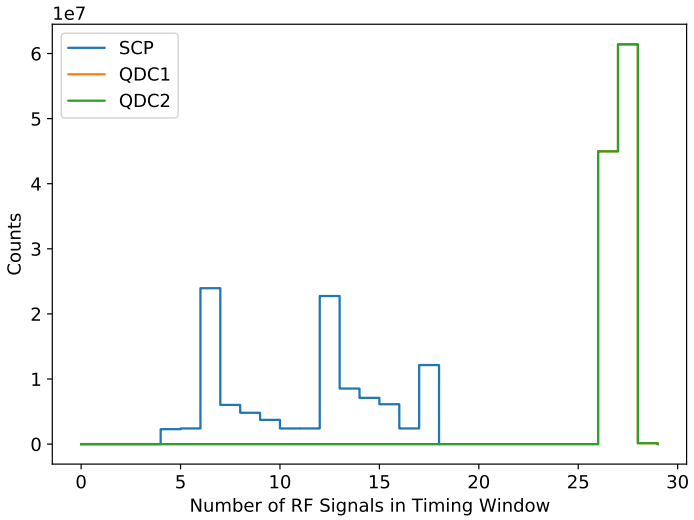


**Figure 4.15. The number of RF signals within each timing window for the boards from run 42. With a cyclotron period of 169.93 ns, there were 26-27 RF signals for each ∼4,500 ns timing window. The RF signals in the QDC boards were properly recorded, but not in the SCP board.**

#### 4.2.5.3 Neutron Wrap Around

The 14 MeV deuteron breakup reaction on carbon created a range of neutron energies up to 16.225 MeV, which is the deuteron kinetic energy plus the binding energy of deuteron (2.225 MeV). Using a pulsed source, the high energy neutrons from the current pulse will get to the target before the low energy neutrons from the previous pulse(s), which is known as neutron wrap around. For the experiment, the cyclotron pulse period was 169.93 ns and the distance between the deuteron break-up target and alumina target was 7.3 m. A 16.225 MeV neutron time of flight over 7.3 m was 132.72 ns. Therefore, the slowest neutron time of flight from the previous pulse that would avoid being overtaken by the fast neutron would arrive in less than 302.65 ns, which equates to a neutron energy of at least 3.056 MeV. The neutron energy of the second and third wrap around is 1.250 and 0.676 MeV, respectively. These energies were well below the reaction threshold for $^{16}$O inelastic scattering and so this effect was ignored.

## 4.3 System Characterization

### 4.3.1 HPGe Energy Calibration

The HPGe detectors were initially calibrated using $^{152}$Eu (0.245, 0.344, 0.779, 0.964, 1.112, and 1.408 MeV peaks). They were then further calibrated using the distinctive gamma-ray lines from the experiment, listed in Table 4.5. The HPGe energy calibration data were fitted to a 2$^{\text{nd}}$-order polynomial.

Gain drift was observed in some of the HPGe detectors; therefore, each HPGe detector was calibrated for each experimental run. Figure 4.16a plots the uncalibrated energy spectra of HPGe clover 4-1 (SCP ch 4) for each experimental run and shows the gain drift of the 7.631 and 7.646 MeV gamma rays from $^{56}$Fe(n,$\gamma$) and Figure 4.16b

**Table 4.5. Gamma rays used from experiment data for HPGe detector energy calibration with their corresponding generating reactions.**

| Energy [MeV] | Reaction |
|---|---|
| 0.511 | Annihilation |
| 0.596 | $^{74}$Ge(n,n') |
| 1.014 | $^{27}$Al(n,n') |
| 1.779 | Decay of $^{28}$Al |
| 6.129 | $^{16}$O(n,n') |
| 7.631 | $^{56}$Fe(n,$\gamma$) |
| 7.646 | $^{56}$Fe(n,$\gamma$) |

plots the calibrated energy spectra for each experimental run.

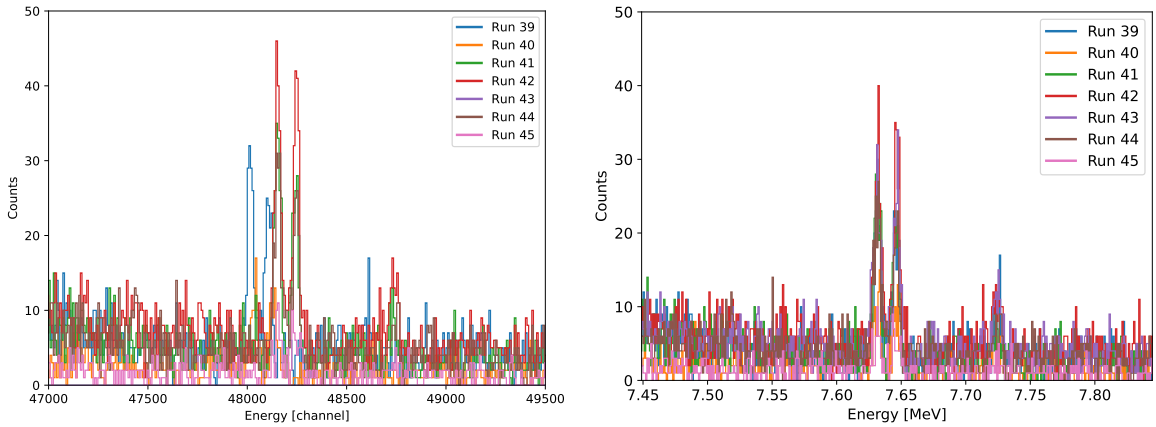


**(a) Uncalibrated energy spectra.** **(b) Calibrated energy spectra.**

**Figure 4.16. (a) uncalibrated and (b) calibrated energy spectra of HPGe clover 4-1 (SCP ch 4) for each experimental run. The gain drift is shown in the 7.631 and 7.646 MeV peaks from $^{56}$Fe(n,$\gamma$) before applying the calibrations.**

### 4.3.2 HPGe Efficiency Calibration

The efficiency of the HPGe clover detectors was calibrated using a 10.05 µCi $^{152}$Eu source and a $^{56}$Co source of unknown activity. The energies used in the efficiency calibration are listed in Table D.1 of Appendix D. The spectrum for each of the HPGe clover detectors was analyzed using PeakEasy [154] to calculate the number of counts under each peak using the best fit to minimize the residual Chi-squared value. The absolute efficiency was calculated as

$$\varepsilon_{abs} = \frac{C_d}{At_e I_\gamma}, \tag{4.6}$$

where $C_d$ was the number of counts under the peak, $A$ was the current activity of the source, $t_e$ was the elapsed time of the calibration, and $I_\gamma$ was the intensity of the gamma-ray emission. The current activity was calculated as

$$A = A_0 e^{-\lambda t}, \tag{4.7}$$

where $A_0$ was the original activity, $t$ was the elapsed time, and $\lambda$ was the decay constant. The uncertainty in the absolute efficiency was calculated as

$$\delta\varepsilon_{abs} = \varepsilon_{abs}\sqrt{\left(\frac{\delta C_d}{C_d}\right)^2 + \left(\frac{\delta I_\gamma}{I_\gamma}\right)^2}. \tag{4.8}$$

Figure 4.17a plots the absolute efficiency of each of HPGe clover detectors using the $^{152}$Eu data. The overlapping energies of $^{152}$Eu and $^{56}$Co were used to estimate the activity of the uncalibrated $^{56}$Co, which was estimated to be ∼8 µCi at the time of the calibration measurement. Figure 4.17b plots the absolute efficiency of each of HPGe clover detectors using the $^{56}$Co data.

#### 4.3.2.1 HPGe Efficiency Calibration Extrapolation

Unfortunately, the calibration data of $^{152}$Eu and $^{56}$Co only extend up to 3.451 MeV which is significantly lower than the energies of the expected gamma rays from $^{16}$O(n,n'). There are several empirical (Kis *et al.* [155]) and semi-empirical (Gallagher and Cipolla [156]) fit functions for HPGe efficiency data that could be used to extrapolate to higher energy ranges. Additionally, the GENESIS GEANT4 simulations, described in Chapter 3, could be used to determine the efficiency at the relevant energies, once experimentally benchmarked at lower energies.

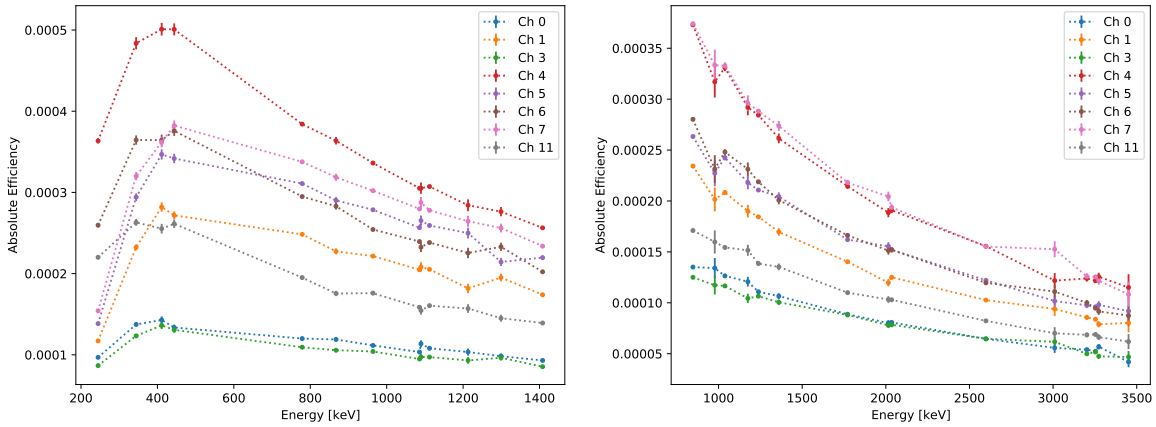


**(a) $^{152}$Eu source.** **(b) $^{56}$Co source.**

**Figure 4.17. Absolute efficiency of the HPGe clover detectors using (a) $^{152}$Eu and (b) $^{56}$Co. The activity of the uncalibrated $^{56}$Co source was determined from $^{152}$Eu-determined efficiencies for overlapping energy ranges.**

Unfortunately, the semi-empirical functions from [156] are not applicable in the energy regime where pair production is significant and therefore will not work for this application. No equivalent semi-empirical functions were found that applied to this energy regime. Additionally, radiation transport simulations are known to provide poor results unless several parameters are tweaked to align the simulated results with measured data, which does not currently exist above 3.451 MeV.

Extrapolation using the empirical functions of [155] remained as the only viable solution. Four of the algorithms (Debertin, Gray, Lin and Fazekas) from [155] were fit to the $^{152}$Eu (244.70-1408.01 keV) and $^{56}$Co (846.76-3548.27 keV) experimental data from [155]. The function extrapolated results were then compared to the $^{36}$Cl (516.73-8578.21 keV) and $^{49}$Ti (1381.75-6760.13 keV) experimental data of Kis *et al.* [155] to determine how well the fits performed at extrapolation in this region given data similar to what was available for GENESIS. Figure 4.18a plots the experimental efficiency data for $^{152}$Eu, $^{56}$Co, $^{36}$Cl, $^{49}$Ti, and the Debertin algorithm using the data from $^{152}$Eu and $^{56}$Co. As expected, the algorithms are not able to extrapolate with high accuracy at higher energies, as shown in Figure 4.18b. Unfortunately, there remained

no successful HPGe efficiency calibration at the higher energies.

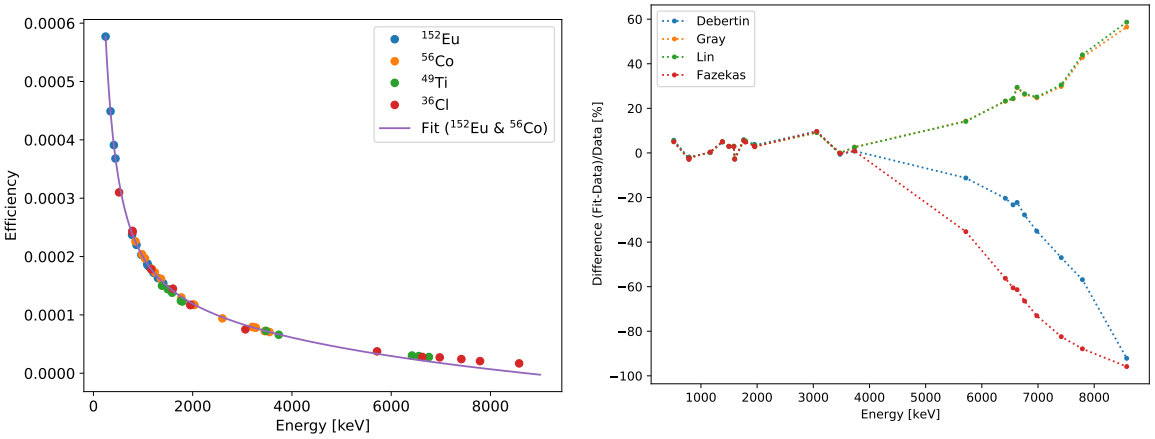


**(a) HPGe efficiency data with Debertin fit**

**(b) Difference between efficiency fit and measured data**

**Figure 4.18. HPGe efficiency extrapolation analysis using different algorithms to fit the (a) experimental efficiency data from $^{152}$Eu and $^{56}$Co and (b) compare the extrapolated fit to experimental efficiency data of $^{36}$Cl and $^{49}$Ti [155].**

#### 4.3.2.2 Plans for Improved High-Energy Efficiency Calibration

In order to measure the efficiency of the HPGe detectors at higher energies above the 3.451 MeV of $^{56}$Co, two ideas were proposed. The first idea was to use gamma-ray emission from the decay of $^{66}$Ga, which emits gamma rays up to 4.806 MeV with a half-life of 9.49 hours [157]. A zinc target was placed into the deuteron beam to create $^{66}$Ga from the $^{66}$Zn(d,2n)$^{66}$Ga reaction. This activated target was then be placed at the target location. The $^{66}$Ga decay does not extend high enough to calibrate the HPGe detectors for gamma rays from $^{16}$O(n,n'$\gamma$), but can extend the current measured efficiency data, which can be used to further benchmark the GEANT4 model and provide more confidence in the simulation to produce the higher-energy HPGe efficiency calibration.

The second proposed idea was to use the gamma rays emitted from thermal neutron capture on $^{35}$Cl, which emits gamma rays up to 7.790 MeV [54, 158]. Table 4.6 lists the most probable gamma rays from thermal neutron capture of $^{35}$Cl

with their associated relative intensities (relative to the most intense).

**Table 4.6. Gamma rays and relative intensity ($I_\gamma/I_{max}$) from thermal neutron capture on $^{35}$Cl [54, 158].**

| Energy [MeV] | $I_\gamma/I_{max}$ [%] |
|---|---|
| 0.517 | 85.073 |
| 0.786 | 38.373 |
| 0.788 | 60.831 |
| 1.164 | 100.000 |
| 1.951 | 71.043 |
| 1.959 | 46.015 |
| 6.111 | 73.962 |
| 6.620 | 28.395 |
| 7.414 | 36.925 |
| 7.790 | 29.854 |

A $^{35}$Cl target was created by pressing 42.368 g of salt (sodium chloride) into a 50 mm diameter, 10.60 mm thick disc. The salt was ≥99.5% pure from Sigma-Aldrich [159]. The salt target was placed at the target location and a $^{252}$Cf source was placed approximately two inches away from the salt target and surrounded with polypropylene to thermalize the neutrons. The activity of the $^{35}$Cl target was calculated through decay gamma rays that overlap the $^{152}$Eu, and $^{56}$Co energy ranges. These sources are either calibrated sources with known activities ($^{152}$Eu) or have decay lives favorable for determining the activity from HPGe spectroscopy ($^{56}$Co).

### 4.3.3 Timing Results

The incident neutron energy was determined by the neutron time of flight, Equation 4.1, which was dependent on characterization of the timing between the HPGe clover detectors, EJ-309 scintillator, and cyclotron RF signal. Figure 4.19 illustrates the positions of the targets and detectors and the parameters used to characterize the timing.

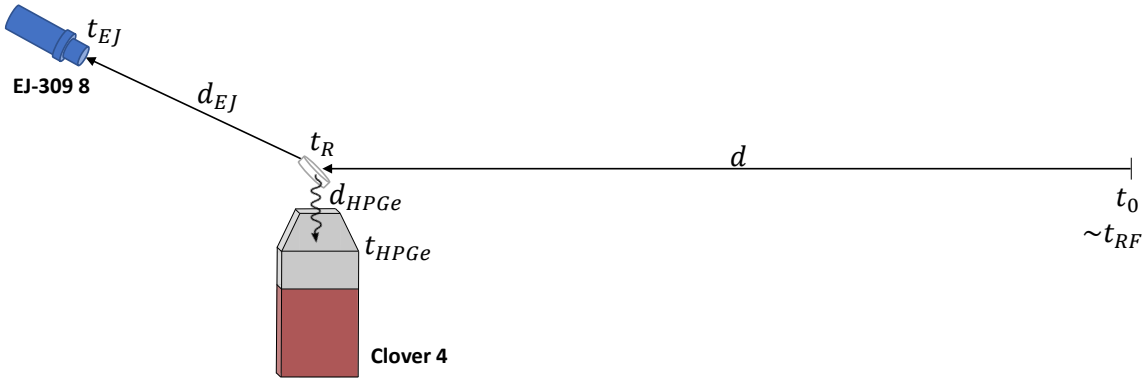


**Figure 4.19. Illustration of the the positions of the targets and detectors and the parameters used to characterize the timing between the HPGe clover detectors, EJ-309 scintillator and cyclotron RF signal.**

#### 4.3.3.1 HPGe and RF Timing

The timing delay and uncertainty between the HPGe detectors and RF signal were measured using the gamma-ray flash from the deuteron pulse on the carbon break-up target which successively Compton scattered off of the alumina target and into the HPGe detectors. All the recorded detection events from the HPGe detectors on the SCP board were correlated to the RF signals from the QDC board within the same timing window (same timestamp). Since the deuteron breakup target was carbon, a portion of the gamma-ray flash would be 4.44 MeV gamma rays (4.20 MeV Compton edge) from the 1st excited state of carbon. A high energy cut from 3.55 to 4.20 MeV was performed on the detected gamma-ray spectrum to isolate more of the events from the 4.44 MeV gamma ray. An additional low-energy cut from 0.421 to 0.466 MeV was performed on the spectrum. Figure 4.20 plots the time difference of the HPGe detector (SCP ch4) and the RF signal (QDC1 ch 33) for all the events in the HPGe along with the high- and low-energy events. There are multiple peaks, which are due to the single event in the HPGe detector being compared to all the RF signals within the same timing window. The delay and uncertainty were calculate using the first positive peak.

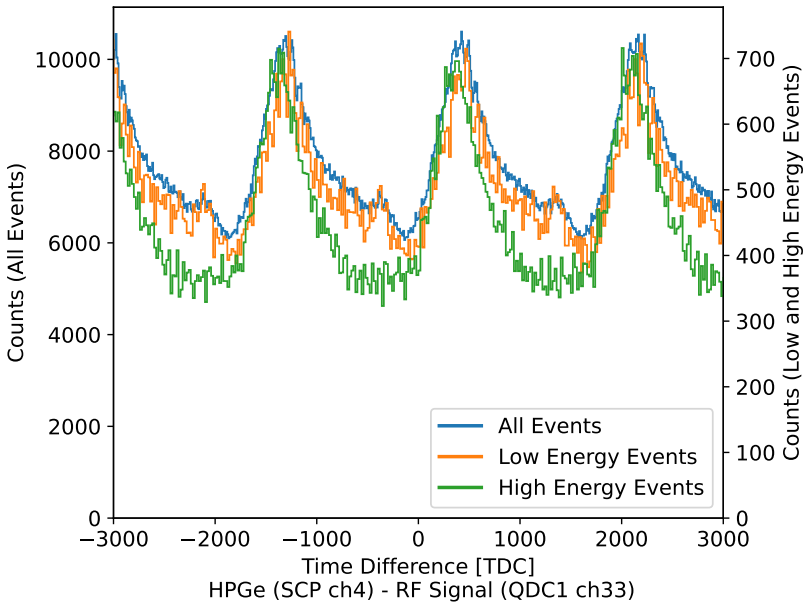


**Figure 4.20. Time difference of the HPGe detector (SCP ch4) and the RF signal (QDC1 ch 33) for all the events (left axis) in the HPGe and with the high (3.55-4.20 MeV) and low (0.421-0.466 MeV) energy events (right axis) from run 42.**

The timing difference using the low energy events followed the same trend as compared to all the events in the HPGe detector, which included the Compton-scattered gamma-ray flash, gamma-rays from the target, neutron interactions within the HPGe detector, and gamma rays from neutron and gamma-ray interactions with other materials in the room. The timing difference using the high energy events follows more of a Gaussian distribution, which would be expected from a Compton-scattered gamma-ray flash. Therefore, the timing difference using the high energy events from all the runs was used to calculate the timing delay and uncertainty. Figure 4.21a plots the time difference between the high energy events (3.55-4.20 MeV) in the HPGe detector (SCP ch4) and the RF signal (QDC1 ch 33) for all the runs, and Figure 4.21b plots time difference with all the runs combined along with the Gaussian distribution fit. The mean and standard deviation of the distribution was 38.01 ns and 20.09 ns, respectively. The distance from the deuteron break-up target to the alumina target plus the distance to the center of the HPGe detector was 7.5869 m, which equates to

a gamma-ray time of flight of 25.31 ns. Therefore, the timing delay and uncertainty between the HPGe detector (SCP ch 4) and RF signal (QDC1 ch 33) was 12.70 ns and 20.09 ns, respectively.

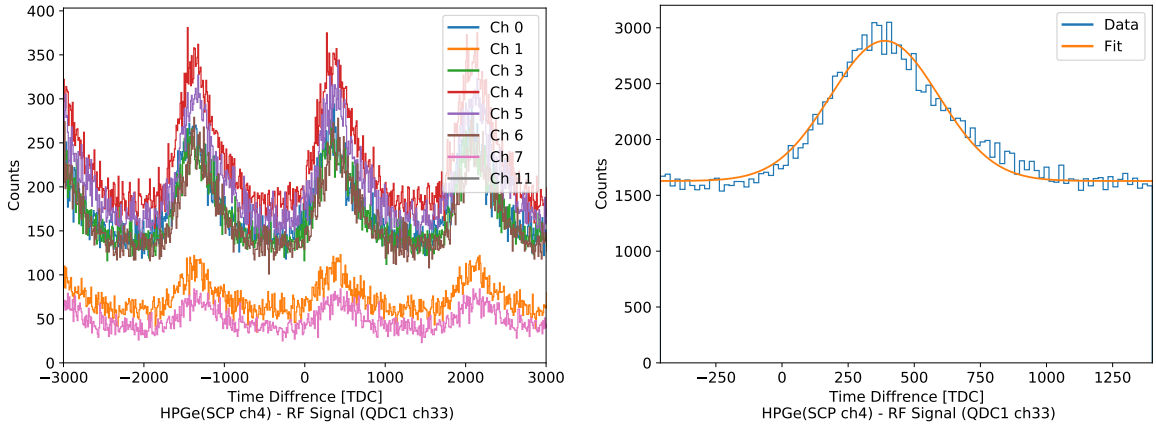


**(a) Individual HPGe and RF timing difference** **(b) Combined HPGe and RF timing difference**

**Figure 4.21. The (a) individual and (b) combined timing difference between the high energy events (3.55-4.20 MeV) in the HPGe detector (SCP ch4) and the RF signal (QDC1 ch33). A (b) Gaussian fit of the combined timing difference obtained a mean and standard deviation of 38.01 ns and 20.09 ns, respectively.**

#### 4.3.3.2 EJ-309 and RF Timing

The timing delay and uncertainty between the EJ-309 scintillator and RF signal was measured using the gamma-ray flash from the deuteron pulse onto the carbon break-up target, which successively Compton-scattered off of the alumina target and into the EJ-309 scintillator. The EJ-309 detector used in the analysis was detector EJ-309 8 (channel 8 on the QDC1 board), which was the most forward positioned detector in the GENESIS array located at a distance of 0.7678 m from the alumina target.

All the recorded detection events from the EJ-309 scintillator were correlated to the RF signals (QDC1 ch33) within the same timing window. The events in the EJ-309 scintillator were separated into gamma ray and neutrons events using a PSD and energy cut, as shown in Figure 4.22a. Figure 4.22b plots the timing difference

between neutron, gamma-ray, and all events in the EJ-309 scintillator and the RF signal. There are multiple peaks, which are due to the single event in the EJ-309 being compared to all the RF signals within the same timing window.

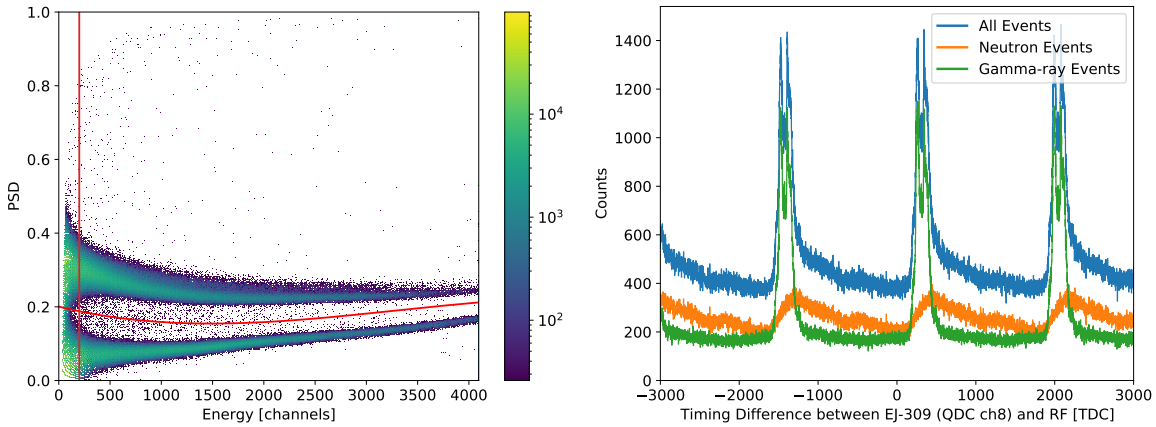


**(a) EJ-309 PSD and energy histogram with energy and PSD cuts (red lines).**

**(b) Timing difference between EJ-309 and RF signal.**

**Figure 4.22. (a) PSD and energy histogram of the EJ-309 scintillator (QDC1 ch8) from run 42. The red lines indicate the energy (>200 channels) and PSD cuts used to separate gamma-ray and neutron events. (b) The timing difference between neutron, gamma-ray, and all events in the EJ-309 scintillator and the RF signal in run 42. The multiple peaks are due to the events in the EJ-309 scintillator being compared to all the RF signals in the same timing window. The gamma-ray events in the EJ-309 scintillator were used to measure the timing characteristics between the EJ-309 scintillator and RF signal via the Compton-scattered gamma-ray flash.**

The data from all the runs were combined to calculate the timing delay and uncertainty, as shown in Figure 4.23. The shape of the timing peak between the gamma-ray events in the EJ-309 scintillator and the RF signal is attributed to the non-uniformity of the deuteron beam from the cyclotron, which likely featured extraction from multiple turns within the cyclotron, as shown in Figure 4.23a. Figure 4.23b plots the combined timing difference between the EJ-309 scintillator and the RF signal from all the runs. The mean of the peak was 31.65 ns, and the FWHM of the peak was 17.052 ns, which equates to a $\sigma$ of 7.24 ns. The distance from the deuteron break up target to the alumina target plus the distance to the center of the EJ-309 scintillator was 8.0935 m, which equates to a gamma-ray time of flight of 27 ns. Therefore, the

timing delay and uncertainty between the EJ-309 scintillator and RF signal is 4.65 ns and 7.24 ns, respectively.

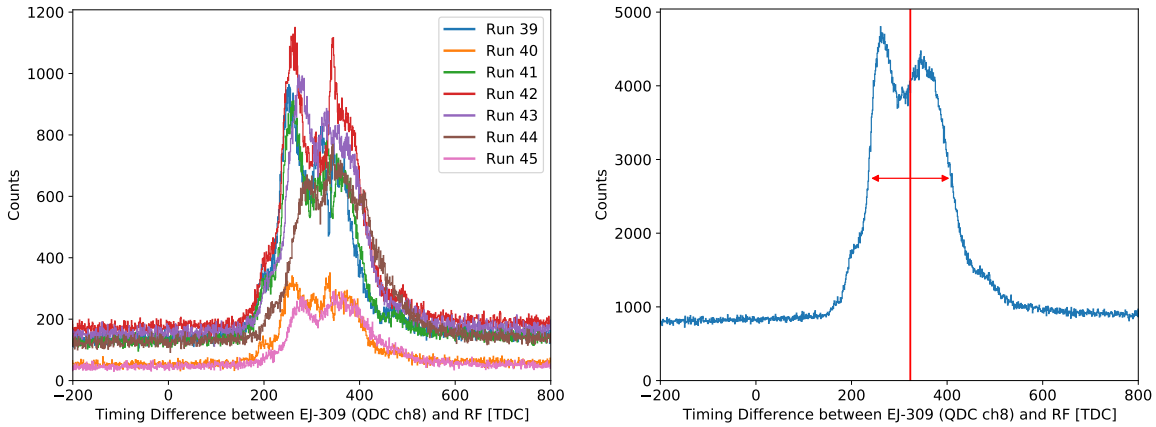


**(a) Timing difference for each run.** **(b) Combined timing difference.**

**Figure 4.23. (a) The timing difference between the gamma-ray events in the EJ-309 scintillator (QDC1 ch 8) and the RF signal (QDC1 ch 33) for (a) each run and (b) combined. The shape of the peak is attributed to the non-uniformity of the deuteron beam pulse from the cyclotron, which was not consistent throughout the experiment. The red lines in (b) indicated the mean and FWHM, which were 323 (31.654 ns) and 174 (17.052 ns), respectively.**

#### 4.3.3.3 HPGe and EJ-309 Timing

The timing delay and uncertainty between the HPGe detectors and EJ-309 scintillator (QDC1 ch8) was measured using the prompt fission gamma-ray emission of a 0.96 µg $^{252}$Cf source located at the target location. All the recorded events in the EJ-309 scintillator were correlated with the events in the HPGe detectors that occurred within the same ∼4,500 ns timing window. The events in the EJ-309 scintillator were separated into gamma-ray and neutrons events using a PSD cut. Figure 4.24a plots the timing difference between neutron, gamma-ray, and all events in the EJ-309 scintillator (QDC1 ch 8) and all events in the HPGe detector (SCP ch 4). The mean and standard deviation of the timing difference was measured by applying a Gaussian distribution fit to the timing difference of the gamma-ray events in the EJ-309 scintillator and HPGe detector, as shown in Figure 4.24b,

which for the EJ-309 scintillator (QDC1 ch8) and HPGe detector (SCP ch4) were 12.40 ns and 5.53 ns, respectively.

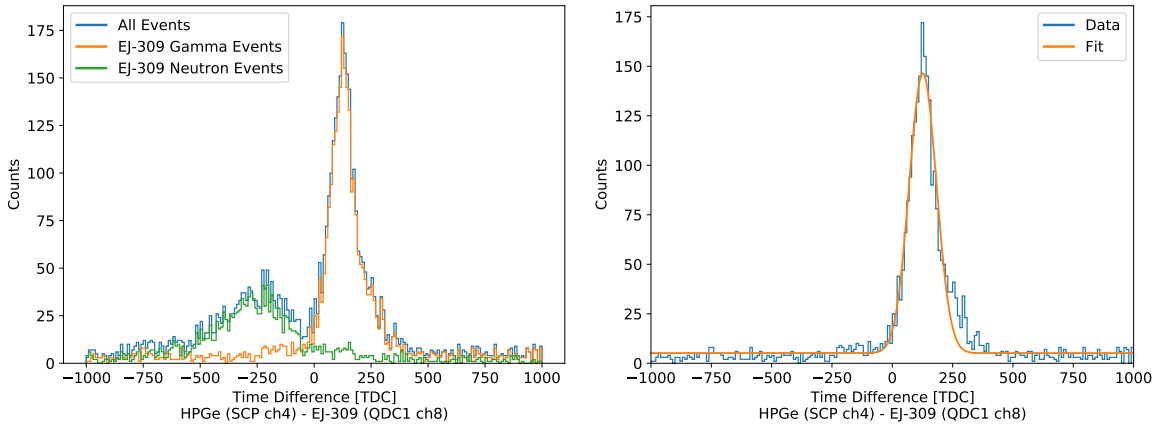


**(a) Timing difference between all, neutron, and gamma-ray events in the EJ-309 and HPGe.**

**(b) Timing difference between gamma-ray events in the EJ-309 and HPGe.**

**Figure 4.24. Timing difference between (a) neutron, gamma-ray, and all events and (b) gamma-ray only events in the EJ-309 scintillator (QDC1 ch 8) and one of the HPGe detectors (SCP ch 4). The timing difference mean and standard deviation were 12.40 ns and 5.53 ns, respectively.**

The gamma-ray times of flight between the target location and the center of the EJ-309 scintillator (QDC1 ch 8) and HPGe detector (SCP ch 4) were 2.65 ns and 0.96 ns, respectively, equating to a real delay of 1.69 ns between the EJ-309 scintillator and HPGe detector. However, in the experiment, the HPGe detector event was recorded after the EJ-309 scintillator event, due to the longer response time of the HPGe detector relative to the EJ-309 scintillator. Therefore, the delay between the EJ-309 scintillator (QDC1 ch 8) and the HPGe detector (SCP ch 4) was -14.09 ns with an uncertainty of 5.53 ns. Table 4.7 lists the timing delay and uncertainty between the HPGe detectors and EJ-309 scintillator (QDC1 ch8). All the HPGe detectors have similar delay and uncertainty, except for Clover 3-3 (ch 11). The difference in Clover 3-3 is due to the integration and differentiation time setting for the timing filter (TF_int_diff) on the MDPP-16 SCP board for channel 11 being accidentally set to 3 instead of 1, which was the setting for all the other HPGe

detectors.

**Table 4.7. Timing delay and uncertainty between the HPGe detectors and EJ-309 scintillator (QDC1 ch 8).**

| Detector | Channel | TF_int_diff | Delay [ns] | Uncertainty [ns] |
|---|---|---|---|---|
| Clover 3-1 | 0 | 1 | -14.13 | 4.78 |
| Clover 3-2 | 1 | 1 | -15.32 | 4.75 |
| Clover 3-3 | 11 | 3 | -67.72 | 11.76 |
| Clover 3-4 | 3 | 1 | -12.08 | 5.19 |
| Clover 4-1 | 4 | 1 | -14.09 | 5.53 |
| Clover 4-2 | 5 | 1 | -14.49 | 5.18 |
| Clover 4-3 | 6 | 1 | -14.68 | 5.53 |
| Clover 4-4 | 7 | 1 | -18.96 | 6.52 |

#### 4.3.3.4 Delay and Uncertainty

The two methods were analyzed to calculate the timing delay and uncertainty between the HPGe detectors and RF signal, as discussed in Section 4.2.5.1. Calculating the timing delay and uncertainty between the HPGe detector (SCP ch 4) and RF signal (QDC1 ch 33) using the first method and Equation 4.2, resulted in a delay and uncertainty of 12.70 ns and 20.09 ns, respectively. In comparison, using the second method and Equations 4.3, 4.4, and 4.5, resulted in a delay and uncertainty of 18.74 ns and 9.11 ns, respectively. Therefore, with the reduction in uncertainty, the second method was used to calculate the timing delay and uncertainty between the HPGe detectors and RF signal, which are listed in Table 4.8. Besides Clover 3-3 (SCP ch 11), which had the different timing setting, the timing uncertainties between the HPGe detectors and RF signal were very similar, with an average of 9.02 ns and standard deviation of 0.34 ns.

**Table 4.8. Timing delay and uncertainty between the HPGe detectors and RF signal (QDC1 ch 33).**

| Detector | Channel | TF_int_diff | Delay [ns] | Uncertainty [ns] |
|---|---|---|---|---|
| Clover 3-1 | 0 | 1 | 18.78 | 8.68 |
| Clover 3-2 | 1 | 1 | 19.97 | 8.66 |
| Clover 3-3 | 11 | 3 | 72.37 | 13.81 |
| Clover 3-4 | 3 | 1 | 16.73 | 8.91 |
| Clover 4-1 | 4 | 1 | 18.74 | 9.11 |
| Clover 4-2 | 5 | 1 | 19.14 | 8.90 |
| Clover 4-3 | 6 | 1 | 19.33 | 9.11 |
| Clover 4-4 | 7 | 1 | 23.61 | 9.74 |

## 4.4 Analysis and Results

The detected gamma-ray spectrum, shown in Figure 4.25 for each of the HPGe detectors from the $^{16}$O experiment, can be binned by the neutron spectrum in the target that created the gamma ray that was subsequently detected by the HPGe detector. The incident neutron energy, $E_n$, was calculated using the neutron time of flight method as

$$E_n = m_n c^2 \left( \frac{1}{\sqrt{1 - \left(\frac{d}{(nToF)c}\right)^2}} - 1 \right), \tag{4.9}$$

where $m_n$ was the neutron mass, $c$ was the speed of light, $d$ was the distance traveled by the neutron, and $nToF$ was the neutron time of flight, which was calculated using Equation 4.1. For the $^{16}$O(n,n') reaction, the most probable gamma-ray emission is 6.129 MeV from the 2$^{\text{nd}}$ excited state.

### 4.4.1 Full Energy Peak

All the runs for each HPGe detector were combined and each event recorded in the HPGe detector was correlated to all the RF signals within the same timing window. After applying the run-dependent energy calibration, the data were cut around the full energy peak to only analyze the events from the 2$^{\text{nd}}$ excited state of $^{16}$O (6.129 MeV),

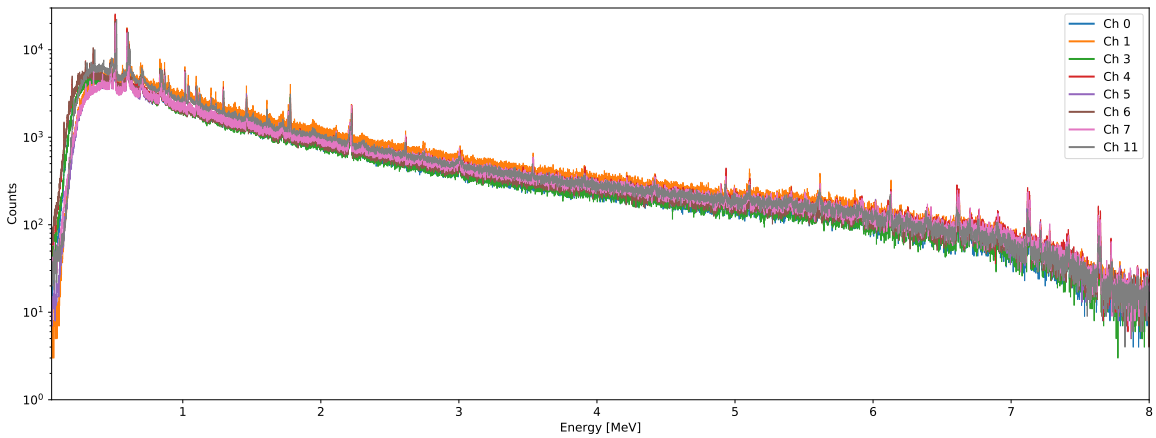


**Figure 4.25. Energy spectra from each of the HPGe detectors from the $^{16}$O experiment (all runs).**

as shown in Figure 4.26.

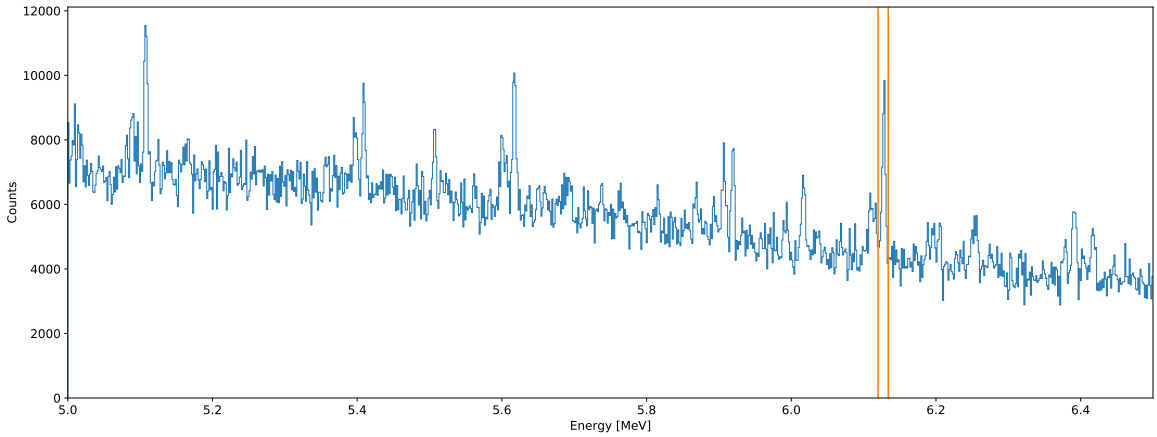


**Figure 4.26. Calibrated HPGe energy spectrum of Clover 4-1 (SCP ch 4) for all runs showing the energy cut on the 6.129 MeV peak (6.120-6.134 MeV) from 2$^{nd}$ excited state of $^{16}$O from the $^{16}$O(n,n') reaction.**

The neutron time of flight, calculated using Equation 4.1 and the timing delay in Table 4.8, was histogrammed with bin edges originating at the 6.542 MeV neutron threshold energy for the $^{16}$O(n,n') 2$^{nd}$ excited state. The time of flight for a 6.542 MeV neutron at 7.3 m is 207.43 ns. The neutron time-of-flight histogram was fit to determine the constant background due to chance coincidence events. Figure 4.27 plots the neutron time-of-flight histogram for the events under the 6.129 MeV peak for HPGe Clover 4-1 (SCP ch 4) along with the fit to calculate the

chance coincidence background. The events in the neutron time-of-flight histogram below 207.43 ns are from the neutrons above 6.542 MeV, which was expected. The events above 207.43 ns, which would indicated reactions below the threshold energy and cannot physically occur, are from the repeated HPGe events that were correlated to the other RF signals within the same timing window (4.5 $\mu$s). These events were discarded after converting the neutron time of flight to neutron energy.

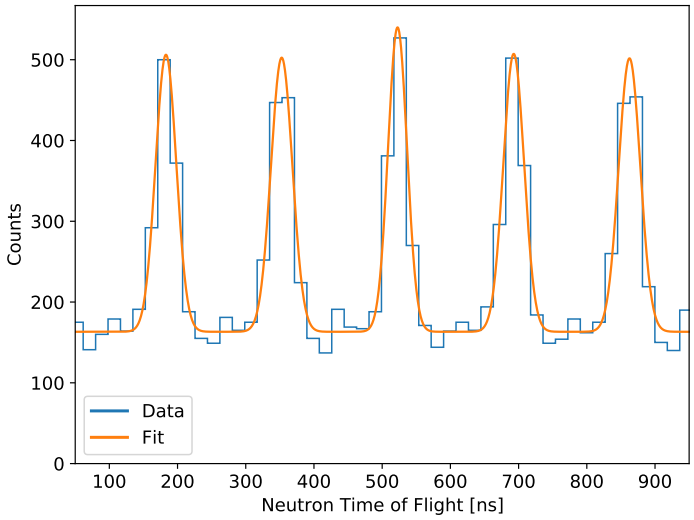


**Figure 4.27. Number of detection events under the 6.129 MeV peak in the HPGe Clover 4-1 (SCP ch 4) as a function of incident neutron time of flight with fit to calculate the chance coincidence background.**

The neutron energy was calculated using Equation 4.9, and the neutron energy bin widths were set at twice the timing uncertainty for each bin. Figure 4.28 plots the number of background-subtracted detection events under the 6.129 MeV peak in the HPGe Clover 4-1 (SCP ch 4) as a function of incident neutron energy.

### 4.4.2 Full and Escape Peaks

To improve the counting statistics, the data were cut around the single and double escape peaks, as well as the full energy peak, for the 2$^{nd}$ excited state of $^{16}$O (6.129 MeV), as shown in Figure 4.29, which tripled the number of events.

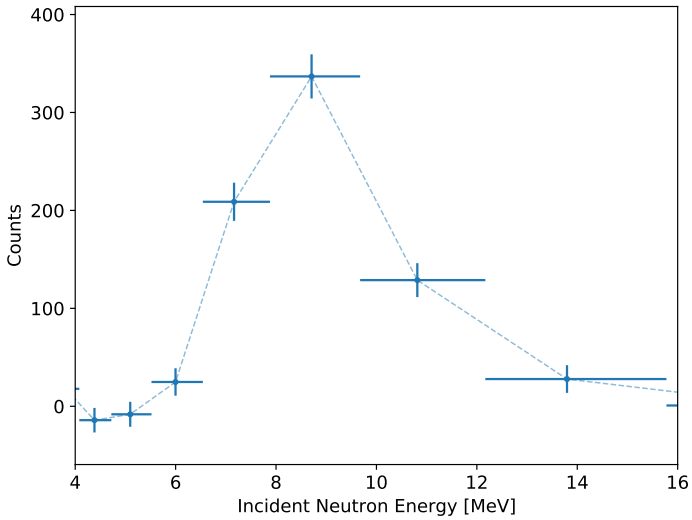


**Figure 4.28. Number of detection events under the 6.129 MeV peak in the HPGe Clover 4-1 (SCP ch 4) as a function of incident neutron energy with the background subtraction.**

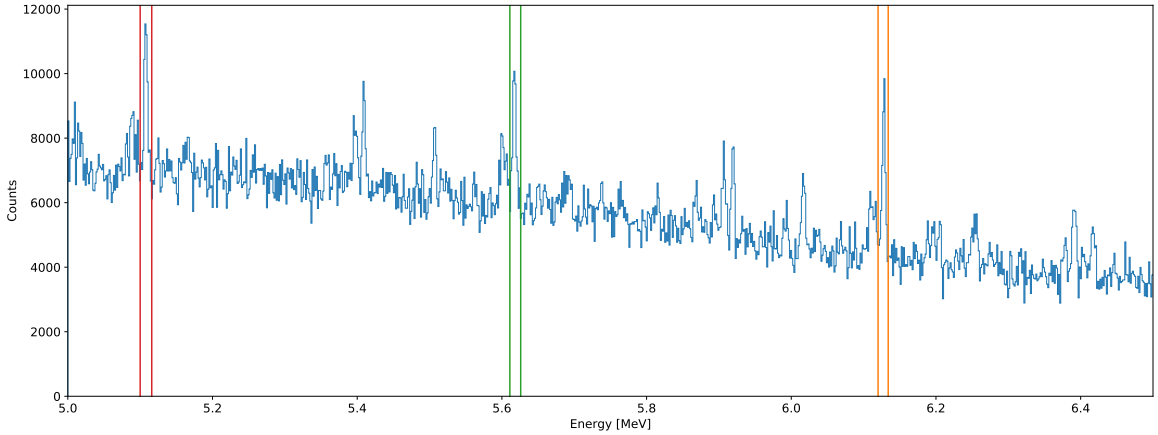


**Figure 4.29. Calibrated HPGe energy spectrum of Clover 4-1 (SCP ch 4) for all runs with the energy cut on the 6.129 MeV peak (6.120-6.134 MeV), single escape peak (5.611-5.626 MeV), and double escape peak (5.100-5.116 MeV) from the 2$^{nd}$ excited state from the $^{16}$O(n,n') reaction.**

The neutron time of flight was calculated and binned as described in Section 4.4.1. Figure 4.30a plots the neutron time-of-flight histogram for the events under the 6.129 MeV peak, single escape peak (5.618 MeV) and double escape peak (5.107 MeV) for HPGe Clover 4-1 (SCP ch 4), and Figure 4.30b plots the neutron time-of-flight for the combined counts from the three peaks along with the fit to calculate the chance coincidence background.

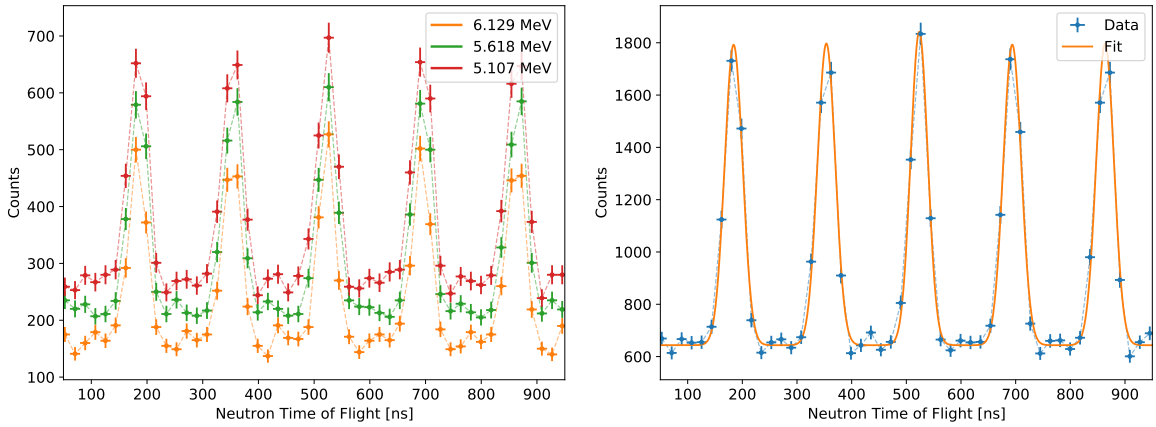


**(a) Individual neutron time-of-flight histograms** **(b) Combined neutron time-of-flight histogram**

**Figure 4.30. (a) Individual and (b) combined neutron time of flight histograms for the events under the 6.129 MeV peak, single escape peak (5.618 MeV), and double escape peak (5.107 MeV) for HPGe Clover 4-1 (ch 4).**

The calculated number of detection events under the 6.129 MeV full energy and escape peaks in the HPGe Clover 4-1 (SCP ch 4) as a function of incident neutron energy with the background subtraction are plotted in Figure 4.31.

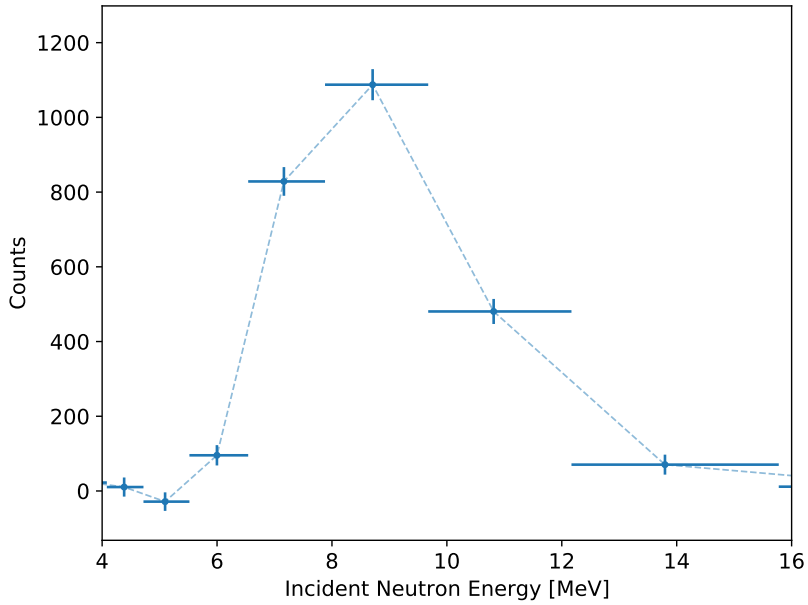


**Figure 4.31. Combined number of background-subtracted detection events under the 6.129 MeV peak, single escape peak (5.618 MeV), and double escape peak (5.107 MeV) in the HPGe Clover 4-1 (SCP ch 4) as a function of incident neutron energy.**

Table 4.9 lists the four energy differential values obtained in this experiment for

each of the detector channels. For comparison, the neutron energy bin widths were set at twice the weighted uncertainty of the timing, which was 9.00 ns.

**Table 4.9. Energy differential values from the 2nd excited state of $^{16}$O (6.129 MeV) obtained in this experiment for each of the detector channels.**

| Energy | Counts | | | | | | |
|---|---|---|---|---|---|---|---|
| Range [MeV] | Ch 0 | Ch 1 | Ch 3 | Ch 4 | Ch 5 | Ch 6 | Ch 7 |
| 6.5 - 7.9 | 503±33 | 904±39 | 537±33 | 818±38 | 523±33 | 522±32 | 559±34 |
| 7.9 - 9.7 | 924±39 | 1371±44 | 810±37 | 1050±41 | 845±37 | 913±38 | 1021±40 |
| 9.7 - 12.1 | 529±33 | 796±37 | 523±33 | 508±33 | 452±32 | 550±33 | 610±34 |
| 12.1 - 15.6 | 167±27 | 249±29 | 177±27 | 83±26 | 92±25 | 95±25 | 123±26 |

#### 4.4.2.1 Complications from $^{16}$O(n,p)$^{16}$N

$^{16}$N created from the $^{16}$O(n,p)$^{16}$N reaction decays back to $^{16}$O via $\beta^-$ decay with a half-life of 7.1 s emitting a 6.129 MeV gamma ray 67% of the time [49]. This could complicate the measurement of the $^{16}$O(n,n') reaction 2nd excited state that also emits a 6.129 MeV gamma ray. However, the higher energy threshold and lower cross section of the $^{16}$O(n,p) reaction compared to the $^{16}$O(n,n') reaction will reduce the probability of the reaction occurring. Furthermore and most importantly, the half life of the $^{16}$N decay is very long, compared to the short duration of the beam period (∼200 ns) and the window in which the $^{16}$O(n,n') reaction is being measured. Over a span of 200 ns, the amount of $^{16}$N decay is only $2 \times 10^{-6}$%, which is considered negligible. Therefore, events from the $^{16}$N decay will contribute to the chance coincidence background and will not affect the $^{16}$O(n,n') measurement.

### 4.4.3 Higher $^{16}$O States

The next excited state in $^{16}$O above 6.129 MeV is at 6.917 MeV, which has a threshold energy ∼7.349 MeV and emits a 6.916 MeV gamma ray 99.97% of the time. Unfortunately, there was not a distinct 6.916 MeV peak above the background,

as shown in Figure 4.32a, which is due to the low cross section, higher threshold energy, and short experimental time.

The following excited state above 6.917 MeV is 7.117 MeV, which has a threshold energy of ∼7.562 MeV and the most probable gamma-ray emission from that state is 7.116 MeV. Unfortunately, the 7.116 MeV gamma ray falls under 7.120 MeV peak, which is the single escape peak from the 7.631 MeV gamma ray from the neutron capture reaction on $^{56}$Fe [160], as shown in Figure 4.32a. Cutting on the 7.120 MeV peak and plotting the neutron time of flight histogram, as shown in Figure 4.32b, shows a uniform background, as compared to Figures 4.27, 4.30a, and 4.30, which indicates almost all the events in the 7.120 MeV peak are from neutron capture on $^{56}$Fe and negligible amount are from $^{16}$O(n,n').

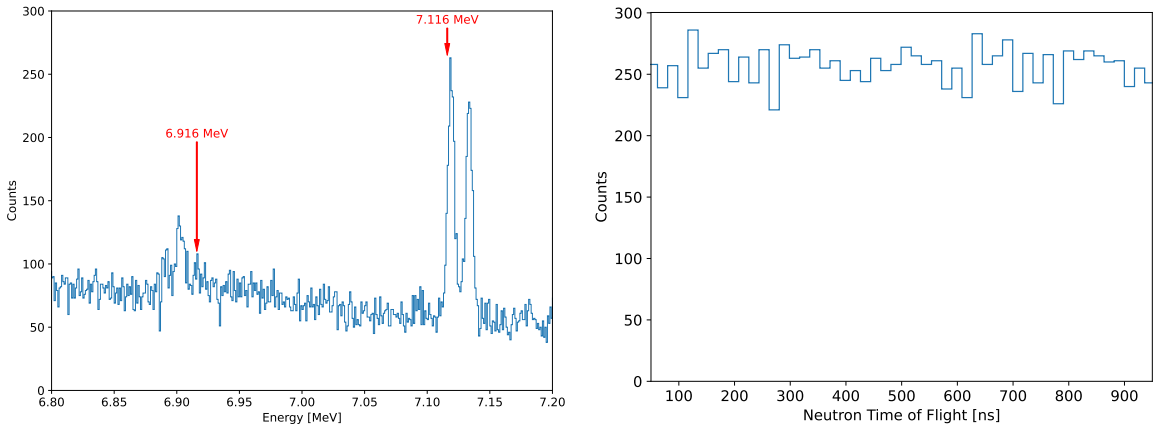


**(a) HPGe Clover 4-1 (SCP ch 4) energy spectrum** **(b) 7.120 MeV peak neutron time-of-flight**

**Figure 4.32. (a) HPGe energy spectrum and (b) neutron time-of-flight histogram for the events under the 7.120 MeV peak (7.108-7.127 MeV energy bin) from Clover 4-1 (SCP ch 4) with all runs combined.**

These results are not surprising given the run conditions of the experiment. The higher energy states require a higher neutron threshold energy and the evaluated cross sections for these higher states are lower than for the second excited state, as shown in Figure 4.5b. Increasing the deuteron energy from 14 to 23 MeV, thereby increasing the energy and intensity of the neutron beam, coupled with longer experimental run

times will allow for measurement of these higher $^{16}$O states and other data products highlighted in 4.1.2 and Sections 4.1.4.

### 4.4.4 Information Needed for Cross Section Measurement

The partial cross section of specific excited state ($E^*$) as a function of neutron energy ($E_n$) is given as

$$\sigma(E^*, E_n) = \frac{R(E^*, E_n)}{I(E_n) N \Delta x}, \tag{4.10}$$

where $R(E^*, E_n)$ is the reaction rate in the target for the specific excited state as a function of neutron energy, $I(E_n)$ is the intensity of the incident neutrons, $N$ is the density of nuclei in the material (nuclei/cm$^3$), and $\Delta x$ is the target thickness.

Above, only the detection rate was presented. To calculate the partial cross section (Section 2.3), the HPGe efficiency is needed to calculate the number of reactions in the alumina target and the incident neutron flux from the beam needs to be properly characterized. The current high-energy efficiency calibration is lacking fidelity and a proposed experiment to improve the calibration and benchmark the GEANT4 GENESIS model was outlined in Section 4.3.2.2. Determination of the incident beam flux is an ongoing effort conducted by another GENESIS researcher.

Once these values are obtained, the number of reactions in the alumina target for a given excited state as a function of incident neutron energy can be calculated as

$$R(E^*, E_n) = \left( \frac{C_P(E_\gamma, E_n)}{\varepsilon_P(E_\gamma)} + \frac{C_{SE}(E_\gamma, E_n)}{\varepsilon_{SE}(E_\gamma)} + \frac{C_{DE}(E_\gamma, E_n)}{\varepsilon_{DE}(E_\gamma)} \right) \frac{1}{I_\gamma(E^*) f_\ell} - BK, \tag{4.11}$$

where $C_P(E_\gamma, E_n)$, $C_{SE}(E_\gamma, E_n)$, and $C_{DE}(E_\gamma, E_n)$ are the number of counts from the primary, single and double escape peaks, respectively, of a specific gamma ray as a function of neutron energy. $\varepsilon_P(E_\gamma)$, $\varepsilon_{SE}(E_\gamma)$, and $\varepsilon_{DE}(E_\gamma)$ are the HPGe detector

efficiencies of the primary, single escape, and double escape peaks, respectively, of a specific gamma ray. $I_\gamma(E^*)$ is the intensity of the gamma ray from the excited state, $f_\ell$ is the live-time of the HPGe detector, and $BK$ is the chance coincidence background.

## 4.5 Conclusion

There is a need to experimentally measure the inelastic scattering neutron cross section of $^{16}$O at a wide range of neutron energies to provide more accurate data and fill gaps of missing cross-section data. The new GENESIS capability at the 88-Inch Cyclotron in Lawrence-Berkeley National Laboratory was designed to measure neutron inelastic scattered cross sections using a array of high-resolution HPGe clover detectors to measure the gamma rays from the excited target nuclei and 26 EJ-309 liquid organic scintillators to measure the inelastically scattered neutrons. When taken in coincidence, the GENESIS detector array can measure the partial double differential cross section. This work helped develop, improve, and characterize the GENESIS capability and developed the code and algorithms to process the GENESIS data to support these measurements.

A preliminary and scoping experiment was conducted on $^{16}$O by placing an alumina ($Al_2O_3$) target in the neutron beam generated from 14 MeV deuterons breaking up on a carbon target. The analyses of the data from the ∼6 hour run was successful in calculating the number of counts in the HPGe clover detectors from the 2$^{nd}$ excited state of $^{16}$O using the 6.129 MeV full energy and escape peaks. To calculate the partial cross section of the 2$^{nd}$ excited state, the HPGe detector efficiency at high energies (>6 MeV) and characterization of the incident neutron beam is needed: efforts to study both of these quantities are currently in progress. Additionally, the limited experimental time and low energy neutron beam prevented

the analyses of higher $^{16}$O states and outgoing neutron coincidence data.

## 4.6 Current and Future Work

Current work continues to measure and calibrate the efficiency of the HPGe detectors at higher energies and characterize the incident neutron beam using the sToF system, both of which are needed to calculate the cross section. The next experiment with $^{16}$O will be conducted over a few days and with 23 MeV deuterons, enabling the measurement of higher energy states of $^{16}$O and outgoing neutron coincidence data. Additionally, the BGO shields from the HPGe clover detectors will be removed to reduce the number of $^{16}$O inelastically scattered neutron events outside of the $^{16}$O target. In addition to the $^{16}$O(n,n') measurement, the longer run time and higher energy neutron beam will possibly enable the measurement of the partial cross section for other reactions, such as $^{27}$Al(n,p)$^{27}$Mg, $^{16}$O(n,$\alpha$)$^{13}$C, $^{27}$Al(n,d)$^{26}$Mg, $^{16}$O(n,n+$\alpha$)$^{12}$C, $^{27}$Al(n,n+p)$^{26}$Mg, $^{16}$O(n,p)$^{16}$N, and $^{16}$O(n,d)$^{15}$N.

# V. Fast-, Light-Cured Scintillating Plastic

This chapter was derived from a manuscript submitted on 3 Jan 2022 with *Nuclear Instruments and Methods in Physics Research Section A: Accelerators, Spectrometers, Detectors and Associated Equipment* titled "Fast-, Light-Cured Scintillating Plastic for 3D-Printing Applications." The author list included Brian G. Frandsen, Michael Febbraro, Thomas Ruland, Theodore W. Stephens, James E. Bevins, Juan J. Manfredi, and Paul A. Hausladen. The article has been modified to fit this dissertation format; however, the content was unchanged.

## 5.1 Abstract

Additive manufacturing techniques enable a wide range of possibilities for novel radiation detectors spanning simple to highly complex geometries, multi-material composites, and metamaterials that are either impossible or cost prohibitive to produce using conventional methods. The present work identifies a set of promising formulations of photocurable scintillator resins capable of neutron-gamma pulse shape discrimination (PSD) to support additive manufacturing of fast neutron detectors. The development of these resins utilized a step-by-step, trial-and-error approach to identify different monomer and cross linker combinations that meet the requirements for 3D printing followed by a 2-level factorial parameter study to optimize the radiation detection performance, including light yield, PSD, optical clarity, and hardness. The formulations resulted in hard, clear, PSD-capable plastic scintillators that were cured solid within 10 seconds using 405 nm light. The best performing scintillator produced a light yield 83% of EJ-276 and a pulse shape discrimination figure of merit equaling 1.28 at 450-550 keVee.

## 5.2 Introduction

Plastic scintillators are among the most commonly used radiation detection materials used due to their low costs, ease of fabrication, fast response time, and ability to distinguish between neutron and gamma-ray interactions [30–38]. Application of additive manufacturing (AM) techniques to plastic scintillators offers the potential for new and exciting uses. For instance, 3D printing allows for the fabrication of complex geometries and multi-material composites that are either impossible or cost prohibitive to produce using conventional methods.

Successful 3D printing of plastic scintillators requires development of a printing process as well as suitable feedstock material that is similar in cost to a conventional scintillator and has mechanical, chemical, and optical properties suitable for the 3D printing process. The combination of the feedstock and printing process will need to result in printed parts having mechanical, optical, and scintillation (light yield and pulse shape discrimination, or PSD) performance near or exceeding that of conventional plastic scintillators.

There are a wide range of 3D printing methods available, including filament-based methods such as fusion deposition modeling (also called fused filament fabrication), powder-based laser sintering, and light-based resin curing. Of the common 3D printing methods, light-based methods — that is, methods based on photopolymerization of a liquid resin — such as stereolithography (SLA) and digital light processing (DLP) offer the best optical clarity. A few researchers have developed formulations of scintillating resins that either have or can be used in light-based 3D printers, but the light yield of these scintillators was low (∼35% of commercially available plastic scintillators) [39–41] and PSD was not reported. Other recent research reported a DLP 3D printed scintillator with light yield up to 67% of BC408 plastic scintillator. This formulation used BPA(EO)15DMA as the

primary solvent, 1-methyl-naphthalene as the secondary solvent, PPO as the primary dye, ADS086BE as the wavelength shifter, and TPO as the photoinitiator [42, 43]. However, like the other light-based, 3D-printable formulations, PSD performance was not reported. A novel, light-cured, PSD plastic scintillator was recently reported in [161], but the required cure time of tens of minutes makes its use in 3D printing impractical.

This work reports significant advances in the development of a light-based, PSD-capable plastic scintillator formulation that cures in seconds using industry-standard 405 nm light and is suitable for 3D printing of radiation detectors. In particular, this work reports the development of the fast-curing formulation, the material properties and radiation detection performance of the resulting light-cured scintillators, a parametrically optimized formulation, and an initial aging study.

## 5.3 Materials and Methods

### 5.3.1 Scintillator Development

The goal of this work was to create a mechanically hard, optically clear 3D printable PSD plastic scintillator with light output comparable to commercially-available PSD plastic scintillators, i.e. EJ-276. The formulation of the resin was based on five basic components; a monomer, a crosslinker, a photo-initiator to induce photopolymerization, and a primary and secondary fluorescent dye to produce light from radiation excitation. Several compounds were evaluated as part of the formulation development for each component.

In developing a 3D printable scintillator resin, the monomer forms the base of the resin and is the largest component by mass. The monomer needs to have good optical clarity at the scintillation wavelength, exhibit high solubility for fluorescent

dyes, and not lead to quenching of the scintillation light. Monomers, such as vinyltoluene or styrene, which are primarily used in plastic scintillators [34, 38], were found to exhibit low reactivity during photopolymerization [162]. Attempts to use these types of monomers resulted in cure times of >30 mins to multiple hours, which is not acceptable for 3D printing applications. Methacrylate and acrylate compounds exhibited much higher reactivity, on the order of 10s of seconds, which is suitable for 3D printing applications. Attempts to find a off-the-shelf aromatic methacrylate or acrylate were unsuccessful. Compounds such as ethylene glycol phenyl ether acrylate or phenyl acrylate resulted in either poor hardness making mechanical polishing difficult or poor light yield. In lieu of a suitable aromatic methacrylate, or acrylate monomer, the compound isobornyl acrylate (IBOA) was chosen due to its optical clarity, low cost, high boiling point, and high glass transition temperature. For this work, ≥85% technical-grade IBOA from Sigma-Aldrich with 200 ppm monomethyl ether hydroquinone inhibitor was used [163].

Crosslinkers are needed to increase hardness and decrease the gel time of the photocured resins. Multiple cross linkers were tested during this work such as difunctionized 1,6-hexanediol dimethacrylate (HDDMA), bisphenol-A dimethacrylate (BPADMA), divinylbenzene (DVB), and tetrafunctionized cross linkers such as pentaerythritol tetraacrylate (PETA) [164–167]. The HDDMA was ≥90% pure and contained 100 ppm hydroquinone as an inhibitor, BPADMA was >98% pure with no inhibitor, PETA contained 350 ppm monomethyl ether hydroquinone as inhibitor, and DVB was 80% pure. The photo-initiator used to start the polymerization from incident 405 nm light was diphenyl (2,4,6-trimethylbenzoyl) phosphine oxide (TPO) from Sigma-Aldrich, which was 97% pure [168]. All compounds were used as received.

For the production of light yield in the plastic scintillators, the fluors tested were EJ-309 [67,103,169–173], diisopropyl naphthalene (DIN) from Eljen Technology (base EJ-309 solvent with no fluors), and 2,5-diphenyloxazole (PPO) from Sigma-Aldrich, which was scintillation grade and 99% pure [174]. 1,4-Bis(2-methylstyryl)benzene (Bis-MSB) from Sigma-Aldrich, diphenyl stilbene (DPS) from Luxottica Exciton, and Exalite 416 from Luxottica Exciton were evaluated as wavelength shifters [175–177].

The compounds for the desired formulation to be tested were weighed and placed into a 28×57 mm (20 mL) reaction vial. The compounds were thoroughly mixed together using an alternating combination of a ultra sonic bath and hot plate to gently warm the mixture. To reduce oxygen-induced quenching, the reaction vial was transferred to a glove box pressurized with a nitrogen atmosphere ($<$ 0.1 ppm $O_2$ and $<$ 1 ppm $H_2O$). Dissolved oxygen was removed by sparging with nitrogen for 10 min, and the reaction vial was sealed before removal from the glove box. During this process, care was taken to minimize exposure to ambient light. Finally, the resin solution was cured using a commercially-available 405 nm Formlabs Form Cure and Dymax BlueWave AX-550 VisiCure [178, 179].

In the formulation development and preliminary light output experiments conducted at ORNL, it was observed that the obtained light yield was dependent on the curing parameters. To understand the effects of light yield as a function of the total curing dose and ensure the curing process resulted in a scintillator with the maximum light yield, a formulation representative of the final samples (AFIT130) was placed in a glass cuvette and cured in the Formlabs Form Cure for 5 mins and Dymax BlueWave AX-550 VisiCure for 4 mins. At periodic intervals during the curing process, the cuvette was removed from the Form Cure or BlueWave and placed in a Horiba FluoroMax Plus to measure the emission spectrum of the scintillator while being excited at 350 and 380 nm, asynchronously. Figure 5.1a

plots the emission spectrum of the plastic scintillator at the different integrated curing times from the excitation wavelength of 380 nm. Figure 5.1b plots the intensity of the peak emission as a function of time during the curing process for 380 nm excitation light. The light emission from the scintillator first decreased during the first minute of curing in the Form Cure, then increased during the remaining duration of the curing process in the Form Cure and BlueWave. The 4-minute curing in the BlueWave increased the peak emission by 55% and 79% for the 350 and 380 nm, respectively, compared to a 5-minute cure in the Form Cure alone. The increase in the light yield output was attributed to increased TPO burn up as the samples were solid after ∼10-20 sec.

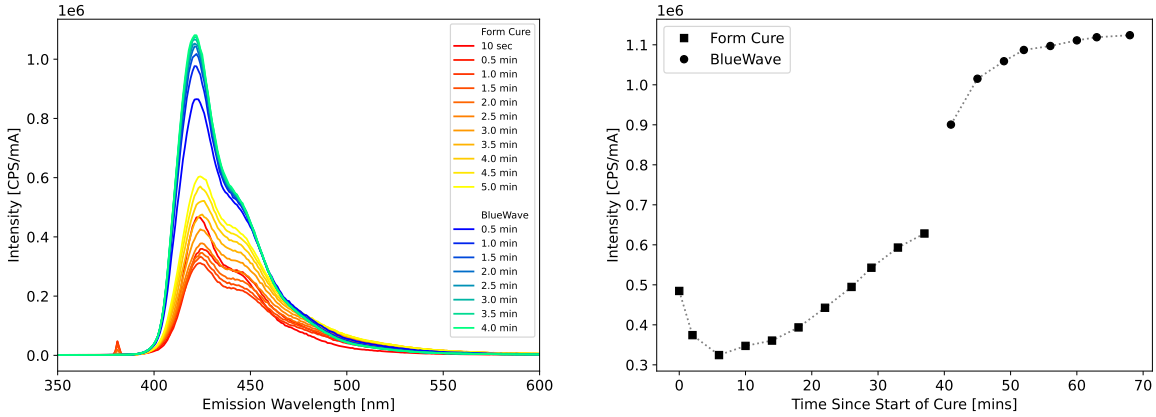


**(a) Emission spectra** **(b) Peak emission intensity**

**Figure 5.1. Light emission (a) spectra and (b) peak intensity of AFIT130 excited with 380 nm light as a function of integrated curing times in the Formlabs Form Cure and Dymax BlueWave AX-550 VisiCure.**

After a curing procedure of 5 minutes in the Form Cure and 4 minutes in the BlueWave, the peak emission was seen to plateau, indicating the maximum light yield was obtained. This process was used to create all reported scintillator results, with variations in the curing sequence explored to improve the mechanical hardness and optical properties of the scintillator, as reported in subsequent sections.

### 5.3.2 Scintillator Characterization

For each scintillator, the hardness of the plastic scintillators was measured using a Shore A durometer. For the curing studies, the light emission spectrum of the scintillators was measured by a Horiba FluoroMax Plus [180].

The relative light yield and PSD figure of merit (FoM) were measured for each scintillator. For the scintillators that leached (see Section 5.5.1.2 for details), the hazy film was cleaned off using mild soap and water before the measurements. Each scintillator was wrapped with two layers of MIL-T-27730A PTFE tape and coupled to a 2" Hamamatsu R7724 PMT biased at -1050 V [181]. The signal was processed using CAEN CoMPASS software on a CAEN DT5730, a 500 MS/s, 14-bit waveform digitizer with the DPP-PSD firmware for pulse integration and PSD [182, 183]. Figure 5.2 plots an example neutron and gamma-ray waveform from the AFIT101 plastic scintillator formulation as recorded by the digitizer. The pulse shape is similar to that of other organic scintillators.

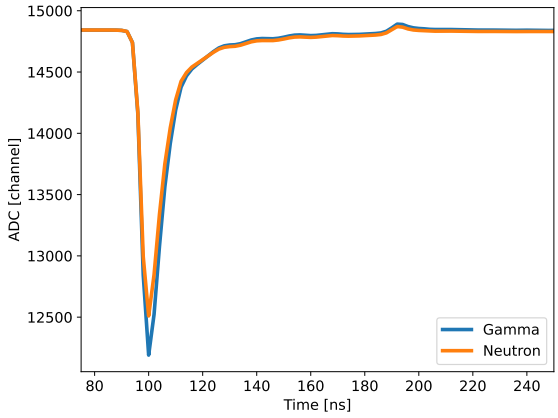


**Figure 5.2. Example recorded waveforms for a neutron (orange) and gamma-ray (blue) event in AFIT101 using a Caen DT5730 digitizer. Each waveform is the average from all the pulses between 0.9-1.1 MeVee and a PSD of 0.10-0.14 for gamma rays and 0.19-0.23 for neutrons.**

The relative light yield of the scintillators was compared to EJ-276 [184] and measured using the Compton edges from the 0.511 MeV and 1.275 MeV $^{22}$Na gamma

rays and the 0.662 MeV $^{137}$Cs gamma ray. The EJ-276 plastic scintillator was a bare 1" diameter x 1" long right circular cylinder, dated 30 October 2020 from the manufacturer, which has known aging degradation [38, 173, 185]. It was removed from its nitrogen-environment shipping container on 26 April 2021 for its first use in measurements.

The Compton edge location in the recorded spectrum was determined by fitting a half-Gaussian distribution to the edge as shown in Figure 5.3 for the $^{22}$Na 0.511 MeV gamma ray in EJ-276. The Compton edge, which was used for comparing the relative light yield between scintillators, was calculated as

$$CE = \mu + \sigma\sqrt{2\ln 2}, \tag{5.1}$$

where $\mu$ and $\sigma$ are the mean and standard deviation of the Gaussian distribution [186]. For each scintillator, including EJ-276, the average and standard deviation of each of the three Compton edges was calculated from multiple measurements of each scintillator. The relative light yield was then calculated as the ratio of the average Compton edge for each scintillator to EJ-276 for each of the three Compton edges. The reported relative light yield is an average of the three relative light yields obtained for each scintillator for the three Compton edges measured.

Second, neutron and gamma-ray induced events were discriminated using waveform charge integration PSD as shown in Figure 5.4a [169]. After calibrating the energy of the spectrum using the Compton edges from the 0.511 MeV, 0.662 MeV, and 1.275 MeV gamma rays, a PSD histogram was generated from the events between 450 and 550 keVee. The histogram was then fit with two Gaussians, shown in Figure 5.4b, and the quality of the PSD was quantified using a FoM given as [169]

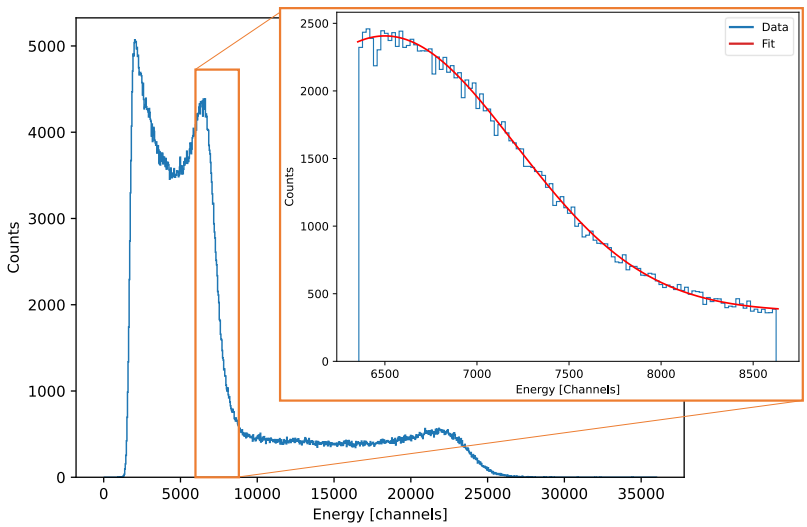


**Figure 5.3. An example $^{22}$Na pulse integral spectrum from EJ-276 illustrating the half-Gaussian fit to the 0.511 MeV gamma-ray Compton edge.**

$$FoM = \frac{\mu_2 - \mu_1}{\mathrm{FWHM}_2 + \mathrm{FWHM}_1}, \tag{5.2}$$

where $\mu$ and $FWHM$ are the mean and full-width, half-max for each of the Gaussian distributions, respectively. For each waveform, the pretrigger was set to 48 samples (96 ns), and the baseline was calculated using the first 40 samples (80 ns). The long gate was set to 400 ns, and the short gate was varied to optimize the PSD FoM for each scintillator. The short gate averaged approximately 23 samples (46 ns). Both the long and short gate began immediately after the 40 sample baseline window.

## 5.4 Formulation Development

### 5.4.1 Exploratory Studies

A step-by-step, trial-and-error approach was taken to identify promising combinations to achieve a formulation that would create a mechanically hard, optically clear plastic with high light output and neutron/gamma-ray discrimination. While not an exhaustive search of the parameter space, the series of

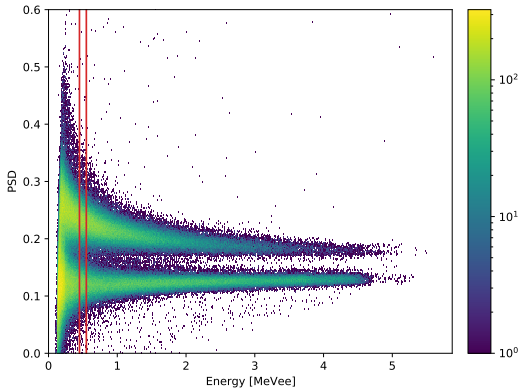


(a) 2D AmBe PSD/energy histogram from AFIT101

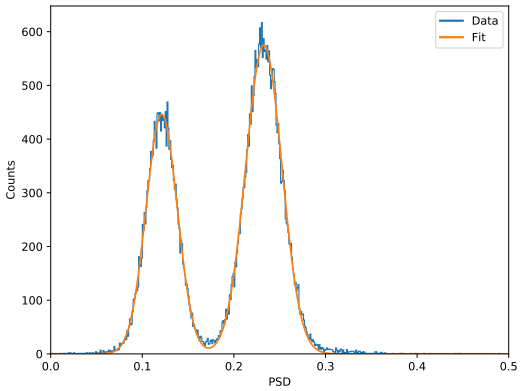


(b) 1D AmBe PSD histogram from AFIT101

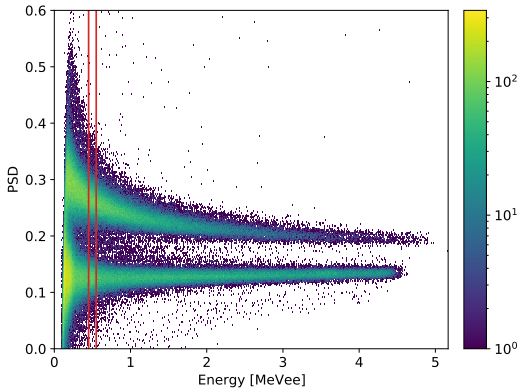


(c) 2D AmBe PSD/energy histogram from EJ-276

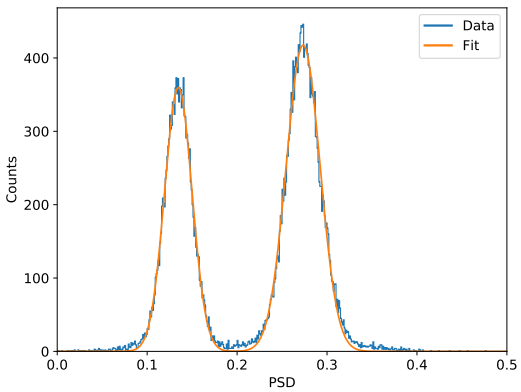


(d) 1D AmBe PSD histogram from EJ-276

**Figure 5.4. 2D PSD/energy histogram from exposing (a) AFIT101 and (c) EJ-276 to an AmBe source. A cut was made over the 450 and 550 keVee range, represented by the red lines, to generate a 1D AmBe PSD histogram where a double Gaussian fit was used to calculate the PSD FoM according to Equation 5.2 for (b) AFIT101 and (d) EJ-276. The visual comparison highlights the first reported PSD results for a fast-, light-cured scintillator capable of 3D printing on par with commercial plastic scintillators.**

small studies detailed below led to a promising general formulation that was then parametrically optimized as described in Section 5.4.2. All samples were approximately 10 g and each was given a name in the format "AFITXXX" in order to track the various formulations.

The first study explored the compatibility of different wave shifters with the 405 nm cure light. Three samples were created with 0.2 wt% of Bis-MSB, Exalite 416, and DPS. The other chemicals in the scintillators, kept constant for all three, included 59.5% IBOA, 25.5% BPADMA (85 wt% total and a 70/30 ratio of IBOA

to BPADMA), 15 wt% PPO, and 0.1 wt% TPO. The DPS did not dissolve into solution. The Bis-MSB and Exalite 416 formulations were cured for 1 min in the Form Cure; each one was solid after 10 sec exposure. On further investigation, it was found that the scintillator with Bis-MSB was solid throughout but softer in the center than on the outside, while the Exalite 416 formulation was consistently hard throughout. It was determined that the Bis-MSB had a higher absorption at 405 nm, shown in Figure 5.5, which was preventing the light from penetrating the entire depth of the resin preventing a complete cure. Therefore, Exalite 416 was selected as the wave shifter for all future formulations.

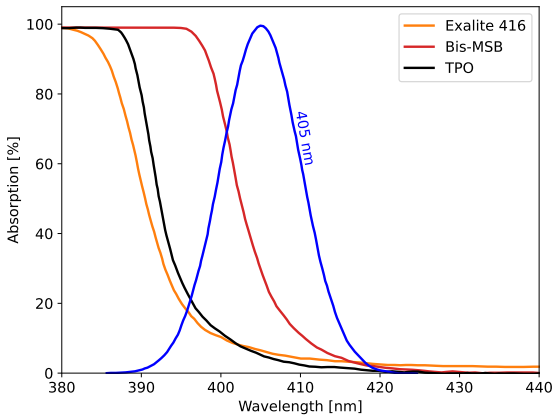


**Figure 5.5. The light absorption of the secondary dyes, Exalite 416 (orange) and Bis-MSB (red), and of the photoinitiator, TPO (black), compared to the emission spectrum of the 405 nm cure light (blue).**

Both the Bis-MSB and Exalite 416 scintillators were cloudy, which was attributed to the high amount of crosslinker used in the initial formulation. Therefore, the next step was to reduce the amount of BPADMA to create an optically clear plastic while maintaining the overall hardness of the plastic. The amount of PPO (15 wt%), Exalite 416 (0.2 wt%), and TPO (0.1 wt%) remained the same as used previously, but the BPADMA was reduced to 10 wt% and IBOA was increased to 75 wt%. After curing the scintillator for 1 min (30 sec to become solid), the scintillator was clearer than before, but still cloudy. Reduced crosslinker had

previously been observed to result in soft, gummy-like cures indicating that an alternative should be explored. Additionally, qualitative light yield studies showed a relatively low light yield indicating that increased fluor should be explored.

In the next step, the ratio of plastic-forming to light-yielding compounds was switched to 60/40 and 30 wt% EJ-309 was used with 10 wt% PPO to increase the light output of the scintillator Also, the solid BPADMA was replaced with liquid HDDMA to explore formulations that lead to a clearer plastic, since the liquid HDDMA better dissolved and did not precipitate out of solution. Three formulations with different IBOA/HDDMA ratios (70/30, 60/40, and 50/50) were explored. The formulations with the 60/40 and 50/50 IBOA/HDDMA ratios were too cloudy, similar to previous results. The formulation the with 70/30 IBOA/HDDMA ratio was clear but too soft, similar to a hard rubber. PETA and DVB crosslinkers were also tried but did not provide better results than HDDMA or BPADMA. Additionally, all attempts to use DVB or any vinyl monomer significantly increase the required cure time.

Therefore, an IBOA/HDDMA ratio of 70/30 was used for future formulations, and variations were made to improve the hardness and radiation detection performance. First, the amount of EJ-309 and PPO was reduced from the 60/40 plastic-forming to light-yielding ratio used in AFIT013 to allow more IBOA and HDDMA to improve the hardness of the plastic. Two additional formulations, AFIT016 and AFIT017, respectively, were developed with 20 wt% (70 wt% IBOA and HDDMA) and 10 wt% (80 wt% IBOA and HDDMA) EJ-309, while the amount of PPO was held constant at 10 wt%. The Exalite 416 and TPO were held the same at 0.2 wt% and 0.1 wt%, respectively. Second, the amount of Exalite 416 was doubled from 0.2 wt% (AFIT017) to 0.4 wt% (AFIT022). Third, an approximately 50/50 ratio of HDDMA and BPADMA was tested as the crosslinker. This resulted in five clear and hard plastic scintillators; their chemical compositions are listed in

Table 5.1. Each of these were cured for 4-5 min in a Formlabs Form Cure, cured for 1 min in the Dymax BlueWave AX-550 VisiCure, and were then sanded and polished using 180 grit, 400 grit, 1000 grit, and 2000 grit sand paper, and a 300 nm alumina slurry.

**Table 5.1. Scintillator chemical composition compounds by mass percent (nominal).**

| | Component Fraction in Scintillator [wt%] | | | | | | |
|---|---|---|---|---|---|---|---|
| **Scintillator** | **EJ-309** | **PPO** | **Exalite** | **IBOA** | **HDDMA** | **BPADMA** | **TPO** |
| AFIT013 | 30 | 10 | 0.2 | 36 | 24 | 0 | 0.1 |
| AFIT016 | 20 | 10 | 0.2 | 49 | 21 | 0 | 0.1 |
| AFIT017 | 10 | 10 | 0.2 | 56 | 24 | 0 | 0.1 |
| AFIT022 | 20 | 10 | 0.4 | 49 | 21 | 0 | 0.1 |
| AFIT023 | 20 | 10 | 0.2 | 49 | 11 | 10 | 0.1 |

The hardness of the scintillators was measured, and any defects, such as leaching and surface cracking, were noted. The results are presented in Table 5.2. An increase in the plastic-forming compounds to 80 wt% (AFIT017) and the addition of the BPADMA crosslinker (AFIT023) resulted in scintillators that were harder than the baseline 60/40 ratio for plastic-forming to light-yielding compounds (AFIT013).

**Table 5.2. Performance characterization for the scintillators in Table 5.1.**

| **Scintillator** | **Shore A Hardness** | **Surface Cracking** | **Leaching** | **Relative Light Yield [%]** | **PSD FoM** |
|---|---|---|---|---|---|
| AFIT013 | 88 | Yes | No | 63.85 | 1.07 |
| AFIT016 | 86 | Yes | No | 63.43 | 0.89 |
| AFIT017 | 93 | No | No | 57.97 | 0.74 |
| AFIT022 | 87 | Yes | No | 65.29 | 0.91 |
| AFIT023 | 93 | No | No | 62.39 | 0.92 |

The radiation detection performance of these scintillators demonstrated reasonable light yield (up to 65% of EJ-276) and PSD (up to a FoM of 1.07). The full results for the nine scintillators are listed in Table 5.2. It was observed that increasing the PPO and EJ-309 above a combined total of 30 wt% (AFIT013) did

not provide more light yield, attributable to the scintillator's reduced clarity, but it did improve the PSD performance. However, a reduction to 20 wt% of light-yielding compounds did result in an ∼5% reduction in light yield and a ∼16% reduction in PSD performance. Doubling the amount of Exalite 416 (AFIT022 vs. AFIT023) only slightly increased the light yield. Finally, the addition of BPADMA with HDDMA (AFIT016 vs. AFIT023) resulted in similar light yield and PSD performance. While it was observed that the scintillator with an 80/20 ratio of plastic-forming to light-yielding compounds was the clearest and hardest, the reduced EJ-309 and PPO resulted in relatively low light yield and PSD FoM. Thus, a 70/30 ratio was carried forward.

### 5.4.2 Two-Level Factorial Parameter Study

The initial formulation development was successful in creating an optically clear and mechanically hard plastic with acceptable light yield and PSD. A two-level factorial parameter study of the fluors (DIN and PPO) and crosslinkers (HDDMA and BPADMA) was developed to analyze the effects of increasing the BPADMA crosslinker and PPO to hopefully find the optimal formulation to prevent leaching and allow the highest light yield output. One level inversely varied the amount of PPO and DIN, which replaced the EJ-309 from the initial formulation development, while maintaining the combined PPO and DIN contribution at 30 wt% of the mass of the scintillator. The other level inversely varied the amount of HDDMA and BPADMA from 0 to 21 wt%, maintaining the combined mass of IBOA and crosslinker at 70 wt% and the IBOA to crosslinker ratio of 70/30. The remaining chemicals were the same for each of the scintillators: IBOA was 49 wt%, Exalite 416 was 0.2 wt%, and TPO was 0.1 wt%. This resulted in thirteen scintillators developed with the same general procedures described in Section 5.3.1. The

scintillators were cured for 5 min in a Formlabs Form Cure (solid in 10-20 sec) followed by 4 min in the Dymax BlueWave AX-550 VisiCure. Each one was sanded and polished using 180 grit, 400 grit, 1000 grit, 2000 grit sand paper and 300 nm alumina slurry.

## 5.5 Results

### 5.5.1 Observational Characterization

The observational characterization of the scintillators developed as part of the parameter study included the measuring the hardness of the scintillators and visual observations of purpling, leaching, surface cracking, and reduced clarity. The hardness, surface cracking, and leaching results are shown in Figure 5.6, along with the two-factor formulation matrix utilized for this parameter study. A clear trend is seen with higher PPO concentrations leading to increased leaching and reduced surface cracking.

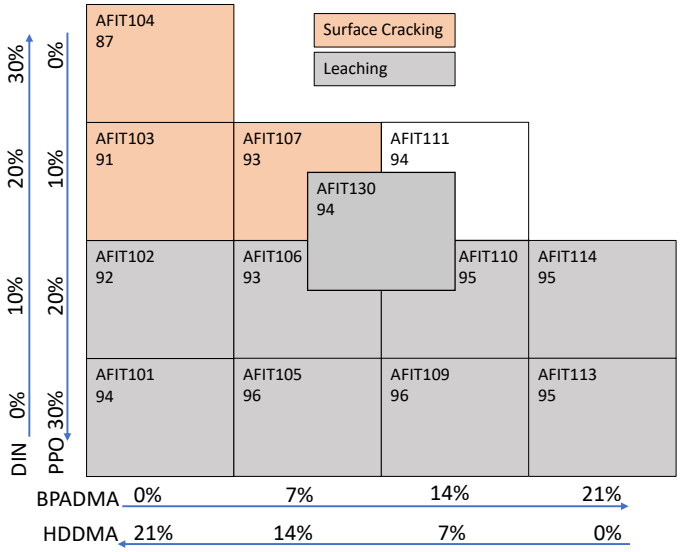


**Figure 5.6. Shore A hardness (indicated by the value within each box), surface cracking, and leaching from the scintillators in the parameter study. A clear trend is seen with higher PPO concentrations leading to increased leaching and reduced surface cracking.**

#### 5.5.1.1 Purpling

It was observed that some of the scintillators became purple upon exposure to the cure light. The purple color intensity and duration increased with the amount of PPO, as shown in Figure 5.7 of AFIT025 and AFIT026, which contained 20 wt% and 25 wt% PPO, respectively. This purple color did dissipate with time, with the decay time on the order of minutes to a few weeks. The decay time for the purpling to dissipate was seen to increase for increasing PPO concentration and increasing BPADMA concentration, as illustrated in Figure 5.7, where the purple color in AFIT113 (21 wt% BPADMA) can still be seen after 3 weeks.

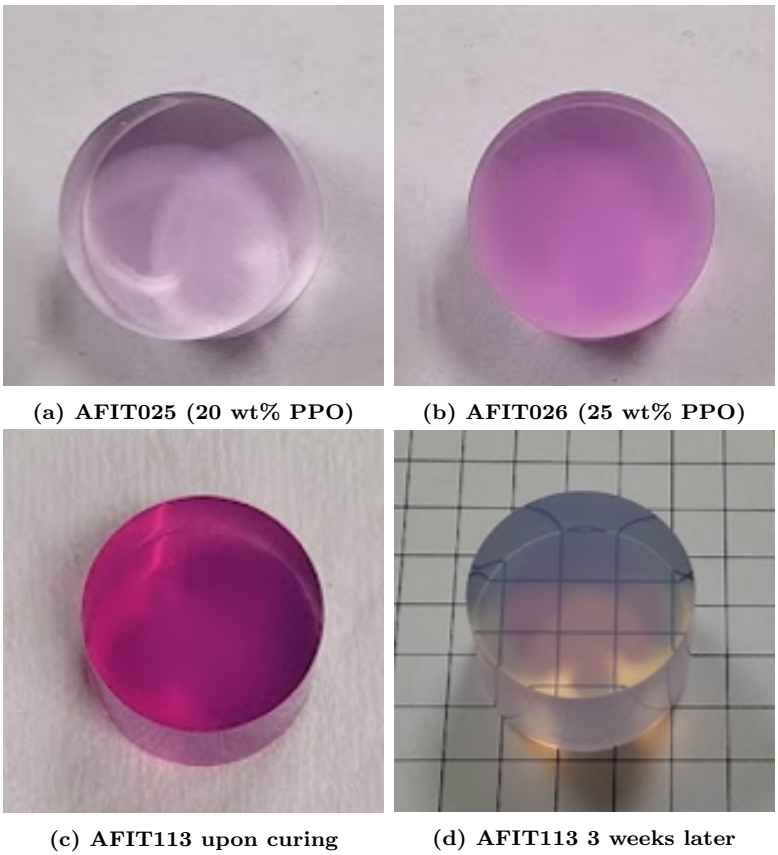

**(a) AFIT025 (20 wt% PPO)** **(b) AFIT026 (25 wt% PPO)**

**(c) AFIT113 upon curing** **(d) AFIT113 3 weeks later**

**Figure 5.7. The intensity of the purple color observed increased with increased PPO concentration as illustrated by (a) AFIT025 (20 wt% PPO) and (b) AFIT026 (25 wt% PPO). The duration of the purpling varied based on the PPO and BPADMA concentration as illustrated in (c) AFIT113 (30 wt% PPO and 21 wt% BPADMA) shortly after being cured and (d) 3 weeks after being cured.**

The direct cause of the purpling effect was not determined, but it appears to be related to an interaction between PPO and TPO. Methods to accelerate the dissipation were explored, the most promising being a heat treatment. To test this treatment, three scintillators were made with the same formulation as AFIT101. One was placed in a 4° C refrigerator, one was left on the counter at room temperature, and another was placed in an 60° C oven. After a couple hours, the scintillator from the refrigerator and room temperature maintained similar levels of purpling. However, the purple color in the scintillator from the oven had significantly faded indicating that a post-cure heat treatment can be used to accelerate the dissipation of the purpling effect and obtain steady-state performance.

From preliminary light output experiments conducted at ORNL, the scintillator light yield was reduced while purpling was observed in the scintillator compared to when the purpling had faded away, even for the slight purpling shown in Figure 5.8. When there was still purpling observed in AFIT230A (30 wt% PPO, 0 wt% DIN), Figure5.8a, the relative light yield was 67%. After the purpling had faded away, Figure5.8b, the relative light yield had increased to 71%.

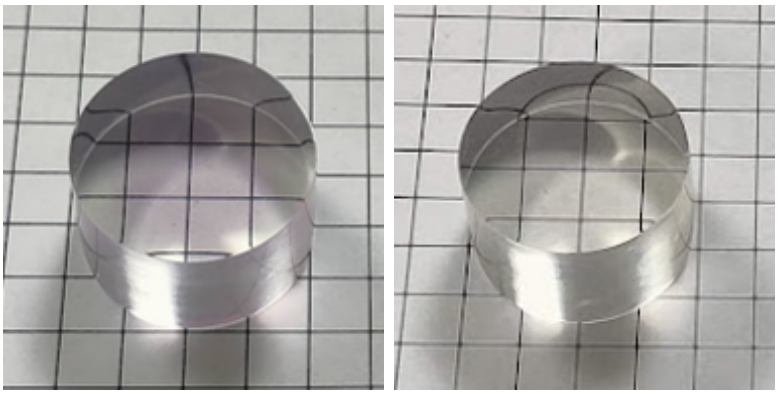

**(a) AFIT230A (10 Aug)** **(b) AFIT230A (16 Aug)**

**Figure 5.8. Purpling observed in AFIT230A (a) 6 days after being produced, but not at (b) 12 days.**

The light emission of AFIT131, which had the same formulation as AFIT130,

was measured after the plastic was completely cured to better characterize the post-cure light emission. Post cure, the cuvette was placed in a Horiba FluoroMax Plus to measure the emission spectrum of the scintillator while being excited at 350 and 380 nm, asynchronously. The Horiba FluoroMax Plus was set up to take measurements for up to 7 hours post cure. Figure 5.9a plots the emission spectrum of the plastic scintillator as a function of time after the curing process from excitation wavelength of 380 nm. The light emission was fairly constant for the first 90 mins post cure and then increased, as plotted in Figure 5.9b. This increase in the peak emission had not stopped at 7 hours post cure. This is attributed to the dissipation of the purpling in the scintillator, and the timescales correlate well to significant observational reductions in scintillator purpling.

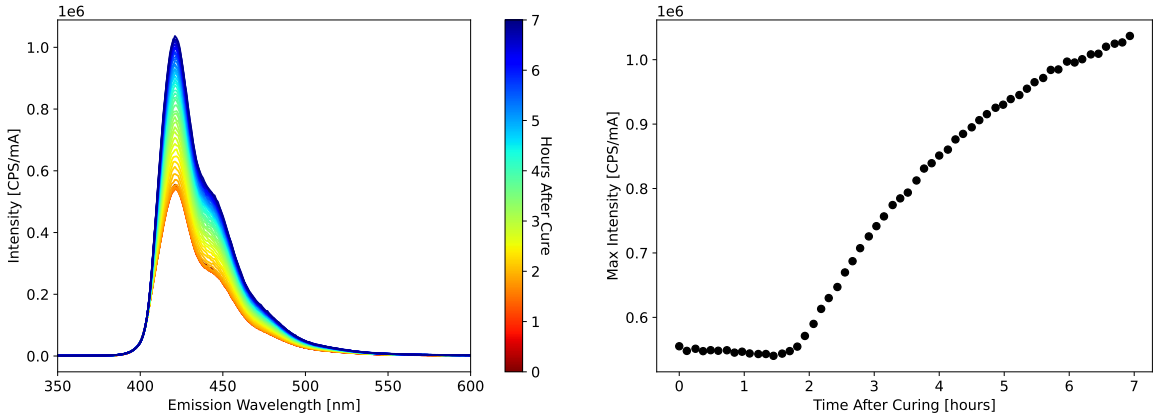


**(a) Light emission spectra** **(b) Peak light emission**

**Figure 5.9. (a) Light emission spectra and (b) peak like emission from AFIT131 using a Horiba FluoroMax Plus with an excitation wavelength of 380 nm.**

#### 5.5.1.2 Leaching

In addition to the purpling, the scintillators with higher PPO amounts (above 10 wt%) leached and created a hazy, white film on the surface of the scintillators proportional to the PPO concentration. Figure 5.10 shows AFIT026 (25 wt% PPO) and AFIT114 (20 wt% PPO) with the hazy film from the leaching and the clear

scintillators after being washed using mild soap and water. The BPADMA, such as in AFIT114, did not prevent the leaching as compared to AFIT026, which contained HDDMA. However, the scintillators would continue to leach and would again develop the hazy film on the surface within tens of minutes to hours (≥20 wt% PPO) or days (15 wt% PPO).

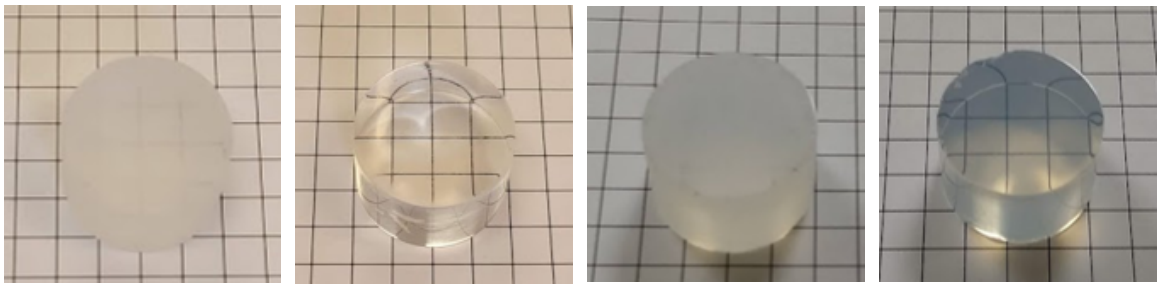

**(a) Hazy AFIT026 before washing** **(b) Clear AFIT026 after washing** **(c) Hazy AFIT114 before washing** **(d) Clear AFIT114 after washing**

**Figure 5.10. Hazy film from PPO leaching on (a) AFIT026 and (c) AFIT114 before and (b,d) after being washed using mild soap and water. The BPADMA in AFIT114 did not prevent the leaching as compared to AFIT026, which contained HDDMA.**

#### 5.5.1.3 Surface Cracking and Reduced Clarity

The softer scintillators exhibited surface cracking, as shown in Figures 5.11a and 5.11b of AFIT016 and AFIT104, which continued to degrade the integrity of the plastic over time. The scintillators with more than 10 wt% PPO did not crack on the surface, and the increase in BPADMA prevented surface cracking at a 10 wt% PPO concentration as observed in AFIT111. Unfortunately, the increase in BPADMA did not prevent leaching, and it did reduce the optical clarity of the scintillator, as shown in the difference between AFIT101 (0 wt% BPADMA), Figure 5.11c, and AFIT113 (21 wt% BPADMA), Figure 5.11d, after both have been washed.

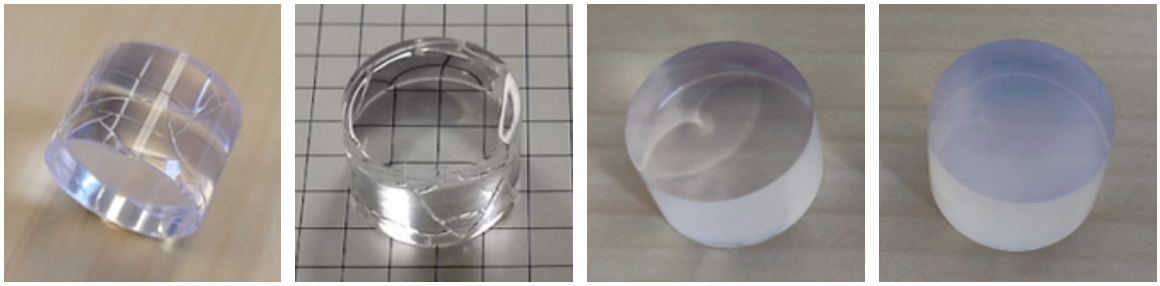

**(a) Surface cracking in AFIT016** **(b) Surface cracking in AFIT104** **(c) Clarity of AFIT101 (21 wt% HDDMA)** **(d) Clarity of AFIT113 (21 wt% BPADMA)**

**Figure 5.11. Surface cracking was observed in softer scintillators such as (a) AFIT016 and (b) AFIT104. While BPADMA did increase hardness and prevent cracking, it led to reduced clarity as illustrated by (d) AFIT113 (21 wt% BPADMA) compared to (c) AFIT101 (0 wt% BPADMA).**

### 5.5.2 Radiation Detection Performance

Figures 5.12a and 5.12b show the light yield relative to EJ-276, PSD FoM, and associated trends for several candidate formulations. The relative light yield was compared to the average of eight measurements of EJ-276 from 30 Jun to 1 Sep. These scintillators obtained a relative light yield of up to 78% of EJ-276 and a PSD figure of merit of 1.31 (74% of EJ-276) in the 450-550 keVee bin. The increase in PPO increased the light yield and PSD FoM for a set combination of crosslinkers. Unfortunately, the increase in BPADMA, while generally resulting in harder scintillators, did not prevent the leaching and reduced the clarity of the scintillators thereby decreasing the light yield and PSD FoM. Overall, AFIT101 was found to be the best formulation for simplicity (less compounds used), radiation detection performance, and overall hardness and integrity over time.

### 5.5.3 Aging

AFIT101 leached quickly and significantly, raising questions about the stability of the scintillator's performance over time. Figure 5.13 shows the relative light yield of AFIT101 ad AFIT102 from 30 June to 15 November. Over 4.5 months, AFIT101 and

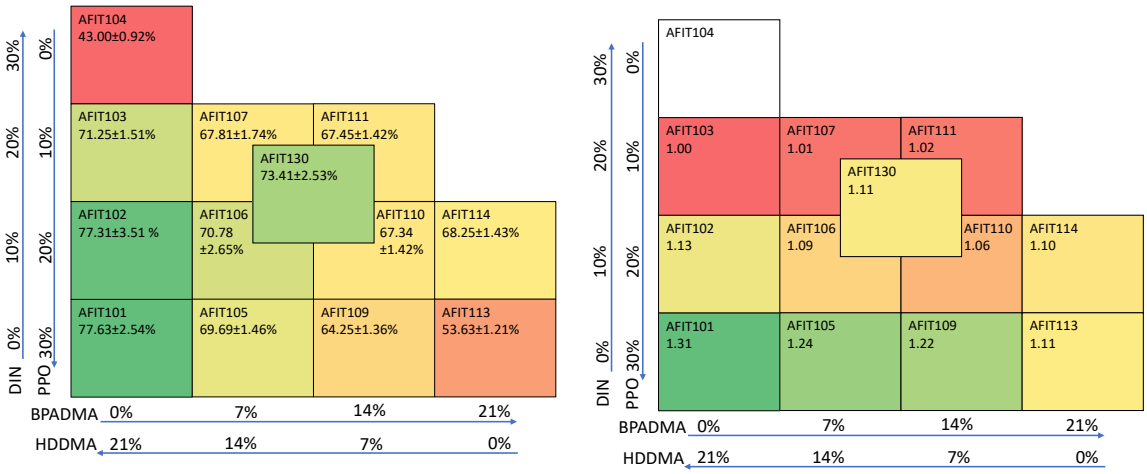


**(a) Formulation matrix of the scintillators in the parameter study with the associated relative light yield compared to EJ-276.**

**(b) Formulation matrix of the scintillators in the parameter study with the associated PSD FoM.**

**Figure 5.12. Radiation detection performance of the scintillators used for the parameter study.**

AFIT102's relative light yield decreased by 4.3% and 7.8%, respectively. The light yield in EJ-276 has also been shown to decrease over time. Compared to EJ-309, the relative light yield of EJ-276 decreased from 79% to 62% over 13 months [38,173,185], a 21.5% decrease. Over the 4.5 months observed in this study, a decrease of 5.5% was observed in the EJ-276 light yield. The uncertainty reported in Figure 5.13 for AFIT101 on 12 July includes the variance from five measurements of the AFIT 101 light yield, the variance from eight measurements of EJ-276, and the associated fit methodology uncertainty.

As the systematic uncertainty observed associated with the measurement and mounting each scintillator was comparable, all of the other reported uncertainties were based on the fit uncertainty for one measurement of the scintillator and the systematic uncertainty from eight measurements of EJ-276.

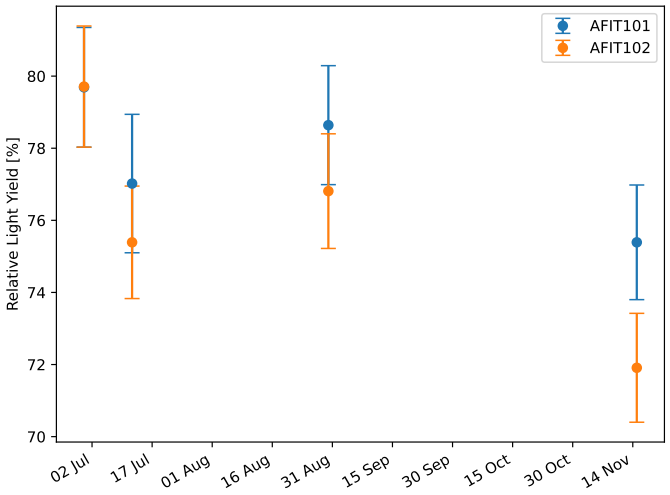


**Figure 5.13. Relative light yield of AFIT101 and AFIT102 from 30 Aug to 15 Nov.**

### 5.5.4 Leaching and Ethanol Treatment

While initial results with the formulations presented in this work do not seem to indicate a significant performance degradation over time, a significant advantage over EJ-276, the leaching of some formulations poses a challenge for printing and application use. The leaching is primarily from the PPO near the surface that crystallizes, creating the hazy film. In Lawrence Livermore National Laboratory's development of PSD plastic scintillators, leaching was also observed on the surface of the scintillators [38]. To prevent the leaching, Zaitseva *et al.* developed a method to treat the scintillators with ethanol post cure. While the specifics of this treatment were not described in [38], a study was performed on the effects of an ethanol treatment on the light-cured scintillators in an attempt to reduce the leaching of PPO over time.

Four formulations were produced for the study that contained 49 wt% IBOA, 0.2 wt% Exalite 416, 0.1 wt% TPO, and the differences in the DIN, PPO, HDDMA and BPADMA as listed in Table 5.3. Each ∼20 g formulation was prepared as described in Section 5.3.1 before splitting it equally into two separate glass containers

inside the glove box. Each scintillator was cured for 5 min in the Formlabs Form Cure and 4 min in the Dymax BlueWave AX-550 VisiCure, sanded with 180 grit, 400 grit, 1000 grit and 2000 grit sand paper, and polished with 300 nm alumina slurry. One of the scintillators from each pair was placed in a 200-proof ethanol bath for 1 hr, and the other was left at room temperature in a standard atmosphere. The treated sample showed no evidence of leaching while the untreated sample leached as expected. The untreated sample was washed with mild soap and water (as described previously) and then both samples were characterized.

**Table 5.3. Mass percentage composition and the radiation detection performance of ethanol-treated and untreated scintillators.**

| | Fraction of Scintillator [wt%] | | | | Rel. Light Yield [%] | | PSD FoM | |
|---|---|---|---|---|---|---|---|---|
| **Scintillator** | **DIN** | **PPO** | **HDDMA** | **BPADMA** | **Treated** | **Untreated** | **Treated** | **Untreated** |
| AFIT230 | 0 | 30 | 21 | 0 | 74.84 ± 1.84 | 72.28 ± 1.62 | 1.26 | 1.25 |
| AFIT225 | 5 | 25 | 21 | 0 | 83.03 ± 2.11 | 82.24 ± 2.34 | 1.28 | 1.28 |
| AFIT220 | 10 | 20 | 21 | 0 | 77.46 ± 1.75 | 77.78 ± 2.31 | 1.13 | 1.15 |
| AFIT221 | 10 | 20 | 14 | 7 | 75.69 ± 1.66 | 74.25 ± 1.65 | 1.14 | 1.12 |

The scintillators were weighed before and after the ethanol treatment to measure the amount of material that was removed by treatment before mounting them to PMTs as described in Section 5.3.2. The ethanol treatment resulted in relative light yield and PSD performance statistically consistent with the untreated scintillators as shown in Table 5.3. As the ethanol treatment did not remove a significant amount of material (0.2-0.37% by mass), this is an expected result as the overall composition is similar and removed material likely was poorly incorporated into the matrix. Importantly, no visual observation of subsequent leaching has been observed in any ethanol-treated scintillator to date (>5 months), while the non-treated samples continue to leach.

## 5.6 Conclusion

This research was successful in developing fast-, light-cured plastic scintillator formulations that can be used for light-based 3D printing using industry-standard 405 nm light. The most promising formulations for creating a clear and hard plastic contained a combined total of EJ-309/DIN and PPO of 30 wt% and a combined total of IBOA and crosslinker of 70 wt% with a IBOA/crosslinker ratio of 70/30. The plastic scintillators were generally solidified within 10-20 seconds in the 405 nm light from a Formlabs Form Cure. The scintillator with 25-30 wt% of PPO provided the highest radiation detection performance with the light yield up to 83% of EJ-276's and up to a PSD FoM of 1.31. The leaching and a hazy film that developed on these high PPO scintillator formulation was eliminated by placing the scintillators in an ethanol bath for 1 hour. The overall best performing scintillator was AFIT225B, which contained 5 wt% DIN, 25 wt% PPO, 21 wt% HDDMA, 0.2 wt% Exalite 416, and 0.1 wt% TPO, did not leach due to the ethanol treatment and produced a relative light yield of 83% of EJ-276 and PSD FoM of 1.28. Other noted issues such as surface cracking, haziness, and purpling were addressed through improved formulations and post-cure heat treatments.

## 5.7 Future Work

Future work includes further analysis of the effects of light yield due to curing time and TPO burn up, continuation of the formulation development to prevent leaching and/or increase radiation detection performance, and production of scintillator using a light-based 3D printer.

**Acknowledgements**

This research was supported by the Defense Threat Reduction Agency under grant HDTRA1136911, U.S. Department of Energy, Office of Science, Office of High Energy Physics, under Award Number DE-AC05-00OR22725, and the ORNL Laboratory Directed Research Development Program.

# VI. Thermal Neutron Sensitive Measurements

## 6.1 Introduction

The Nuclear Energy Agency (NEA) maintains the High Priority Nuclear Data Request List (HPRL) [8, 188] that emphasizes the need for important cross section measurements for the nuclear industry. The HPRL currently contains 25 requests for $^{252}$Cf spectrum-averaged cross section (SACS) measurements for different reactions to improve the International Reactor Dosimetry and Fusion File (IRDFF) [44, 45]. The IRDFF is the library of nuclear data for fission and fusion neutron metrology applications where the energy-dependent cross-section evaluations are benchmarked against a standard neutron field, defined as the neutron energy spectrum from $^{252}$Cf spontaneous fission [45]. Most of the measured $^{252}$Cf SACS reactions are from endothermic reactions and produce radioactive daughter nuclei, measurable using foil activation gamma-ray spectroscopy to determine the number of reactions and corresponding cross section [189].

However, there are several reactions, such as $^{10}$B(n,$\alpha$)$^{7}$Li and $^{6}$Li(n,t)$^{4}$He, that produce stable reactions products, thereby requiring in-situ spectroscopy or other methods to measure the SACS in a field. Additionally, many of these reactions are exothermic and have high thermal neutron cross sections, which significantly complicate the measurement of the $^{252}$Cf SACS due to thermalized neutrons in an experimental environment. Unsurprisingly, many of these reactions do not have a $^{252}$Cf SACS experimental measurement [44].

Neutrons from a $^{252}$Cf source, or any other neutron source, that do not interact directly with the target nuclei will interact with the walls, ceiling, floor, and other materials within the room. These interactions with the room reduce the neutron energy and result in a room full of thermal and epi-thermal neutrons that are

uniformly distributed throughout the room, known as room return [47]. Scattered neutrons create a uniform distribution within a room and larger rooms reduce the thermal neutron fluence [46]. For reactions with high thermal neutron cross sections, the thermalized room-return neutrons will dominate the reaction rate and prevent a correct measurement of the $^{252}$Cf SACS.

Cadmium has been used to absorb thermal neutrons as a method to address the thermal room-return issue in some $^{252}$Cf SACS measurements [190]. $^{113}$Cd has a high thermal neutron capture cross section and absorbs neutrons below ~0.5 eV (cadmium cut-off), as shown in Figure 6.1. However, there are two challenges with using cadmium to address this challenge. First, cadmium will also absorb low energy neutrons from the $^{252}$Cf in addition to the room-return neutrons thereby potentially depressing the population of neutrons in the target to below the expected $^{252}$Cf distribution. Second, in the epi-thermal region above the cutoff, the low energy, room-return neutrons will not be absorbed by the cadmium and can still complicate the $^{252}$Cf SACS measurement.

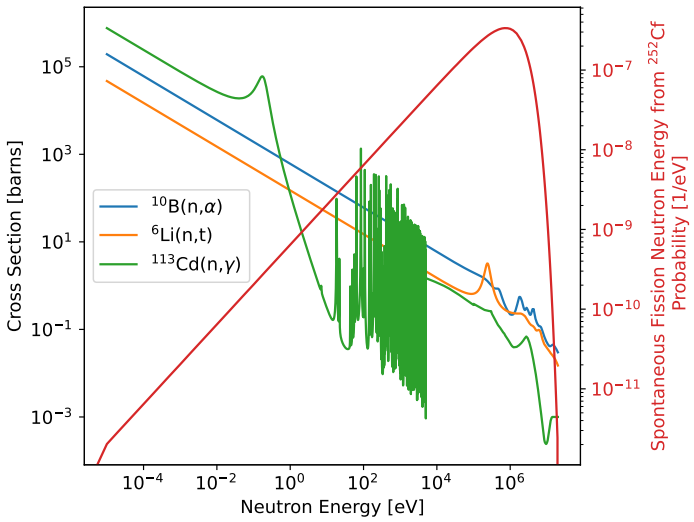


**Figure 6.1. Cross sections of $^{10}$B(n,$\alpha$)$^{7}$Li, $^{6}$Li(n,t)$^{4}$He, and $^{113}$Cd(n,$\gamma$). For comparison, in red is the spontaneous fission neutron spectrum from $^{252}$Cf [59].**

Another common method of reducing room-return neutrons is by locating the

target in a separate room from the source with a direct line-of-sight between the source and target using a hole or port within the wall. This can significantly reduce the room-return neutrons, but neutrons can still interact with the walls of the hole and thermalize. Since these walls are often made of low-Z materials such as concrete, the thermalization of the source spectrum can be significant.

This research explores a third approach: a collimator placed within the port separating the source and target. Previous examples of this approach included conically diverging collimator designs [191–193] which reduced the neutron background in the experimental area. However, some of these approaches suffered from using polyethylene [192, 193] to moderate the fast neutrons not directly line of sight to the desired target location, which worked well for the time-of-flight systems, but would create a higher thermal neutron environment in the collimator. This work improves upon this concept through the parametric design optimization of a collimator designed to reduce the thermal neutron population in thermal-neutron-sensitive measurements. Specifically, this work discusses the design approach and modeling of the proposed collimator; the construction, installation, and experimental characterization of the designed collimator; and a demonstration of a proof-of-principle application for thermal-sensitive measurements using the $^{6}$Li(n,t)$\alpha$ reaction in a $Cs_2LiYCl_6$:Ce (CLYC) detector.

## 6.2 Collimator Design

The fast neutron facility located in the basement of the Air Force Institute of Technology's (AFIT) old reactor was designed for neutron experiments. The thick walls and ceiling are made from solid concrete blocks that provide excellent shielding from neutrons and gamma rays. Figure 6.2 illustrates the layout and dimensions of the fast neutron facility. The ceiling in the room is $\sim$2.54 m high. A 4" diameter hole

was drilled through the 1.4 m-thick south wall of the neutron room at 0.74 m from the floor and 1.82 m from the west wall. A 3.5" schedule 80 PVC pipe was inserted into the hole of the wall to allow easy installation and removal of the collimator. Alternative materials to PVC, such as aluminum, were considered for the beam port sleeve, but the impact on performance was found to be negligible.

On the experimental side of the collimator, there is a 4.8 m flight path to the 1.30 m-high mezzanine that serves as the beam stop. The ceilings are ∼4.68 m high with the west wall located ∼2.11 m from the beam. The long flight path and large, open room serves to minimize room-return neutron created from the beam itself in the experimental location.

### 6.2.1 Design Optimization and Modeling Considerations

The collimator dimensions had two constraints imposed during the parametric optimization. The first was a 140 cm length to span the length of the beam port located in the south concrete wall of the fast neutron facility, as shown in Figure 6.2. Second, the collimator was constrained to have a desired 3" (7.62 cm) beam spot (collimator inner diameter) at the experimental end of the collimator. This limitation was imposed to ensure that the beam was larger than planned experiments to provide even irradiation while minimizing the excess beam size that would contribute to excess room-return neutrons at the experimental location.

Inspiration for shape and materials of the collimator design was drawn from previous research on collimators designed to minimize the number of thermal neutrons [191–194]. The two shapes considered were a conically diverging collimator and a combination of a conically converging-diverging approach. Conically converging designs were eliminated due to practical considerations of the desired beam size (7.62 cm).

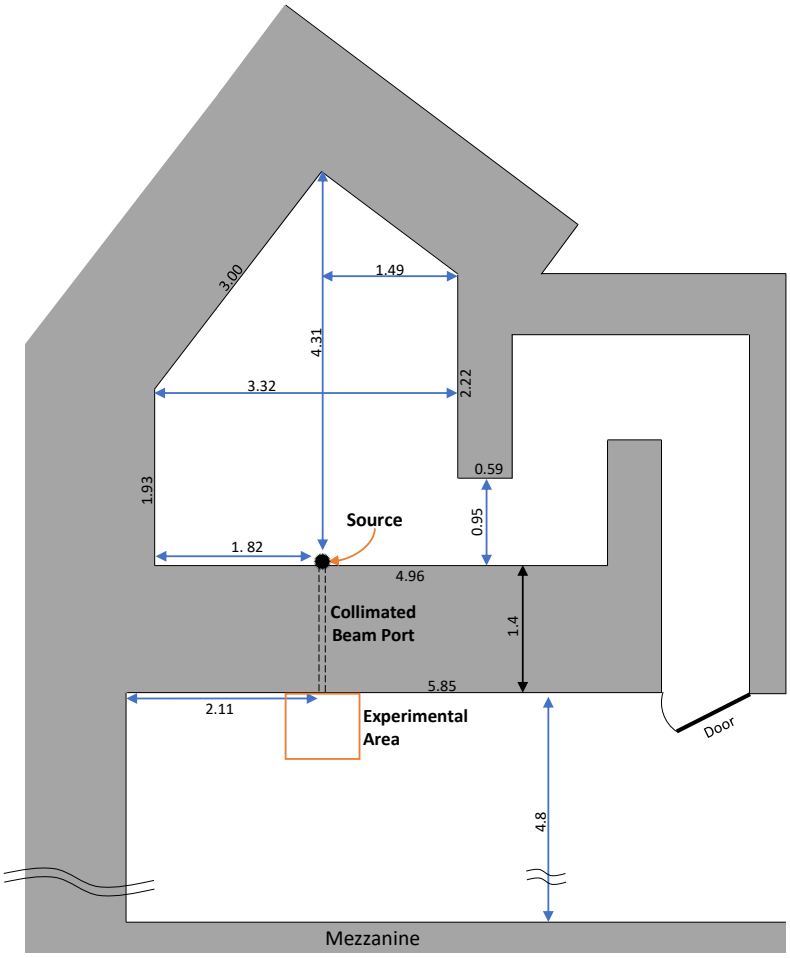


**Figure 6.2. Top view of the fast neutron facility located in the basement of AFIT's decommissioned nuclear reactor showing the facility layout and source and experiment locations in relation to the newly installed collimated beam port. All dimensions are in meters.**

The materials considered for the collimator were limited to those that had been demonstrated to be effective in previous collimators: copper, mild steel, tungsten, aluminum, and lead. Other materials, such as bismuth and tantalum, would likely have made excellent choices (high density, low neutron thermalization) but were ruled out due to cost.

The shape (nozzle location and size) and materials were parametrically optimized progressively in the order of nozzle location (defined as the transition between the converging and diverging sections of the collimator), material, and nozzle size. To

compare the performance of each collimator design, the objective function was defined as minimizing the difference between the $^{10}$B(n,$\alpha$)$^{7}$Li reaction rate in a $B_4C$ target as compared to the reaction rate in the same target when exposed to a "pure" $^{252}$Cf spectrum. In this way, collimators that produced reaction rates closer to the ideal reaction rate from a $^{252}$Cf spectrum were deemed to be preferable.

The neutron room with the concrete walls, ceiling, floor, and collimator (shown in Figure 6.2) were modeled in MCNP [195]. The $^{252}$Cf source was modeled as a point source located 1 cm from the entrance of the collimator with a Watt emission spectrum, defined as

$$p(E) = e^{(-E/a)} \sinh{(bE)}^{1/2}, \tag{6.1}$$

where a=1.025 and b=2.926 [196]. A F4 tally with a FM reaction rate modifier card measured the number of (n,$\alpha$) reactions in a $25 \times 25 \times 0.5$ mm, 2.52 g/cm$^3$ $B_4C$ (19.9% $^{10}$B) target located at 10 cm from the end of the collimator. The collimators were modeled with an outer diameter and length of 9.62 cm and 140 cm, respectively.

#### 6.2.1.1 Collimator Nozzle Location

Four designs were considered sequentially to determine the collimator shape. For each, copper was selected as the baseline material based on previous research experience with the GENESIS facility (see Chapter 3). First, the conically diverging design was modeled with an entrance and exit inner diameter of 0.062 cm and 7.62 cm, respectively. The reaction rate in the $B_4C$ target results are shown in Table 6.1. For reference, the ideal number of (n,$\alpha$) reactions in the $B_4C$ target, determined computationally by maintaining the same geometry but voiding all the materials besides the $B_4C$ target, resulted in a reaction rate of $0.1117 \pm 0.0001$ s$^{-1}$. The uncertainty values are the statistical uncertainties reported from MCNP.

Next, the conically converging-diverging designs were considered. For each design,

**Table 6.1. $B_4C(n,\alpha)$ reaction rates for copper collimator with different designs and nozzle locations.**

| Nozzle Location [cm] | Nozzle Diameter [cm] | Reaction Rate [$s^{-1}$] |
|---|---|---|
| N/A | N/A | $0.1280 \pm 0.0026$ |
| 20 | 1.08 | $0.1206 \pm 0.0025$ |
| 40 | 2.16 | $0.1230 \pm 0.0027$ |
| 70 | 3.78 | $0.2165 \pm 0.0102$ |

the inner diameter was sized such as to result in a ∼7.62 cm beam at the end of the collimator. The next design considered placed the nozzle location at approximately one-third of the collimator length with the reaction rate result shown in Table 6.1. This design outperformed the pure conically-diverging design.

Next, the nozzle point was moved to the the half way point (further away from the source) and to 20 cm (closer to the source). The results are again shown in Table 6.1 and demonstrate the moving the nozzle to 20 cm resulted in the best performance. However, this result was within 1-$\sigma$ of the result for the nozzle location at 40 cm. Subsequent perturbations on the 20 cm location resulted in minor, not statistically significant improvements. Therefore, 20 cm was chosen for the nozzle location in subsequent optimization. For reference, Figure 6.3 illustrates the four different collimator designs considered.

#### 6.2.1.2 Collimator Material

With the collimator nozzle location set, the next parameter to optimize was the collimator material. Using the converging-diverging design shown in Figure 6.3b, MCNP was used to model the performance of copper, mild steel, tungsten, aluminum, and lead collimators. The reaction rates obtained for each collimator material are listed in Table 6.2. Tungsten, due to it's high density and low moderating power, resulted in a reaction rate remarkably close to the ideal reaction rate of 0.1117±0.0001

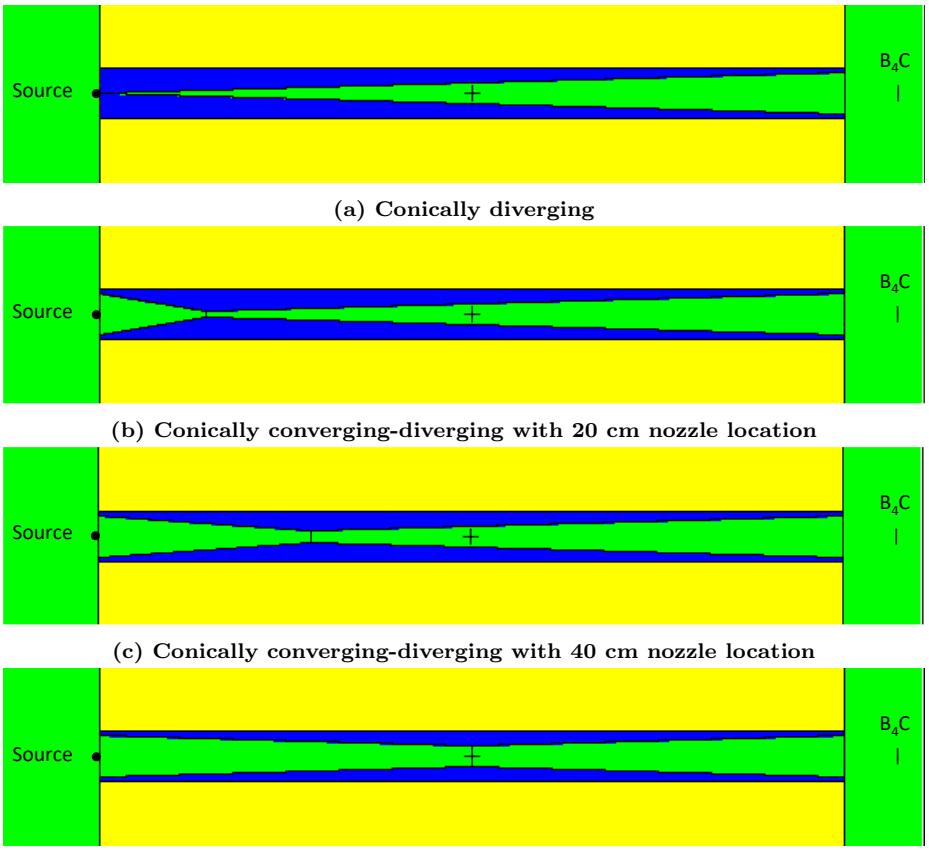


**(a) Conically diverging**

**(b) Conically converging-diverging with 20 cm nozzle location**

**(c) Conically converging-diverging with 40 cm nozzle location**

**(d) Conically converging-diverging with 70 cm nozzle location**

**Figure 6.3. View of the different collimator designs modeled in MCNP. The concrete wall, collimator and air are represented by yellow, blue and green, respectively.**

$s^{-1}$. Therefore, tungsten was chosen as the collimator material.

**Table 6.2. $B_4C(n,\alpha)$ reaction rates for different collimator materials.**

| Material | Reaction Rate [$s^{-1}$] |
|---|---|
| Copper | $0.1244 \pm 0.0010$ |
| Mild Steel | $0.1311 \pm 0.0011$ |
| Tungsten | $0.1130 \pm 0.0005$ |
| Aluminum | $0.6987 \pm 0.0073$ |
| Lead | $0.3801 \pm 0.0051$ |

#### 6.2.1.3 Nozzle Diameter

The last parameter to consider, the nozzle diameter, was explored using the tungsten collimator with a 20 cm nozzle location. Five different collimator designs

were modeled in MCNP with nozzle diameters spanning from 0.68-1.28 cm. The resulting $B_4C$ (n,$\alpha$) reaction rates for each diameter are shown in Table 6.3.

**Table 6.3. $B_4C$(n,$\alpha$) reaction rates for varying nozzle diameters.**

| **Diameter [cm]** | **Reaction Rate [$s^{-1}$]** |
|---|---|
| 1.28 | $0.1193 \pm 0.0010$ |
| 1.08 | $0.1130 \pm 0.0005$ |
| 0.88 | $0.1124 \pm 0.0005$ |
| 0.78 | $0.1120 \pm 0.0004$ |
| 0.68 | $0.1117 \pm 0.0004$ |

In general, reducing the nozzle diameter did reduce the overall reaction rate in the $B_4C$ target, and was able to even achieve the ideal value reaction rate of 0.1117±0.0001 $s^{-1}$. However, this model was examining the effects on the 25 × 25 mm $B_4C$ target, which only covered a small portion of the exit beam diameter. Reducing the nozzle diameter significantly reduced the quality and uniformity of the beam over the larger desired 7.62 cm diameter at the end of the collimator, as shown in Figure 6.4. At the largest diameter, 1.28 cm, the diverging beam created by the collimator "scrapes" the outer edge of the collimator resulting in an increased down-scatter component of the beam.

Given the relatively small changes in reaction rates for nozzle diameters that result in a beam size of less than 7.62 cm at the end of the beam, the final collimator design kept the original objective to create a uniform ∼7.62 beam at end of the collimator. Therefore, a nozzle diameter of 1.135 cm was chosen, which provided a line-of-sight from the source at 1 cm in front of the collimator to the 7.62 cm diameter edge at the end of the collimator. If desired, the source can be moved closer or farther away from the collimator entrance to affect the beam size and uniformity to optimize specific experimental objectives.

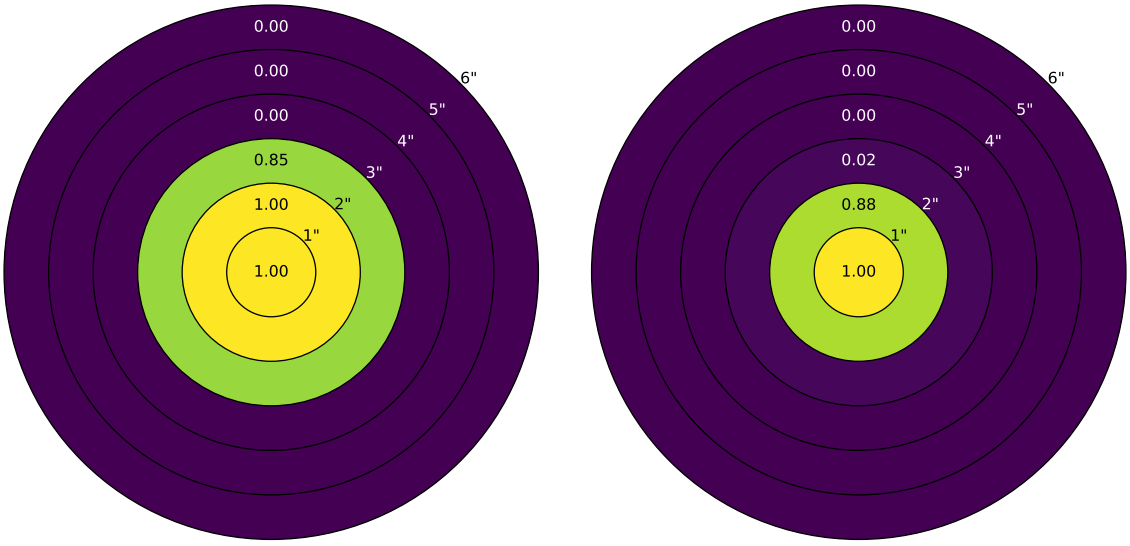


**(a) 1.08 cm middle inner diameter** **(b) 0.68 cm middle inner diameter**

**Figure 6.4. Relative total neutron flux from the collimator in 1" wide concentric rings from the tungsten converging-diverging collimator design with a middle inner diameter of (a) 1.08 cm and (b) 0.68 cm. The exit inner diameter of the collimator was 7.62 cm. The smaller nozzle diameter of the collimator significantly reduces the beam uniformity at the end of the collimator.**

### 6.2.2 Final Design

The final design of the tungsten collimator was a conical converging-diverging shape with a nozzle diameter of 1.135 cm located at 20 cm and entrance and exit inner diameters of 7.62 cm, as illustrated in Figure 6.5. The tungsten collimator was cut from 8.89 cm diameter, ≥99.95% pure, tungsten rods from Midwest Tungsten Service into 14 equal length segments for manufacturability. The inner conical holes of the collimator were cut using electrical discharge machining (EDM) [197].

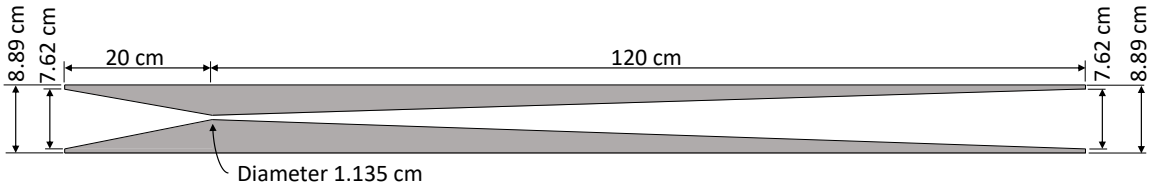


**Figure 6.5. Tungsten collimator design and dimensions.**

The concrete wall, PVC pipe, and collimator were modeled in MCNP to simulate

the performance of the final tungsten collimator design. The 19.3 g/cm$^3$ tungsten collimator was modeled with the dimensions shown in Figure 6.5. The 140 cm long, 1.38 g/cm$^3$ PVC pipe was modeled on the outside of the collimator with inner and outer diameters of 8.94 cm and 10.16 cm, respectively. Figure 6.6a compares the neutron spectrum from the $^{252}$Cf source and neutron spectrum into the entrance and out of the exit of the collimator (away from the source).

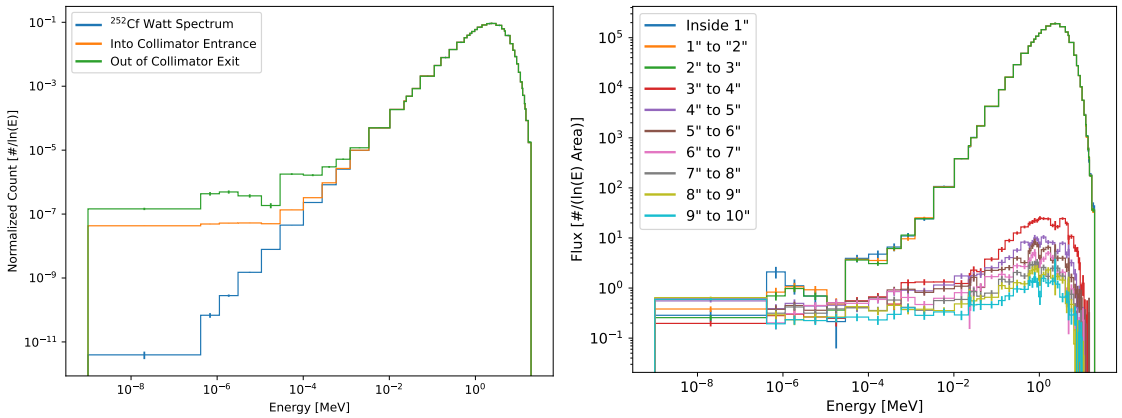


**(a) Neutron spectra at entrance and exit.** **(b) Spatial neutron spectra distribution at exit.**

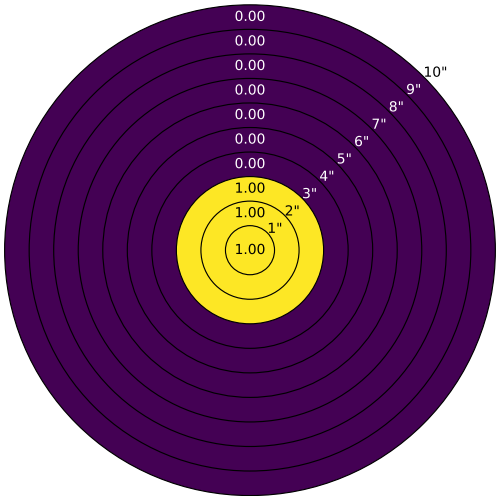


**(c) Relative total neutron flux at collimator exit.**

**Figure 6.6. (a) Comparison of the normalized neutron spectra from the $^{252}$Cf source, into the entrance, and out of the exit of the collimator (away from the source) demonstrating minimal thermalization from the collimator design. Additionally, the (b) neutron spectrum and (c) spatial uniformity of the beam at the collimator exit planes, discretized into in 1"-wide concentric rings, is shown.**

Figures 6.6b plots the neutron spectrum leaving the collimator exit plane towards

the experimental area in 1"-wide concentric rings, and Figure 6.6c plots the integrated relative total neutron flux through each of those rings. The collimator-created beam is uniform both in energy and spatial distribution within the 7.62 cm beam diameter while the concrete wall significantly reduces the leakage from outside of the collimator.

## 6.3 Experimental Setup

### 6.3.1 Beam Profile

The profile of the neutron and gamma radiation field of a $^{252}$Cf source from the collimator was mapped using a 2-D (horizontal and vertical) motorized Velmex BiSlide [198]. Two detectors were used to map the fast neutron, gamma-ray, and thermal neutron distributions. A 1"×1" right circular cylinder EJ-309 scintillator [103] was used for the fast neutron measurement, and a 1"×1" right circular cylinder, 95% $^{6}$Li enriched CLYC detector [199, 200] was used to measure the gamma-ray and thermal neutron distributions. The EJ-309 scintillator from Eljen Technology was mounted to a 1" Hamamatsu R6094 PMT [201] biased at -800 V. The CLYC detector from Radiation Monitoring Devices, Inc. was mounted to a 2" Hamamatsu R7724 PMT [181] biased at -1300 V.

A CAEN DT5533E high voltage power supply and the GECO2000 software was used to bias the PMTs [202,203]. The signals were processed using CAEN CoMPASS software on a CAEN DT5730, a 500 MS/s, 14-bit waveform digitizer with the DPP-PSD firmware for pulse integration and pulse shape discrimination (PSD) [182, 183]. Table 6.4 lists the settings used for the EJ-309 scintillator and CLYC detector.

The Velmex BiSlide controller and DT5730 were configured to raster the collimated neutron beam automatically, and the digitizer was triggered so as to stop recording during transitions and start recording events when the detector was in each position. A 6.2 mCi (as of 24 Jan 2022) $^{252}$Cf source contained within a

**Table 6.4. Settings of the CAEN DT5730 digitizer for the EJ-309 scintillator and CLYC detector used for the characterization of the neutron and gamma radiation field from the tungsten collimator. LSB stands for least significant bit.**

| Setting | EJ-309 | CLYC |
|---|---|---|
| Record Length (ns) | 592 | 800 |
| Pre-trigger (ns) | 96 | 96 |
| Polarity | Negative | Negative |
| NS baseline (Samples) | 256 | 256 |
| DC Offset (%) | 10 | 10 |
| Input dynamic (Vpp) | 2 | 2 |
| Discrimination mode | Leading edge | CFD |
| Threshold (LSB) | 40 | 200 |
| Trigger Hold Off (ns) | 600 | 600 |
| CFD Delay (ns) | 6 | 20 |
| CFD Fraction (%) | 75 | 50 |
| Input Smoothing (samples) | Disabled | Disabled |
| Energy course gain (fC/(LSB) | 40 | 40 |
| Gate (ns) | 350 | 600 |
| Short Gate (ns) | 60 | 200 |
| Pre-gate (ns) | 20 | 100 |
| Energy N channels | 8192 | 8192 |
| PSD N channels | 8192 | 8192 |
| 2D Energy N channels | 512 | 512 |
| 2D PSD N channels | 512 | 512 |
| Saturation rejection enable | Enabled | Disabled |
| Pileup rejection (PUR) | Enabled | Enabled |
| PUR gap (lsb) | 1000 | 1000 |

stainless steel capsule from Frontier Technology Corporation was placed in an elevated holder connected to a manual horizontal and vertical translation stage, which allowed precision movements to align the source with the collimator. The dwell times for each position using the EJ-309 scintillator and CLYC detector were 15 and 60 min, respectively.

### 6.3.2 Thermal Neutron Environment

In addition to mapping the beam profile, the CLYC detector was used to compare the performance of the collimator in reducing the thermal neutron environment to

demonstrate the practical application of performing thermally-sensitive measurements with the new facility. The CLYC detector was positioned in the center of the beam and 7.62 cm left of the center both with and without the tungsten collimator. Additionally, the CLYC detector was placed in the room with the $^{252}$Cf source. The $^{252}$Cf source was located in the center of the room and the CLYC detector was placed 1.42 m away from the source and 0.73 m from the closest wall. These three measurements demonstrate the relative effectiveness of the three approaches described in Section 6.1 (distance, beam ports, and collimation) for reducing the thermal neutrons population from room return. Data was collected for 12 hours for each measurement.

A MCNP model of the experimental setup was created using the concrete wall, PVC pipe and tungsten collimator previously described in Section 6.2.2. A 30×30×30 cm box at the back of the collimator was added for use with the MCNP source surface write (SSW) card, allowing all particles entering into the box to be written to a surface source file to accelerate subsequent simulations. Additionally, the use of the SSW card allowed for the separation of particles based on their collision history prior to reaching the surface using the COL card. To generate the surface source, $10^{11}$ source histories were simulated resulting in 18,040,305 tracks in the SSW region.

The CLYC detector, housing, and PMT were modeled in MCNP within the dimensions of the source surface region located at the collimator exit. The 95% enriched, 2.56 cm diameter, and 2.96 cm long CLYC detector was modeled with an 0.3 cm thick aluminum housing and 0.3 cm thick borosilicate glass window. The 5.2 cm outer diameter, 11.2 cm long PMT was modeled as 0.2 cm thick borosilicate glass with an interior of 5% density of iron to account for the internal PMT electronics. The PMT was modeled in a 6.05 cm outer diameter, 19.5 cm long, and 0.1 cm thick stainless steel housing with a 7.62 cm outer diameter and 0.94 cm wide

aluminum flange. The back portion of the PMT housing was modeled as 5% dense iron to account for the electronics. The CLYC detector was modeled with a 0.15 cm thick aluminum housing mount that connected the detector to PMT. Figure 6.7 illustrates the modeled CLYC detector and PMT.

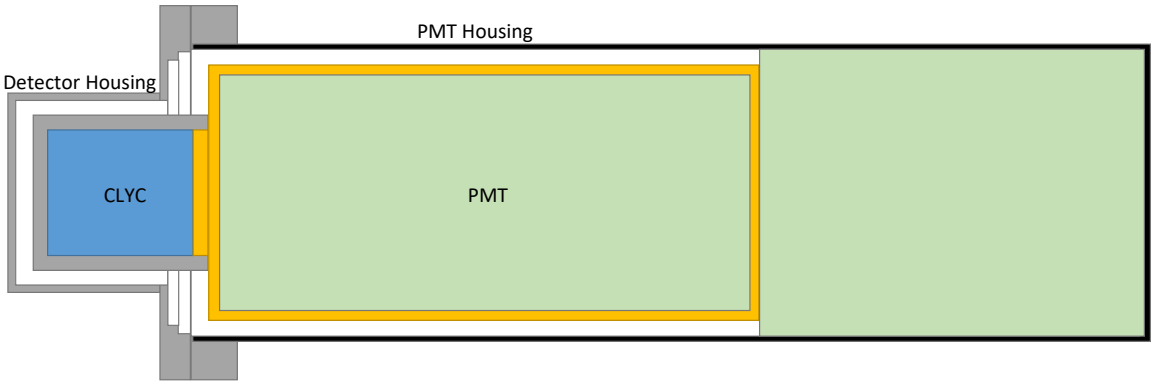


**Figure 6.7. Modeled CLYC detector and PMT.**

The MCNP model of the CLYC detector and PMT simulated the neutrons from the surface source file and allowed the simulation of reaction-generated protons, tritons and alphas from $^{6}$Li and $^{35}$Cl. The simulation provided the tracks of all particles through the CLYC detector using the PTRAC card, which was then analyzed to calculate the number of protons, tritons, and alphas created in the CLYC detector with their corresponding energies [204].

## 6.4 Results

### 6.4.1 Beam Profile

Due to the size and cylindrical shape of the detectors used, map positions resulting in the detector not being fully in beam are reduced by the relative percentage of the detector that falls out the beam. Consequently, 7"×7" and 8"×8" maps of the neutron and gamma radiation field at the collimator exit were conducted to better illustrate the beam profile uniformity. The relative radiation field maps obtained using the

EJ-309 scintillator and CLYC detectors, normalized where the maximum numbers of events is one, are shown in Figures 6.8 and 6.9, respectively. Neutron and gamma-ray events were separated in both detectors using the tail-to-total charge integration PSD method [169]. $^{6}$Li(n,t) capture events were then separated from the fast neutron $^{35}$Cl(n,p) response in the CLYC detector by fitting a Gaussian distribution of the thermal neutron energy peak on the fast neutron background in the neutron spectrum. For fast neutrons and gamma rays, the beam results in an uniform 7.62 cm diameter beam, demonstrated with both detector measurements and in agreement with the simulated results shown in Figure 6.6c. For thermal neutrons, the beam is generally uniform and consistent with the fast neutron and gamma-ray maps, with the slight variations likely induced by the fast neutron background subtraction routine.

### 6.4.2 Thermal Neutron Environment

Figures 6.8 and 6.9 demonstrated a uniform, high-contrast beam, but did not provide information on the performance of the tungsten collimator in reducing the thermal neutron environment, which was the second optimization design objective. Measurements with and without the tungsten collimator were conducted to demonstrate the relative reduction of thermal and room-return neutrons. First, the CLYC detector was placed in the center of the beam with and without the tungsten collimator, and the 2D energy and PSD histograms are shown in Figures 6.10a and 6.10b. The upper band in both plots is from neutron reactions in the detector, which include the fast ($^{35}$Cl(n,p) and $^{35}$Cl(n,$\alpha$)) and thermal ($^{6}$Li(n,t)) neutron-induced reactions. Visually, the thermal neutron capture peak in Figure 6.10a (with collimator) is significantly reduced compared to Figure 6.10b (without collimator).

Additional measurements with the CLYC detector out of beam and in the same

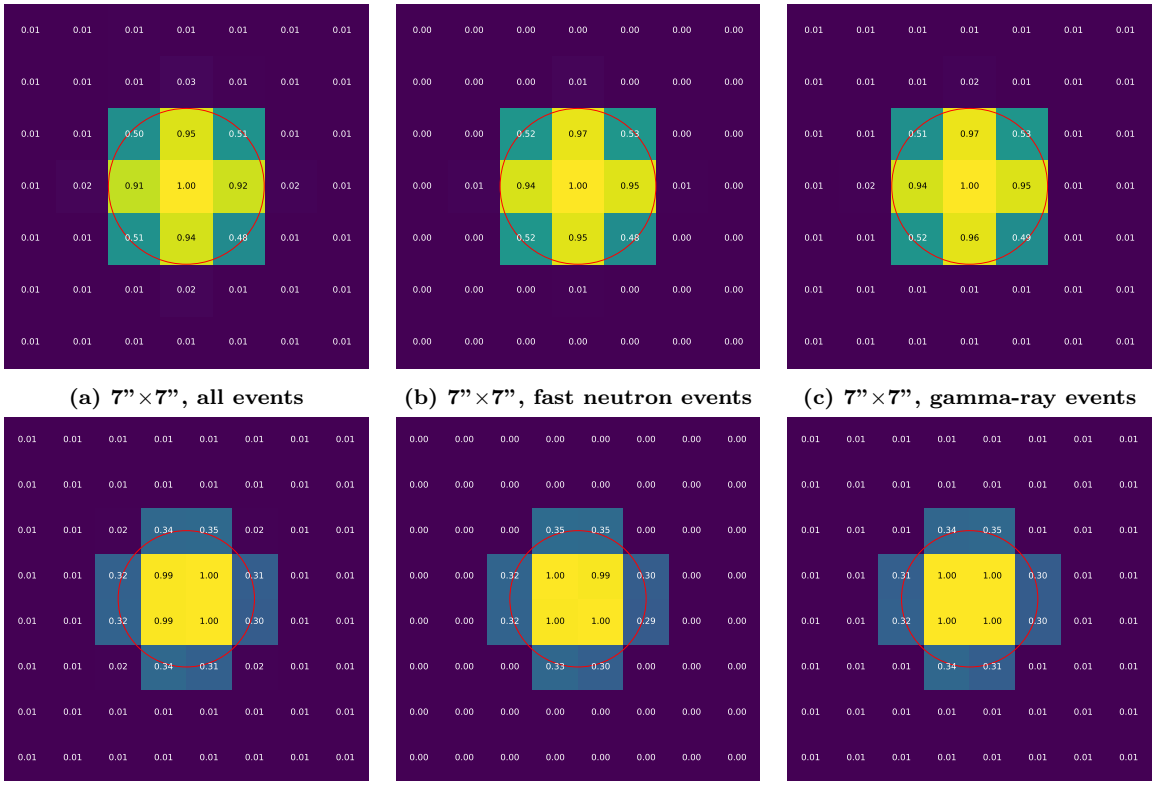

(a) 7”×7”, all events (b) 7”×7”, fast neutron events (c) 7”×7”, gamma-ray events

(d) 8”×8”, all events (e) 8”×8”, fast neutron events (f) 8”×8”, gamma-ray events

**Figure 6.8. Map of the radiation field from the collimator using the 1” EJ-309 scintillator for (a) all, (b) fast neutron, and (c) gamma-ray events of the 7”×7” raster and (d) all, (e) fast neutron, and (f) gamma-ray events of the 8”×8” raster. The values in each position are the relative number of events in that position to the maximum number of events in any location. The red circle indicates the location of the inner diameter of the collimator at the exit plane.**

room as the source were performed as described in Section 6.3 to quantify the reduction in thermal capture events. Figure 6.11 plots the resulting energy histogram for all neutron events in the CLYC detector for each of the five environments. The beam port in the wall reduced the number the number of thermal neutron events by $\sim 50\times$ compared to the number of thermal events with the CLYC detector in the same room as the source. The tungsten collimator further reduced the thermal rate by $\sim 15\times$ compared to the number of thermal events without the collimator when the CLYC detector was in beam. Compared to the number of thermal events with the CLYC detector in the same room as the $^{252}$Cf

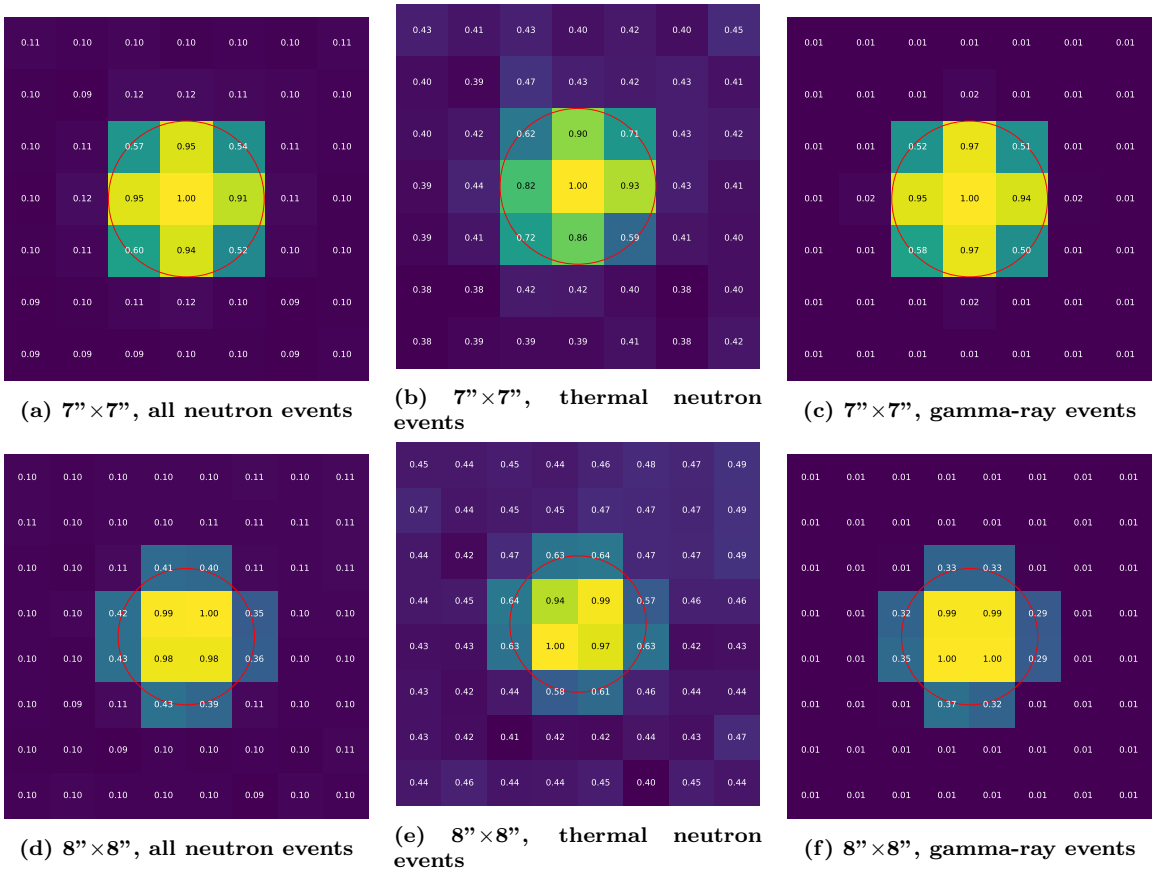


**(a) 7”×7”, all neutron events** **(b) 7”×7”, thermal neutron events** **(c) 7”×7”, gamma-ray events**

**(d) 8”×8”, all neutron events** **(e) 8”×8”, thermal neutron events** **(f) 8”×8”, gamma-ray events**

**Figure 6.9. Map of the radiation field from the collimator using the 1” CLYC detector for (a) all, (b) thermal neutron, and (c) gamma-ray events of the 7”×7” raster and (d) all, (e) thermal neutron, and (f) gamma-ray events of the 8”×8” raster. The values in each position are the relative maximum number of events in any location. The red circle indicates the location of the inner diameter of the collimator at the exit plane.**

source, the tungsten collimator reduced the thermal neutron environment by $\sim 778\times$. Both approaches are far superior to the distance-based method, although with the caveat that larger rooms would reduce the count rate compared to the room used as shown previously by [46].

When comparing the in the beam with collimator (solid green) to without collimator (solid orange) results in Figure 6.11b, it is clear that most of the reduction is due to the thermal capture events evidenced by the drastic reduction of the capture peak but similar rates at other parts of the spectrum are dominated by fast reactions. Comparing the out of beam with collimator (dashed green) and

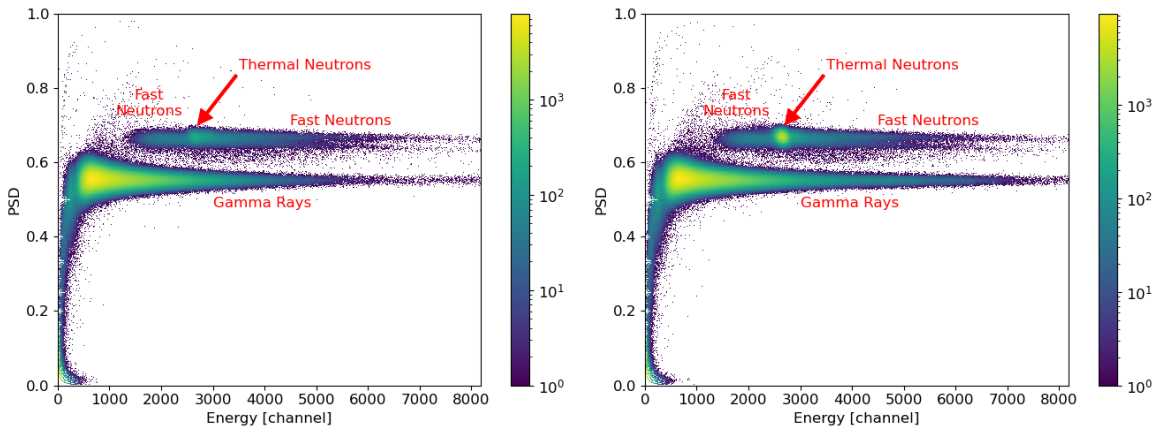


**(a) With collimator** **(b) Without collimator**

**Figure 6.10. Energy and PSD histograms from the CLYC detector place in the center of the neutron beam (a) with and (b) without the tungsten collimator.**

without collimator (dashed orange) results allow direct isolation of the thermal events and similar $\sim 14\times$ reduction was observed.

However, the experimental thermal reaction rate in beam was 2350 cph (counts per hour) as compared to the ideal $^{252}$Cf $^{6}$Li(n,t)$\alpha$ reaction rate of ~250 cph ($\leq$ 100 keV) from the simulation, which is presented in Section 6.4.3. The additional contribution is due to four sources: collimator scatter, room return in the experimental area, room return in the source room, and cosmic and terrestrial neutrons. The contribution from the collimator scatter was considered in the optimization process (as comparing reaction rates with the collimator to the ideal $^{252}$Cf reaction rate) and is explored further in Section 6.4.3 for the as-built design. The out of beam measurements capture the thermalization from scatter in the experimental room, primarily from the beam interacting with the mezzanine and creating a uniform thermal neutron environment as described in [46]. Fortunately, this can be directly subtracted from the in-beam measurements using the out-of-beam measurements, and this constitutes about 49% of the number of thermal events in beam, accounting for 1140 cph of the excess 2100 cph thermal capture events. Note, this measurement would include the third contribution, cosmic and terrestrial neutrons, which was not considered or measured

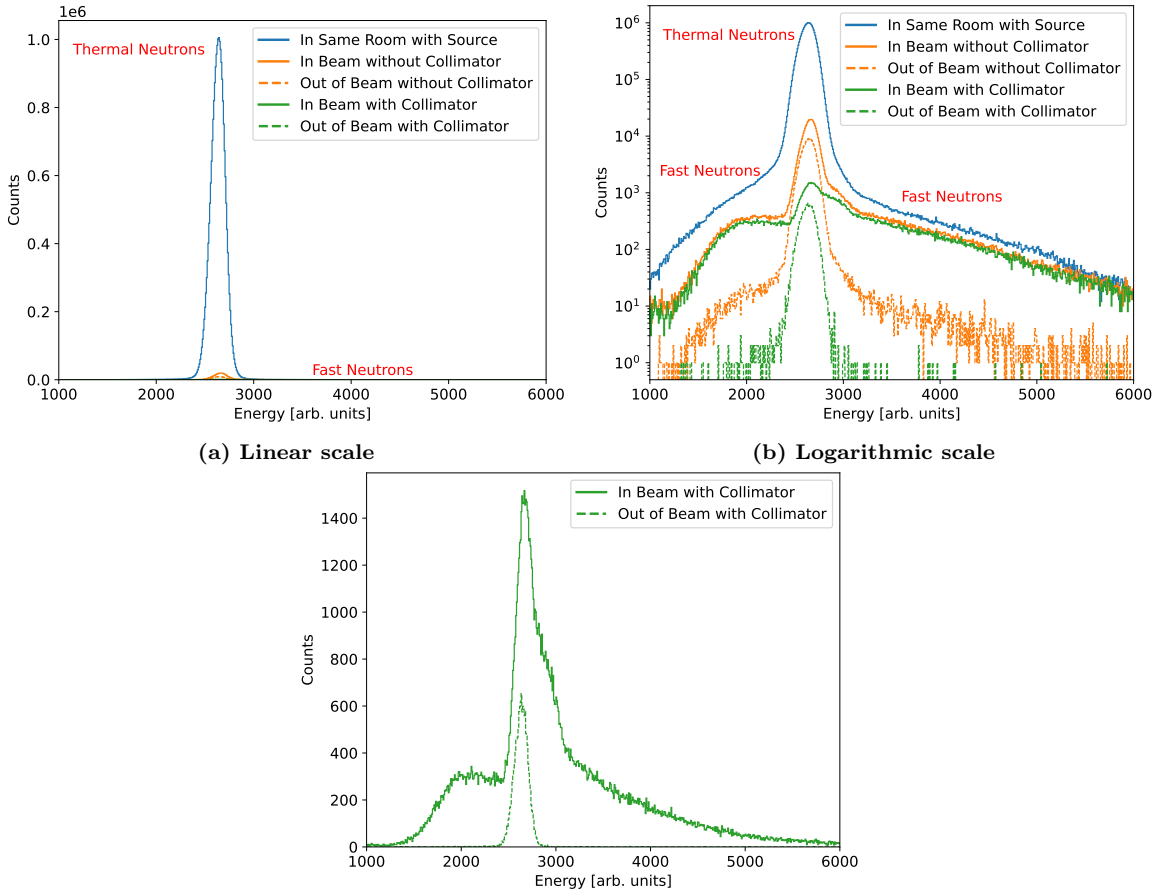


**(a) Linear scale**

**(b) Logarithmic scale**

**(c) In and out of beam with collimator**

**Figure 6.11. (a) linear and (b) logarithmic energy histogram for the neutron events in the CLYC detector placed in the center of the collimator and 7.62 cm left of the center with and without the tungsten collimator. An additional measurement was done with the CLYC detector placed 1.42 m away from the source and 0.73 m from the closest wall in the fast neutron facility. (c) energy histogram for the neutron events in the CLYC detector placed in and out of beam with the tungsten collimator.**

separately. The final contribution, room-return neutrons from the source room that escape down the collimator, was not characterized but could be mitigated with thin thermal capture filters located at the collimator entrance.

### 6.4.3 Simulated Results

The MCNP model described in Section 6.2.2 (collimator) and Section 6.3.2 (detector and tallies) tracked the creation of protons, tritons, and alphas in the CLYC detector. The $^{35}$Cl(n,p) and $^{35}$Cl(n,$\alpha$) deposited energy was calculated from

the energy of the created protons and alphas from neutrons on $^{35}$Cl, and the $^{6}$Li(n,t)$\alpha$ deposited energy was calculated from the energy of the created tritons and alphas from fast and thermal neutron capture on $^{6}$Li. Figures 6.12a and 6.12b plot the deposited energy from the three reactions in the CLYC detector using all the particles from the source surface file (COL=0) and only using the particles from the source surface file that did not have a previous collision (COL=-1), respectively. The simulation provides a similar energy spectrum shape compared to the experimental results in Figure 6.11c, but all simulated energy deposition results do not consider detector resolution broadening to allow for the identification, in simulation space, of specific reaction features.

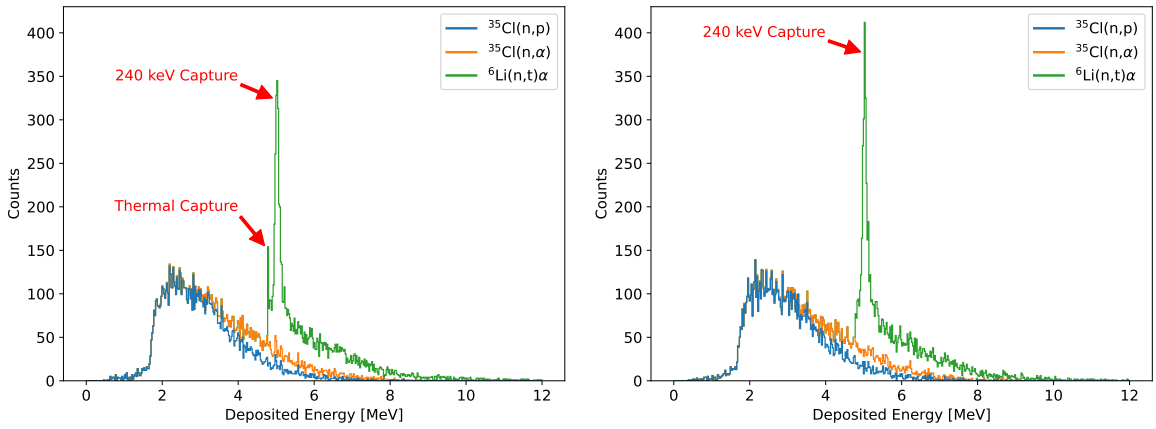


**(a) All surface source particles** **(b) No previous collision particles**

**Figure 6.12. Simulated stacked energy histogram for the $^{35}$Cl(n,p), $^{35}$Cl(n,$\alpha$), and $^{6}$Li(n,t)$\alpha$ events in the CLYC detector placed in the center of the collimator using (a) all the particles from the source surface file (COL=0) and (b) only the particles from the source surface file that did not have a previous collision (COL=-1). The 240 keV capture is the increase in $^{6}$Li(n,t) cross section at 240 keV.**

The tungsten collimator and surrounding wall geometry lead to some beam thermalization as evidenced by the addition of the thermal capture peak in Figures 6.12a when considering neutron histories with a previous collision (COL=0). However, the number of $^{6}$Li(n,t)$\alpha$ reactions using all the particles from the source surface file (COL=0) was only 1.6% more than than the number of $^{6}$Li(n,t)$\alpha$

reactions using only the particles from the source surface file that did not have a previous collision (COL=-1). This indicates, as desired, that the tungsten collimator effects are almost minimal, as designed, accounting for ∼91 cph of the observed increase in thermal capture reaction rate, defined as ≤100 keV as above. While this is a 54.5% increase in the thermal (≤100 keV) capture rate from an ideal $^{252}$Cf source, this is only a 1.6% increase in the overall $^{6}$Li(n,t) reaction rate from the same idealized source.

## 6.5 Conclusion

Low thermal neutron environments are needed to perform thermal neutron sensitive experiments, such as $^{252}$Cf SACS cross-section measurements for $^{10}$B(n,$\alpha$)$^{7}$Li and $^{6}$Li(n,t)$^{4}$He. However, in neutron experimental facilities which use thick concrete or shielding for radiation protection, the neutrons scattering off the surfaces of the room create a room full of thermal and epi-thermal neutrons that are uniformly distributed. These room-return neutrons can complicate or render the measurements impossible. By placing the neutron source in a separate room from the experimental area and using a direct line-of-sight hole or port within the wall, most of the room return neutrons will be contained within the room. However, neutrons can still interact with the walls of the port and thermalize. This research examined the effects of using a collimator optimized to reduce the thermal neutron environment.

Different collimator designs and materials were modeled and simulated in MCNP to reduce the number of thermal neutrons from the collimator, which resulted in the final design of a conical converging-diverging tungsten collimator with a nozzle diameter of 1.135 cm located at 20 cm from the beginning of the collimator and entrance and exit inner diameters of 7.62 cm. The 140 cm long tungsten collimator

was cut from 8.89 cm (3.5") diameter, ≥99.95% pure, tungsten rods into 14 equal length segments for manufacturability and portability and the inner conical holes of the collimator were cut using electrical discharge machining. A 4" hole was bored out of the 140 cm thick concrete wall which separated the neutron source from the experimental area. The hole was lined with a 3.5" schedule 80 PVC pipe to easily install and remove the tungsten collimator.

The neutron and gamma radiation field of a $^{252}$Cf source from the collimator was mapped using a 1"×1" EJ-309 scintillator and 1"×1", 95% $^{6}$Li enriched CLYC detector connected to a 2-D (horizontal and vertical) motorized Velmex BiSlide, which resulted in a uniform distribution of gamma rays, and fast and thermal neutrons.

The thermal neutron environment was characterized by placing the CLYC detector in the center of the beam and 7.62 cm left of the center both with and without the tungsten collimator. Additionally, the CLYC detector was placed in the room with the $^{252}$Cf source, located 1.42 m from the source and 0.73 m from the closest wall. The tungsten collimator significantly reduced the thermal neutron events by $\sim 778\times$ compared to the number of thermal neutron events with the CLYC detector in the same room as the source, and it reduced the number of thermal neutron events by $\sim 15\times$ compared to number of the thermal neutron events without the collimator.

Modeling the tungsten collimator and CLYC detector in MCNP, the simulation indicated that the tungsten collimator allows a near-pure neutron spectrum from the neutron source to the target area (1.6% increase in $^{6}$Li(n,t) reaction rate). The increased thermal neutron events in the experimental data (in beam with tungsten collimator) are possibly from cosmic and terrestrial neutrons, room return neutrons in the experimental area, and room return neutrons from the room with the neutron source that leak out of the room through the collimator. Initial characterization of the experimental area room-return neutrons and cosmic and terrestrial neutrons

indicated that ∼49% of the in-beam thermal neutron capture $^{6}$Li(n,t) reaction rate can be accounted for by these two sources.

### 6.5.1 Future work

The fast neutron facility capability with the tungsten collimator could be enhanced by installing a remotely controlled, 3D motorized translation stage to position the neutron source with the collimator and to design a new source holder to reduce the thermalized neutrons from the holder.

The neutron environment from the collimator can be further characterized by using a $^{7}$Li-enriched CLYC detector to measure the $^{35}$Cl reactions, which can then be subtracted from the events in the $^{6}$Li-enriched CLYC detector to better estimate the fast and thermal $^{6}$Li(n,t) capture events. Furthermore, thermal neutron absorption materials, such as cadmium, can be placed in different locations to possibly further reduce the thermal neutron environment at the end of the collimator.

Finally, the fast neutron facility with the tungsten collimator can be used for thermal neutron sensitive measurements, such as calculating the $^{252}$Cf SACS for reactions with high thermal neutron cross sections and researching the fast neutron detection efficiency in thermal neutron sensitive detectors, such as CLYC.

## 6.6 Acknowledgment

This material is based upon work supported by the Defense Threat Reduction Agency Grant HDTRA1033292.

# VII. Conclusions and Recommendations

This research successfully developed unique capabilities to improve neutron nuclear data measurement in the areas of neutron inelastic scattering cross section measurements, including $^{16}$O(n,n'$\gamma$), plastic scintillator formulations that can be used in light-based 3D printing for fast neutron imagery and high spatial resolution neutron detection, and thermal neutron sensitive measurements. This resulted in the establishment of GENESIS at Lawrence Berkeley National Laboratory, establishment of the fast neutron facility at AFIT, development of a new, 3D printable scintillator formulation being submitted for a patent, and demonstration of proof-of-principle methods to conduct novel measurements to address long-standing nuclear data gaps.

## 7.1 Inelastic Scattering Cross Section Measurements

There is a need to experimentally measure the inelastic scattering neutron cross section of $^{16}$O at a wide range of neutron energies to provide more accurate data and fill gaps of missing cross-section data. The new GENESIS capability at the 88-Inch Cyclotron at Lawrence Berkeley National Laboratory was designed to measure neutron inelastic scattering cross sections using an array of high-resolution HPGe clover detectors to measure the gamma rays from the excited target nuclei and 26 EJ-309 liquid organic scintillators to measure the inelastically scattered neutrons. When taken in coincidence, the GENESIS detector array can measure the partial double-differential cross section. This work helped develop, improve, and characterize the GENESIS capability and developed the code and algorithms to process the GENESIS data to support these measurements.

A preliminary and scoping experiment was conducted on $^{16}$O by placing an

alumina ($Al_2O_3$) target in the neutron beam generated from 14 MeV deuterons breaking up on a carbon target. The analyses of the data from the ∼6 hour run was successful in calculating the number of counts in the HPGe clover detectors from the 2$^{nd}$ excited state of $^{16}$O using the 6.129 MeV full energy and escape peaks. To calculate the partial cross section of the 2$^{nd}$ excited state, the HPGe detector efficiency at high energies (>6 MeV) and characterization of the incident neutron beam is needed, which are currently in progress. Additionally, the limited experimental time and low energy neutron beam prevented the analyses of higher $^{16}$O states and outgoing neutron coincidence data.

### 7.1.1 Current and Future Work

Current work continues to measure and calibrate the efficiency of the HPGe detectors at higher energies and characterize the incident neutron beam using the sToF system, both of which are needed to calculate the cross section. The next experiment with $^{16}$O will be conducted over multiple days and with 23 MeV deuterons, enabling the measurement of higher energy states of $^{16}$O and outgoing neutron coincidence data. Additionally, the BGO shields from the HPGe clover detectors will be removed to reduce the number $^{16}$O inelastically scattered neutron events outside of the $^{16}$O target. In addition to the $^{16}$O(n,n') measurement, the longer run time and higher energy neutron beam will possibly enable the measurement of the partial cross section for other reactions, such as $^{27}$Al(n,p)$^{27}$Mg, $^{16}$O(n,$\alpha$)$^{13}$C, $^{27}$Al(n,d)$^{26}$Mg, $^{16}$O(n,n+$\alpha$)$^{12}$C, $^{27}$Al(n,n+p)$^{26}$Mg, $^{16}$O(n,p)$^{16}$N, and $^{16}$O(n,d)$^{15}$N.

## 7.2 Plastic Scintillators for 3D Printing

This research was successful in developing fast-, light-cured plastic scintillator formulations that can be used for light-based 3D printing using industry-standard 405 nm light. The most promising formulations for creating a clear and hard plastic contained a combined total of EJ-309/DIN and PPO of 30 wt% and a combined total of IBOA and crosslinker of 70 wt% with a IBOA/crosslinker ratio of 70/30. The plastic scintillators were generally solidified within 10-20 seconds in the 405 nm light from a Formlabs Form Cure. The scintillator with 25-30 wt% of PPO provided the highest radiation detection performance with the light yield up to 83% of EJ-276's and up to a PSD FoM of 1.31. The leaching and a hazy film that developed on these high PPO scintillator formulations was eliminated by placing the scintillators in an ethanol bath for 1 hour. The overall best performing scintillator was AFIT225B, which contained 5 wt% DIN, 25 wt% PPO, 21 wt% HDDMA, 0.2 wt% Exalite 416, and 0.1 wt% TPO, did not leach due to the ethanol treatment, and produced a relative light yield of 83% of EJ-276 and PSD FoM of 1.28. Other noted issues such as surface cracking, haziness, and purpling were addressed through improved formulations and post-cure heat treatments.

### 7.2.1 Future Work

Future work includes further analysis of the effects of light yield due to curing time and TPO burn up, continuation of the formulation development to prevent leaching and/or increase radiation detection performance, and production of scintillators using a light-based 3D printer.

## 7.3 Reduction of Thermal Neutron Environments

Low thermal neutron environments are needed to perform thermal neutron sensitive experiments, such as $^{252}$Cf SACS cross section measurements for $^{10}$B(n,$\alpha$)$^{7}$Li and $^{6}$Li(n,t)$^{4}$He. However, in neutron experimental facilities, which use thick concrete or shielding for radiation protection, the neutrons scattering off the surfaces of the room create a room full of thermal and epi-thermal neutrons that are uniformly distributed. These room return neutrons can complicate or render the measurements impossible. By placing the target outside the room with the neutron source with a line-of-sight port to the neutron source and a collimator in the beam port, the thermal neutron environment at the target can be significantly reduced.

Different collimator designs and materials were modeled and simulated in MCNP to reduce the number of thermal neutrons from the collimator, which resulted in the final design of a conical converging-diverging tungsten collimator with a nozzle diameter of 1.135 cm located at 20 cm from the beginning of the collimator and entrance and exit inner diameters of 7.62 cm. The 140 cm long tungsten collimator was cut from 8.89 cm (3.5") diameter, $\geq$99.95% pure, tungsten rods into 14 equal length segments for manufacturability and portability and the inner conical holes of the collimator were cut using electrical discharge machining. A 4" hole was bored out of the 140 cm thick concrete wall at the AFIT fast neutron facility, which separated the neutron source from the experimental area. The hole was lined with a 3.5" schedule 80 PVC pipe to easily install and remove the tungsten collimator.

The neutron and gamma radiation field of a $^{252}$Cf source from the collimator was mapped using a 1"$\times$1" EJ-309 scintillator and 1"$\times$1", 95% $^{6}$Li enriched CLYC detector connected to a 2-D (horizontal and vertical) motorized Velmex BiSlide, which resulted in a uniform distribution of gamma rays, fast, and thermal neutrons.

The thermal neutron environment was characterized by placing the CLYC detector

in the center of the beam and 7.62 cm left of the center both with and without the tungsten collimator. Additionally, the CLYC detector was placed in the room with the $^{252}$Cf source, located 1.42 m from the source and 0.73 m from the closest wall. The tungsten collimator significantly reduced the thermal neutron events by ∼778 times compared to the number of thermal neutron events with the CLYC detector in the same room as the source, and it reduced the number of thermal neutron events by ∼15 times compared to number of the thermal neutron events without the collimator.

Modeling the tungsten collimator and CLYC detector in MCNP, the simulation indicated that the tungsten collimator allows a near-pure neutron spectrum from the neutron source to the target area (1.6% increase in $^{6}$Li(n,t) reaction rate). The increased thermal neutron events in the experimental data (in beam with tungsten collimator) are possibly from cosmic and terrestrial neutrons, room return neutrons in the experimental area, and room return neutrons from the room with the neutron source that leak out of the room through the collimator. Initial characterization of the experimental area room-return neutrons and cosmic and terrestrial neutrons indicated that ∼49% of the in-beam thermal neutron capture $^{6}$Li(n,t) reaction rate can be accounted for by these two sources.

### 7.3.1 Future work

The fast neutron facility capability with the tungsten collimator could be enhanced by installing a remotely controlled, 3D motorized translation stage to position the neutron source with the collimator and to design an new source holder to reduce the thermalization of neutrons in the holder.

The neutron environment from the collimator can be further characterized by using a $^{7}$Li-enriched CLYC detector to measure the $^{35}$Cl reactions, which can then be subtracted from the events in the $^{6}$Li-enriched CLYC detector to better estimate

the $^{6}$Li(n,t) events. Furthermore, thermal neutron absorption materials, such as cadmium, can placed in different locations to possibly further reduce the thermal neutron environment at the end of the collimator.

The fast neutron facility with the tungsten collimator can be used for thermal neutron sensitive measurements, such as calculating the $^{252}$Cf SACS for reactions with high thermal neutron cross sections, and to research the fast neutron detection efficiency in thermal neutron sensitive detectors such as CLYC.

# Appendix A. EJ-309 Positions

**Table A.1. Position of all the EJ-309 scintillators relative to the target location used in the $^{16}$O(n,n') experiment.**

| Detector | x [m] | y [m] | z [m] | d [m] |
|---|---|---|---|---|
| EJ-309 0 | 0.7253 | 0.1494 | -0.0183 | 0.7408 |
| EJ-309 1 | 0.5464 | 0.2747 | -0.0166 | 0.6118 |
| EJ-309 2 | 0.3812 | 0.3927 | -0.0170 | 0.5476 |
| EJ-309 3 | 0.1686 | 0.2499 | -0.3369 | 0.4520 |
| EJ-309 4 | -0.0514 | 0.2499 | -0.3365 | 0.4222 |
| EJ-309 5 | -0.2588 | 0.2523 | -0.3356 | 0.4932 |
| EJ-309 6 | -0.4082 | 0.3925 | -0.0238 | 0.5668 |
| EJ-309 7 | -0.5720 | 0.2795 | -0.0257 | 0.6371 |
| EJ-309 8 | -0.7526 | 0.1503 | -0.0219 | 0.7678 |
| EJ-309 9 | 0.7331 | -0.2575 | 0.2554 | 0.8179 |
| EJ-309 10 | 0.7361 | -0.0047 | 0.2542 | 0.7788 |
| EJ-309 11 | 0.6871 | 0.2391 | 0.2306 | 0.7632 |
| EJ-309 12 | 0.4790 | 0.2371 | 0.2300 | 0.5819 |
| EJ-309 13 | 0.3296 | 0.2500 | 0.2377 | 0.4771 |
| EJ-309 14 | 0.0805 | 0.2408 | 0.2300 | 0.3426 |
| EJ-309 15 | -0.1262 | 0.2416 | 0.2263 | 0.3543 |
| EJ-309 16 | -0.3197 | 0.2430 | 0.2266 | 0.4610 |
| EJ-309 17 | -0.5318 | 0.2432 | 0.2262 | 0.6270 |
| EJ-309 18 | -0.7112 | 0.2466 | 0.2242 | 0.7854 |
| EJ-309 19 | -0.7827 | -0.0002 | 0.2498 | 0.8215 |
| EJ-309 20 | 0.5180 | -0.0238 | 0.4369 | 0.6781 |
| EJ-309 21 | 0.3169 | -0.0222 | 0.4356 | 0.5392 |
| EJ-309 22 | 0.1117 | -0.0242 | 0.4347 | 0.4494 |
| EJ-309 23 | -0.0868 | -0.0211 | 0.4321 | 0.4412 |
| EJ-309 24 | -0.2879 | -0.0197 | 0.4326 | 0.5200 |
| EJ-309 25 | -0.4916 | -0.0216 | 0.4325 | 0.6551 |

# Appendix B. MDPP-16 Board Inputs

**Table B.1. Inputs for each of the MDPP-16 boards.**

| | MDPP-16 Board | | |
|---|---|---|---|
| **Channel** | **SCP (17)** | **QDC1 (18)** | **QDC2 (19)** |
| 0 | Clover 3-1 | EJ-309 0 | EJ-309 16 |
| 1 | Clover 3-2 | EJ-309 1 | EJ-309 17 |
| 2 | | EJ-309 2 | EJ-309 18 |
| 3 | Clover 3-4 | | EJ-309 19 |
| 4 | Clover 4-1 | EJ-309 4 | EJ-309 20 |
| 5 | Clover 4-2 | EJ-309 5 | EJ-309 21 |
| 6 | Clover 4-3 | EJ-309 6 | EJ-309 22 |
| 7 | Clover 4-4 | | EJ-309 23 |
| 8 | BGO 3 | EJ-309 8 | EJ-309 24 |
| 9 | BGO 4 | EJ-309 9 | EJ-309 25 |
| 10 | | EJ-309 10 | |
| 11 | Clover 3-3 | EJ-309 11 | |
| 12 | | EJ-309 12 | |
| 13 | | EJ-309 13 | LaBr |
| 14 | | EJ-309 14 | EJ-309 3 |
| 15 | | EJ-309 15 | EJ-309 7 |
| 32 | Trigger In | Trigger In | Trigger In |
| 33 | RF | RF | RF |

# Appendix C. MDPP-16 Board Settings

**Table C.1. "Module Init" settings for the MDPP-16 boards.**

| Register | Value | Description |
|---|---|---|
| 0x6042 | 2 | TDC resolution (0.098 ns) |
| 0x605C | 0 | Record all events per channel in window |
| 0x6050 | 15424 | Window start (-1500 ns from trigger input) |
| 0x6054 | 2880 | Window width (4500 ns) |
| 0x6058 | 0x001 | Trigger source (trigger 0 input) |
| 0x605E | 0x100 | Trigger output (all channels) |
| 0x6068 | 1 | NIM4 input (trigger 0 input) |
| 0x606C | 1 | NIM2 input (trigger 1 input) |
| 0x6096 | 0b00 | Time stamp source (VME) |
| 0x6044* | 3 | QDC output format (long and short integral and time) |

* QDC boards only

**Table C.2. MDPP-16 SCP board "Frontend Settings".**

| Register | Name | All | 0 & 1 | 2 & 3 | 4 & 5 | 6 & 7 | 8 & 9 | 10 & 11 | 12 & 13 | 14 & 15 |
|---|---|---|---|---|---|---|---|---|---|---|
| 0x6100 | select_chan_pair | 8 | 0 | 1 | 2 | 3 | 4 | 5 | 6 | 7 |
| 0x6110 | tf_int_diff | 3 | 1 | 1 | 1 | 1 | 20 | | 1 | 1 |
| 0x6112 | PZ0 | 4650 | 3950 | 4050 | 4000 | 4050 | 20 | 4050 | 4550 | 4500 |
| 0x6114 | PZ1 | 4650 | 4100 | 4150 | 4350 | 4220 | 20 | 3920 | 4500 | 4500 |
| 0x611A | gain | 2000 | 235 | 225 | 285 | 285 | 3000 | 105 | 697 | 697 |
| 0x611C | threshold0 | 0x800 | 280 | 250 | 220 | 260 | 600 | 600 | 400 | 300 |
| 0x611E | threshold1 | 0x800 | 220 | 280 | 300 | 260 | 700 | 250 | 300 | 1050 |
| 0x6124 | shaping_time | 480 | | | | | 20 | | 440 | 440 |
| 0x612A | signal_rise_time | 120 | | | | | 0 | | | |
| 0x6126 | BLR | 1 | | | | | | | | |
| 0x6128 | reset_time | 16 | | | | | | | | |

**Table C.3. MDPP-16 QDC boards "Frontend Settings".**

| Register | Name | All |
|---|---|---|
| 0x6100 | select_chan_pair | 8 |
| 0x6110 | signal_width | 12 |
| 0x6112 | input_amplitude | 6000 |
| 0x6114 | jumper_range | 6000 |
| 0x6118 | integration_long | 40 |
| 0x611A | integration_short | 2 |
| 0x611C | threshold0 | 0x200 |
| 0x611E | threshold1 | 0x200 |

For the LaBr detector, which was connected to channel 13 on the MDPP-16 QDC2 board, had the same settings except for what is listed in Table C.4.

**Table C.4. MDPP-16 QDC boards "Frontend Settings" for LaBr detector.**

| Register | Name | All |
|---|---|---|
| 0x6100 | select_chan_pair | 6 |
| 0x6110 | signal_width | 16 |
| 0x6118 | integration_long | 30 |
| 0x611A | integration_short | 1 |

# Appendix D. HPGe Efficiency Calibrations

**Table D.1. Gamma rays from $^{152}$Eu and $^{56}$Co used for HPGe detector efficiency calibration with their corresponding intensities.**

| Source | Energy [MeV] | Intensity [%] |
|---|---|---|
| $^{152}$Eu | 0.245 | 7.583 ± 0.019 |
| | 0.344 | 26.500 ± 0.400 |
| | 0.411 | 2.234 ± 0.004 |
| | 0.444 | 3.148 ± 0.027 |
| | 0.779 | 12.942 ± 0.019 |
| | 0.867 | 4.245 ± 0.019 |
| | 0.964 | 14.605 ± 0.021 |
| | 1.086 | 10.207 ± 0.021 |
| | 1.090 | 1.727 ± 0.006 |
| | 1.112 | 13.644 ± 0.021 |
| | 1.213 | 1.422 ± 0.006 |
| | 1.299 | 1.623 ± 0.008 |
| | 1.408 | 21.005 ± 0.024 |
| $^{56}$Co | 0.847 | 100.000 ± 0.000 |
| | 0.977 | 1.439 ± 0.015 |
| | 1.038 | 13.990 ± 0.100 |
| | 1.175 | 2.279 ± 0.020 |
| | 1.238 | 67.600 ± 0.400 |
| | 1.360 | 4.330 ± 0.040 |
| | 1.771 | 15.690 ± 0.150 |
| | 2.015 | 3.080 ± 0.030 |
| | 2.035 | 7.880 ± 0.070 |
| | 2.598 | 17.280 ± 0.150 |
| | 3.010 | 1.049 ± 0.010 |
| | 3.202 | 3.240 ± 0.030 |
| | 3.253 | 7.930 ± 0.060 |
| | 3.273 | 1.889 ± 0.020 |
| | 3.451 | 0.953 ± 0.100 |

# Bibliography


1. G. F. Knoll, *Radiation Detection and Measurement, 4th Edition.* Hoboken, NJ: John Wiley & Sons, 2010.

2. N. Tsoulfanidis and S. Landsberger, *Measurement & detection of radiation.* CRC press, 2021.

3. A. J. Bell, "Analysis of gps satellite allocation for the united states nuclear detonation detection system (usnds)," Master's thesis, Air Force Institute of Technology, Wright-Patterson AFB, OH, 2002. [Online]. Available: https://scholar.afit.edu/etd/4511/

4. K. Moody, P. Grant, and I. Hutcheon, *Nuclear Forensic Analysis.* CRC Press, 2015.

5. V. Fedchenko, *The New Nuclear Forensics: Analysis of Nuclear Materials for Security Purposes.* Oxford university press, 2015.

6. M. J. Kristo, "Chapter 13 - nuclear forensics," in *Handbook of Radioactivity Analysis: Volume 2 (Fourth Edition)*, fourth edition ed., M. F. L'Annunziata, Ed. Academic Press, 2020, pp. 921–951. [Online]. Available: https://www.sciencedirect.com/science/article/pii/B9780128143957000131

7. S. Glasstone, P. J. Dolan *et al.*, *The effects of nuclear weapons.* US Department of Defense, 1977, vol. 50, no. 3.

8. N. E. Agency". Nea nuclear data high priority request list. [Online]. Available: https://www.oecd-nea.org/dbdata/hprl/search.pl?vhp=on

9. L. Bernstein, D. Brown, A. Hurst, J. Kelly, F. Kondev, E. McCutchan, C. Nesaraja, R. Slaybaugh, and A. Sonzogni, "Nuclear data needs and capabilities for applications," 2015.

10. N. E. Agency". Collaborative international evaluated library organisation pilot project. [Online]. Available: https://www.oecd-nea.org/science/wpec/sg40-cielo/

11. Department of Energy, Office of Science, "Nuclear Data Interagency Working Group (NDIAWG) Research Program, DE-FOA-00002440," 2020.

12. C. Romano, "The nuclear data working group: Accomplishments and future plans," Oak Ridge National Laboratory, Tech. Rep., 2017. [Online]. Available: https://www.osti.gov/servlets/purl/1414710

13. R. Bahran, C. Romano, C. Sloan, T. Hallman, S. Gorski *et al.*, "Proceedings of the 2018 nuclear data road-mapping and enhancement workshop (ndrew)," Institut Atomnoi Energii I.V. Kurchatova, Tech. Rep. LA-UR-18-22315, 2018. [Online]. Available: https://permalink.lanl.gov/object/tr?what=info:lanl-repo/lareport/LA-UR-18-22315

14. L. Bernstein, C. Romano, D. Brown, R. Casperson, M.-A. Descalle, M. Devlin, C. Pickett, B. Rearden, and C. Vermeuelen, "Final report for the workshop for applied nuclear data activities (wanda)," Oak Ridge National Laboratory, Tech. Rep., 2019. [Online]. Available: https://nucleardata.berkeley.edu/wanda/docs/WANDA_2019_Final_Report_040119.pdf

15. C. E. Romano, L. A. Bernstein, T. Bailey, F. Bostelmann, D. A. Brown *et al.*, "Proceedings of the workshop for applied nuclear data: Wanda2020," Tech. Rep., 7 2020. [Online]. Available: https://www.osti.gov/biblio/1649010

16. P. Mermod, J. Blomgren, C. Johansson, A. Ohrn, M. Osterlund *et al.*, "95 mev neutron scattering on hydrogen, deuterium, carbon, and oxygen," *Phys.Rev. C*, vol. 74, 2006.

17. A.Takahashi, M.Gotoh, Y.Sasaki, and H.Sugimoto, "Double and single differential neutron emission cross sections at 14.1 mev for natfe, 16o and and natni," Osaka University, Tech. Rep. OKTAVIAN Report 92-01, 1992.

18. N. Olsson, E. Ramström, and B. Trostell, "Neutron elastic and inelastic scattering from beryllium, nitrogen and oxygen at en = 21.6 mev," *Nuclear Physics A*, vol. 509, no. 1, pp. 161 – 177, 1990. [Online]. Available: http://www.sciencedirect.com/science/article/pii/037594749090379Z

19. G. Boerker, R. Boettger, H. Brede, H. Klein, W. Mannhart, and B. Siebert, "Elastic and inelastic differential neutron scattering cross sections of oxygen between 6 and 15 mev," Physikalisch-Technische Bundesanstalt, Tech. Rep., 1989.

20. M. Baba, M. Ishikawa, T. Kikuchi, H. Wakabayashi, N. Yabuta, and N. Hirakawa, "Double differential neutron emission cross sections of be-9, o-16, al-27, v-51, mn-55," *Conference on Nuclear Data For Science and Technology*, p. 209, 1988.

21. M. S. Islam, R. W. Finlay, and J. S. Petler, "Elastic and inelastic scattering of nucleons from $^{16}$o," *Nucl.Phys.*, vol. A464, p. 395, 1987.

22. P. Grabmayr, J. Rapaport, and R. Finlay, "Elastic and inelastic scattering of 24 mev nucleons from oxygen isotopes," *Nuclear Physics A*, vol. 350, no. 1, pp. 167 – 189, 1980. [Online]. Available: http://www.sciencedirect.com/science/article/pii/0375947480903954

23. W. E. Kinney and F. G. Perey, "Neutron elastic- and inelastic-scattering cross sections for oxygen in the energy range 4.34 to 8.56 mev," Oak Ridge National Laboratory, Tech. Rep. ORNL-4780, 1972.

24. G. C. Bonazzola, T. Bressani, E. Chiavassa, and L. Naldi, "Backward scattering of 14.1 mev neutrons from $^{16}$o," *Lett.Nuovo Cim.*, vol. 5, p. 226, 1972.

25. D. Meier, M. Brullmann, H. Jung, and P. Marmier, "Elastische und inelastische streuung von 14, 1-mev-neutronen an $^{16}$o und $^{18}$o," *Helv.Phys.Acta*, vol. 42, p. 813, 1969.

26. W. J. McDonald, J. M. Robson, and R. Malcolm, "Scattered neutrons and gamma rays from the $^{16}$o(n, n'$\gamma$)$^{16}$o reaction at e = 14.1 mev," *Nucl.Phys.*, vol. 75, p. 353, 1966.

27. R. W. Bauer, J. D. Anderson, and L. J. Christensen, "Scattering of 14 mev neutrons from nitrogen and oxygen," *Nucl.Phys.*, vol. 47, p. 241, 1963.

28. F. G. J. Perey, "Inelastic scattering of 14-mev neutrons by carbon, oxygen and lithium," *Bulletin of the American Physical Society*, vol. 5, p. 18, 1960.

29. T. Kozlowski, W. Kusch, and J. Wojtkowskat, "Angular distribution of gamma rays from inelastic scattering of 14.1 mev neutrons on c-12 and o-16," Inst. Badan Jadr. (Nucl. Res.), Tech. Rep. 661, 1965.

30. J. B. Birks, *The theory and practice of scintillation counting: International series of monographs in electronics and instrumentation.* Elsevier, 2013, vol. 27.

31. F. Brooks, "Development of organic scintillators," *Nuclear Instruments and Methods*, vol. 162, no. 1-3, pp. 477–505, 1979.

32. M. Sénoville, F. Delaunay, M. Pârlog, N. Achouri, and N. Orr, "Neutron-$\gamma$ discrimination with organic scintillators: Intrinsic pulse shape and light yield contributions," *Nuclear Instruments and Methods in Physics Research Section A: Accelerators, Spectrometers, Detectors and Associated Equipment*, vol. 971, p. 164080, 2020.

33. S. Moser, W. Harder, C. Hurlbut, and M. Kusner, "Principles and practice of plastic scintillator design," *Radiation Physics and Chemistry*, vol. 41, no. 1, pp. 31–36, 1993. [Online]. Available: https://www.sciencedirect.com/science/article/pii/0969806X9390039W

34. N. Zaitseva, B. L. Rupert, I. PaweŁczak, A. Glenn, H. P. Martinez, L. Carman, M. Faust, N. Cherepy, and S. Payne, "Plastic scintillators with efficient neutron/gamma pulse shape discrimination," *Nuclear Instruments and Methods in Physics Research Section A: Accelerators, Spectrometers, Detectors and Associated Equipment*, vol. 668, pp. 88–93, 2012.

35. H. Nakamura, H. Kitamura, O. Shinji, K. Saito, Y. Shirakawa, and S. Takahashi, "Development of polystyrene-based scintillation materials and its mechanisms," *Applied Physics Letters*, vol. 101, no. 26, p. 261110, 2012.

36. N. Hawkes and G. Taylor, "Analysis of the pulse shape mechanism in a plastic scintillator with efficient neutron/gamma pulse shape discrimination," *Nuclear Instruments and Methods in Physics Research Section A: Accelerators, Spectrometers, Detectors and Associated Equipment*, vol. 729, pp. 522–526, 2013.

37. G. H. Bertrand, M. Hamel, and F. Sguerra, "Current status on plastic scintillators modifications," *Chemistry–A European Journal*, vol. 20, no. 48, pp. 15 660–15 685, 2014.

38. N. Zaitseva, A. Glenn, A. Mabe, M. Carman, C. Hurlbut, J. Inman, and S. Payne, "Recent developments in plastic scintillators with pulse shape discrimination," *Nuclear Instruments and Methods in Physics Research Section A: Accelerators, Spectrometers, Detectors and Associated Equipment*, vol. 889, pp. 97–104, 2018. [Online]. Available: https://www.sciencedirect.com/science/article/pii/S0168900218301268

39. Y. Mishnayot, M. Layani, I. Cooperstein, S. Magdassi, and G. Ron, "Three-dimensional printing of scintillating materials," *Review of Scientific Instruments*, vol. 85, no. 8, p. 085102, 2014.

40. J. Zhu, Y. Ding, J. Zhu, D. Qi, M. Su, Y. Xu, Y. Bi, R. Lin, and L. Zhang, "Preparation and characterization of a novel uv-curable plastic scintillator," *Nuclear Instruments and Methods in Physics Research Section A: Accelerators, Spectrometers, Detectors and Associated Equipment*, vol. 817, pp. 30–34, 2016.

41. S. Lee, J. Son, D. G. Kim, J. Choi, and Y. K. Kim, "Characterization of plastic scintillator fabricated by uv led curing machine," *Nuclear Instruments and Methods in Physics Research Section A: Accelerators, Spectrometers, Detectors and Associated Equipment*, vol. 929, pp. 23–28, 2019.

42. D. geon Kim, S. Lee, Y. H. Kim, S. J. Seon, J. Sejin, J. Y. Jeong, and Y. K. Kim, "Scintillation light output of 3d printed plastic scintillators," presented at Transactions of the Korean Nuclear Society Spring Meeting, Jeju, Korea, 2018. [Online]. Available: https://www.kns.org/files/pre_paper/39/18S-260%EA%B9%80%EB%8F%99%EA%B1%B4.pdf

43. D. geon Kim, S. Lee, J. Park, J. Son, T. H. Kim, Y. H. Kim, K. Pak, and Y. K. Kim, "Performance of 3d printed plastic scintillators for gamma-ray detection," *Nuclear Engineering and Technology*, vol. 52, no. 12, pp. 2910–2917, 2020. [Online]. Available: https://www.sciencedirect.com/science/article/pii/S1738573319308071

44. International Atomic Energy Agency Nuclear Data Services, "Testing and Improving the International Reactor Dosimetry and Fusion File (IRDFF)," Accessed 7 Jan 2022 [Online]. [Online]. Available: https://www-nds.iaea.org/IRDFFtest/

45. A. Trkov, P. Griffin, S. Simakov, L. Greenwood, K. Zolotarev *et al.*, "Irdff-ii: A new neutron metrology library," *Nuclear Data Sheets*, vol. 163, pp. 1–108, 2020. [Online]. Available: https://www.sciencedirect.com/science/article/pii/S0090375219300687

46. H. R. Vega-Carrillo, E. Manzanares-Acuña, M. Pilar Iñiguez, E. Gallego, and A. Lorente, "Study of room-return neutrons," *Radiation Measurements*, vol. 42, no. 3, pp. 413–419, 2007. [Online]. Available: https://www.sciencedirect.com/science/article/pii/S1350448707000443

47. R. Khabaz, "Analysis of neutron scattering components inside a room with concrete walls," *Applied Radiation and Isotopes*, vol. 95, pp. 1–7, 2015. [Online]. Available: https://www.sciencedirect.com/science/article/pii/S0969804314003327

48. S. Yip, *Nuclear Radiation Interactions.* World Scientific Publishing Company, 2014.

49. D. Tilley, H. Weller, and C. Cheves, "Energy levels of light nuclei a = 16–17," *Nuclear Physics A*, vol. 564, no. 1, pp. 1 – 183, 1993. [Online]. Available: http://www.sciencedirect.com/science/article/pii/0375947493900737

50. K. S. Krane, *Introductory to Nuclear Physics.* John Wiley & Sons, Inc., 1988.

51. A. Koning and H. Akkermans, *Pre-Equilibrium Nuclear Reactions: An introduction to classical and quantum-mechanical models*, 01 1999.

52. W. D. Loveland, D. J. Morrissey, and G. T. Seaborg, *Modern nuclear chemistry.* John Wiley & Sons, 2006.

53. TUNL Nuclear Data Evaluation Project, "$^{17}$o thermal neutron capture evaluated data." [Online]. Available: http://www.tunl.duke.edu/nucldata/TNC/17O.shtml

54. Nuclear Data Center, "Thermal Neutron Capture $\gamma$'s (CapGam)," Brookhaven National Laboratory. [Online]. Available: https://www.nndc.bnl.gov/capgam/

55. D. A. Brown. Delivering endf libraries to end-users: the nuclear data pipeline. National Nuclear Data Center, Brookhaven National Laboratory. [Online]. Available: http://www.oecd-nea.org/dbdata/meetings/jeff_stakeholders_2019/JSW_16.pdf

56. L. A. Bernstein, D. A. Brown, A. J. Koning, B. T. Rearden, C. E. Romano, A. A. Sonzogni, A. S. Voyles, and W. Younes, "Our future nuclear data needs," *Annual Review of Nuclear and Particle Science*, vol. 69, no. 1, pp. 109–136, 2019. [Online]. Available: https://doi.org/10.1146/annurev-nucl-101918-023708

57. N. Otuka, E. Dupont, V. Semkova, B. Pritychenko, A. Blokhin *et al.*, "Towards a more complete and accurate experimental nuclear reaction data library (exfor): International collaboration between nuclear reaction data centres (nrdc)," *Nuclear Data Sheets*, vol. 120, pp. 272–276, 2014. [Online]. Available: https://www.sciencedirect.com/science/article/pii/S0090375214005171

58. V. Zerkin and B. Pritychenko, "The experimental nuclear reaction data (exfor): Extended computer database and web retrieval system," *Nuclear Instruments and Methods in Physics Research Section A: Accelerators, Spectrometers, Detectors and Associated Equipment*, vol. 888, pp. 31 – 43, 2018. [Online]. Available: http://www.sciencedirect.com/science/article/pii/S0168900218300627

59. D. Brown, M. Chadwick, R. Capote, A. Kahler, A. Trkov *et al.*, "Endf/b-viii.0: The 8th major release of the nuclear reaction data library with cielo-project cross sections, new standards and thermal scattering data," *Nuclear Data Sheets*, vol. 148, pp. 1 – 142, 2018, special Issue on Nuclear Reaction Data. [Online]. Available: http://www.sciencedirect.com/science/article/pii/S0090375218300206

60. A. Santamarina, D. Bernard, P. Blaise, M. Coste, A. Courcelle *et al.*, "The jeff-3.1.1 nuclear data library," Nuclear Energy Agency, Tech. Rep., 2009.

61. K. Shibata, O. Iwamoto, T. Nakagawa, N. Iwamoto, A. Ichihara *et al.*, "Jendl-4.0: A new library for nuclear science and engineering," *Journal of Nuclear Science and Technology*, vol. 48, no. 1, pp. 1–30, 2011. [Online]. Available: https://doi.org/10.1080/18811248.2011.9711675

62. Z. Ge, Z. Zhao, H. Xia, Y. Zhuang, T. Liu, J. Zhang, and H. Wu, "The updated version of chinese evaluated nuclear data library (cendl-3.1)," *Journal of the Korean Physical Society*, vol. 59, pp. 1052–1056, 2011. [Online]. Available: https://doi.org/10.3938/jkps.59.1052

63. A. Blokhin, E. Gai, A. Ignatyuk, I. Koba, V. Manokhin, and V. Pronyaev, "New version of neutron evaluated data library brond-3.1," *Problems of Atomic Science and Technology. Series: Nuclear and Reactor Constants*, vol. 2, p. 62, 2016. [Online]. Available: https://vant.ippe.ru/en/brond-3-1.html

64. R. D. Evans, *The Atomic Nucleus*. New York: McGraw-hill, Inc., 1955.

65. G. F. Knoll, *Radiation Detection and Measurement*. John Wiley & Sons, Inc., 2010.

66. R. Casanovas, J. Morant, and M. Salvadó, "Development and calibration of a real-time airborne radioactivity monitor using gamma-ray spectrometry on a particulate filter," *IEEE Transactions on Nuclear Science*, vol. 61, 01 2014.

67. F. Pino, L. Stevanato, D. Cester, G. Nebbia, L. Sajo-Bohus, and G. Viesti, "The light output and the detection efficiency of the liquid scintillator ej-309," *Applied Radiation and Isotopes*, vol. 89, pp. 79–84, 2014. [Online]. Available: https://www.sciencedirect.com/science/article/pii/S0969804314000682

68. S. Prahl, "POPOP," 2017. [Online]. Available: https://omlc.org/spectra/PhotochemCAD/html/077.html

69. H. Du, R.-C. A. Fuh, J. Li, L. A. Corkan, and J. S. Lindsey, "PhotochemCAD: A Computer-Aided Design and Research Tool in Photochemistry," *Photochemistry and photobiology*, vol. 68, no. 2, pp. 141–142, 1998.

70. J. M. Dixon, M. Taniguchi, and J. S. Lindsey, "PhotochemCAD 2: A Refined Program with Accompanying Spectral Databases for Photochemical Calculations," *Photochemistry and Photobiology*, vol. 81, no. 1, pp. 212–213, 2005.

71. L. H. Sperling, *Introduction to physical polymer science*. John Wiley & Sons, 2005.

72. S. M. Sze and K. K. Ng, *Physics of semiconductor devices*. John wiley & sons, 2006.

73. R. F. Pierret, *Semiconductor device fundamentals*. Pearson Education India, 1996.

74. N. Tsoulfanidis, *Measurement and Detection of Radiation*. CRC press, 2010.

75. "Ortec", "Lanthanum bromide scintillation detectors." [Online]. Available: https://www.ortec-online.com/-/media/ametekortec/brochures/lanthanum.pdf

76. K. Harrig, B. Goldblum, J. Brown, D. Bleuel, L. Bernstein, J. Bevins, M. Harasty, T. Laplace, and E. Matthews, "Neutron spectroscopy for pulsed beams with frame overlap using a double time-of-flight technique," *Nuclear Instruments and Methods in Physics Research Section A: Accelerators, Spectrometers, Detectors and Associated Equipment*, vol. 877, pp. 359 – 366, 2018. [Online]. Available: http://www.sciencedirect.com/science/article/pii/S0168900217310215

77. J. R. Oppenheimer, "The disintegration of the deuteron by impact," *Physical Review*, vol. 47, pp. 845–846, Jun 1935. [Online]. Available: https://link.aps.org/doi/10.1103/PhysRev.47.845

78. S. M. Dancoff, "Disintegration of the deuteron in flight," *Physical Review*, vol. 72, pp. 1017–1022, Dec 1947. [Online]. Available: https://link.aps.org/doi/10.1103/PhysRev.72.1017

79. B. V. Carlson, R. Capote, and M. Sin, "Elastic and inelastic breakup of deuterons with energy below 100 mev," 2015.

80. D. Bleuel, M. McMahan, L. Ahle, B. Barquest, J. Cerny, L. Heilbronn, and C. Jewett, "Characterization of a tunable quasi-monoenergetic neutron beam from deuteron breakup," *Nuclear Instruments and Methods in Physics Research Section B: Beam Interactions with Materials and Atoms*, vol. 261, no. 1, pp. 974–979, 2007, the Application of Accelerators in Research and Industry. [Online]. Available: https://www.sciencedirect.com/science/article/pii/S0168583X07009238

81. M. McMahan, L. Ahle, D. Bleuel, L. Bernstein, B. Barquest, J. Cerny, L. Heilbronn, C. Jewett, I. Thompson, and B. Wilson, "Neutron beams from deuteron breakup at the 88-inch cyclotron at lawrence berkeley national laboratory," *International Conference on Nuclear Data for Science and Technology*, 01 2007. [Online]. Available: http://dx.doi.org/10.1051/ndata:07456

82. G. Baur, F. Rösel, D. Trautmann, and R. Shyam, "Fragmentation processes in nuclear reactions," *Physics Reports*, vol. 111, no. 5, pp. 333–371, 1984. [Online]. Available: https://www.sciencedirect.com/science/article/pii/0370157384901388

83. R. Serber, "The production of high energy neutrons by stripping," *Physical Review*, vol. 72, pp. 1008–1016, Dec 1947. [Online]. Available: https://link.aps.org/doi/10.1103/PhysRev.72.1008

84. A. C. Helmholz, E. M. McMillan, and D. C. Sewell, "Angular distribution of neutrons from targets bombarded by 190-mev deuterons," *Physical Review*, vol. 72, pp. 1003–1007, Dec 1947. [Online]. Available: https://link.aps.org/doi/10.1103/PhysRev.72.1003

85. J.-P. Meulders, P. Leleux, P. C. Macq, and C. Pirart, "Fast neutron yields and spectra from targets of varying atomic number bombarded with deuterons from 16 to 50 mev (for radiobiology and radiotherapy)," *Physics in Medicine & Biology*, vol. 20, no. 2, p. 235, 1975.

86. L. A. Bernstein, D. A. Brown, A. J. Koning, B. T. Rearden, C. E. Romano, A. A. Sonzogni, A. S. Voyles, and W. Younes, "Our future nuclear data needs," *Annual Review of Nuclear and Particle Science*, vol. 69, no. 1, pp. 109–136, 2019. [Online]. Available: https://doi.org/10.1146/annurev-nucl-101918-023708

87. R. C. Runkle, D. L. Chichester, and S. J. Thompson, "Rattling nucleons: New developments in active interrogation of special nuclear material," *Nuclear Instruments and Methods in Physics Research Section A: Accelerators, Spectrometers, Detectors and Associated Equipment*, vol. 663, no. 1, pp. 75–95, 2012. [Online]. Available: https://www.sciencedirect.com/science/article/pii/S016890021101847X

88. N. E. Agency, "NEA nuclear data high priority request list," https://www.oecd-nea.org/dbdata/hprl/search.pl?vhp=on, 2020, accessed: 28 Dec 2021.

89. L. Bernstein, D. Brown, A. Hurst, J. Kelly, F. Kondev, E. McCutchan, C. Nesaraja, R. Slaybaugh, and A. Sonzogni, "Nuclear data needs and capabilities for applications," Lawrence Berkeley National Laboratory, Berkeley, CA, Tech. Rep., May 2015. [Online]. Available: https://arxiv.org/pdf/1511.07772.pdf

90. C. Romano, "The Nuclear Data Working Group: Accomplishments and Future Plans," Oak Ridge National Laboratory, Tech. Rep. 1414710, 2017. [Online]. Available: https://www.osti.gov/servlets/purl/1414710

91. R. Bahran, C. Romano, C. Sloan, T. Hallman, S. Gorski *et al.*, "Proceedings of the 2018 Nuclear Data Road-mapping and Enhancement Workshop (NDREW)," Los Alamos National Laboratory, Tech. Rep. LA-UR-18-22315, 2018. [Online]. Available: https://permalink.lanl.gov/object/tr?what=info:lanl-repo/lareport/LA-UR-18-22315

92. L. Bernstein, C. Romano, D. Brown, R. Casperson, M.-A. Descalle, M. Devlin, C. Pickett, B. Rearden, and C. Vermeuelen, "Final Report for the Workshop for Applied Nuclear Data Activities (WANDA)," Lawrence Livermore National Laboratory, Tech. Rep. LLNL-PROC-769849, 2019. [Online]. Available: https://nucleardata.berkeley.edu/wanda/docs/WANDA_2019_Final_Report_040119.pdf

93. C. E. Romano, L. Bernstein, T. Bailey, R. Bostelmann, D. A. Brown *et al.*, "Proceedings of the workshop for applied nuclear data: Wanda 2020," Oak Ridge National Laboratory, Tech. Rep. ORNL/TM-2020/1617, July 2020. [Online]. Available: https://www.osti.gov/biblio/1649010

94. K. Harrig, B. Goldblum, J. Brown, D. Bleuel, L. Bernstein, J. Bevins, M. Harasty, T. Laplace, and E. Matthews, "Neutron spectroscopy for pulsed beams with frame overlap using a double time-of-flight technique," *Nuclear Instruments and Methods in Physics Research Section A: Accelerators, Spectrometers, Detectors and Associated Equipment*, vol. 877, pp. 359 – 366, 2018. [Online]. Available: http://www.sciencedirect.com/science/article/pii/S0168900217310215

95. D. L. Bleuel, M. A. McMahan, L. Ahle, B. R. Barquest, J. Cerny, L. H. Heilbronn, and C. C. Jewett, "Characterization of a tunable quasi-monoenergetic neutron beam from deuteron breakup," *Nuclear Inst. and Methods in Physics Research B*, vol. 261, pp. 974–979, 2007.

96. J. E. Bevins, Z. Sweger, N. Munshi, B. Goldblum, J. Brown, D. Bleuel, L. Bernstein, and R. Slaybaugh, "Performance evaluation of an energy tuning assembly for neutron spectral shaping," *Nuclear Inst. and Methods in Physics Research A*, vol. 923, pp. 79–87, 2019.

97. R. Serber, "The production of high energy neutrons by stripping," *Phys. Rev.*, vol. 72, pp. 1008–1016, 1947.

98. J. P. Meulders, P. Leleux, P. C. Macq, and C. Pirart, "Fast neutron yields and spectra from targets of varying afomic number bombarded with deuterons from 16 to 50 mev," *Phys. Med. Biol.*, vol. 20, no. 2, pp. 235–243, 1975.

99. K. A. Weaver, "Neutrons from deuteron bombardment of light nuclei," Ph.D. dissertation, University of Wisconsin, 1972.

100. M. A. Lone, C. B. Bigham, J. S. Fraser, H. R. Schneider, T. K. Alexander, A. J. Ferguson, and A. B. McDonald, "Thick target neutron yields and spectral distributions from the $^{7}$Li($^{d}_{p}$,n) and $^{9}$Be($^{d}_{p}$,n) reactions," *Nuclear Inst. and Methods*, vol. 143, pp. 331–344, 1977.

101. J. Allison, K. Amako, J. Apostolakis, P. Arce, M. Asai *et al.*, "Recent developments in GEANT4," *Nuclear Inst. and Methods in Physics Research A*, vol. 835, pp. 186–225, 2016.

102. E. Mendoza, D. Cano-Ott, T. Koi, and C. Guerrero, "New standard evaluated neutron cross section libraries for the GEANT4 code and first verification," *IEEE Transactions on Nuclear Science*, vol. 61, no. 4, pp. 2357–2364, 2014.

103. Eljen Technology, "Neutron/Gamma PSD EJ-301, EJ-309," Accessed 5 Oct 2021 [Online]. [Online]. Available: https://eljentechnology.com/products/liquid-scintillators/ej-301-ej-309

104. Hamamatsu Photonics, "Photomultiplier tube assembly H6533," https://www.hamamatsu.com/us/en/product/type/H6533/index.html, accessed: 7 Dec 2021.

105. Hamamatsu Photonics, "Photomultiplier tube assembly H1949-51," https://www.hamamatsu.com/eu/en/product/type/H1949-51/index.html, accessed: 3 Dec 2021.

106. Hamamatsu Photonics, "Photomultiplier tube assembly H2431-50," Accessed: 3 Dec 2021. [Online]. Available: https://www.hamamatsu.com/us/en/product/type/H2431-50/index.html

107. Eljen Technology, "Silicone Grease EJ-550, EJ552," https://eljentechnology.com/products/accessories/ej-550-ej-552, accessed: 3 Dec 2021.

108. CAEN Technologies, "R8033," https://www.caen.it/products/r8033/, accessed: 3 Dec 2021.

109. CAEN Technologies, "R1470ET," https://www.caen.it/products/r1470et/, accessed: 3 Dec 2021.

110. Hamamatsu Photonics, "Photomultiplier tube R3998-02," https://www.hamamatsu.com/us/en/product/type/R3998-02/index.html, accessed: 3 Dec 2021.

111. iseg, "NHR: High Precision Versatile High Voltage Module in NIM Standard," https://iseg-hv.com/en/products/detail/NHR, accessed: 3 Dec 2021.

112. Mesytec, "MDPP-16," https://www.mesytec.com/products/nuclear-physics/MDPP-16.html, accessed: 3 Dec 2021.

113. A. Ruben, P. Bender, P. Chowdhury, P. L. Kerr, F. Lüke, G. Montermann, A. M. Rogers, and R. Schneider, "A new, versatile, high-performance digital pulse processor with application to neutron/gamma-ray pulse-shape discrimination in scintillator detectors," 07 2018.

114. mesytec, "Software Module MDPP-16-QDC," https://www.mesytec.com/products/datasheets/MDPP-16_QDC.pdf, accessed: 9 Jan 2022.

115. mesytec, *MDPP-16 SCP/RCP*, https://www.mesytec.com/products/datasheets/MDPP-16_SCP-RCP.pdf, accessed: 9 Jan 2022.

116. LeCroy, "429A Quad Logic Fan-in/Fan-Out," https://teledynelecroy.com/lrs/dsheets/428.htm, accessed: 3 Dec 2021.

117. G. Duchêne, F. A. Beck, P. J. Twin, G. de France, D. Curien, L. Han, C. W. Beausang, M. A. Bentley, P. J. Nolan, and J. Simpson, "The Clover: a new generation of composite Ge detectors," *Nuclear Inst. and Methods in Physics Research A*, vol. 432, pp. 90–110, 1999.

118. G. Dietze and H. Klein, "Gamma-calibration of NE 213 scintillation counters," *Nuclear Instruments and Methods in Physics Research*, vol. 193, no. 3, pp. 549–556, 1982.

119. W. Mannhart, "Status of the Cf-252 fission neutron spectrum evaluation with regard to recent experiments," in *International Nuclear Data Committee: Consultants' meeting on physics of neutron emission in fission.* International Atomic Energy Agency, 1989, pp. 305–336. [Online]. Available: https://www.osti.gov/servlets/purl/1414710

120. R. Stone, "Surprise nuclear strike? here's how we'll figure out who did it," *Science*, 2016. [Online]. Available: https://www.science.org/content/article/surprise-nuclear-strike-heres-how-well-figure-out-who-did-it

121. M. Boromiza, C. Borcea, P. Dessagne, D. Ghita, T. Glodariu *et al.*, "Nucleon inelastic scattering cross sections on $^{16}$O and $^{28}$Si," *Phys. Rev. C*, vol. 101, p. 024604, Feb 2020. [Online]. Available: https://link.aps.org/doi/10.1103/PhysRevC.101.024604

122. D. N. Grozdanov, N. A. Fedorov, V. M. Bystritsky, Y. N. Kopach, I. N. Ruskov *et al.*, "Measurement of angular distributions of gamma-rays from the inelastic scattering of 14.1-mev neutrons by carbon and oxygen nuclei," *Physics of Atomic Nuclei*, vol. 81, pp. 588–594, 2018. [Online]. Available: http://dx.doi.org/10.1134/S106377881805006X

123. R. O. Nelson, M. B. Chadwick, A. Michaudon, and P. G. Young, "High-resolution measurements and calculations of photon-production cross sections for 16o(n,x$\gamma$) reactions induced by neutrons with energies between 4 and 200 mev," *Nuclear Science and Engineering*, vol. 138, no. 2, pp. 105–144, 2001.

124. M. Thoennessen, "The discovery of isotopes," *Switzerland: Springer Int. Publ*, 2016.

125. M. Wang, W. Huang, F. Kondev, G. Audi, and S. Naimi, "The AME 2020 atomic mass evaluation (II). tables, graphs and references$*$," *Chinese Physics C*, vol. 45, no. 3, p. 030003, mar 2021. [Online]. Available: https://doi.org/10.1088/1674-1137/abddaf

126. F. Kondev, M. Wang, W. Huang, S. Naimi, and G. Audi, "The NUBASE2020 evaluation of nuclear physics properties $*$," *Chinese Physics C*, vol. 45, no. 3, p. 030001, mar 2021. [Online]. Available: https://doi.org/10.1088/1674-1137/abddae

127. K. Nyberg-Ponnert, B. Jonsson, and I. Bergqvist, "Gamma rays produced by the interaction of 15 mev neutrons in n, o, mg and al," *Phys.Scr.*, vol. 4, p. 165, 1971.

128. V. J. Orphan, C. G. Hoot, and J. John, "Gamma-ray production cross sections for the 16o(n,x$\gamma$) reaction from 6.35- to 16.52-mev neutron energy," *Nuclear Science and Engineering*, vol. 42, no. 3, pp. 352–366, 1970. [Online]. Available: https://doi.org/10.13182/NSE70-A21223

129. J. K. Dickens and F. G. Perey, "The 16o(n,x$\gamma$) reaction for $6.7 \leq$ en $\leq 11$ mev," *Nuclear Science and Engineering*, vol. 40, no. 2, pp. 283–293, 1970. [Online]. Available: https://doi.org/10.13182/NSE70-A19689

130. E. M. Burymov, "Cross sections for excitation of $o^{16}$, $al^{27}$, $cr^{52}$, and $zn^{64,66,68}$ levels by 14.6-mev neutrons," *Yadern.Fiz.*, vol. 9, p. 933, 1969.

131. A. I. Lashuk and I. P. Sadokhin, "Gamma-quanta production cross-sections at inelastic scattering of the neutrons on the nuclei of reactor construction materials," *Vop. At.Nauki i Tekhn.,Ser.Yadernye Konstanty*, vol. 1, p. 26, 1994.

132. V. M. Besotosnyj, V. M. Gorbachev, L. M. Suvorov, and M. S. Shvecov, "Cross section of gamma-rays production at inelastic interaction of 14 mev neutrons with different nuclei," Institut Atomnoi Energii I.V. Kurchatova, Tech. Rep. Yadernye Konstanty, No.19, 1975.

133. W.E.Tucker, D.O.Nellis, P.S.Buchanan, and J.A.Stout, "Gamma-ray production in nitrogen and oxygen," Texas Nuclear Corp, Tech. Rep. Oak Ridge Operations Office, contract report, No.2791-30, 1969.

134. V. M. Bezotosnyi, V. G. Vershinin, L. M. Surov, and M. S. Shvetsov, "Cross sections for the production of gamma quanta in inelastic interaction between 14-mev neutrons and c, o, al, fe, and pb nuclei," *Yadern.Fiz.*, vol. 3, p. 861, 1966.

135. V. V. Nefedov, V. I. Popov, and Y. S. Yazvitskii, "Gamma-radiation in inelastic interaction between fast neutrons and atomic nuclei," in *Soviet Progress in Neutron Physics*, 1963, p. 241.

136. L. C. Thompson and J. R. Risser, "Gamma rays from the inelastic scattering of 14-mev neutrons in $c^{12}$ and $o^{16}$," *Phys.Rev.*, vol. 94, p. 941, 1954.

137. R. B. Day, "Gamma rays from neutron inelastic scattering," *Phys.Rev.*, vol. 102, p. 767, 1956.

138. K. Hasegawa, M. Mizumoto, S. Chiba, M. Sugimoto, Y. Yamanouti, M. Igashira, and H. Kitazawa, "Gamma-ray production cross section measurements of some structural materials between 7.8 and 13.0 mev," in *Nuclear Data for Science and Technology*, S. M. Qaim, Ed. Berlin, Heidelberg: Springer Berlin Heidelberg, 1992, pp. 329–331.

139. C. Nordborg, L. Nilsson, H. Conde, and L. G. Stromberg, "Gamma-ray production cross sections of neutron-induced reactions in oxygen," *Nucl.Sci.Eng.*, vol. 66, p. 75, 1978.

140. T. Yamamoto, Y. Hino, S. Itagaki, and K. Sugiyama, "Gamma-ray production cross sections for interactions of 14.8 mev neutrons with o, na, al, cl, cr, fe, ni, cu and pb," *J.Nucl.Sci.Tech.*, vol. 15, p. 797, 1978.

141. B. Lundberg, L. G. Stromberg, and H. Conde, "Gamma rays from inelastic neutron scattering in oxygen," *Phys.Scr.*, vol. 2, p. 273, 1970.

142. A. Bertin, F. Bertrand, and G. Clayeux, "Cross sections for production of gamma-rays by neutrons of 5 mev, 6.6 mev and 8.7 mev on nitrogen, oxygen, scandium and gold," Centre d'Etudes Nucleaires, Tech. Rep. Saclay Reports, No.4047, 1969.

143. B. I. Sukhanov and N. P. Tkach, "Gamma rays in inelastic interaction of 14.-mev neutrons with n,o,al, and fe nuclei," *Soviet Journal of Nuclear Physics*, vol. 11, p. 17, 1970.

144. G. Clayeux and G. Grenier, "Recoil spectra produced by 14.1 mev neutrons," Centre d'Etudes Nucleaires, Tech. Rep. Saclay Reports, No.3807, 1969.

145. I. L. Morgan, J. B. Ashe, and D. O. Nellis, "Angular distribution of gamma rays from c, o, and n at en=14.8 mev," Texas Nuclear Corp, Tech. Rep. Div. of Tech. Info. U.S. AEC Reports, No.22012, 1964.

146. J. T. Prud'Homme, I. L. Morgan, J. H. McCrary, J. B. Ashe, and O. M. H. Jr, "A study of neutrons and gamma rays from neutron induced reactions in several elements," Texas Nuclear Corp, Tech. Rep. Air Force Spec.Weap.Center Kirtland A.F.B.Repts., No.60-30, 1960.

147. M. Shamsuzzoha Basunia, "Nuclear data sheets for a = 27," *Nuclear Data Sheets*, vol. 112, no. 8, pp. 1875–1948, 2011. [Online]. Available: https://www.sciencedirect.com/science/article/pii/S0090375211000664

148. K. A. Weaver, "Spectra of neutrons from deuteron bombardment of light nuclei (ucrl-51310)," University of California/Livermore, Tech. Rep., 1973.

149. "Goodfellow. Ceramic - physical properties. [Online]. Available: https://www.goodfellow.com/catalogue/GFCat2C.php?ewd_token=tphTA606DZfrrvdNpJan7loqRvDVbM&n=WEY314Y7nwfIiEStfK733G7bLdwvQO&ewd_urlNo=GFCat26&type=60&prop=2

150. N. C. for Biotechnology Information". Aluminum oxide, cid=9989226. [Online]. Available: https://pubchem.ncbi.nlm.nih.gov/compound/Aluminum-oxide

151. Leica Geosystems, "Leica DISTO S910," Accessed 23 Dec 2021 [Online]. [Online]. Available: https://shop.leica-geosystems.com/buy/package/s910

152. mesytec GmbH & Co. KG, "MDPP-16 SCP/RCP," Accessed 11 Dec 2021 [Online]. [Online]. Available: https://www.mesytec.com/products/datasheets/MDPP-16_SCP-RCP.pdf

153. mesytec GmbH & Co. KG, "MDPP-16 QDC," Accessed 11 Dec 2021 [Online]. [Online]. Available: https://www.mesytec.com/products/datasheets/MDPP-16_QDC.pdf

154. B. Rooney, S. Garner, P. Felsher, P. Karpius, and M. Lombardi, *PeakEasy 4.99 [Computer Program]*, Los Alamos National Laboratory, Release LA-CC-13-040, 2020. [Online]. Available: https://PeakEasy.lanl.gov

155. Z. Kis, B. Fazekas, J. Östör, Z. Révay, T. Belgya, G. Molnár, and L. Koltay, "Comparison of efficiency functions for ge gamma-ray detectors in a wide energy range," *Nuclear Instruments and Methods in Physics Research Section A: Accelerators, Spectrometers, Detectors and Associated Equipment*, vol. 418, no. 2, pp. 374–386, 1998. [Online]. Available: https://www.sciencedirect.com/science/article/pii/S0168900298007785

156. W. J. Gallagher and S. J. Cipolla, "A model-based efficiency calibration of a si(li) detector in the energy region from 3 to 140 kev," *Nuclear Instruments and Methods*, vol. 122, pp. 405–414, 1974. [Online]. Available: https://www.sciencedirect.com/science/article/pii/0029554X74905084

157. E. Browne and J. Tuli, "Nuclear data sheets for a = 66," *Nuclear Data Sheets*, vol. 111, no. 4, pp. 1093–1209, 2010. [Online]. Available: https://www.sciencedirect.com/science/article/pii/S0090375210000360

158. J. Chen, J. Cameron, and B. Singh, "Nuclear Data Sheets for A = 35," *Nuclear Data Sheets*, vol. 112, no. 11, pp. 2715–2850, 2011. [Online]. Available: https://www.sciencedirect.com/science/article/pii/S0090375211000950

159. MilliporeSigma, "Sodium chloride," Accessed 10 Jan 2022 [Online]. [Online]. Available: https://www.sigmaaldrich.com/US/en/product/sigald/31434

160. H. Junde, H. Su, and Y. Dong, "Nuclear data sheets for a = 56," *Nuclear Data Sheets*, vol. 112, no. 6, pp. 1513–1645, 2011. [Online]. Available: https://www.sciencedirect.com/science/article/pii/S0090375211000457

161. A. Lim, A. Mahl, J. Latta, H. A. Yemam, U. Greife, and A. Sellinger, "Plastic scintillators with efficient light output and pulse shape discrimination produced via photoinitiated polymerization," *Journal of Applied Polymer Science*, vol. 136, no. 15, p. 47381, 2019.

162. M. Febbraro, "3d printing of photocurable scintillating and low-background materials," presented at CPAD Instrumentation Frontier Workshop, Stony Brook, NY, USA, 2021.

163. MilliporeSigma, "Isobornyl acrylate," Accessed 3 Nov 2021 [Online]. [Online]. Available: https://www.sigmaaldrich.com/US/en/product/aldrich/392103

164. MilliporeSigma, "1,6-Hexanediol dimethacrylate," Accessed 3 Nov 2021 [Online]. [Online]. Available: https://www.sigmaaldrich.com/US/en/product/aldrich/411736

165. MilliporeSigma, "Bisphenol A dimethacrylate," Accessed 3 Nov 2021 [Online]. [Online]. Available: https://www.sigmaaldrich.com/US/en/product/aldrich/156329

166. MilliporeSigma, "Pentaerythritol tetraacrylate," Accessed 3 Nov 2021 [Online]. [Online]. Available: https://www.sigmaaldrich.com/US/en/product/aldrich/408263

167. MilliporeSigma, "Divinylbenzene," Accessed 3 Nov 2021 [Online]. [Online]. Available: https://www.sigmaaldrich.com/US/en/product/aldrich/414565

168. MilliporeSigma, "Diphenyl(2,4,6-trimethylbenzoyl)phosphine oxide," Accessed 3 Nov 2021 [Online]. [Online]. Available: https://www.sigmaaldrich.com/US/en/product/aldrich/415952

169. I. Pawełczak, S. Ouedraogo, A. Glenn, R. Wurtz, and L. Nakae, "Studies of neutron–$\gamma$ pulse shape discrimination in ej-309 liquid scintillator using charge integration method," *Nuclear Instruments and Methods in Physics Research Section A: Accelerators, Spectrometers, Detectors and Associated Equipment*, vol. 711, pp. 21–26, 2013. [Online]. Available: https://www.sciencedirect.com/science/article/pii/S0168900213000880

170. A. Tomanin, J. Paepen, P. Schillebeeckx, R. Wynants, R. Nolte, and A. Lavietes, "Characterization of a cubic ej-309 liquid scintillator detector," *Nuclear Instruments and Methods in Physics Research Section A: Accelerators, Spectrometers, Detectors and Associated Equipment*, vol. 756, pp. 45–54, 2014. [Online]. Available: https://www.sciencedirect.com/science/article/pii/S0168900214003222

171. M. A. Norsworthy, A. Poitrasson-Rivière, M. L. Ruch, S. D. Clarke, and S. A. Pozzi, "Evaluation of neutron light output response functions in ej-309 organic scintillators," *Nuclear Instruments and Methods in Physics Research Section A: Accelerators, Spectrometers, Detectors and Associated Equipment*, vol. 842, pp. 20–27, 2017.

172. J. A. Brown, B. L. Goldblum, T. A. Laplace, K. P. Harrig, L. A. Bernstein, D. L. Bleuel, W. Younes, D. Reyna, E. Brubaker, and P. Marleau, "Proton light yield in organic scintillators using a double time-of-flight technique," *Journal of Applied Physics*, vol. 124, no. 4, p. 045101, 2018. [Online]. Available: https://doi.org/10.1063/1.5039632

173. T. Laplace, B. Goldblum, J. Bevins, D. Bleuel, E. Bourret *et al.*, "Comparative scintillation performance of ej-309, ej-276, and a novel organic glass," *Journal of Instrumentation*, vol. 15, no. 11, p. P11020, 2020.

174. MilliporeSigma, "2,5-Diphenyloxazole," Accessed 3 Nov 2021 [Online]. [Online]. Available: https://www.sigmaaldrich.com/US/en/product/aldrich/d210404

175. MilliporeSigma, "1,4-Bis(2-methylstyryl)benzene," Accessed 3 Nov 2021 [Online]. [Online]. Available: https://www.sigmaaldrich.com/US/en/product/aldrich/15090

176. Luxottica Exciton, "DPS," Accessed 3 Nov 2021 [Online]. [Online]. Available: https://exciton.luxottica.com/pub/media/productattach/Datasheet/04060.pdf

177. Luxottica Exciton, "Exalite 416," Accessed 3 Nov 2021 [Online]. [Online]. Available: https://exciton.luxottica.com/pub/media/productattach/Datasheet/04160.pdf

178. formlabs, "Form Cure," Accessed 3 Nov 2021 [Online]. [Online]. Available: https://formlabs.com/store/form-cure/

179. Dymax, "Flood Curing Systems," Accessed 3 Nov 2021 [Online]. [Online]. Available: https://dymax.com/products/equipment/light-curing-equipment/flood-curing-systems

180. "FluoroMax - Steady State and Lifetime Benchtop Spectrofluorometer," Accessed 3 Nov 2021 [Online]. [Online]. Available: https://www.horiba.com/en_en/products/detail/action/show/Product/fluoromax-1576

181. Hamamatsu Photonics, "Photomultiplier tube r7724," 2021. [Online]. Available: https://www.hamamatsu.com/jp/en/product/type/R7724/index.html

182. CAEN S.p.A, "Compass - multiparametric daq software for physics applications," 2021. [Online]. Available: https://www.caen.it/products/compass/

183. CAEN S.p.A, "Dt5730/dt5730s," 2021. [Online]. Available: https://www.caen.it/products/dt5730/

184. Eljen Technology, "Pulse Shape Discrimination EJ-276 & EJ-276G," Accessed 4 Nov 2021 [Online]. [Online]. Available: https://eljentechnology.com/products/plastic-scintillators/ej-276

185. O. McCormack, L. Giacomelli, G. Croci, A. Muraro, G. Gorini *et al.*, "Characterization and operational stability of ej276 plastic scintillator-based detector for neutron spectroscopy," *Journal of Instrumentation*, vol. 16, no. 10, p. P10002, 2021.

186. G. Chikkur and N. Umakantha, "A new method of determining the compton edge in liquid scintillators," *Nuclear Instruments and Methods*, vol. 107, no. 1, pp. 201–202, 1973. [Online]. Available: https://www.sciencedirect.com/science/article/pii/0029554X73900347

187. D. Horrocks, *Applications of Liquid Scintillation Counting*. Elsevier Science, 2012.

188. A. Plompen, T. Fukahori, H. Henriksson, A. Ignatyuk, T. Iwasaki, G. Manturov, R. McKnight, G. Rimpault, and D. Smith, "The nea high priority nuclear data request list for future needs," in *International Conference on Nuclear Data for Science and Technology*. EDP Sciences, 2007, pp. 765–768.

189. M. Schulc, M. Košťál, S. Simakov, V. Rypar, D. Harutyunyan *et al.*, "Validation of differential cross sections by means of 252cf spectral averaged cross sections," *Applied Radiation and Isotopes*, vol. 132, pp. 29–37, 2018. [Online]. Available: https://www.sciencedirect.com/science/article/pii/S0969804317309752

190. Z. Dezso and J. Csikai, "Average cross sections for the $^{252}$cf neutron spectrum," 1977. [Online]. Available: https://www-nds.iaea.org/exfor/servlet/X4sShowPubl?File=C,77KIEV,3,32,1977

191. C. Dupont, P. Leleux, P. Lipnik, P. Macq, and A. Ninane, "Study of a collimated fast neutron beam," *Nuclear Instruments and Methods in Physics Research Section A: Accelerators, Spectrometers, Detectors and Associated Equipment*, vol. 256, no. 2, pp. 197–206, 1987. [Online]. Available: https://www.sciencedirect.com/science/article/pii/0168900287902105

192. D. Schlegel-Bickmann, G. Dietze, and H. Schölermann, "A collimator system for fast neutron scattering experiments," *Nuclear Instruments and Methods*, vol. 169, no. 3, pp. 517–526, 1980. [Online]. Available: https://www.sciencedirect.com/science/article/pii/0029554X80909519

193. E. Lee, C.-W. Lee, S.-C. Yang, Y.-O. Lee, and G. Cho, "Study on collimator design for neutron science facility of raon accelerator complex," *Nuclear Instruments and Methods in Physics Research Section A: Accelerators, Spectrometers, Detectors and Associated Equipment*, vol. 902, pp. 138–143, 2018. [Online]. Available: https://www.sciencedirect.com/science/article/pii/S0168900218307319

194. A. Jalil, A. Chetaine, H. Amsil, K. Embarch, A. Benchrif, K. Laraki, and H. Marah, "Determining pgaa collimator plug design using monte carlo simulation," *Nuclear Engineering and Technology*, vol. 53, no. 3, pp. 942–948, 2021. [Online]. Available: https://www.sciencedirect.com/science/article/pii/S1738573320308354

195. C. J. Werner, J. S. Bull, C. J. Solomon, F. B. Brown, G. W. McKinney, M. E. Rising, D. A. Dixon, R. L. Martz, H. G. Hughes, and L. J. Cox, "Mcnp6.2 release notes," Los Alamos National Lab (LANL), Los Alamos, NM (United States), Tech. Rep., 2018.

196. C. J. Werner, J. S. Bull, C. J. Solomon, F. B. Brown, G. W. McKinney, M. E. Rising, D. A. Dixon, R. L. Martz, H. G. Hughes, and L. J. Cox, "Mcnp users manual - code version 6.2," Los Alamos National Lab (LANL), Los Alamos, NM (United States), Tech. Rep., 2018.

197. M. P. Groover, *Fundamentals of modern manufacturing: materials, processes, and systems*. John Wiley & Sons, 2020.

198. Velmex, Inc., "BiSlide," Accessed 24 Jan 2022 [Online]. [Online]. Available: https://www.velmex.com/Products/BiSlide/BiSlide_Motorized.html?gclid=Cj0KCQiAubmPBhCyARIsAJWNpiOawI0n5_pt1ITrbvVYpL4K6ydIea2YzFc0TxqPmIk89GnJ74eMPJUaAv-5EALw_wcB

199. N. D'Olympia, P. Chowdhury, C. Lister, J. Glodo, R. Hawrami, K. Shah, and U. Shirwadkar, "Pulse-shape analysis of clyc for thermal neutrons, fast neutrons, and gamma-rays," *Nuclear Instruments and Methods in Physics Research Section A: Accelerators, Spectrometers, Detectors and Associated Equipment*, vol. 714, pp. 121–127, 2013. [Online]. Available: https://www.sciencedirect.com/science/article/pii/S0168900213002349

200. M. Bourne, C. Mussi, E. Miller, S. Clarke, S. Pozzi, and A. Gueorguiev, "Characterization of the clyc detector for neutron and photon detection," *Nuclear Instruments and Methods in Physics Research Section A: Accelerators, Spectrometers, Detectors and Associated Equipment*, vol. 736, pp. 124–127, 2014. [Online]. Available: https://www.sciencedirect.com/science/article/pii/S0168900213013764

201. Hamamatsu Photonics, "Photomultiplier tube r6094," 2021. [Online]. Available: https://www.hamamatsu.com/jp/en/product/type/R6094/index.html

202. CAEN S.p.A, "Dt5533e," 2022. [Online]. Available: https://www.caen.it/products/dt5533e/

203. CAEN Technologies, "GECO2020," https://www.caen.it/products/geco2020/, accessed: 3 Dec 2021.

204. C. Solomon, C. Bates, and J. Kulesza, "The mcnptools package: Installation and use," *Los Alamos National Laboratory Technical Report (LA-UR-29981)*, 2017.

# REPORT DOCUMENTATION PAGE

*Form Approved*
*OMB No. 0704–0188*



| 1. REPORT DATE *(DD–MM–YYYY)* | 2. REPORT TYPE | 3. DATES COVERED *(From — To)* |
|---|---|---|
| 04-03-2022 | PhD Dissertation | Sep 2018 — Mar 2022 |

**4. TITLE AND SUBTITLE**

Capability Development for Advanced (n,x) Nuclear Data Measurements

**5a. CONTRACT NUMBER**

**5b. GRANT NUMBER**

HDTRA1033292

**5c. PROGRAM ELEMENT NUMBER**

**6. AUTHOR(S)**

Frandsen, Brian G, Major, USAF

**5d. PROJECT NUMBER**

**5e. TASK NUMBER**

**5f. WORK UNIT NUMBER**

**7. PERFORMING ORGANIZATION NAME(S) AND ADDRESS(ES)**

Air Force Institute of Technology
Graduate School of Engineering and Management (AFIT/EN)
2950 Hobson Way
WPAFB OH 45433-7765

**8. PERFORMING ORGANIZATION REPORT NUMBER**

AFIT-ENP-DS-22-M-091

**9. SPONSORING / MONITORING AGENCY NAME(S) AND ADDRESS(ES)**

ATTN: LTC Nickolas Duncan (nickolas.duncan@westpoint.edu)
Defense Threat Reduction Agency
8725 John J. Kingman Rd. Stop 6201
Fort Belvoir, VA 22060-6201

**10. SPONSOR/MONITOR'S ACRONYM(S)**

DTRA

**11. SPONSOR/MONITOR'S REPORT NUMBER(S)**

**12. DISTRIBUTION / AVAILABILITY STATEMENT**

APPROVED FOR PUBLIC RELEASE; DISTRIBUTION UNLIMITED.

**13. SUPPLEMENTARY NOTES**

**14. ABSTRACT** Nuclear reaction data are the heart of radiation transport calculations, models, and simulations. Unique approaches are required to improve the measurement capability for many reactions where data are inaccurate or do not exist. First, the newly developed Gamma Energy Neutron Energy Spectrometer for Inelastic Scattering (GENESIS) provides the ability to measure neutron inelastic scattering cross sections on different targets. An initial experiment measuring the $^{16}$O(n,n'$\gamma$) reaction calculated the count rate from the second excited state using the full energy and escape peaks. Second, a set of photocurable scintillator resin formulations capable of neutron-gamma discrimination were developed to support light-based 3D printing applications for advanced nuclear physics measurements. The formulations resulted in hard, clear, PSD-capable plastic scintillators that cured within 10 seconds using 405 nm light, produced a light yield up to 83% of EJ-276, and a pulse shape discrimination figure of merit of 1.28 at 450-550 keVee. Lastly, a fast neutron beam facility was established to improve thermal-neutron sensitive experiments by designing and installing a tungsten collimator that reduced the thermal neutron background by $\sim$778x.

**15. SUBJECT TERMS**

Nuclear data, inelastic scattering, radiation detection, plastic scintillator, neutron collimator

| 16. SECURITY CLASSIFICATION OF: | | | 17. LIMITATION OF ABSTRACT | 18. NUMBER OF PAGES | 19a. NAME OF RESPONSIBLE PERSON |
|---|---|---|---|---|---|
| a. REPORT | b. ABSTRACT | c. THIS PAGE | | | Maj James E. Bevins, AFIT/ENP |
| U | U | U | U | 218 | 19b. TELEPHONE NUMBER *(include area code)* (937) 255-3636 |